Utility and Limitations of Cardiac Tissue Slices for the Study of Cardiac Electrophysiology

Thesis submitted for the degree of Doctor of Philosophy

Ken Wang
Merton College
Department of Computer Science

Supervisor:
Prof. David Gavaghan, Prof. Peter Kohl, Dr. Gary Mirams

Abstract

Cardiac tissue slices, a rarely used pseudo two-dimensional preparation, have gained increasing popularity for applications such as drug testing over the last ten years as they combine ease of handling with patho-physiologically relevant cell-type representation, distribution and inter-connection.

The most well-established methods to measure electrophysiology in cardiac tissue are sharp electrodes and multi-electrode-arrays, techniques which are limited in spatial resolution or signal content. In this work, we have applied dual voltage Ca^{2+} optical mapping on cardiac slices, allowing us to record these two key parameters simultaneously at high spatio-temporal resolution, yielding better visualisation of conduction waves, spatial dispersion in action potential (AP) characteristics, and intracellular Ca^{2+} transient (CaT). The slice preparation method and the measurement protocols were refined to yield good reproducibility. Data analysis routines were developed to extract relevant parameters reliably.

Despite being a promising candidate for drug testing, little is known about how slice and intact whole-heart AP properties are interrelated, and how to scale-up from observations in two dimensions (2D) to the three dimensional (3D) heart. In this thesis, we present a method to compare directly AP properties of intact whole-heart and tissue slices, and show the extent to which slices preserve AP characteristics.

We have explored the suitability of tissue slices as an experimental model to study stretch induced changes in AP and CaT. During axial stretch, a dynamic profile of both AP and CaT was observed with an initial shortening of both AP and CaT duration, followed by a gradual recovery/prolongation.

We have also used tissue slices to study spatial heterogeneity of AP and CaT properties in the rabbit left ventricular free wall. A transmural gradient can be captured in CaT and AP

(with the longest APD and CaT durations being captured in the subendocardium). No large AP prolongation was found in the mid-myocardium.

We conclude that the cardiac tissue slice preparation preserves some key functional parameters of the whole heart and is a promising model to study cardiac electrophysiology.

Acknowledgement

I would like to express my sincere gratitude to my supervisors, Prof. David Gavaghan, Prof. Peter Kohl and Dr. Gary Mirams for their invaluable guidance and patient support during the course of my study. Their knowledge and enthusiasm gave me great strength throughout my thesis research and have made a profound impact on my future career endeavours.

I would like to thank Dr. Christian Bollensdorff for all his support, guidance and companionship during the course of this study. Without him, the tissue slice experiments would not have been possible.

I would like to thank the team in Harefield Heart Science Centre as well as the team in Oxford for all their support and assistance. I would like to thank Dr. Padmini Sarathchandra and Dr. Brian Mitchelson for all their advice and help in the histology work. And I would like to thank Dr. Peter Lee for all his technical support on optical mapping.

I would like to thank Prof. Charlotte Deane, Dr. Gail Preston and Prof. David Gavaghan at the Doctoral Training Centre for opening the door to my doctorate and providing the biological, mathematical and computational training needed to conduct interdisciplinary research.

A special thanks to my parents for their long term emotional and generous financial support that enabled me to finish my study.

I would like to thank Microsoft Research for funding my study and British Heart Foundation for funding the research work.

Table of abbreviations:

AP	Action Potential
APD	Action Potential Duration
APD20	Action Potential at 20% Repolarisation
APD50	Action Potential at 50% Repolarisation
APD80	Action Potential at 80% Repolarisation
APD90	Action Potential at 90% Repolarisation
ATP	Adenosine Triphosphate
AV	Atrio-Ventricular
BDM	2,3-Butanedione 2-Monoxime
Ca,L	L-type Ca^{2+} Channel
CaT	Intracellular Ca^{2+} Concentration Transient
CaT50	CaT Duration at 50% Decay of CaT
CaT80	CaT Duration at 80% Decay of CaT
Ca^{2+}	Calcium Ion
$[Ca^{2+}]_i$	Intracellular Ca^{2+} Concentration
CO_2	Carbon Dioxide
DMSO	Dimethyl Sulfoxide
EC_{50}	Half Maximal Effective Concentration
ECG	Electrocardiogram
EM	Electron Microscopy
EMCCD	Electron Multiplying Charge-Coupled Device
FPD	Field Potential Duration
HEPES	4-(2-Hydroxyethyl)-1-

	Piperazineethanesulfonic Acid
I_{Ks}	Slowly Activated Delayed Rectifier Potassium Ion Current
I_{Kr}	Rapidly Activated Delayed Rectifier Potassium Ion Current
Ito	Transient Outward Potassium Ion Current
K^+	Potassium Ion
K_{ATP}	ATP-Sensitive Potassium Channel
LED	Light-Emitting Diode
LV	Left Ventricle
MEA	Multi-Electrode Array
MEF	Mechano-Electric Feedback
$[Na^+]_i$	Intracellular Sodium Ion Concentration
Na^+	Sodium Ion
NCX	Sodium-Calcium Exchanger
O_2	Oxygen
PDMS	Polydimethylsiloxane
RV	Right Ventricle
RT	Room Temperature
RyR	Ryanodine Receptor
SAC	Stretch Activated Channel
SAN	Sino-Atrial Node
SD	Standard Deviation
SERCA	Sarco-Endoplasmic-Reticulum-Calcium-ATPase
SR	Sarcoplasmic Reticulum
V_m	Trans-Membrane Potential

2D	Two Dimensional
3D	Three Dimensional

Contents

Chapter 1

General Introduction and Methodology

The primary function of the cardiovascular system is the rapid transport of oxygen, nutrients, and water to tissues, and the efficient washout of metabolic waste products. The human heart is the primary pump for this system; it consists of four chambers and pumps ~200 million litres of blood via ~3 billion contractions over a lifetime. The contraction of the heart is governed and synchronised by electrical signals which originate from the Sino-Atrial Node (SAN) and give rise to a wave of electrical excitation in the following sequence: SAN, right and left atria, Atrio-Ventricular (AV) node, His bundle and Purkinje system, interventricular septum, left and right ventricle. This synchronised contraction pattern can be disrupted and this can lead to life-threatening arrhythmias where the heart cannot pump blood efficiently. Cardiovascular disease remains one of the primary causes of death in the world. There are different underlying pathological conditions (both congenital and externally induced) that contribute to cardiovascular risk. To improve the diagnosis and treatment of cardiovascular diseases, it is important to understand both the function of a healthy heart and the pathological mechanisms in a diseased heart. These mechanisms are not only studied in patients in the clinic, but also on human biopsy material, engineered cardiac tissue and animal models (*in vitro* and *in vivo*) in the laboratory. The engineered cardiac tissue and animal models provide possibilities to investigate mechanisms and to test hypotheses with a range of protocols in a (potentially) better controlled manner, compared to patient *in vivo* measurements. Different *ex vivo* experimental preparations and models were developed to

study cardiac function and disease mechanisms. Depending on the targeted question and the tissue type available, some experimental preparations may be more desirable than others. This thesis focuses on describing a pseudo two dimensional (2D) preparation, the live cardiac tissue slice, along with multi-parametric optical mapping to study several cardiac phenomena (e.g. mechano-electric feedback (MEF), action potential (AP) spatial heterogeneity, or changes in electrophysiological parameters under drug interventions). In this first chapter, commonly used *ex vivo* preparations and the utility and limitations of the optical mapping technique are reviewed.

1.1 Commonly used Preparations for Studying Trans-membrane Potential and Intracellular Ca^{2+} Concentration Transient

At the cellular level, the membrane of a cardiac myocyte depolarises and repolarises due to the activities of ion channels, exchangers and pumps (with initial depolarisation triggered by neighbouring cells for non pace-maker cells). During depolarisation of the cell membrane, the L-type Ca^{2+} channels (Ca,L) are activated due to increased membrane voltage, allowing initial entry of Calcium ions (Ca^{2+}) into the cell. This local increase in Ca^{2+} level triggers Ca^{2+} release from the sarcoplasmic reticulum (SR), the main intracellular Ca^{2+} store, via ryanodine receptors (RyR). This leads to a large rise in intracellular Ca^{2+} concentration ($[Ca^{2+}]_i$) [1] (see Figure 1.1). Binding of Ca^{2+} to troponin C causes a change to its molecular configuration which results in exposure of myosin binding sites on actin, enabling cross-bridge movement, and subsequent contraction [2].

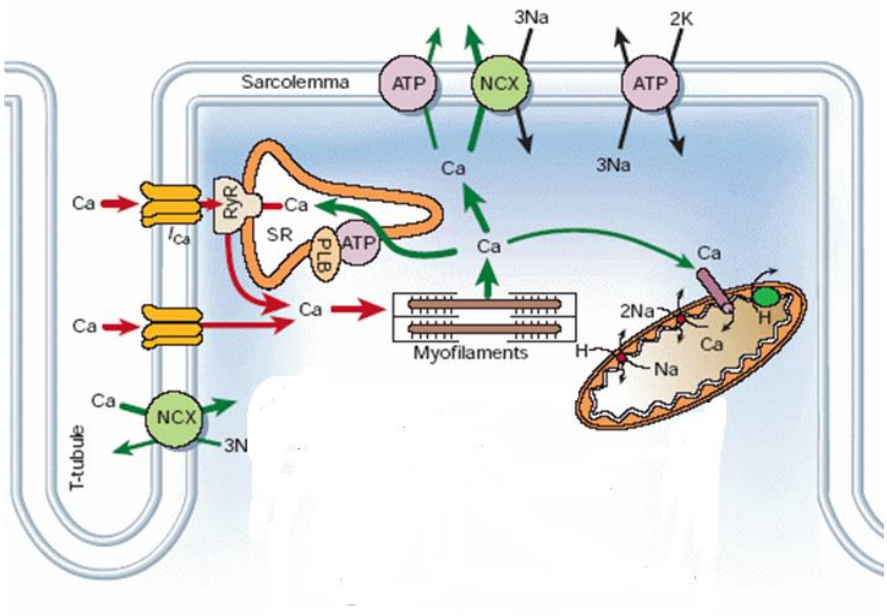

Figure 1.1 Schematic diagram showing Ca^{2+} handling in the cardiac muscle cells: Ca^{2+} enters the cell via Ca,L inducing Calcium-induced-Calcium-release from SR (via RyR), Ca^{2+} binds to myofilaments and initiates contraction, cytosolic Ca^{2+} is then taken up by the sarco-endoplasmic reticulum ATPase (SERCA) into the SR or extruded by sarcolemmal Ca^{2+} pump and sodium/Calcium (Na^{+}/Ca^{2+}) exchanger (NCX). This figure also shows mitochondria buffering of Ca^{2+}. Modified from [3]. The red arrows indicate the entry of Ca^{2+} from Ca,L, the release of Ca^{2+} from SR (these two processes are responsible for the increase in the $[Ca^{2+}]_i$) and binding of Ca^{2+} onto the myofilaments. The green arrows indicate unbinding of Ca^{2+} from the myofilaments, uptake of Ca^{2+} into the SR and mitochondria and the extrusion of Ca^{2+} from the cell via NCX. The black arrows indicate the uptake and extrusion of some other relevant ions (such as sodium and potassium ions).

Both the trans-membrane potential and the $[Ca^{2+}]_i$ transient (CaT) are key parameters in cardiac physiology, and the delicate interplay between these two parameters is crucial for cardiac function. A lot of effort has been invested in studying these two parameters using different preparations including: single cells; cell cultures; papillary muscles and trabeculae, Langendorff-perfused whole hearts or *in vivo* measurements. In scaling up from single cells to the whole heart, this preparation reflects the *in vivo* situation better, although at the same time complexity increases, making it more difficult to deduce the mechanisms underlying any observed phenomena (see Figure 1.2). In the section below, the measurement techniques

applied to some of the commonly used preparations are reviewed briefly, together with their uses and limitations.

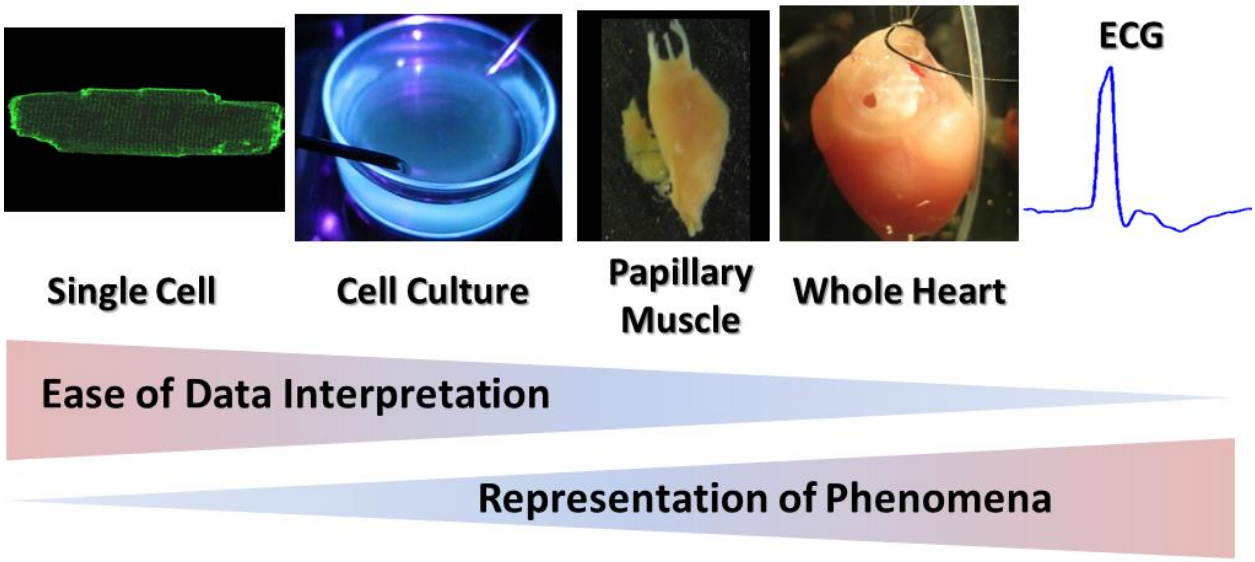

Figure 1.2 Pictures showing some commonly used preparations for studying heart function: single cell, cell culture, papillary muscle, whole heart and *in vivo* electrocardiogram (ECG) measurement.

1.1.1 Isolated Single Cell

The introduction of methods to isolate viable embryonic heart cells dates back at least to the 1950s when the embryonic chick heart was digested using trypsin [4]. Isolation of cells from the adult heart seemed to be more difficult compared to the embryonic heart due to stronger connections between cells. Different methods have been investigated including mechanical disruption (homogenisation) [5, 6], and digestion with proteolytic enzymes [7-10]. In 1976, Powell et al. (London Middlesex) published a method for isolation of adult rat myocardium (perfusion with collagenase containing Calcium-free bicarbonate buffered solution) which significantly increased the yield of intact single cells that tolerated external Ca^{2+} [11]. Since then, efficient methods have been developed for isolation of myocardial cells from different species, including human [12].

The $[Ca^{2+}]_i$ at single cell level can be measured optically with Ca^{2+} sensitive dyes (a more detailed review is given in the next section). Apart from the overall CaT, at single cell level intracellular Ca^{2+}-related events such as Ca^{2+} waves [13] or Ca^{2+} sparks [14] can also be resolved and captured with confocal microscopy.

The trans-membrane potential of isolated single cells can be monitored optically [15, 16] or via sharp electrode [17] and whole-cell patch clamp [18]. The utility and limitations of the optical method will be described in the next section. Channel activities underlying the trans-membrane potential, can also be recorded with whole-cell patch clamp [19] using different voltage-clamp protocols for, for example: Ca,L current [20] or rapidly activated delayed rectifier potassium ion current (I_{Kr}) [21]. With a cell-attached configuration or cell-free excised patch [19], single channel dynamics can be captured. Using patch clamp on single cells enables exploration of the underlying mechanisms at channel (or exchanger) level. For example, by performing patch clamp on a single cell, one can test and verify whether a change in AP e.g. during mechanical stretch [22] or pharmacological intervention [21] is caused by a specific ion channel.

The unique advantage of isolated single cells is the possibility to explore intracellular mechanisms at the protein level (e.g. ion channels). At the same time, these preparations are relatively low in throughput and lack important aspects of the *in vivo* situation, for example cell-cell connections and the extracellular matrix.

1.1.2 Cell Culture

In 1907, Harrison demonstrated the possibility of growing and developing embryonic frog neuronal tissue *in vitro* [23]. In the light of this important finding, Burrow et al. attempted to culture pieces of explanted embryonic chick heart in 1912 and observed both active growth of cells into the surrounding media and the rhythmic beating of the cultured heart cells [24].

Apart from embryonic or neonatal heart cells, which can have quite different properties compared to mature cells, it is also possible to culture adult myocytes *in vitro* [25]. A lot of effort has also been put into developing methods to culture human stem cells and to transform them into myocyte-like cells [26, 27].

The trans-membrane potential of cultured myocytes (individual cells) can be measured using microelectrodes [28] and the overall trans-membrane potential signal of a cell culture can be measured optically [29-31] or via a multi-electrode array (MEA) [32]. The CaT in cell cultures can be measured via optical mapping [29, 30].

As a multi-cellular preparation, cell cultures provide the possibility of studying tissue-level phenomenon such as conduction wave, source-sink relation as well as re-entry. The use of cell cultures provides the possibility of carrying out studies over a more extended period of time compared to freshly isolated tissue (cultures can be maintained for days instead of hours) [33], thus allowing alteration of protein expression by gene targeting [34]. The cardiac cell culturing technique is beneficial for maintaining human biopsy material (especially to generate cultures from heart tissue with pathological conditions) [35, 36] and opens up exciting opportunities to engineer cardiac tissue to treat diseased hearts (reviewed in [37]). However, even adult myocyte cell cultures (particularly long term cultures) show differences in morphology [38, 39] and electrophysiology [28, 39] compared to freshly isolated tissue. Although investigations have been carried out to reduce the difference between cell culture and freshly isolated tissue: e.g. co-culturing the myocyte with fibroblasts [40], or improving the directional alignment of cells [41], native cell-cell connections are disrupted during the culturing process. It is also difficult to maintain the natural spatial cell type distribution (e.g. myocyte, fibroblast, endothelial cells) of the *in vivo* myocardium in cell cultures.

1.1.3 Papillary Muscle and Trabeculae

Isolated papillary muscle and trabeculae are frequently used experimental models and have been used to study changes in electrophysiology under external environmental challenges (e.g. hyperthermia) [42], external mechanical perturbation [43], or drug intervention [44-46]. For this preparation, the trans-membrane potential is most commonly monitored by micro-electrodes [42-45] but it is also possible to measure it optically [46]; CaT can also be mapped in this preparation [47].

Compared to cell cultures and single isolated cells, papillary muscles and trabeculae are native tissues of the heart with natural cell types and cell-cell connections preserved. However, these two preparations are dissected from specific parts of the heart and therefore do not reflect other regions of the heart (like the mid-myocardium of the ventricular wall). These preparations can also potentially suffer from limited diffusion of oxygen into the core of the tissue if the dissected preparation is too thick (above the oxygen diffusion limit [48]).

1.1.4 Perfused Whole Heart

The perfused heart is a classical cardiac preparation. Pioneered by Oscar Langendorff in 1895, the method of retrograde heart perfusion has been extended and refined (please see [49] for detailed review and description of this method). Other perfused heart preparation methods such as the working heart have also been developed [50]. Perfused whole heart preparations have been used to study a broad range of cardiac physiological properties (e.g. contractility [51], MEF [52], electrophysiology [53]), pathophysiology (fibrillation [54], remodelling of physiological parameters in diseased hearts [55]), drug action [56]). The trans-membrane potentials in perfused whole heart can be measured by plunge electrodes [57], surface electrodes [58], or optical mapping [59]. CaT can be measured through mapping with Ca^{2+} sensitive dyes [59].

Compared to other *in vitro* preparations, the perfused heart is an intact organ and is thought to reflect the *in vivo* situation well. Compared to *in vivo* preparations, this approach can isolate the heart from other organs (e.g. the nervous system) in studies and therefore reduces the complexity of the system. However, compared to other *ex vivo* preparations such as cell culture or single cell, perfused whole heart is more complex and data interpretation is not always easy.

1.1.5 *In vivo* Measurement

Cardiac electrophysiology has also been studied extensively *in vivo*. Non-invasive methods like the ECG are widely used in the clinic to diagnose cardiac abnormalities in patients. Research has been carried out to refine ECG recordings to improve their ability to capture abnormalities: for example a special 67 lead ECG has been developed which can pick up Brugada syndrome much more accurately than a conventional 12 lead ECG [60]. Apart from these non-invasive ECG studies, catheter-based endocardial electrical mapping has been performed [61]. Studies have also been performed on open-chest patients [62] or animal models [63]. Plunge electrodes have been used to record electrophysiological parameters (such as the activation-repolarisation interval) in open chest subjects [62, 63]. There have also been attempts to employ optical mapping in open chest *in vivo* preparations (rat) to study trans-membrane potential and CaT [64].

The data recorded from *in vivo* preparations has direct clinical relevance. However the highly complicated system underlying *in vivo* measurements such as the ECG makes it difficult to pin-point the exact mechanism underlying a observed changes.

1.2 Living Tissue Slices

The tissue slice, an *in vitro* pseudo 2D model, is not a new preparation to study physiology and biochemical phenomena. Since Otto Warburg introduced the use of living tissue slices in

1923 [65], the technique has been developed to harvest living slices from different organ systems, for example: brain [66], liver [67], lung [68] and kidney [69]. The key to utilising this preparation is to keep the slice thin enough for oxygen to diffuse into the core of the tissue. Warburg calculated the maximum slice thickness to be around 500 μm with an oxygen consumption rate of 3 mL/g/h.

Despite being a frequently used preparation for organs like the brain; cardiac tissue slices have not been very popular compared to preparations such as single cells or Langendorff-perfused hearts. This is probably mainly due to the difficulty in obtaining viable slices from the tough tissue. Organs like the brain and the liver can be sectioned with a relatively simple microtome, but a more precise sectioning methodology with slow blade advance speed and minimal z-direction deflection is needed to reduce damage to cardiac cells and thus yield a healthy cardiac slice. In the sections below, the applications and the uses of cardiac slices as a model to study cardiac electrophysiology are briefly reviewed. The use of cardiac tissue slices has also been reviewed elsewhere [70, 71].

1.2.1 Uses of Cardiac Tissue Slices

Cardiac tissue slices have been used for metabolism-related research such as investigations into oxygen consumption [72-74] and ATP production [73] under control conditions [72] or with drug intervention [73, 74]. Cardiac slices have also been used to investigate the biochemical properties of heart tissue: e.g. studying the regulation of DNA synthesis [75]. Using an Rb^+ uptake assay, a series of studies have been performed to explore the impact of dietary magnesium [76], digitaloids [77, 78] and ageing [78] upon cardiac Na^+/K^+ pump activity using tissue slices. These studies showed the possibility of using tissue slices as a model to study cardiac electrophysiology.

However, it was not until 1990 that Burnashev et al. expanded the use of patch clamp techniques on brain slices to cardiac slices [79]. In this study, they demonstrated it was possible to measure both single channel activity (with the cell attached configuration) and whole cell current (with the whole-cell mode). Since then, other electrophysiological recording techniques, like sharp electrodes [80-82] and MEAs [83, 84], have been used on cardiac slices to monitor trans-membrane potential. Among these studies, the work from Bussek et al. [83, 85] and Camelliti et al. [84] demonstrated the suitability of cardiac slices as an *ex vivo* model to study the impact of pharmaceutical compounds on electrophysiological parameters. It was also reported that it is possible to maintain cardiac slices over several days for extended studies [80]. The trans-membrane potential from cardiac slices has also been mapped using optical dyes [86-88] and this combination was used to study re-entry in the pseudo '2D' preparation [86, 87].

1.2.2 Benefits of Cardiac Tissue Slices

Although cardiac slices have not received much attention, this preparation can offer unique insights into cardiac electrophysiology. Depending on the question, this preparation can be the most appropriate choice compared to other preparations.

Considering the complexity of the system and its ability to capture *in vivo* phenomena, tissue slices can bridge nicely the gap between two popular models: isolated single cells and perfused whole hearts. Compared to single cells, preserved cell-cell connections enable tissue slices to capture tissue-level phenomena like conduction waves, and the locally intact extracellular microenvironment avoids the potential 'remodelling' of physiological properties due to the loss of extracellular matrix and the damage during the cell isolation process. Compared to perfused whole heart, tissue slice is a much simpler model which makes the interpretation of structure-function relationships (e.g. the correlation between cell direction

and conduction speed) much easier to assess. Tissue slice also allows full access to mid-myocardial tissue, which is more difficult to study in a perfused whole heart.

Compared to other 2D models (e.g. the cell culture), the tissue slice preserves native cell-cell connections and natural cell type distribution. Being a freshly isolated tissue preparation, tissue slices can also reduce the morphological and physiological remodelling of cardiac cells that can occur during any cell culturing process. These properties make tissue slices a more *in vivo*-like preparation compared to cell cultures. Tissue slices and isolated papillary muscles are preparations where perfusion depends purely on passive diffusion. Tissue slice is less intact compared to papillary muscle. However, since the thickness of the slice can be controlled in a relatively accurate manner, one can ensure that the tissue slice is well oxygenated (even in the core of the tissue) and can avoid the potential risk of ischaemia. Tissue slices also open up the possibility of studying tissue from different regions of the heart: for example, the left ventricular (LV) and right ventricular (RV) free wall and the septum.

1.3 Optical Mapping

Fluorescent imaging techniques have been used widely in biological research. Since the development of voltage sensitive [89] and Ca^{2+} sensitive dyes, it is possible to monitor trans-membrane potential and CaT optically. Optical mapping is now an established method for most cardiac preparations [15, 16, 29, 30, 46, 47, 59, 64]. In the section below, the utility of optical mapping and the methodology to perform dual voltage and Ca^{2+} mapping (focusing more on the combinations used in our group) are briefly reviewed. For more detailed reviews of cardiac optical mapping, please see [90-92].

1.3.1 Uses and Limitations of Optical Mapping

The use of fluorescent imaging has significantly advanced the understanding of cardiac physiology and has led to a number of important findings: for example the proof of Calcium-induced Calcium-release – a key mechanism of mechanical-electrical coupling [93]. The use of Ca^{2+} sensitive dye allows monitoring of the change in free [Ca^{2+}] in the cytosol [13, 14, 59], SR [94] and mitochondria [95]. As a non-invasive method, use of optical mapping to record the trans-membrane potential can avoid potential disturbances in the targeted parameter due to rupture and damage of the cell membrane when recording this parameter with techniques such as patch clamp or sharp electrodes. Compared to field potentials recorded via contact electrodes (such as MEAs), optical mapping can capture the entire AP shape instead of just the activation recovery interval, and is very beneficial for studies involving interventions or pathological conditions that can significantly alter AP shape. A camera-based optical mapping system can provide higher spatial resolution compared to other recording techniques like sharp electrodes, or even MEAs, and is potentially beneficial to study tissue-level phenomena such as fibrillation.

1.3.2 Dual Voltage and Ca^{2+} Mapping

Recording trans-membrane potential and CaT simultaneously allows one to study the complex interplay between these two key parameters, and dual voltage and Ca^{2+} optical mapping is a good method to achieve high spatial resolution. Depending on the spectral properties of the dyes, there are different configurations for dual voltage and Ca^{2+} mapping:

1) A single excitation source for both dyes, two sensors to capture emission of voltage and Ca^{2+} sensitive dyes separately (or use of an optical splitter to project the image onto two parts of one sensor);

2) Two separate excitation sources, 2 sensors to capture emission of voltage and Ca^{2+} sensitive dyes separately;
3) Two separate excitation sources, one sensor to capture emission of voltage and Ca^{2+} sensitive dyes in a shared-frame basis.

The first option is suitable for combinations of dyes which have overlapping excitation wavelengths and separate emission wavelengths. The combination of RH237 and Rhod-2 falls into this category [94, 96, 97]. The second option suits dyes with different excitation wavelengths and separate emission wavelengths. The third option requires dyes that have different optimal excitation wavelengths. For dual mapping of trans-membrane potential and CaT using dye combinations such as Di-4-ANBDQPQ and Rhod (see chapter 2), Di-4-ANBDQBS and Fluo (see chapter 2), Fura and Di-4-ANBDQPQ [59] or Fura and Di-4-ANEPPS, one can make use of dual excitation configurations.

In our group, the third configuration (one-sensor based) is often used, which is based on synchronisation of light switching and camera frame [59]. When the camera takes a frame, one of the light sources is switched on, when the camera finishes taking that frame, the light source is switched off, and for the next frame, the other light source is switched on. In this way the camera captures voltage and Ca^{2+} signals in consecutive frames (i.e. one frame voltage signal, one frame Ca^{2+} signal). Since the frame rate used in our study (including all of the studies shown in this thesis) is reasonably fast (~500 frames per second for a spatial resolution of 128x128 pixels), the pseudo-simultaneous mapping method works well for capturing the temporal correlation between the parameters recorded. It is potentially beneficial to use the one-sensor based configuration (i.e. option 3) to avoid problems like spatial miss-alignment of $Ca^{2+}$and voltage images. Some of these dyes, for example Di-4-ANBDQPQ and Fura, have multiple excitation wavelengths which can yield a good signal, and so these dyes can be used for ratiometric measurements [59].

1.3.3 Limitations

Most of the optical mapping measurements are performed on 'immobilised' tissue. In addition to the fact that some of the uncouplers (such as 2,3-Butanedione 2-monoxime (BDM)) used to immobilise the tissue can alter the electrophysiological parameters (by directly interacting with ion channels/pumps [98]), reduction or removal of the impact of MEF upon electrophysiological parameters can also change observed behaviour [99]. To overcome this problem, techniques such as motion correction and motion tracking will be needed. Tracking/correcting motion with highly accurate pixel alignment is still a challenge that remains to be resolved.

Photon scattering is another drawback of optical mapping. As both the excitation and the emission light travel and scatter in the tissue, the signal recorded from 'one point' via optical mapping does not only come from that point, but from a tissue volume around that point. Due to photon scattering, the upstroke of optically mapped signals from tissue preparations such as a Langendorff-perfused whole heart can be blurred [100]. Simulation methods can help to understand the distortion of signals due to photon scattering [101].

There are also other limitations such as photo-toxicity of the dye (mainly for voltage-sensitive dyes) and wash-out or bleaching over time (particularly problematic for a long study). These can be potentially improved with refinement of dyes. Ca^{2+} sensitive dye leakage from cytoplasmic matrix into the extracellular medium can be reduced by using an organic anion transporter inhibitor (such as probenecid) [102]. As Ca^{2+} sensitive dyes are Ca^{2+} chelators, they disturb the Ca^{2+} handling process (this can be particular a problem for Ca^{2+} sensitive dyes with high Ca^{2+} binding affinity, these high affinity dyes are needed for monitoring the very low resting $[Ca^{2+}]_i$ in cardiac cells).

1.4 Structure of Thesis

To date, the trans-membrane potential of cardiac slices has been measured mainly with low spatial-resolution methods such as sharp electrode or MEAs, and without monitoring the $[Ca^{2+}]_i$. In our study, we combine cardiac tissue slices with dual voltage and Ca^{2+} mapping. This enables us to study the interrelation of these two key parameters in this pseudo 2D preparation (see Figure 2.12 and 2.13). Here, the high spatial resolution allows us to visualise spatial heterogeneities in conduction wave-front and the AP duration (APD) (see Figure 2.23).

Since this mapping technique provided information (e.g. AP shape distribution) which is not obtained with other measuring techniques, it appeared to us that refinements both in the slice preparation and in measurement protocols were needed to achieve high reproducibility in the data obtained from this system. The refined preparation methodology and measuring techniques are detailed in chapter 2. Notes of caution together with data supporting them are also included in chapter 2. The methodology described in chapter 2 (2.2.1 General methodology for this Thesis) is also applied (at least partially) to the studies described in chapter 3, 4 and 5.

For any *in vitro* experimental model, one of the important questions is how well the model can capture the *in vivo* situation, and how it behaves compared to more intact preparations. However, little is known about how well cardiac slices reflect the situation in intact heart. In chapter 3, our method to section Langendorff-perfused whole hearts at body temperature is detailed. APs recorded from whole heart epicardium/subepicardium are compared with those measured from the epicardial slice.

In chapter 4, we describe a study where we explored the suitability of tissue slices as an experimental model to study MEF. In this study, we measured AP and CaT before, during (several time points) and after application of axial stretch. We found that it is possible to

correlate the stretch direction with the predominant cell direction. The stretch method and results regarding changes in AP and CaT due to stretch are included in chapter 4.

Since cardiac tissue slices provide the unique possibility of having full access to all layers of tissue in the ventricular free wall, we used LV tissue slices, together with dual parameter optical mapping, to study the spatial heterogeneity of APD and CaT duration in rabbit LV free wall. The protocols used and results that we found are detailed in chapter 5.

A brief conclusion is included in chapter 6 together with some suggestions about possible projects (both experiments and simulation) that could be performed in future based on studies presented in this thesis.

Chapter 2

General Methodology: Reliable Extraction of Action Potential and Ca^{2+} Concentration Transient from Cardiac Tissue Slices

Brief Summary of Chapter 2:

In this chapter, we describe in detail the optimised method to prepare cardiac tissue slices from guinea pig and rabbit left ventricular free wall and to perform dual AP and CaT optical mapping on these slices. We describe how reproducibility of AP and CaT data, obtained from cardiac tissue slices, can be increased by careful control of experimental conditions: in particular, the slice recovery protocol and the stimulation method.

A post-cutting recovery time of 40 to 70 min is needed to measure steady state AP from slices. The rapid increase in APD shortly after cutting is mainly due to the ice-cold temperature the tissue experienced during the slicing procedure. For any before/after investigations (such as drug testing), one needs to carefully control the pacing location to exclude contributions of source-sink mismatches from the observed effects.

My contribution to this chapter:

- The tissue slice optical mapping experiments included in this chapter were performed together with Dr. Christian Bollensdorff. I was responsible for improving the tissue slice preparation and the staining procedure, as well as developing a semi-automated analysis tool to extract relevant parameters from our data sets.
- The confocal and electron microscope (EM) work (to check the tissue viability) mentioned in this chapter were done together with Dr. Padmini Sarathchandra.

- The content of this chapter is included in a manuscript submitted to the American Journal of Physiology – Heart and Circulatory Physiology, and is currently under review.

2.1 Introduction

The history of live tissue slices was reviewed in chapter 1. The use of cardiac tissue slices dates back to at least the 1950s in a proof of concept study that explored the possibility of obtaining thin cardiac tissue fragments from the left ventricle (LV) [66]. A number of slice studies since then have demonstrated additional applications, including the study of re-entry induction by premature stimuli [87], research into DNA synthesis [103], measurement of oxygen consumption [74, 104], assessment of the ATP-sensitive potassium channel (K_{ATP}) contributions to ischaemic preconditioning [105], and drug testing [83, 85].

To date, no standardised approach to the preparation and maintenance of cardiac tissue slices has been agreed upon. A few key parameters have been recognised as critical for obtaining minimally-damaged thin live cardiac slices, including: slow advance cutting speeds; minimal z-axis (perpendicular to the cutting plane) deflection of the blade; slice thicknesses < 400 μm; and slicing along a plane tangential to the epicardium. High-precision vibratomes can section tissue with both tightly controlled slow blade advance speeds and minimal z-axis deflection (<1 μm). In previously reported studies, cardiac slice thicknesses varied from 150 μm [81] to 500 μm [86, 87]. In order to maintain sufficient oxygen diffusion to all cells inside the section, investigators now favour slices of no more than 400 μm thickness [48], to avoid potential ischaemia. As initially suggested by Yashura et al. in the 1990s [104], cutting ventricular tissue tangentially to the epicardial surface allows for an optimised alignment of (at least near-epicardial) slices with locally prevailing cell orientation, compared to transmural sections. This was confirmed by Bussek et al., comparing the results of different cutting directions using 2-photon microscopy and histology [83]. In addition,

after cutting, cardiac slices should be placed in buffered solution and allowed to recover before experimental recordings are taken. Previous studies used different recovery protocols, with durations ranging from 30 min [79] to two hours [104], and with different buffer solutions. Thus far, no detailed information about the influence of post-cutting recovery protocols on electrophysiological measurements has been published.

The aim for this part of the project is to refine the experimental conditions, tissue slice preparation, and measurement method to achieve better reproducibility. In this chapter, detailed methods needed for reliably recording reproducible AP and CaT data from rabbit and guinea pig cardiac tissue slices with relatively high spatial resolution are described. As optical mapping generates large data sets per experiment, it can be challenging to extract relevant information from these data sets. In this chapter, a method for processing such data to extract relevant characteristics of the AP and CaT is described.

2.2 Materials & Methods

2.2.1 General Methodology for This Thesis

2.2.1.1 Heart Isolation

New Zealand White rabbits (1-2 kg) and guinea pigs (250-400 g) were humanely killed, either by anaesthetic overdose (pentobarbital, 70 mg/kg for rabbit) or cervical dislocation (guinea pig), in accordance with Schedule 1 of the UK Home Office Animals (Scientific Procedures) Act 1986. Hearts were quickly excised and perfused in Langendorff mode with bicarbonate-buffered solution (containing, in mmol/L: NaCl 123, $CaCl_2$ 1.8, KCl 5.4, $MgCl_2$ 1.2, NaH_2PO_4 1.4, $NaHCO_3$ 24, Glucose 10; bubbled with 95% O_2/5% CO_2; pH 7.4 at 35±2^{o}C). For electro-mechanical uncoupling (after dye loading and before optical mapping and slicing), blebbistatin (10 μmol/L, Ascent Scientific, Cambridge, UK) was added. All chemicals were obtained from Sigma-Aldrich (Dorset, UK), unless otherwise stated.

2.2.1.2 Dye Loading

Rabbit

Fluorescent dyes were loaded via the coronary circulation, applied by injection into the aortic cannula. First, 20 µL of a solution containing the voltage-sensitive dye di-4-ANBDQPQ (27 mmol/L in ethanol, University of Connecticut Health Center, USA) and Pluronic F-127 (2 µL of a 20% stock solution in DMSO added to 20 µL dye solution; Life Technologies, Paisley, UK) was slowly added over a 4–5 min period (i.e. at a perfusion rate of 16-20 mL/min, the dye was diluted in ~ 65-100 mL bicarbonate-buffered solution during application). To improve Ca^{2+} sensitive dye loading and retention of the dye in the cytoplasmic matrix, rabbit hearts were pre-perfused with bicarbonate-buffered solution containing 0.5 mmol/L probenecid. Probenecid is an organic anion transporter inhibitor which has been used to prevent dye leakage from cytoplasmic matrix into the extracellular medium [102]. The Ca^{2+}-sensitive dye Rhod-2-AM (200-250 µL stock solution, 1 mg/mL in DMSO; AAT Bioquest Inc., Sunnyvale, USA) was slowly added over a 5 min period and the dye-containing solution (~70-100 mL) re-circulated for 40 min. After completion of dye loading, hearts were perfused with bicarbonate-buffered solution to wash out excess voltage- and Ca^{2+}- sensitive dye.

Guinea pig

Langendorff-perfused guinea pig hearts were loaded with 15 µL of a solution containing the voltage-sensitive dye di-4-ANBDQBS (29 mmol/L in ethanol, University of Connecticut Health Center, USA) and Pluronic F-127 (2 µL of a 20% stock solution in DMSO added to 20 µL dye solution; Life Technologies, Paisley, UK) through bolus injection over 4–5 min (at a perfusion rate of 8-10 mL/min, the dye was diluted in 40-50 mL bicarbonate-buffered solution during application). The Ca^{2+}-sensitive dye Cal-520-AM (200 µL, 1 mg/mL in DMSO; AAT Bioquest Inc.) was loaded after the voltage dye and recirculated for 40 min (the

same method as described in the above section). Cal-520-AM has a spectrum very similar to Fluo-4, with an improved signal-to-noise ratio. It also remains inside the cell with little or no need for organic-anion transporter inhibitors such as probenecid [106]. For loading Cal-520-AM, no probenecid was added to the buffer solution, without detriment to the signal quality even hours after loading (~7% signal amplitude relative to background after 6 h, the initial signal amplitude to background ratio after loading was 10%).

2.2.1.3 Slice Preparation in Ice-cold Solution

It is essential to keep tissue immobilised during the slicing procedure, to avoid damage to tissue slices caused by tissue block movements relative to the cutting blade. Therefore, electro-mechanical uncouplers were used to diminish the contractile activity of the tissue block during sectioning. In previous studies, 2,3-Butanedione 2-monoxime (BDM) was used [83-85], while blebbistatin is currently a more widely-accepted standard uncoupler for optical mapping. Both uncouplers were tested. After dye-loading, the heart was perfused with either BDM-containing HEPES-buffered solution (in mmol/L: NaCl 140, $CaCl_2$ 1.8, KCl 5.4, $MgCl_2$ 1, Glucose 11, HEPES 5, BDM 10, and probenecid 0.5 for Rhod-2-AM loaded hearts; bubbled with 99.9% medical grade O_2; pH 7.4) or blebbistatin-containing bicarbonate-buffered solution (contents described as above 2.2.1, with 0.5 mmol/L probenecid for Rhod-2-AM loaded hearts) at room temperature, until the heart reached room temperature and did not show any contractions.

To excise the left ventricular free wall from the heart, the apex was cut off at about $1/8^{th}$ of the total length of the heart to gain access into the LV cavity. Then a cut was made anti-clockwise from the apical side of the heart along the LV-septum border. After reaching the base of the LV, the cut was continued below the circumflex artery along the coronary sulcus, and then turned towards the apex again after covering about $2/3^{rd}$ of the left ventricular free wall. The edges and any papillary muscles present were trimmed to enable flattening of the

excised tissue, before gluing it endocardium-down (using histoacryl tissue adhesive; Braun, Melsungen, Germany) onto a block of 4% agar (low melting-temperature agar, Nusieve GTG agarose, Lonza, NL), which in turn had been fixed on top of the vibratome cutting stage. The tissue block was cut in the tangential plane, relative to the epicardial surface, using a high precision vibratome (7000smz tissue slicer, Campden Instruments Ltd., Loughborough, UK) with a ceramic blade (Campden Instruments Ltd) at a progression speed of 0.03 mm/s (blade travel amplitude 2 mm, frequency 80 Hz). Slices were cut at a thickness of 350 to 400 μm. This was chosen to avoid ischaemic conditions in the tissue core, while still serving as a good source of fluorescent signals. During the slicing procedure, the tissue block was kept in ice-cold oxygenated BDM-containing HEPES-buffered solution (bubbled with 99.9% medical grade $O_{2;}$ pH 7.4 at 4^{o}C) or blebbistatin-containing (10 μM) bicarbonate-buffered solution (bubbled with 95% O_2 5% $CO_{2;}$ pH 7.4 at 4^{o}C).

Tissue slices were collected, placed on a small block of Polydimethylsiloxane (Sylgard 184, Dowcorning, Midland, USA), and fixed in position using a plastic framed soft mesh. These assemblies were placed in oxygenated blebbistatin-containing bicarbonate-buffered solution for tissue recovery at 35±2^{o}C.

2.2.1.4 Dual AP and CaT Mapping of Tissue Slices

For imaging, tissue slices were kept in blebbistatin-containing bicarbonate-buffered solution at 35±2^{o}C. A light emitting diode (LED) (LED-CBT-90-R, peak wavelength 624 nm; Luminus Devices, Billerica, USA) with excitation-filter D640/20x was used for excitation of the membrane voltage sensitive dye. A white light illuminating LED (LED-CBT-90-W; Luminus Devices) was used for excitation of the Ca^{2+}-sensitive dye, using excitation-filter S555/25x for Rhod-2-AM (rabbit) or D470/40x for Cal-520-AM (guinea pig). All filters were obtained from Chroma Technology (Bellows Falls, USA) and LED light was collimated with a plano-convex lens (LA1951; Thorlabs, Ely, UK).

The trans-membrane potential and CaT signals were collected by an EMCCD camera (Cascade 128+; Photometrics, Tucson, USA). For rabbit tissue slice mapping (di-4-ANBDQPQ & Rhod-2-AM), a custom-made multi-band filter ET585/50-800/200 (Chroma Technology) and a 561 nm long-pass filter (BLP01-561R-25; Semrock, Rochester, USA; this filter shows significant transmission only at wavelengths longer than 575 nm) were placed in front the camera lens (Navitar, Rochester, USA) for collection of fluorescent emission. For guinea pig slices (di-4-ANBDQBS & Cal-520-AM), a different custom-made multi-band filter was used (ET525/50-800/200; Chroma Technology). The setup is shown in a schematic diagram in Figure 2.1A, and the transmission percentage waveforms of the excitation and emission filters are shown in Figure 2.1B (2.1B-1 for rabbit and 2.1B-2 for guinea pig).

The EMCCD camera was used at its maximum resolution (128x128 pixels) and at a frame rate of 510 Hz. To obtain the trans-membrane potential and CaT data pseudo-simultaneously using one camera, either trans-membrane potential or Ca^{2+} excitation LEDs were switched on, in a non-overlapping frame-accurate sequence [59]. Therefore each parameter was sampled with a frequency of 255 Hz. Linear interpolation was used to estimate data values between two consecutive measurement points for each parameter to enable comparison of temporal correlation.

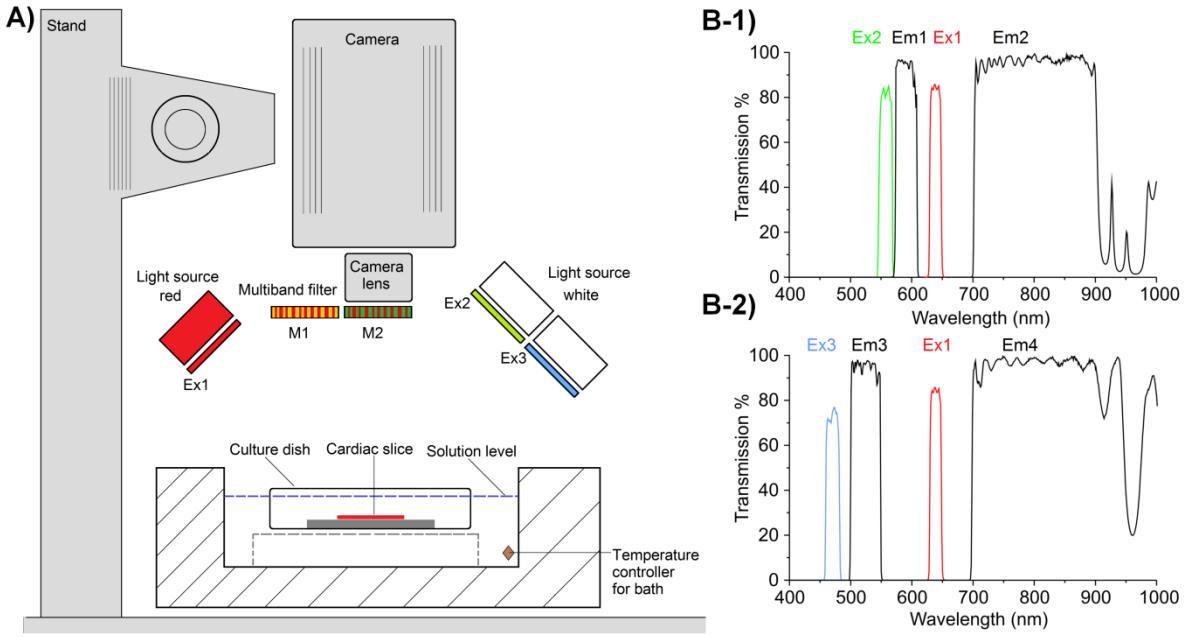

Figure 2.1: Schematic diagram of experimental set-up and filter configuration. A) Diagram showing the optical mapping station for tissue slices. LED sources used are red (for trans-membrane potential), and white (for CaT). The camera is mounted onto an adjustable focussing stand. The water bath (Leica HI1210, Milton Keynes, UK) was maintained at 35 ± 2^{o}C, while slices were kept in a glass cell culture dish in the water-bath, with the level of water around the dish matching the height of the solution inside. The solution was bubbled with 95% O_2/5% CO_2 between measurements, and re-circulated continuously to allow external bubbling throughout the measurements. B-1) Filter characteristics for rabbit slice measurements: the transmission spectra of the multi-band emission filter (M1) and longpass filter, passing emissions from the Ca^{2+} sensitive dye (Em1: 575–610 nm) and the membrane voltage sensitive dye (Em2: 800 ± 100 nm). Note that excitation filters (Ex2 green 555 ± 12.5 nm and Ex1 red 640 ± 10 nm) were chosen to prevent signal bleed-through. B-2) Analogous details for the filter combination used for guinea pig slice measurements: due to the use of a different dye, Ca^{2+}-sensitive fluorescence was collected through a multiband filter (M2) at shorter wavelengths Em3: 525 ± 25 nm; excitation for Ca^{2+}-sensitive dye was filtered in the blue range: 470 ± 20 nm (Ex3); the membrane voltage dye was excited at 640 ± 10 nm (Ex1) and the emission was collected at Em4: 800 ± 100 nm.

2.2.1.5 Pacing

Point Stimulation

Four point electrodes (Lohmann Research, Castrop-Rauxel, Germany) were coupled to a tailor-made electrical stimulator for local stimulation. The four point electrodes were gently placed onto different locations of the tissue slices, as far from one another as possible (affected by slice geometry and ability to induce stimulus capture by the tissue).

Field Stimulation

One set of parallel platinum electrodes were coupled to a tailor-made electrical stimulator for field stimulation. The two platinum electrodes (20 mm x 2 mm x 0.2 mm, placed approximately 3.5 cm apart from each other) were placed parallel to the apex-base direction of the slice.

Pacing Protocol

We recorded trans-membrane potential and CaT signals at 1, 2, 3, 4 and 5 Hz pacing rates (15 APs for each frequency were recorded for each point stimulation site and for field stimulation). The stimulus amplitude was chosen to be 1.5 times the threshold voltage; pulse duration was 2 ms, using a bipolar stimulus to avoid deleterious electrochemical effects.

2.2.1.6 Data Analysis

Due to the large amount of data collected, a semi-automatic data analysis tool was written in Matlab® (The MathWorks, Natick, USA), which automatically analyses the whole data set to extract relevant information. This tool processes the recorded signal, first via polynomial fitting through raw data points, and then extracts information on: signal quality; AP and CaT shape characteristics; AP and CaT duration; CaT amplitude; and conduction velocity throughout a slice. The details for trans-membrane potential signal processing and parameter estimation are shown in Figure 2.2 as a flowchart. The CaT signal processing was conducted in a similar manner. A detailed step-by-step explanation of the analysis routine is included in the Appendix with pseudo code and extracts from the Matlab code.

To extract key information reliably, signal processing is necessary to reduce the impact of noise upon parameter estimation (e.g. APD is calculated from processed trans-membrane potential signal traces). Recorded signal traces were processed through the following steps: 1) identifying the depolarisation time point on the filtered trace to break up the recorded signal trace into individual APs (Figure 2.2 B and C); 2) estimating the maximum (F_{max}) and

baseline (F_0) fluorescence intensity of each identified AP signal and calculating the corresponding signal swing (i.e. $\frac{(F_{max}-F_0)}{F_0} \times 100$ to give the percentage swing) (Figure 2.2D); 3) correcting the initially identified depolarisation time point if needed (Figure 2.2E); 4) polynomial fitting (1^{st} order for depolarisation phase, 4^{th} order for repolarisation phase) through raw data points (Figure 2.2F); 5) linear correction of baseline drift (Figure 2.2G).

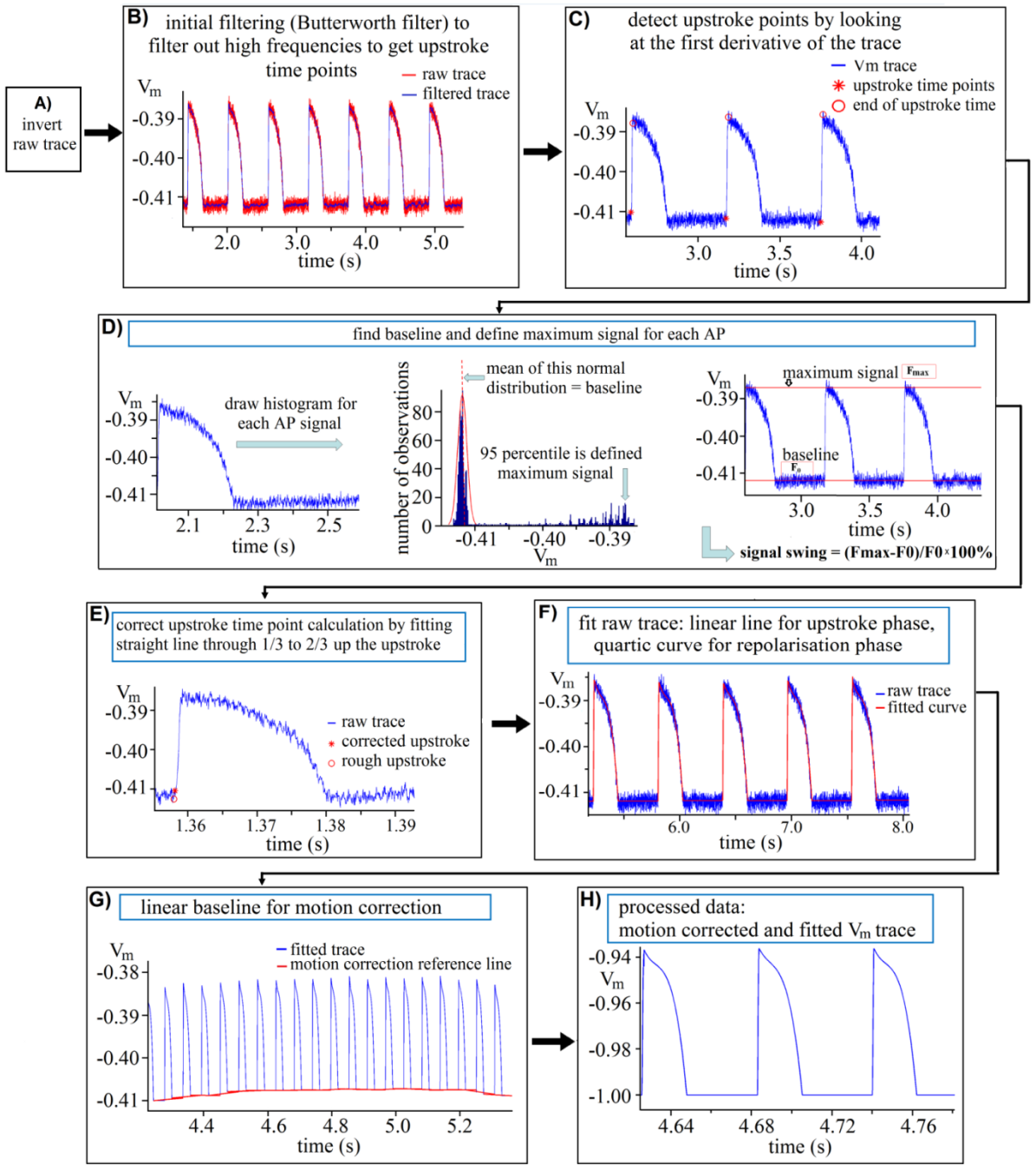

Figure 2.2: Flow chart of optically recorded AP data processing: A) inversion of signal trace; B) low-pass frequency filtering; C) preliminary identification of depolarisation (or upstroke) time points from the filtered trace; D) identification of maximum (F_{max}) and baseline (F_0) of the raw trans-membrane potential (V_m) signal trace; E) correction for the identified upstroke time points; F) polynomial fitting through raw data points; G) linear correction for baseline drift; H) processed trans-membrane potential trace.

Very weak signals (i.e. where the signal swing was <0.3%) were classified as 'no signal'.

Figure 2.3 shows an example of raw and processed trans-membrane potential data from a

representative tissue slice: both de- and repolarisation characteristics can be identified more robustly from the processed data.

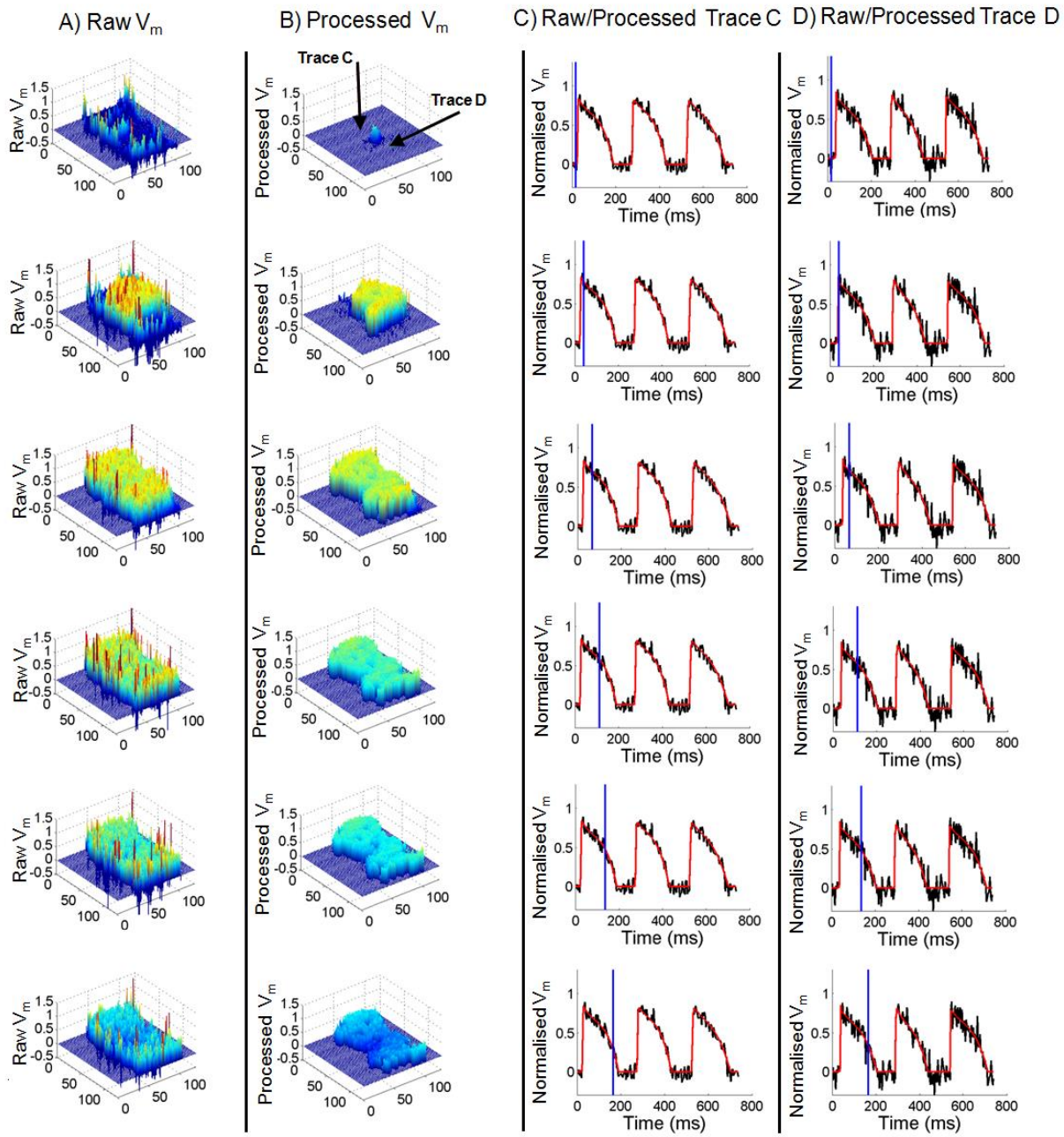

Figure 2.3: Frames, captured at 6 different time-points (15.7, 41.2, 66.6, 111.7, 135.2, 164.6 ms from top row to bottom row) during an activation cycle after stimulation. A) raw trans-membrane potential signal; B) processed and fitted signal, corresponding to the signal processing procedure shown in Figure 2.2A-H. C) and D) are examples of raw signals averaged from a 3x3-pixel square (black) and fitted trace (red) at the location identified by black arrows in the first panel of B, at the different time-points identified by a vertical blue marker.

Particular care needs to be taken when defining the maximum AP amplitude, as this feeds through to the calculation of the APD, customarily defined at set %-repolarisation levels (relative to maximal depolarisation). The maximum AP amplitude is defined by a single data point, which makes peak values extremely sensitive to noise and sampling rate in experimental measurements. Interestingly, similar effects are present in computational simulations, in particular in the presence of pacing-induced amplitude artefacts near a simulated site, as performed in Chaste[1] [107], and shown in Figure 2.4. The red trace in Figure 2.4 was taken from the stimulus site where current injection was applied to the cell model to provoke activation which could artificially increase the AP peak value (the AP peak value in the red trace is much higher compared to the blue trace which was taken from an area away from the stimulus site). This can give rise to artificially exaggerated differences in AP amplitude, with consequent spurious changes in APD estimation (Figure 2.4A). To obtain more physiologically-relevant and robust APD data, both for experimental measurements and simulated traces, a more reproducible identification of the AP 'peak value' is needed. Here, for each AP signal, we use the 95^{th} percentile of the signal amplitude (i.e. the threshold value below which 95% of all data-points of the AP signal fall) as a surrogate for the (apparent) absolute peak value. This parameter is less sensitive to amplitude distortions from any cause, yet allows capture of essential changes in AP shape (see Figure 2.4B). Figure 2.5 shows one AP from an optical mapping measurement (pre-processed with the procedure described in Figure 2.2) with defined maximal value, APD at 50% repolarisation (APD50) and APD at 80% repolarisation (APD80) marked. For our tissue slice optical mapping data, APD80 was used instead of APD at 90% repolarisation (APD90) to reduce the impact of baseline noise on

[1] Chaste is a simulation package aimed at multi-scale, computationally demanding problems arising in biology and physiology. The software is coded in C++. The simulation work presented in this section (as well as the simulation described in section 5.1.2 and 6.3.1) was performed using 'cardiac Chaste' running on Linux platform (using Eclipse as the IDE).

APD estimation. After calculating APDs for each pixel, APD maps can be generated (averaged APD over a number of APs). One example of APD80 and APD50 maps are shown in Figure 2.5.

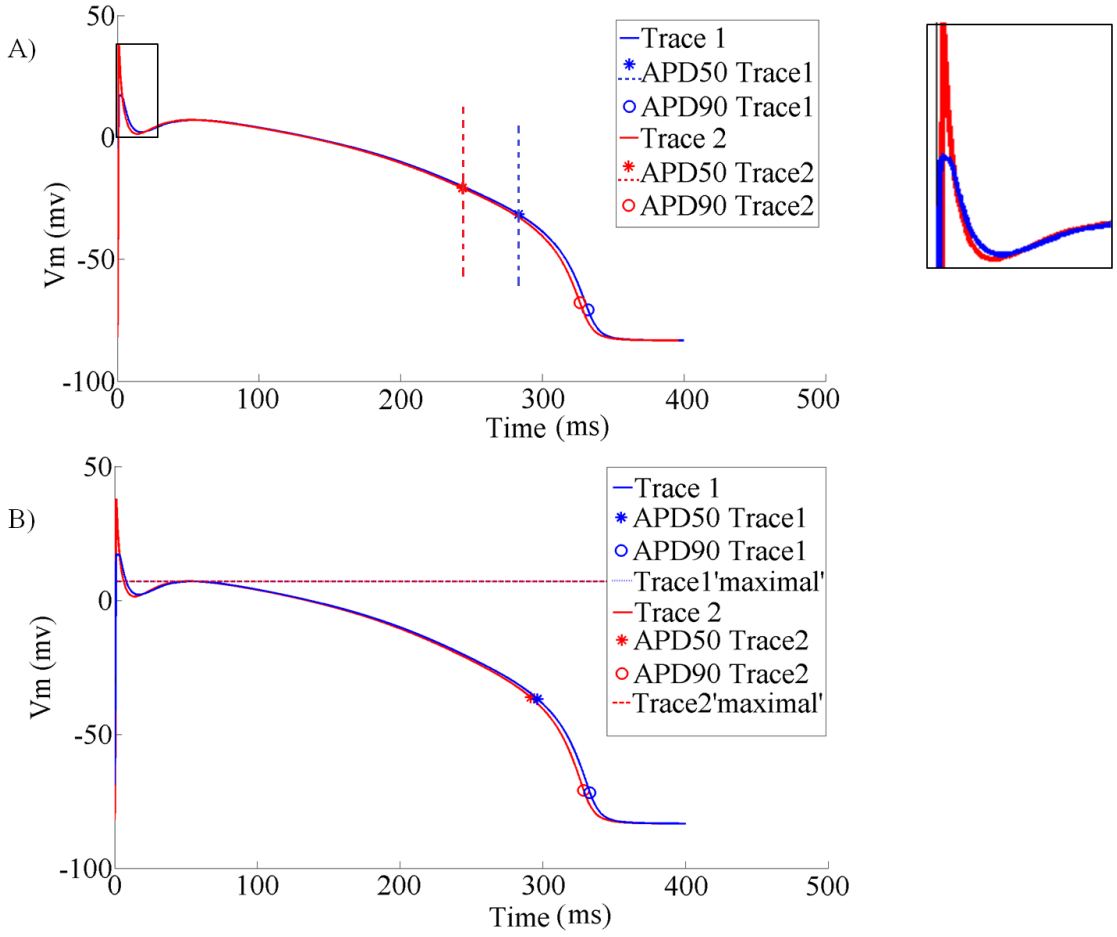

Figure 2.4: Computational simulation showing the effect of identification of spurious AP-maxima on APD parameter calculation. A) AP peak differences (see insert box in A) give rise to a large deviation in APD50. The two simulated AP traces are similar in shape, suggesting that descriptive parameters (such as APD50 and APD90) should have roughly matching values. However, the brief spike of the red trace gives rise to different peak values, which are taken as a reference for APD50 and APD90 calculations. This produces marked differences in the repolarisation time-points identified, in particular for APD50 (here, the difference is as big as 35 ms). B) The same APs, but analysed using our new method for calculating APD50 and APD90. The AP peak identification is based on excluding the top 5 percentile (the 95 percentile thresholds for these two traces are marked as a dotted blue line for trace 1 and a dashed red line for trace 2; note that these 're-identified' maxima are almost overlapping and all data points above these thresholds were excluded) of observed amplitudes. This yields a more reliable reference value, and repolarisation time-points identified are significantly closer to one another (APD50 difference is now 4.4 ms), offering a more robust description of AP shape. AP simulations were conducted using a mono-domain simulation with the Mahajan 2008 cell model [108], simulation performed in Chaste [107].

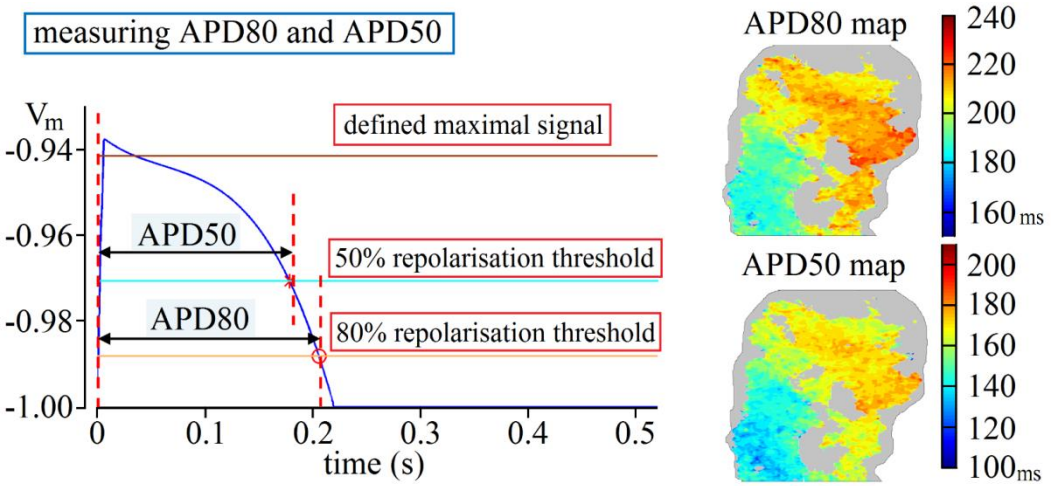

Figure 2.5: Estimation of APD50 and APD80: grey regions in the map indicate tissue with weak or no signal ($(F_{max}-F_0)/F_0$ x100% <0.3%).

To give a quantitative description of the AP shape, two measures are used. The first is the area under AP curve, normalised to the rectangle described by AP amplitude (95^{th} percentile, the defined AP maximal signal amplitude) and APD (described in Figure 2.6, and called the "normalised area ratio"). The smaller this normalised under-curve area, the less rectangular the AP shape. The second indicator (referred to as the AP skewness) was calculated as the skewness (the third standardised moment) of the distribution of all points constituting the processed AP signal: the more negative the skewness, the bigger the portion of time points with high-valued amplitude, indicative of an AP with a more prominent plateau phase (see Figure 2.7).

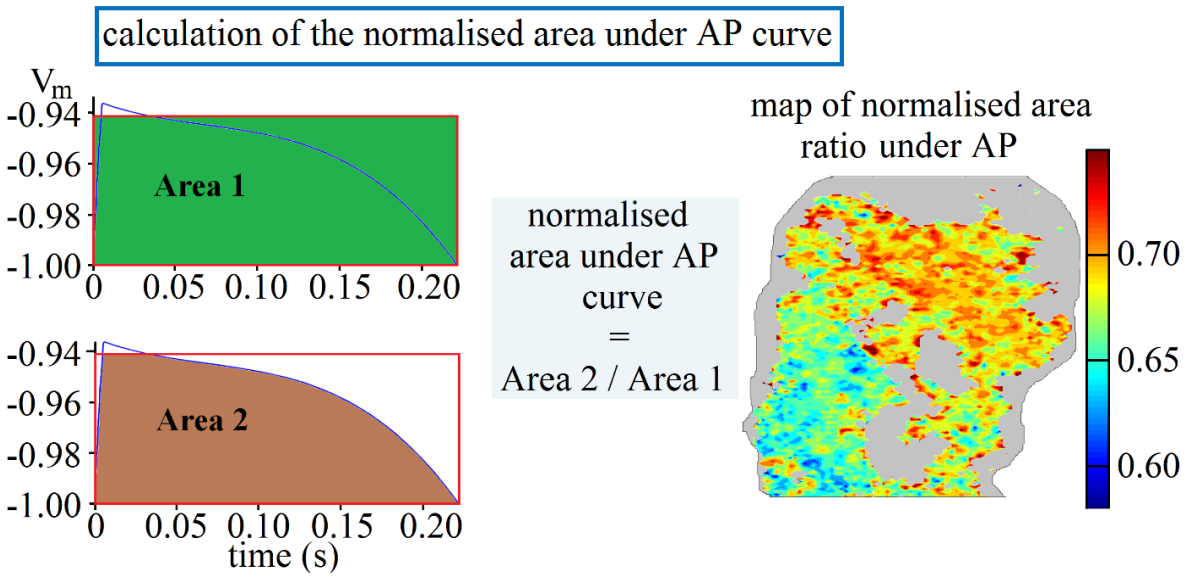

Figure 2.6: Calculation of normalised area ratio: grey regions in the map indicate tissue with weak or no signal ($(F_{max}-F_0)/F_0$ x100% <0.3%). The 95th percentile of the signal amplitude is used as the defined AP peak value for the area calculation instead of the absolute AP peak value.

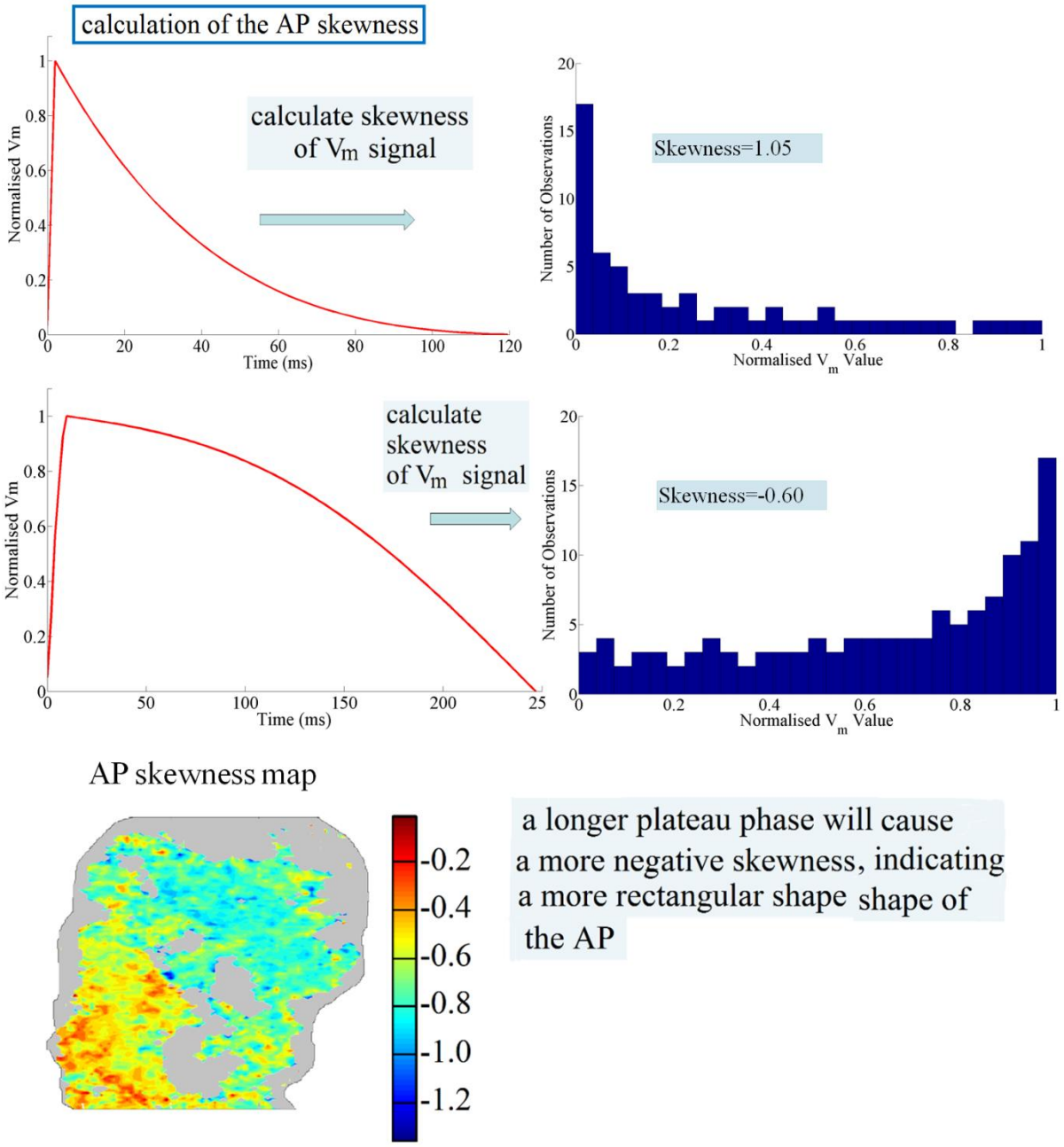

Figure 2.7: Calculation of AP skewness: grey regions in the map indicate tissue with weak or no signal ((F_{max}-F_0)/F_0 x100% <0.3%).

From the processed traces, conduction velocity was estimated using Bayly's method [109] from the upstroke timing in the processed data, the activation wave-front speed was calculated from velocity vectors estimated using activation times across the tissue slice (see Figure 2.8).

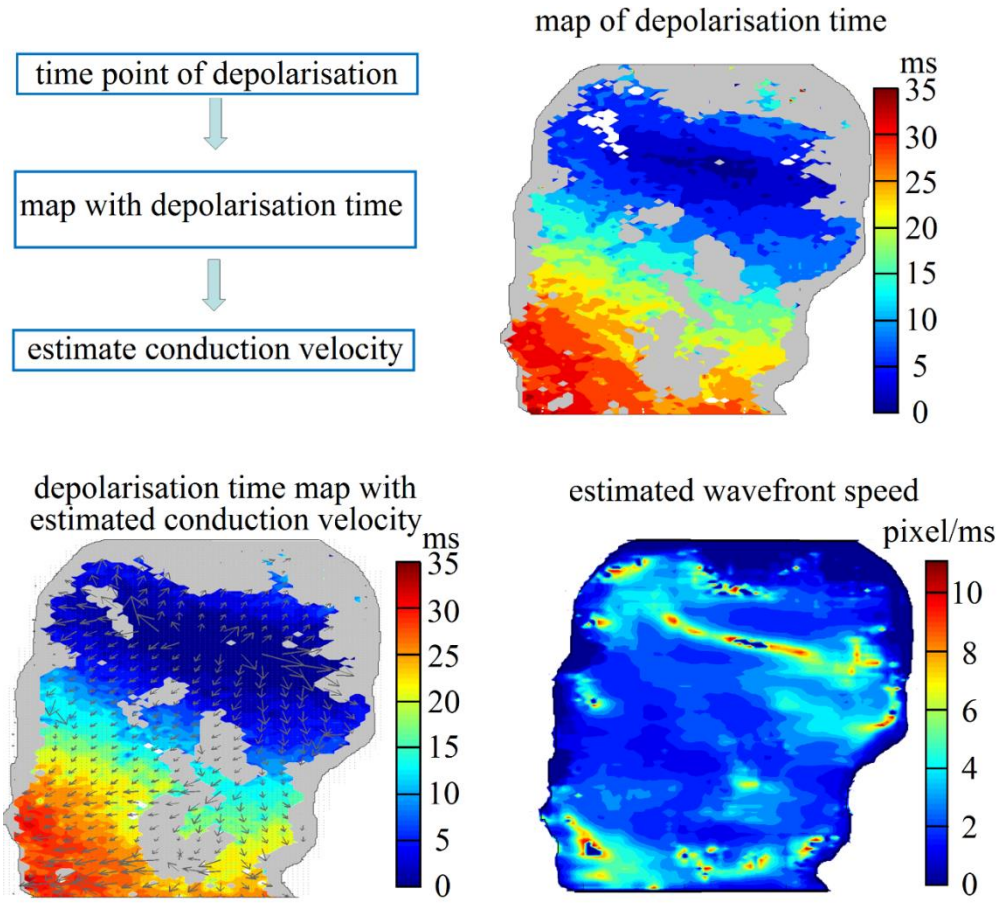

Figure 2.8: Estimation of conduction velocity using Bayly's method: grey regions in the map indicate tissue with weak or no signal ($(F_{max}-F_0)/F_0$ x100% <0.3%).

Before processing each signal trace, spatial filtering (such as mean or Gaussian) can be applied to the optical mapping images. In our case, a mean filter with a range of 3 pixels was applied (i.e. the averaged value of a 3x3 pixel square was taken as the new value of the central pixel in this square). After spatial filtering, the signal trace (i.e. the fluorescent intensity change over time) was read out for each pixel (in the case of dual AP and CaT mapping, AP and CaT traces were separated) and processed with the methods shown in Figure 2.3. Functional parameters (e.g. APD and AP shape indicators) were calculated for each processed AP (or CaT) from the signal trace (as shown in Figures 2.5, 2.6 and 2.7). These functional parameters were then grouped by pacing frequencies, and for each pacing

frequency, the average functional parameter value was taken (for example, 15 steady-state APs were recorded at 2 Hz pacing, and the representative APD value was taken as the average of all 15 APDs). Functional parameter maps (like the APD80 map shown in Figure 2.5 and the AP skewness map shown in Figure 2.7) were plotted for each pacing frequency with each point on the map representing the averaged functional parameter value per slice.

2.2.2 Methodology Specific for Chapter 2

2.2.2.1 Animal Details

Nine Female New Zealand White rabbits (1-2 kg) and three female guinea pigs (250-400 g) were used for the study described in this chapter.

2.2.2.2 Cell Viability Stain

To assess the viability of cells in the tissue slices both immediately after sectioning and after a period of incubation, a cell viability ("live/dead") stain was performed on rabbit left ventricular tissue slices 5 min, 1 h and 4 h after sectioning. During the staining process, tissue slices were placed in oxygenated HEPES buffer solution with 2 μM of Calcein-AM and 4 μM of ethidium homodimer-1 (cell viability assay, Molecular Probes, UK) for half an hour at room temperature. After staining, tissue slices were washed with HEPES buffered solution. Stained slices were imaged by a confocal microscopy (Zeiss, LSM510, Oberkochen, Germany) with excitation wavelength for Calcein-AM and EthD-1 at 488 nm and 594 nm, respectively. The emission of Calcein-AM and EthD-1 were collected at 517 nm and 617 nm, respectively.

2.2.2.3 Electron Microscopy

To assess the health condition of cardiac tissue slices in terms of intracellular structures, slices were fixed with 2.5% buffered glutaraldehyde (Agar Scientific, Stansted, United Kingdom). Samples were taken from several regions of the slice (i.e. from the edges and from

the middle) and embedded in Araldite resin. Sections of 100 nm were cut and imaged using an electron microscope (EM) (Jeol 1200 EX, Welwyn Garden City, United Kingdom).

2.2.2.4 Visualisation of Cardiac Cell Orientation

To get a more macroscopic view of the slice samples (e.g. in terms of the preferred direction of cardiac cells), 1 μm thick sections were cut from the resin embedded tissue samples (these samples were also used for EM imaging) and stained with Toluidine blue (VWR, Lutterworth, United Kingdom). These stained sections were scanned under a digital slide scanner (Nanozoomer RS, Hamamatsu, Japan) at 20x magnification.

2.2.2.5 Whole Heart Epicardial Imaging

For some hearts (rabbit: n = 2; guinea pig n = 2), optical mapping was performed prior to slicing, to assess the dye loading and to collect functional parameters from epicardial/subepicardal regions in the Langendorff-perfused intact heart. During whole heart imaging, the heart was perfused with blebbistatin-containing bicarbonate-buffered solution (contents described above) with the left ventricular free wall facing the camera. Light source, excitation, and emission filters were the same as described above for tissue slice imaging in the two species, respectively.

2.2.2.6 Assessment of Post-Sectioning

To assess whether post-sectioning recovery had reached steady state and to obtain the minimal recovery time needed to measure steady state AP, tissue slices were mapped at several post-cutting time points (2 to 161 min after sectioning in ice-cold solution).

2.3 Results

2.3.1 Assessment of Tissue Slice Viability

An assay was performed to illustrate the viability of cells in cardiac tissue slices. The confocal images of slices 5 min (Subfigure A) and 4 h (Subfigure B) after sectioning are shown in Figure 2.9. The images show live cells (green: fluorescent coming from the cytosol of intact cells) in both cases (with more dead cells (red: stain of nuclei of the dead cells) after 4 h).

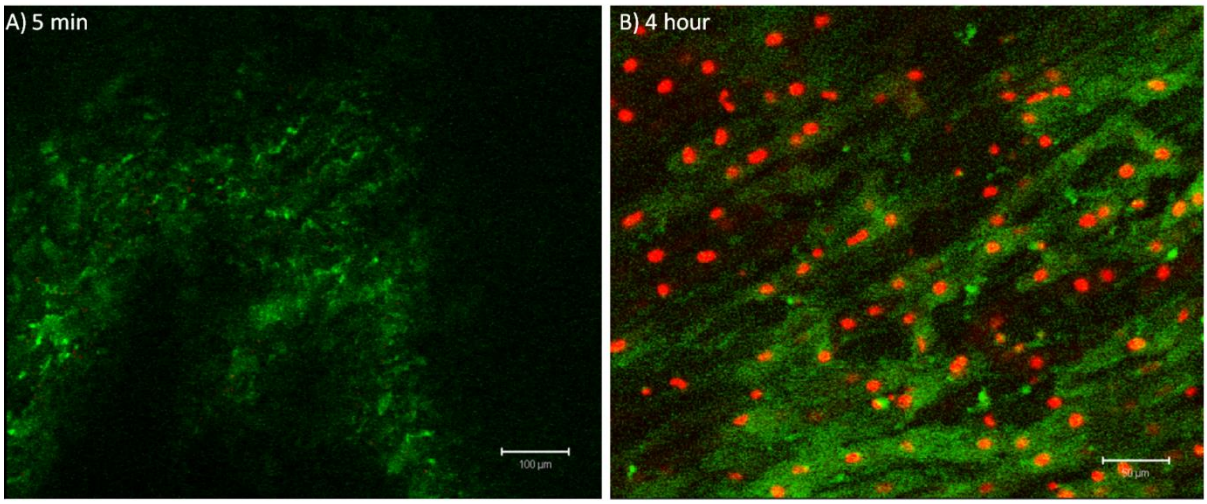

Figure 2.9: Confocal images of tissue slices processed with the cell viability assay at (A) 5 min (B) 4 h after sectioning.

To assess the condition of tissue slices in terms of intracellular structure, electron microscopy (EM) was performed on samples from tissue slices 5 min, 1 h, 4 h and 8 h after cutting (these samples were taken at ~20 µm from the sectioned surface of the tissue slices). Intact mitochondria, Z-lines, and sarcomeres could be seen in all cases (shown in Figure 2.10). However, the intracellular morphology does change over time, with the I band, the A band, and the M-line becoming more difficult to visualise, and signs of mitochondria swelling appearing.

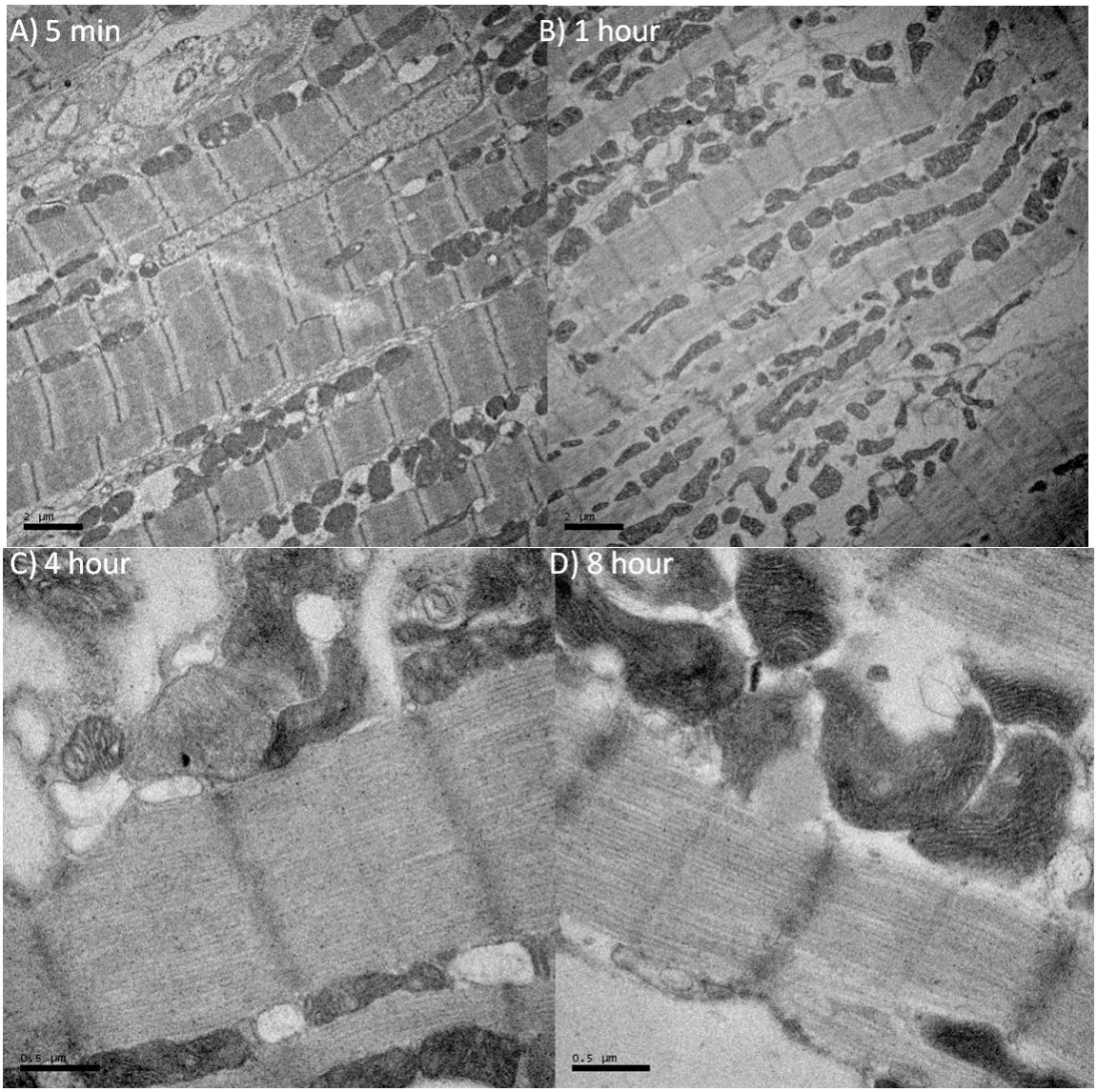

Figure 2.10: EM images of tissue samples taken from slices 5 min (A), 1 h (B), 4 h (C) and 8 h (D) after sectioning.

To assess the fibre morphology of tissue slices, samples embedded in resin were cut into 1 µm sections and stained with Toluidine blue. These stained samples were scanned with a slide scanner. As shown in Figure 2.11, separation of fibres is seen over time, particularly between 1 h and 4 h of incubation.

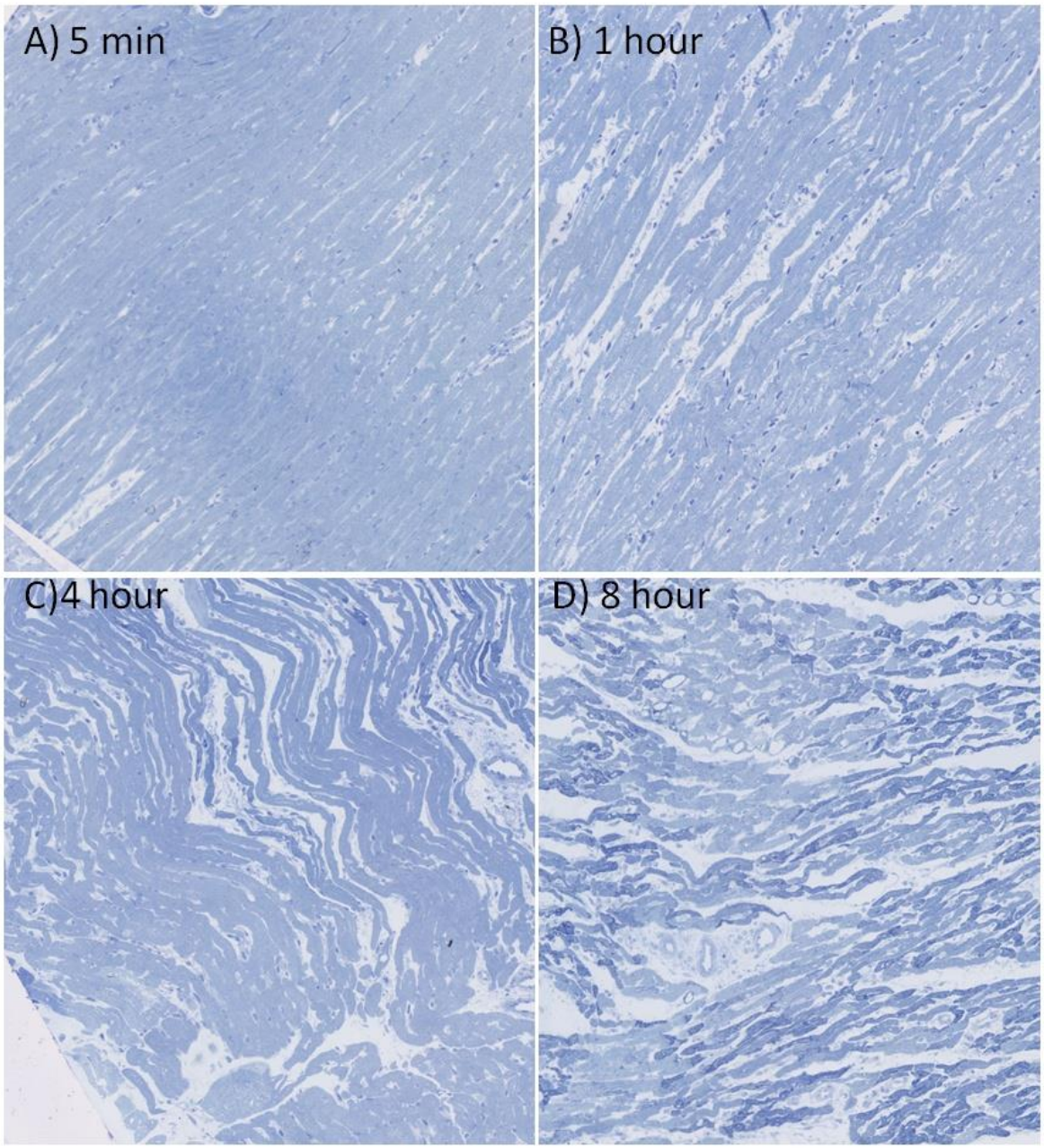

Figure 2.11: Light microscopy scan (10x magnification) of tissue samples stained with Toluidine blue taken from slices 5 min (A), 1 h (B), 4 h (C) and 8 h (D) after sectioning.

2.3.2 Dual Voltage and Ca^{2+} Measurements

We used two dye combinations for dual trans-membrane potential and CaT mapping on tissue slices: di-4-ANBDQPQ in combination with Rhod-2-AM for rabbit, and di-4-ANBDQBS with Cal-520-AM for guinea pig. Figure 2.12 shows an example of the raw

signal acquired from one rabbit (subplot A) LV slice; Figure 2.13 shows a raw signal trace from a guinea pig LV slice (subplot A). Figure 2.12 and 2.13 Panel (B) show the progression of trans-membrane potential and CaT activation waves after point stimulation. The delay in CaT activation, compared to AP upstroke, was 2.21 ± 0.60 ms in rabbit (mean ± standard deviation (SD); 2 animals, 5 slices) and 2.33 ± 1.00 ms in guinea pig (mean ± SD; 2 animals, 9 slices).

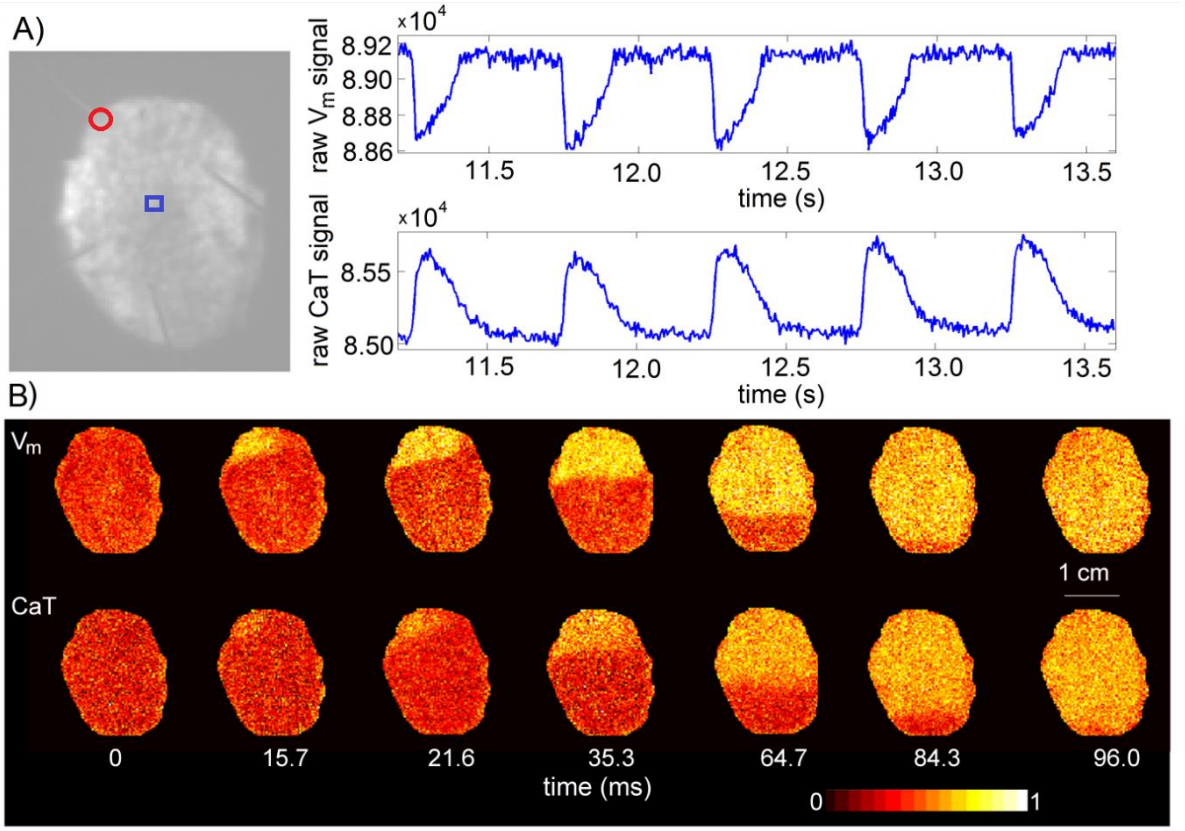

Figure 2.12: Raw signal from dual trans-membrane potential and CaT mapping of a rabbit left ventricular tissue slice**.** A) Left panel: image of rabbit tissue slice, with red circle indicating the stimulation point and blue square indicating the area (3x3 pixels) used to plot the raw AP and CaT traces in the right panels (di-4-ANBDQPQ and Rhod-2-AM; 2 Hz pacing). B) Normalised fluorescence intensity maps for trans-membrane potential and CaT from the same sample as in (A) at 7 time points, showing the progression of trans-membrane potential and CaT activation waves.

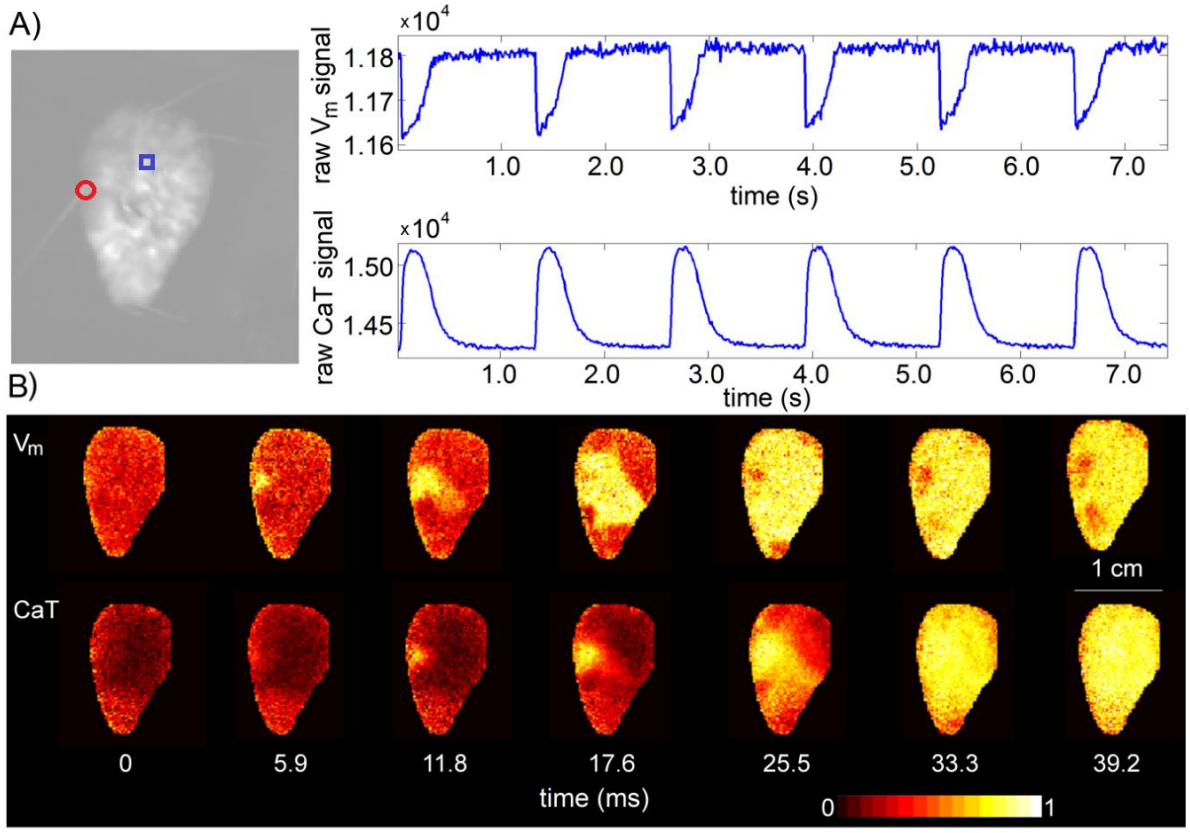

Figure 2.13: Raw signal from dual trans-membrane potential and CaT mapping of a guinea pig left ventricular tissue slice**.** A) Raw signal from dual AP and CaT mapping of a guinea pig left ventricular tissue slice**.** Left panel: image of tissue slice with red circle indicating the stimulation site and the blue square showing the region (3x3 pixels) used for raw AP and CaT traces shown in the right panel (di-4-ANBDQBS with Cal-520-AM; 2 Hz pacing). B) Normalised fluorescence intensity maps of trans-membrane potential and CaT from the same sample as in (A) at 7 time points, showing the progression of trans-membrane potential and CaT activation waves.

Frequency-dependent responses of APD and CaT duration, as described before [110], could be observed in tissue slices from both species, with shortening of both APD and CaT at higher pacing rates. As an example, APD80 and CaT duration at 80% decay of CaT (CaT80) obtained from one representative tissue slice for rabbit and guinea pig at 1, 2, 3 and 4 Hz pacing are shown in Figure 2.14.

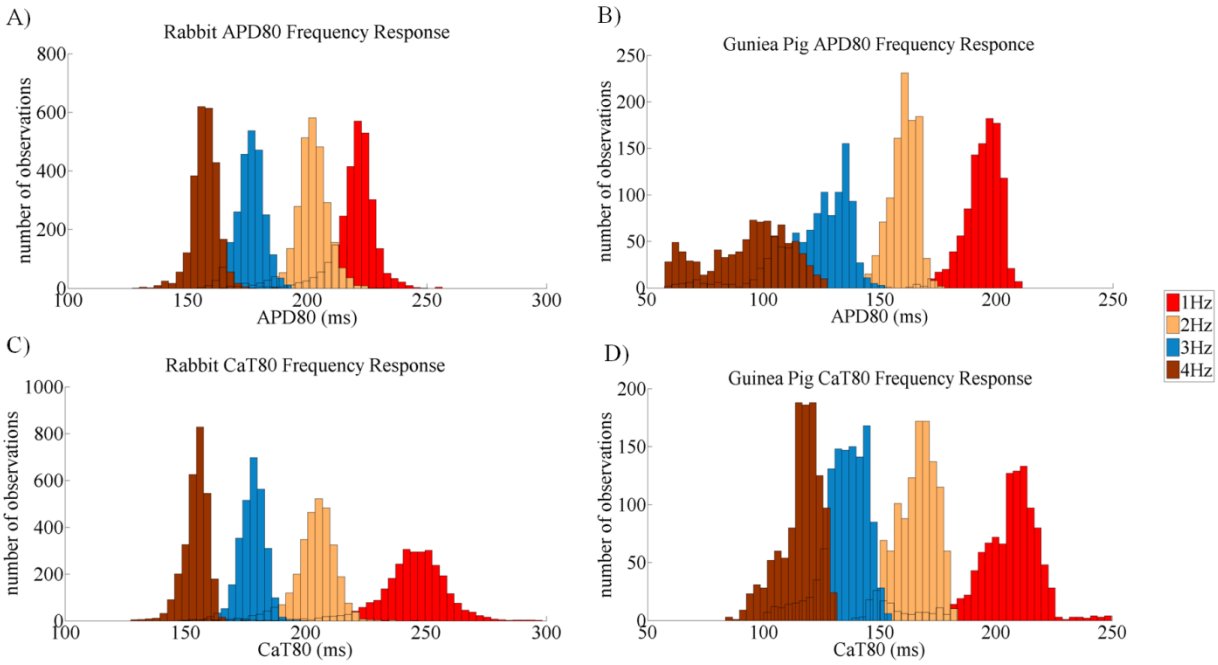

Figure 2.14: Frequency response of APD80 (top) and CaT80 (bottom) from rabbit (left) and guinea pig (right) LV tissue slices at four pacing rates (1, 2, 3 and 4 Hz; see colour coding).

2.3.3 Time to Reach APD Equilibrium After Slicing

To establish when electrophysiological properties reach a steady state after the cutting of slices, measurements were taken from 3 to 300 min after cutting. For both species, very sharp, triangular and short APs without a plateau phase were observed immediately after cutting (when following the standard protocol to slice the tissue in ice cold BDM-containing HEPES buffer). Figure 2.15A-1 (guinea pig) and B-1 (rabbit) show normalised trans-membrane potential signals averaged over the whole tissue from a guinea pig slice at 2 min (blue) and 66 min (red) after cutting and from a rabbit slice at 3 min (blue) and 151 min (red) after cutting illustrating the recovery of AP-shape and duration towards pre-sectioning values (close to the AP shape and duration as observed on the Langendorff-perfused heart). To quantify these observations, AP descriptors (AP skewness and normalised area ratio as described in the methods section) could be used. In Table 2.1, AP descriptors of a guinea pig slice (the slice with AP signal shown in Figure 2.15A) are listed for slice-averaged

measurements at two post-cutting time points (2 and 66 min), as well as for the epicardially-viewed LV of the same heart prior to cutting.

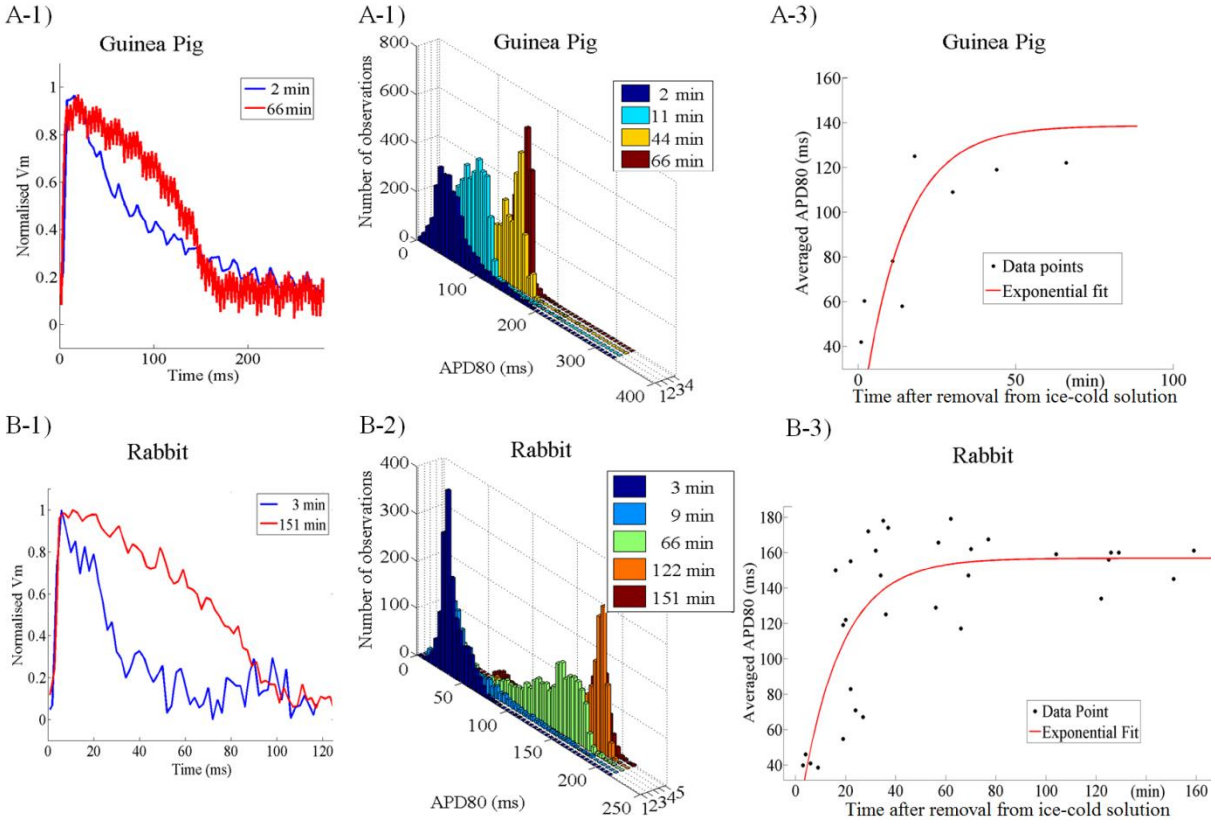

Figure 2.15: Recovery in AP shape properties after cutting of tissue slices. A-1) AP trace, averaged over a guinea pig left ventricular slice, 2 min after cutting (blue) and after 66 min (red). B-1) AP trace, averaged over rabbit left ventricular slice, 3 min after cutting (blue) and after 151 min (red). A-2) and B-2) APD80 histograms from the same guinea pig slice and rabbit slice as in (A-1) and (A-2) respectively during field stimulation at 2 Hz. Time after cutting is colour coded. A-3) and B-3) Summary of mean APD80 during 2 Hz pacing at different time points after cutting for guinea pig slices (3 slices, 2 animal) and rabbit slices (7 slices, 4 animals) with red curves in the plots showing the exponential fitting through these data points.

Table 2.1: Mean and SD of AP indicators, obtained from a guinea pig tissue before and after slicing.

	Average normalised area ratio mean ± SD	**Average AP skewness** mean ± SD
Guinea pig tissue slice: 2 min after cutting	0.567 ± 0.076	0.010 ± 0.243
Guinea pig tissue slice: 66 min after cutting	0.718 ± 0.012	-0.960 ± 0.075
Guinea pig whole heart: before cutting (epicardial aspect of LV)	0.751 ± 0.08	-1.157 ± 0.061

In terms of recovery dynamics, APD increased after cutting, reaching a steady state within about 40-70 min. Figure 2.15A-2 and B-2 show the histograms of APD80, measured from the guinea pig slice and the rabbit slice in Figure 2.15A-1 and B-1 respectively, at several post-sectioning time-points during 2 Hz pacing. Figure 2.15A-3 and B-3 show APD80 (spatially averaged over the whole slice), measured at several time points in guinea pig (3 slices, 2 animals) and rabbit tissue slices (7 slices, 4 animals), respectively, during 2 Hz field stimulation, illustrating that the most prominent recovery occurs in the first 40 minutes. An exponential curve with the following formula:

$$APD80 = A(1-e^{-Bt}) \qquad (2\text{-}1)$$

was fitted through both data sets and is shown as the red curve in the plots. In the formula, A and B are constants to be fitted and t is the time (in min) after removing the slice from ice-cold solution. From this fitting, we can calculate the time when 97.5% of the value of limit at infinity was reached. For these two particular data sets, time to reach 97.5% of the limit value were 49 and 60 min for guinea pig and rabbit, respectively. The data shown in Figure 2.15A-3) and B-3) was also plotted (see Figure 2.16B and Figure 2.17) with data obtained from each slice individually colour coded showing on top of the all the other data points (grey).

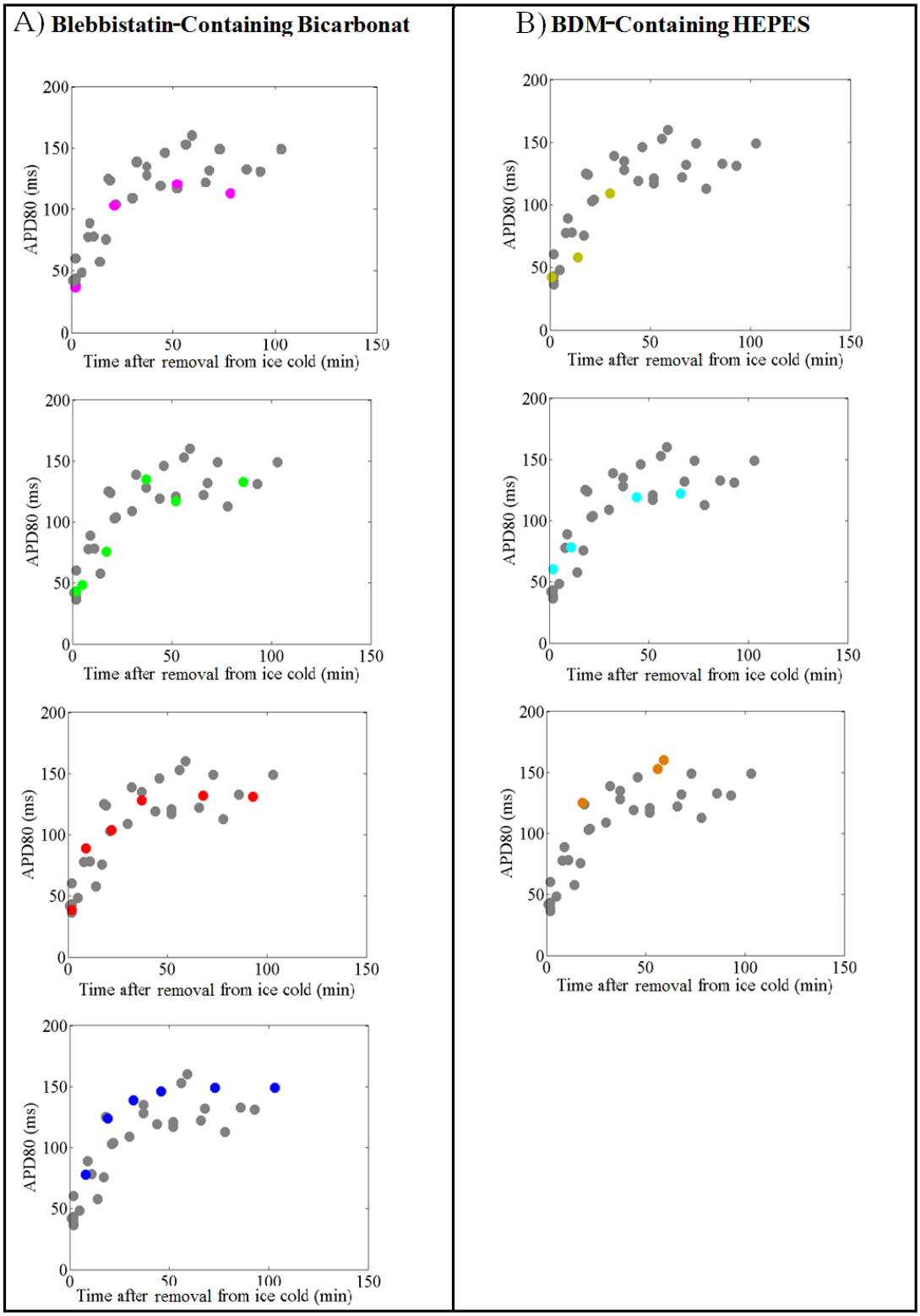

Figure 2.16: Averaged APD80 measured from guinea pig slices at several time points after slicing with data from each slice coded in a different colour. A) Averaged APD80 measured from 5 different slices at several post-sectioning time points when slicing in ice cold blebbistatin-containing bicarbonate buffer. B) Averaged APD80 measured from 3 different slices at several post-sectioning time points when slicing in ice cold BDM-containing HEPES buffer.

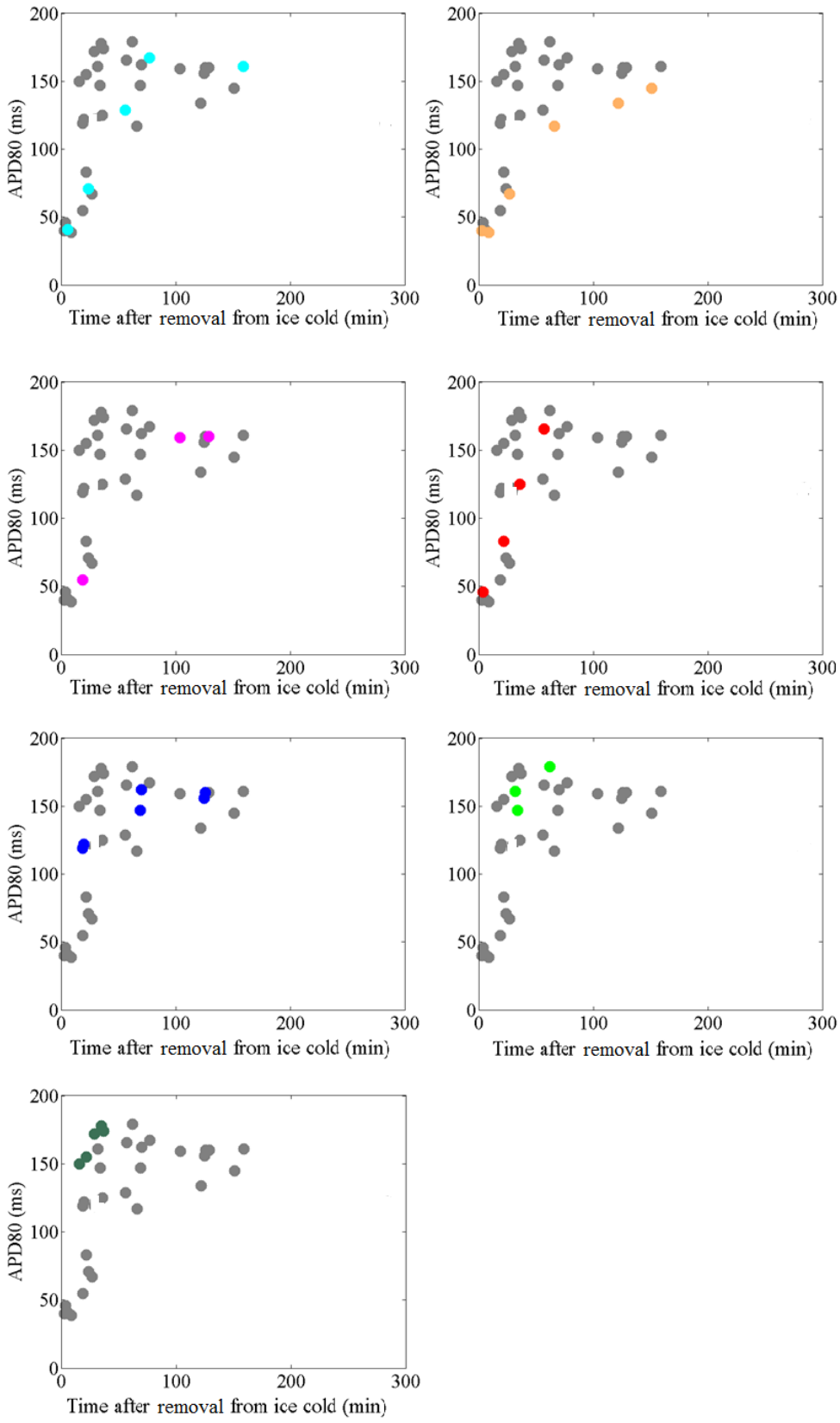

Figure 2.17: Averaged APD80 measured from rabbit slices at several time points after slicing with data from each slice coded in a different colour.

To investigate whether transient exposure to BDM during the slice preparation process was a major contributor to AP recovery dynamics after cutting, the process was repeated in ice-cold bicarbonate-buffered solution containing blebbistatin (guinea pig, 5 slices, 2 animals). Note that all slices, whether cut in BDM or blebbistatin-containing solution, were rinsed in blebbistatin-containing bicarbonate buffer immediately after cutting. In Figure 2.18A, normalised AP signals averaged over the whole tissue from a guinea pig slice sectioned in ice cold blebbistatin-containing bicarbonate buffer at 8 and 73 min after cutting were plotted demonstrating the same sharp AP shortly after cutting even in absence of BDM. The APD80 histogram during 2 Hz field stimulation of the same slice shown in Figure 2.18A measured at 6 different time points after slicing are shown in Figure 2.18B, indicating a rapid increase in APD during the first half hour. Averaged APD80 (averaged over the whole slice) data points measured at several different post-cutting time points from 5 guinea pig tissue slices sectioned in blebbistatin-containing solution are shown in Figure 2.18C, with exponential fit through the data points plotted as a red curve (the time to reach 97.5% of the limit at infinity for this data set is 36min). The measurements show that even when cutting without BDM, a recovery time is needed before a steady state AP can be recorded.

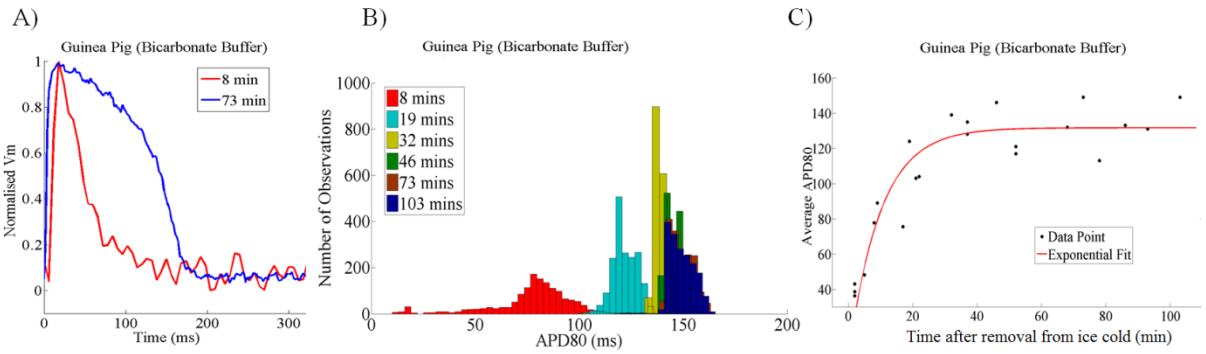

Figure 2.18: Recovery in AP shape properties after cutting in blebbistatin-containing bicarbonate buffer. A) AP trace, averaged over a guinea pig left ventricular slice, 8 min after cutting (red) and after 73 min (blue). B) APD80 histograms from the same guinea pig slice as in (A) during field stimulation at 2 Hz. Time after cutting is colour coded. C) Summary of mean APD80 during 2 Hz pacing at different time points after cutting for guinea pig slices (5 slices, 2 animals, with red curves in the plots showing the exponential fitting through these data points).

Another possible reason for such a rapid change of AP shape after sectioning is the damage of tissue during slicing and recovery of the injury. However, when sectioning guinea pig Langendorff-perfused whole heart (this method will be detailed in chapter 3) at 37 degree Celsius, slices do not show such sharp AP shortly after cutting but rather an AP with shape properties very close to the AP collected from the epicaridal/subepicardial tissue layers prior to cutting.

In Figure 3.5 (see Page 92), the APD80 map from the whole heart LV epicardial/subepicardial region and the APD80 map from an epicardial tissue slice under 4 and 5 Hz field stimulation are shown. In Subfigure 3.5 a red circle on top of the whole heart APD80 map indicates the area where the slice was taken from. The APD80 histograms of the same heart epicaridal/subepicaridal layer (the region inside the red circle marked out in Subfigure 3.5A) and the slice shown in 3.5A were plotted in Subfigure 3.5B. In Figure 3.6C, the averaged AP trace from the tissue slice (red) and from the epicardial/subepicaridal region (inside the red circle) before cutting were overlaid. The slice data shown in Figure 3.5 and 3.6 was obtained 8 min after sectioning.

Data obtained from sectioning the whole heart at body temperature showed that the slices sectioned at body temperature did not show an initially sharp triangular AP shortly after cutting, indicating that leaving tissue at an ice cold temperature for a long period of time (>30 min) and returning the tissue to body temperature may alter AP properties. Such a temperature change may result in lengthening of APD and recovery of AP plateau phase. A set of experiments (protocol described in the methods sections) was performed to collect evidence for this hypothesis (2 rabbits, 3 slices). After reaching AP steady state in body temperature blebbistatin-containing bicarbonate solution after cutting, slices were put back into ice cold BDM-containing HEPES solution for an hour. Slices were then transferred into warm, 35±2^{o}C, solution and a series of measurements (at different time points after exposure to body temperature) was taken. In Figure 2.19 we show an example of the spatially averaged AP trace (2 Hz field stimulation) of a rabbit slice at 79 min after cutting (steady state AP) and at 5 min and 18 min in the re-warming up process (after a 60 min cooling down process in ice-cold solution). Shortly (5 min) after starting re-warming, a sharp AP was observed which seems to recover over time.

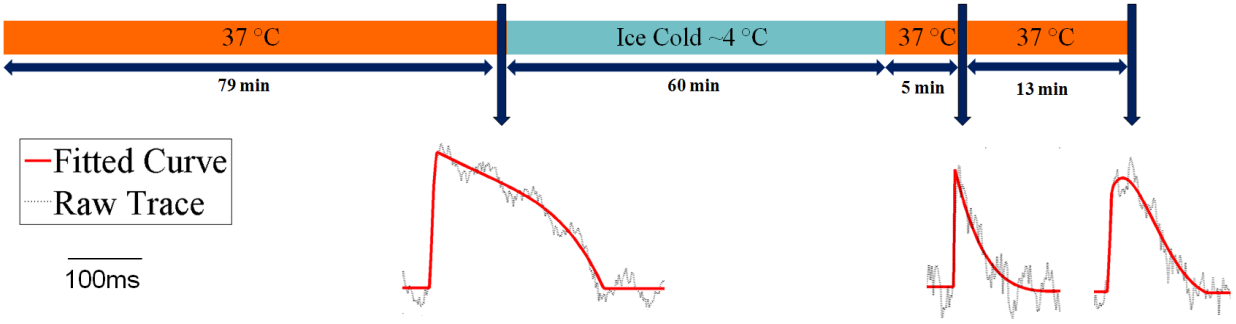

Figure 2.19: Averaged AP trace recorded at 79 min after cutting and 5 and 18 min after incubating in ice cold solution for one hour.

Table 2.2: APD80 from three rabbit LV slice during 2 Hz field stimulation measured at several time points before and after incubating in ice-cold solution for one hour.

Slice	Time after incubation in ice cold (min)	Averaged APD80 (ms)
Slice 1	60 (after slicing before incubation)	220.7
	79 (after slicing before incubation)	225.0
	6 (after re-exposure to ice-cold solution)	89.6
	9 (after re-exposure to ice-cold solution)	91.5
	18 (after re-exposure to ice-cold solution)	121.4
Slice2	23 (after slicing before incubation)	87.6
	30 (after slicing before incubation)	108.1
	46 (after slicing before incubation)	155.7
	60 (after slicing before incubation)	181.4
	72 (after slicing before incubation)	189.3
	20 (after re-exposure to ice-cold solution)	164.7
Slice3	161 (after slicing before incubation)	212.0
	165 (after slicing before incubation)	216.8
	26 (after re-exposure to ice-cold solution)	179.2

The data here indicate that for both species, after incubation of the tissue in ice-cold solution, whether HEPES or bicarbonate-buffered, and regardless of the uncoupler used (BDM, blebbistatin), sharp and triangular AP shapes were observed in slices shortly after sectioning. In all cases a rapid increase in APD and a recovery of the AP plateau was observed. Therefore to measure a steady-state AP, a recovery time is needed after sectioning. To quantify this time, an exponential function was fitted through different data sets. And 97.5% of the value of limit at infinity was calculated (with around 50 min for guinea pig and about

60 min for rabbits). This indicates that the waiting time should not be less than 1 h. From our data and experience with the preparations, we recommend an incubation time of not less than 70 min. For these data, we did not perform any statistical tests to verify whether different species and different conditions (e.g. sectioning solution) show different times to reach an AP "steady state", as the main aim here is just to define a minimum incubation time.

In addition to the sharp triangular APs, tissue slices show relatively weak signal swings shortly after cutting, followed by a rapid increase in signal amplitude, again largely during the initial half hour of the recovery period (see Figure 2.20).

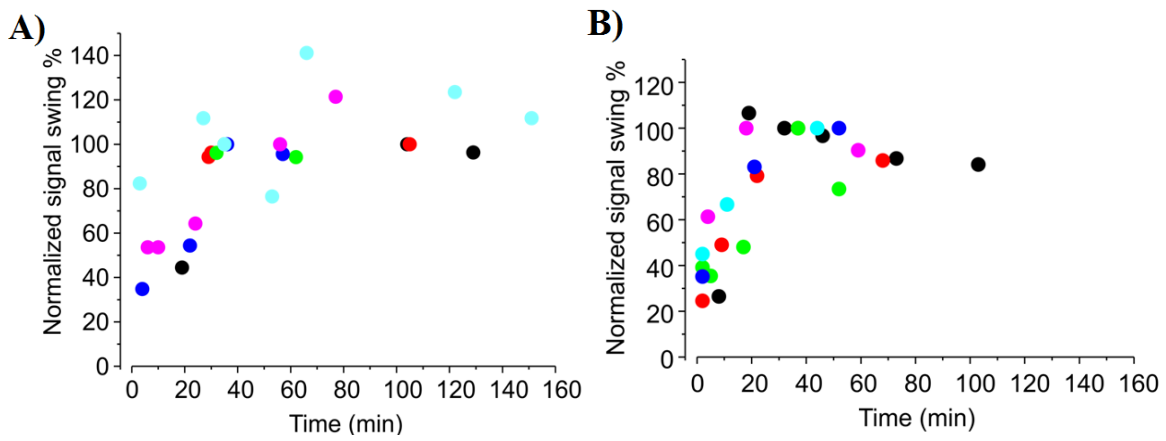

Figure 2.20: Normalised AP signal-to-background ratio at different time-points after slicing. A) Data from guinea pig slices (6 slices: colour coded). B) Data from rabbit slices (6 slices: colour coded). All data normalised to the signal swing at the time-point closest to 40 min (i.e. the signal swing at ~40 min is set to 100%). Note the rapid increase in signal amplitude during the first half hour, followed by near steady state (or a very slow signal decay).

2.3.4 Multiple Point Stimulation

Previous cardiac tissue slice studies tended to use one site for stimulation [83, 84, 111]. To explore the effects of pacing location, we used four different point stimulation sites on the slices, and field stimulation as a reference. APD80 maps obtained with these protocols were compared. To eliminate the initial changes, associated with tissue recovery (above), data for these comparisons were obtained at least 70 min after slice preparation. Measurements were

repeated over the course of one hour, with each set of observations consisting of 5 measurements (4 point and 1 field stimulation) taken in quick succession.

Figure 2.21 shows APD80 maps (Figure 2.21A) and APD80 histograms (Figure 2.21B) from one rabbit slice during pacing at 2 Hz from four different locations (indicated by black circles) and during field stimulation. Pacing-site dependent differences in APD80 maxima and distribution (Figure 2.21B) were observed at all the pacing frequencies tested. Pacing from the first two locations (two left-most panels in Figure 2.21A) yielded longest APD80 (see Table 2.3).

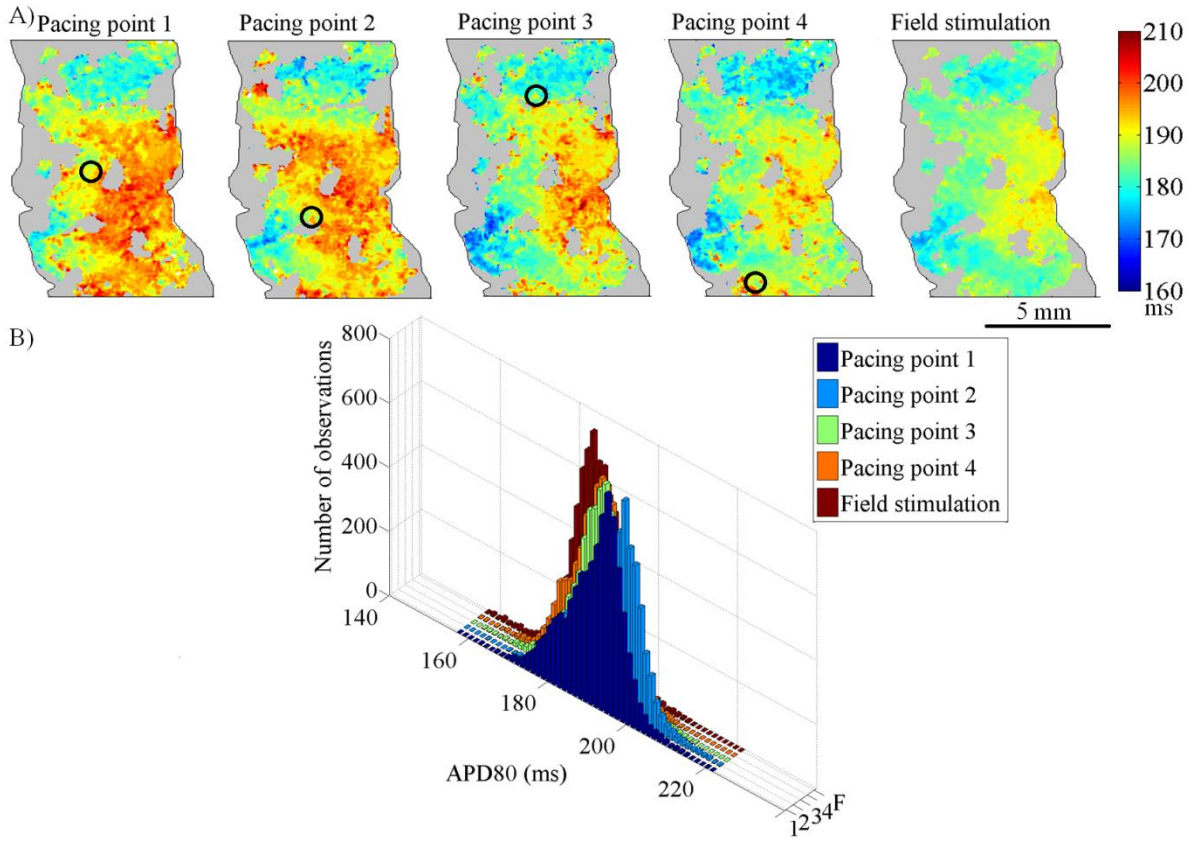

Figure 2.21: APD80 when pacing a rabbit LV tissue slice at different locations. A) APD80 maps during point-stimulation at four sites (indicated by black circles) and during field stimulation (right panel; all at 2 Hz). B) APD80 histograms for the pacing protocols in (A).

The extent of pacing-site dependent differences in APD differed between slices. Such difference can be pronounced in some cases, as shown in Figure 2.22, where pacing from one

end of the slice yielded a region of very short APD that was absent upon pacing from the other end (compare Figure 2.22A-1 and A-2). Conduction velocity (Figure 2.22B-1; vectors plotted on top of the depolarisation time map, where the size of the vector is proportional to the magnitude of the conduction velocity) and conduction speed maps for the first pacing location (Figure 2.22C-1) show that slowed conduction coexists with the short APD region. When pacing from the other end, both conduction velocity and speed (Figure 2.22B-2 and 2.22C-2) were more homogeneous, matching APD distribution. This points to the presence of source-sink mismatches, which could form a potential mechanism for pacing site dependent differences in APD, as discussed below.

Table 2.3: APD80 from a sample rabbit slice, shown in Figure 2.21, paced at different frequencies from four different points, and during field stimulation. Pacing from locations one and two yielded longer APDs, compared to other pacing points. The Mean ± SD is given.

	APD80 (ms) at 2 Hz	**APD80 (ms) at 3 Hz**	**APD80 (ms) at 4 Hz**
Pacing point 1	191.4 ± 6.9	171.1 ± 5.2	154.8 ± 6.3
Pacing point 2	193.3 ± 6.7	170.3 ± 5.1	151.5 ± 5.7
Pacing point 3	189.3 ± 6.4	167.4 ± 4.8	149.1 ± 4.6
Pacing point 4	186.5 ± 6.3	166.8 ± 4.9	147.1 ± 4.3
Field stimulation	184.7 ± 5.7	167.4 ± 4.2	148.8 ± 3.7

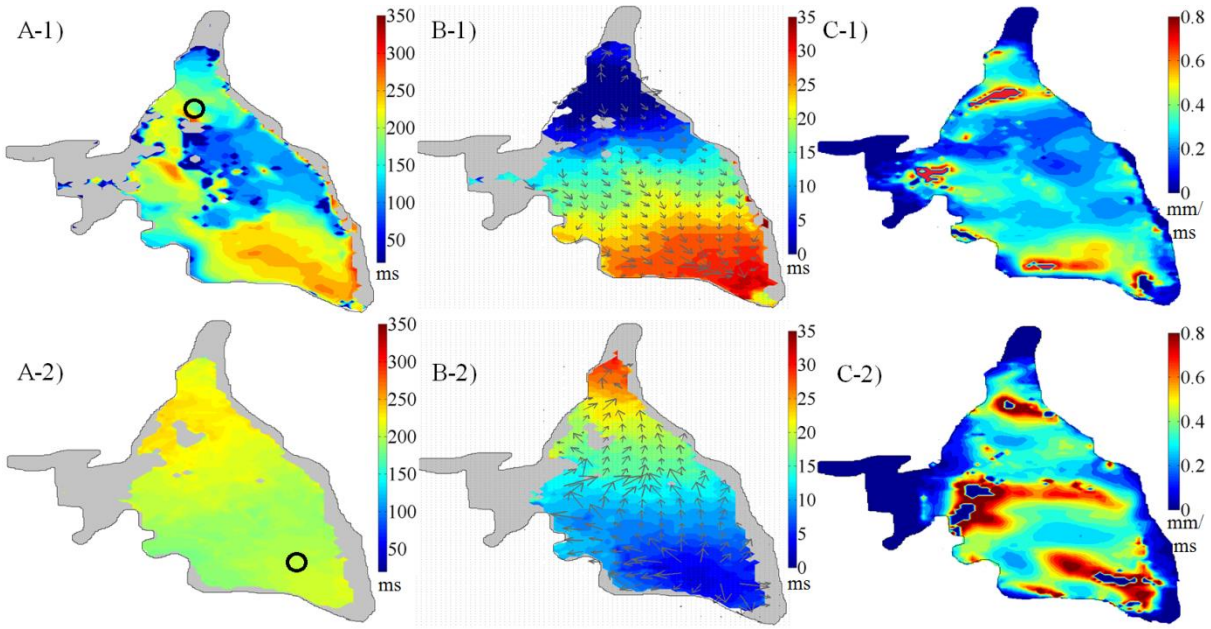

Figure 2.22: APD80, conduction velocity and conduction speed maps of a rabbit slice, paced from two different locations (1 Hz). A-1 and A-2) APD80 maps, with pacing sites indicated by black circles. B-1 and B-2) conduction velocity (grey arrows) plotted on top of the depolarisation time map. C-1 and C-2) conduction speed. Grey regions indicate tissue with no significant signal.

2.4 Discussion

2.4.1 Dual Voltage and Ca^{2+} Measurements

The main advantages of optical mapping, compared to MEA recordings, the currently standard electrophysiological measurement technique for cardiac tissue slices, are its high spatial resolution, its capacity to monitor multiple physiological parameters independently, and the ability to do so simultaneously. In addition, voltage-sensitive dyes can record AP shapes rather than simply activation and repolarisation timings.

Dual AP and CaT mapping has been used frequently for whole heart studies [96, 112-114], but has had limited application to cardiac tissue slices [88]. AP and CaT are key parameters in cardiac physiology and the relationship between them is crucial for electro-mechanical coupling in the heart [115]. Combined AP and CaT optical mapping allows one to study not only the individual characteristics of these two parameters (e.g. the frequency response of AP

and CaT, as reported above), but also the relationship between them [116]. In addition, monitoring both parameters simultaneously can be beneficial for testing pharmacological interventions that may affect the parameters independently. Finally, dynamic high-resolution observation allows one to identify conduction wave-front maps and the spatial distribution of key parameters (e.g. APD).

To illustrate the benefit of obtaining a high spatial resolution (e.g. the difference between an EMCCD camera and MEA), we down-sampled our optical mapping data from 128x128 pixels to 16x16, and then 8x8 points. Figure 2.23A shows the original data from Figure 2.22, while panels 2.23B and 2.23C provide down-sampled versions. As expected, with progressive loss of spatial resolution, it becomes more and more difficult to identify changes in APD80 and conduction properties, such as when pacing at different sites.

On the other hand, MEAs have the advantage of measuring electrical information directly and, potentially at least, over prolonged periods of time, such as in an incubator (whilst fluorescent dyes can be bleached and/or washed out). If prolonged investigations are needed (e.g. over days or weeks) then MEA recordings may be better suited than optical mapping. The same may apply if tissue samples cannot be dye-loaded via blood vessels (e.g. human biopsy material), as fluorescent signals may be too weak for optical methods.

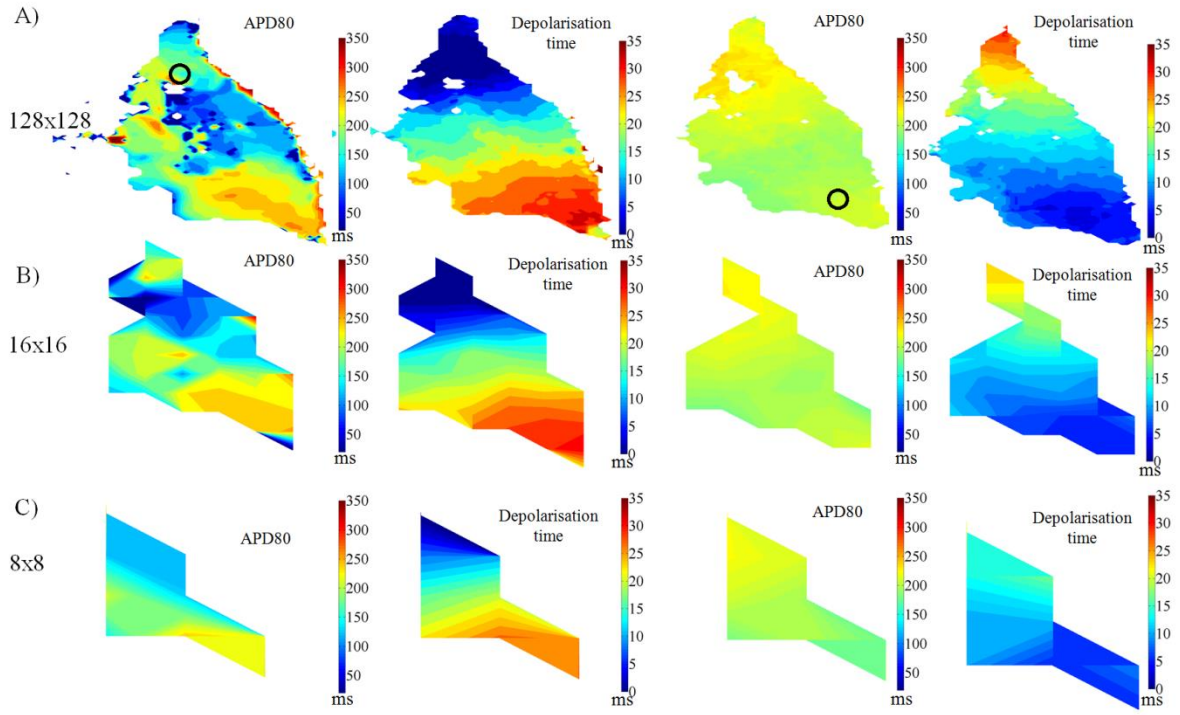

Figure 2.23: Demonstration of information loss with progressive reduction in spatial resolution. A) APD80 and depolarisation time maps of a rabbit slice (same as in Figure 2.22), paced at two different locations (marked by black circles) with 1 Hz, at a spatial resolution of 128x128 data points. B) and C) data after down-sampling to 16x16 points (B) and 8x8 points (C). No tissue contour is plotted here, as low-resolution contact recordings, such as by MEAs, do not offer tissue contour information.

We used two dye combinations for dual AP and CaT mapping, and illustrate their suitability in two species (Figure 2.12 and 2.13). These combinations are not species-specific, although application to other species may require slight modification of excitation and emission filters to optimise recordings, as well as the fine-tuning of dye loading protocols.

Both di-4-ANBDQPQ and di-4-ANBDQBS are voltage-sensitive dyes with significantly improved signal strength and internalisation stability [117]. These characteristics make them ideal for tissue slice optical mapping, as the thin tissue preparation yields less signal compared to arterially-perfused bulk tissue.

Both Rhod-2-AM and Cal-520-AM have relatively high Ca^{2+} affinities (Cal-520: K_d ~320 nM, Rhod-2: K_d ~570 nM; data sheets from AAT Bioquest). High affinity dyes bind Ca^{2+}during early systole, and their slow release of Ca^{2+} may generate inaccuracies in Ca^{2+}

amplitude and Ca^{2+} decay dynamics. Figure 2.12 and 2.13 show that both CaT traces display a fast and slow decay phase; this slow decay phase may, in part at least, be an expression of dye dynamics. Further investigations into CaT properties, including comparisons of CaT signals recorded with high and low affinity Ca^{2+} sensitive dyes, will be useful. Rhod-ff and Cal-520-ff (low affinity versions of Rhod-2 and Cal-520, respectively) have similar spectral properties as the dyes used here, and can therefore be combined with di-4-ANBDQPQ and di-4-ANBDQBS, respectively.

2.4.2 Data Analysis

High-resolution mapping of cardiac slices generates large amounts of data per experiment (hundreds of measurements), which makes data processing challenging. Therefore it is useful to employ automated or semi-automated routines, which analyse data sets, extract targeted information, save results, and generate relevant maps and plots. Various groups use different analysis tools to extract relevant information from data sets. We presented the routine we developed to process data and to calculate parameters for AP and CaT characterisation. Some of the parameters calculated in our routine are standard (e.g. APD, conduction velocity), whilst others (e.g. the AP skewness) were developed in our study, to better characterise the shape of the AP. These new parameters may be also useful for other researchers who are interested in quantifying AP shape.

As fluorescence signals from tissue slices are weaker than those from perfused whole-hearts or tissue wedges, it is important to process the signal trace before parameter evaluation, in order to increase the reliability of the information extracted. As illustrated in Figure 2.3 (see Page 40), processing can significantly reduce the impact of noise distortion on the depolarisation and repolarisation phases of APs. In our measurements, the noise was not from one particular frequency range; thus it was difficult to remove noise using notch filtering

routines. As shown in Figure 2.2, a 4^{th} order polynomial was chosen for the curve-fitting routine since it captured the repolarisation phase of the AP well. In the case of CaT analysis, the decay phase can be better fitted with a bi-exponential curve [118] which could be a part of a future extension to our existing algorithm.

Averaging over a series of APs, obtained in the same pacing conditions with no extra intervention, helps to reduce noise (although it does not take into account inherent beat-to-beat variability). This was not used in our routine to leave open the possibility of analysing AP traces recorded under dynamic restitution protocols.

The maximum upstroke velocity of the AP (dV/dt_{max}) is an important parameter; however the limited temporal resolution (~255 Hz for dual AP/CaT measurement, ~510 Hz for single-parameter mapping) available from our technique makes estimation of dV/dt_{max} challenging. Overlaying a series of AP signals can increase the number of data-points on the depolarisation phase. However in order to increase accuracy for dV/dt_{max} estimation, a measurement technique with higher temporal-resolution (e.g. fibre optics [88]) may be needed and electric recording such as via sharp electrodes may be better to avoid the photon scattering problem that occurs with optical mapping.

2.4.3 Time to Reach Equilibrium After Slicing

We found that there is a critical recovery time period, required for cardiac slices to reach an electrophysiological steady state. During our recovery protocol, we observed, both in rabbit and guinea pig slices, an initially weak AP signal with short and triangular AP shapes (e.g. Figure 2.15). Subsequently, signal amplitudes and AP shape recovered, returning towards pre-sectioning control levels within 40-70 min (Table 2.1).

This is in keeping with previous reports [79] which highlighted that the success rate for electro-physiological measurements on neonatal rat slices using patch clamp increased after

30 to 60 min of incubation, and supports the frequently chosen slice recovery time of ~1 h [86, 87].

There are several possible reasons for the need to allow a recovery period prior to use of slices:

1) tissue slicing is associated with severe damage of cells near the cut surfaces, from which the tissue needs to recover;
2) BDM used during cutting needs to be washed-out;
3) the tissue block may become ischaemic during slicing;
4) during slicing, tissue is kept in ice-cold solution, and the return to body temperature affects its electrophysiological properties.

The first is inevitable, although the period over which this would affect tissue electrophysiology might intuitively be expected to be short. For example, if shunts from the intra-cellular domain of the surviving tissue preparation to the outside persisted, this would cause exceedingly swift, and potentially terminal, deterioration. To assess the second possibility, we performed slicing in cold bicarbonate-buffered solution containing blebbistatin instead of BDM. Similar short and sharp AP configurations, and weak fluorescence signals, were observed, suggesting that the need for BDM wash-out is not an issue *per se*. The third scenario, ischaemic damage, was countered by keeping the tissue block in ice-cold oxygenated buffer solution during sectioning. This, together with electro-mechanical uncoupling, reduces metabolic demand. Interestingly, there was no systematic difference in recovery times between the first slices, taken from the well-oxygenated outer surface of the tissue block, and those taken later and from deeper transmural planes. Therefore, it is unlikely that the observed sharp and short AP configurations are a direct consequence of potentially ischaemic conditions in the tissue block. Finally, we investigated temperature effects. In another study (described in chapter 3), we sliced Langendorff-

perfused guinea pig whole hearts in warm ($35 \pm 2^{o}C$) blebbistatin-containing bicarbonate-buffered solution, to obtain near-epicardial tissue slices. In that case, no sharp and short APs were observed immediately after slicing. In fact, APs recorded from slices shortly after sectioning showed very similar repolarisation morphology and APD compared to pre-sectioning values (Figure 3.5 and 3.6).

Indeed, an influence of temperature on AP configuration has been reported in previous studies. Most studies showed lengthening of AP when lowering the temperature from body temperature to room temperature [119]. However, there is not much literature showing the impact upon APs of returning to body temperature after incubation in an ice-cold solution. Cutting a tissue block at ice cold and cutting a whole heart at body temperature showed completely different AP morphology shortly after sectioning. This seems to suggest the most probable reason for such a post-cutting recovery time is the temperature effect. In order to explore this, fully-recovered slices with normal AP configurations (n = 3) were returned to ice-cold blebbistatin-containing bicarbonate-buffered solution for a period of 30 to 60 min, and then mapped again: the sharp and short AP shape, seen during the initial recovery phase, was again observed after re-exposure to ice-cold solution (Figure 2.19). Therefore, we conclude that the cold temperature during slice preparation is a key contributor to the observed electrophysiological recovery dynamics.

One possible mechanism for such a temperature effect could be accumulation of sodium ion intracellularly due to the inhibition of sodium-potassium pump at ice-cold temperature [120]. After returning the tissue slice to body temperature, the cells need time to extrude the accumulated sodium ions and this could explain the waiting time needed for measuring steady state AP. The increase in intracellular sodium after ice-cold ‘incubation’ could change the resting membrane potential and alter cell excitability. If only some of the cells in a slice are excitable shortly after ice cold incubation (with the proportion of excitable cells

increasing over time in warm solution), then the non-excited cells are possibly acting as a current sink to yield an overall sharp and short AP. The relatively weak signal shortly after sectioning in cold solution could also be explained by a smaller proportion of excitable cells initially. This is a hypothesis to explain the phenomenon observed, further data is needed to assess this.

2.4.4 Frequency Dependent Changes in APD and CaT Duration

Shortening of APD with increasing pacing frequency is a well known property of cardiac muscle [121, 122], and shortening of CaT duration was also reported in the literature [123]. Rate-dependent APD and CaT duration reduction was observed in LV tissue slices from both species (as shown in Figure 2.14). CaT amplitude, an important parameter of CaT which also shows rate-dependent response, was not analysed in our study, as ratiometric intracellular Ca^{2+} concentration measurement was not conducted. As mentioned above, the affinity of the Ca^{2+} sensitive dye used may have influenced both CaT decay and amplitude. Therefore to gain more insight into the frequency response of CaT, a ratiometric approach with high and low affinity dyes (e.g. Fura-2 and Fura-4F for a comparison) would be helpful [29].

2.4.5 Multiple Point Stimulation and Source-Sink Mismatch

APD distribution and AP shapes at any given location in the slice can be very different, depending on pacing location (Figure 2.21 and 2.22). Depolarisation wave-front speeds also differ in parts of the slice, when paced from different locations. A possible explanation for this is based on non-uniform source-sink relations in the tissue. It has previously been observed that source-sink relations induce changes in conduction and/or APD in cell culture [124] and whole heart [125]. Whilst the selection of an epicardium-tangential cutting plane

ensures that a maximal proportion of myocytes are aligned roughly in-plane, there are deviations. Some of these are caused by transmurally increasing deviation of myocyte alignment from the tangential plane (as one progresses towards deeper tissue layers), others may be due to the fact that we are cutting in a true plane while the cardiac surface is curved (so cells in the centre of a slice will be from deeper transmural layers than those at the periphery). Thus, in spite of all efforts, slices can contain non-uniform structures, with varying degrees of cell alignment and coupling. These differences may create asymmetrical source-sink relations, which can be revealed, when pacing at different locations, in the form of differences in APD and conduction velocity.

This means that identification of an unbiased picture of APD distribution in tissue slices requires multiple pacing protocols, and/or field stimulation. This is important for intervention testing, such as drug application / washout studies, in particular if the pacing site is not controlled. If, for example, the pacing location varies before and after drug application, changes in functional parameters that are due to source-sink heterogeneities could be mistakenly attributed to the effects of a compound. Field stimulation would be more reliable for a before-and-after comparison, but the strength and orientation of the electric field relative to the tissue slice would also need to be controlled.

2.4.6 'Best' Recording Time for Tissue Slices:

As suggested by the EM and light microscopy images, both cellular and the tissue level morphology change over time as we incubated the slices. Tissue degradation is an expected outcome and there have been prior reports on the tissue level and intracellular remodelling over time [126]. As discussed before, when sectioned in cold solution, a waiting time of ~70 minutes is needed for the slice to reach electrophysiological steady state. The best time for

measuring tissue slices prepared using the method described should be below 4 h when the fibre separation and mitochondrial swelling are still less pronounced, compared to longer incubation.

Since the mitochondrial swelling is affected by oncotic pressure gradients, adding proteins (like albumin) to the incubation solution may help to reduce the extent of mitochondrial swelling. Incubation in a sterile environment would also be helpful for longer investigations.

2.5 Conclusion

In this chapter, we show that multi-parametric optical mapping, here of trans-membrane potential and CaT, can be reliably conducted on cardiac tissue slices of rabbit and guinea pig left ventricle. The high spatial resolution of the technique offers advantages over more frequently used tools, such as the MEA, but is associated with challenges in data processing and interpretation. We provide a robust method for processing these data sets, and for extracting important descriptors of functional parameters.

The use of cardiac tissue slices benefits from standardisation, and we suggest adherence to the following approach (or at least to document and communicate equivalent aspects of the protocol):

- electro-mechanically uncouple tissue, and cut in a epicardial-tangential plane, using a high-precision vibratome with a blade advance speed around 0.03 mm/s, cutting slices of no more than ~400 μm thickness;
- allow a post-cutting recovery period of 40 to 70 min in warm buffer solution (if slicing is conducted in ice-cold solution), avoiding application of excess mechanical strain (restrain gently with soft mesh, rather than pins, clamps or other external mechanical fixator which can yield inhomogeneous strain of the tissue);

- use multiple-site point stimulation and/or field stimulation for uncovering electrophysiological tissue heterogeneities and, for any before/after investigations (such as drug testing), carefully control pacing location (to exclude contributions of source-sink mismatches to the observed effects).

Having detailed in this chapter the methodology for performing dual AP and CaT optical mapping on cardiac tissue slices in a reliable and reproducible manner in the next chapter we will describe a study comparing AP properties and drug responses of whole heart versus cardiac tissue slices.

Chapter 3

Comparison of Action Potentials Recorded From Cardiac Tissue Slices and Whole Heart

Brief Summary of Chapter 3

In this chapter, a comparison of AP properties and drug responses recorded from Langendorff-perfused hearts and cardiac tissue slices is described. The method to collect tissue slices from Langendorff-perfused hearts at body temperature is detailed. APs recorded from whole heart epicardium/subepicardium are compared with those measured from the corresponding epicardial slice. The APD and the AP repolarisation phase of whole heart epicardium/subepicardium and of epicardial tissue slices are similar. The preliminary drug testing study on whole heart and tissue slices shows that slices are able to reproduce close to whole heart responses to nifedipine.

My contribution to this chapter:

- Part 1, slicing Langendorff-perfused whole heart: the optical mapping experiments were performed together with Dr. Christian Bollensdorff, I was responsible for the study design, the tissue slice preparation, the mapping measurements, and the data analysis. Results of this part are included in the manuscript submitted to AJP (under review).
- Part 2, drug testing on cardiac tissue slices: the optical mapping experiments were performed together with Dr. Peter Lee and Dr. Christian Bollensdorff, I was responsible for the tissue slice preparation and the mapping measurements. Content of part 2 of this chapter is included in the manuscript published in Pflügers Archiv [88].

3.1 Introduction

A number of different preparations have been used to study cardiac electrophysiology in control and during different interventions (e.g. pharmacological interventions). To properly understand data obtained from different preparations and to consolidate these results, it is important to understand how preparations differ from one another in their electrophysiological properties. For any *in vitro* preparation, it is necessary to find out how well it reflects the *in vivo* situation.

As summarised in chapter 1, considering the complexity of preparations, live cardiac tissue slice as a pseudo 2D model can bridge nicely the gap between single isolated cells and Langendorff-perfused whole hearts (the utility of cardiac slices is summarised in chapter 1). Although not a very commonly used preparation, cardiac tissue slices have gained increasing popularity in applications such as pharmacological compound testing [83-85]. However, there is little quantitative evidence to date concerning how different or similar the electrophysiological parameters measured from cardiac tissue slices are, compared to parameters measured from a more integrated/intact preparation (such as Langendorff-perfused whole hearts).

Bussek et al. tested whether tissue slices can be used *in vitro* to capture action potential (AP) changes due to drug action [83, 85]. In their study [83], they used tissue slices obtained from guinea pig ventricle or human papillary muscle, and tested multiple compounds (nifedipine, E4031 and risperidone) that are well-known for inducing electrophysiological changes (shortening of APD for nifedipine, prolongation for E4031 and risperidone). AP changes observed in tissue slices qualitatively agreed with previously reported data. However, when the authors conducted a quantitative comparison of APD 'concentration response' (EC_{50}) between guinea pig ventricular slices and guinea pig papillary muscle (data from literature), a

difference in the sensitivity towards nifedipine was found. In their study from 2009 [83], APD (both control and after application of 1 μM E4031) measured from intact human papillary muscle and papillary muscle slices were also compared, showing a difference in APD in both cases. The findings from Bussek et al. indicate that slices can be used to study drug-induced changes, but that there are some quantitative differences between APD measured from slices and intact tissue. However, in their comparison study, the guinea pig ventricular slices were compared with papillary muscle instead of tissue from the ventricular free wall. This makes interpretation difficult, since there can be intrinsic differences (in terms of electrophysiological properties) between ventricular free wall and papillary muscle [127]. For human tissue, the authors compared intact papillary muscle with papillary slices. This comparison avoided the potential regional AP differences. However, the intact papillary muscle and the papillary slices were from different hearts, therefore inter-individual differences needed to be taken into account (e.g. the difference in APD between different patients, due to age or pathological conditions).

Camelliti et al. [84] described a method to obtain live tissue slices from human heart biopsies and dog ventricular tissue. In their study, field potential duration measured from human and dog slices were compared to previously published APD90 data measured from human and dog papillary muscle, tissue wedge and isolated single cells. The authors concluded that field potential durations in slices were similar to APDs measured from papillary muscle and tissue wedges. The comparison performed in their study did not exclude potential regional and individual differences in electrophysiological properties. Also, the experimental condition-induced differences cannot be overlooked when comparing data obtained in different experimental conditions and via different measurement techniques.

For a better assessment and validation of how well living cardiac slices preserve native myocardial electrophysiological characteristics, a better-controlled comparison is needed. In

our study, we tried to establish a method allowing comparison of AP measured from guinea pig heart left ventricular tissue slices with AP obtained from left ventricular free wall of the same region and the heart. To be able to do a more direct comparison, Langendorff-perfused whole hearts were sectioned at body temperature (instead of the commonly used method of sectioning tissue at ice-cold temperatures). APs were optically mapped from epicardial/subepicardial layers of the heart before tissue slices were cut using a vibratome. Both the slice and freshly exposed surface were optically mapped. In this way APs obtained from whole heart epicardial/subepicardial layers can be compared directly with APs obtained from matching epicardial slices.

In this chapter, the method for sectioning Langendorff-perfused hearts is detailed and preliminary results from this study are summarised. Since we aimed to collect signals from epicaridal/subepicaridal layers only, deep penetration of excitation light into the tissue should be avoided. Therefore a shorter excitation wavelength compared to the red-shifted excitation light sources as described in chapter 2 is desirable for this study. The specification of excitation and emission filters used is detailed below, together with a brief description of how we found the optimal excitation and emission wavelengths combination.

In another proof-of-principle study [88], we tested with dual AP and CaT mapping whether it was possible to capture close-to-whole heart responses in both AP and CaT on tissue slices upon drug intervention. Some of these data are also included in this chapter to conduct a more complete comparison between tissue slices and whole heart.

3.2 Materials & Methods for Whole Heart and Tissue Slice AP Comparison

For heart preparation and dye loading protocol please refer to section 2.2.1.1 and 2.2.1.2.

3.2.1 Animal Details:

Three Female guinea pigs (250-400 g, n = 3) were used for the whole heart and tissue slice AP comparison study.

3.2.2 Dye Testing

To find optimal excitation and emission wavelengths, a range of excitation and emission filters were tested (summarised in the Table 3.1 below).

The filters were purchased from Chroma Technology (Bellows Falls, USA) apart from the 561 nm long-pass filter (Semrock, Rochester, USA: this filter shows significant transmission only at wavelengths longer than 575 nm) and the 500 nm short-pass filter (FES0500, Thorlabs, Ely, UK). Two white LEDs (LED-CBT-90-W; Luminus Devices) were used as the excitation light source.

Table 3.1: Excitation emission wavelengths and filters used to find the optimal setting for di-4-ANBDQPQ imaging (with blue range excitation)

Excitation wavelength (nm)	Excitation filters	Emission collection (nm)	Emission filter
465-500	D485/40m; FES0500	575 onwards	BLP02-561R-25
465-500	D485/40m; FES0500	700 onwards	ET700LP
465-500	D485/40m; FES0500	602-662	ET632/60m
465-500	D485/40m; FES0500	560-600	D580/40m
430-450	D440/20X	575 onwards	BLP02-561R-25

3.2.3 Procedures for Sectioning Langendorff-perfused Whole Heart

The heart was continuously perfused in Langendorff mode with bicarbonate-buffered solution (same contents as in section 3.2.1 with 10 µmol/L blebbistatin) and was placed into a tailor-made heated slicing chamber, fixed on the vibratome. The heart was positioned with the left ventricle facing up, while the right ventricle was pinned down with several needles onto a soft Polydimethylsiloxane (PDMS) cushion, glued onto the metal base of the slicing chamber, to hold hearts in place (please see Figure 3.1 and 3.2). Soft tubing was inserted into

the left ventricle, from the atrium, to avoid build-up of pressure in the left ventricle (build-up of pressure can mechanically load and deform the left ventricle).

Slices of left ventricular free wall were cut in the tangential plane, relative to the epicardial surface, using a high precision vibratome (7000smz tissue slicer, Campden Instruments Ltd., Loughborough, UK) at a progression speed of 0.01 mm/s (blade travel amplitude 2 mm, frequency 80 Hz, note this speed is lower than the normal progression speed used to cut the tissue block). It is difficult to achieve an exact thickness in the first slice (desirable thickness is around 350 µm). The most critical step here is to set the first contact between blade and tissue correctly. Since there was only limited visual control, the heart was approached by the blade in small vertical steps (350 µm) for several times until the first cut was conducted. In this way, it was ensured that the first slice was not thicker than 350 µm, to avoid any potential risk of ischaemia. The heart was further sectioned into 350 µm slices as long as it did not show a clear ischaemic AP shape (which is short and triangular).

Figure 3.1: Images showing the Langendorff-perfused heart in the slicing chamber before (A) and after (B) sectioning. Subfigure C shows the tissue slice sectioned from the heart.

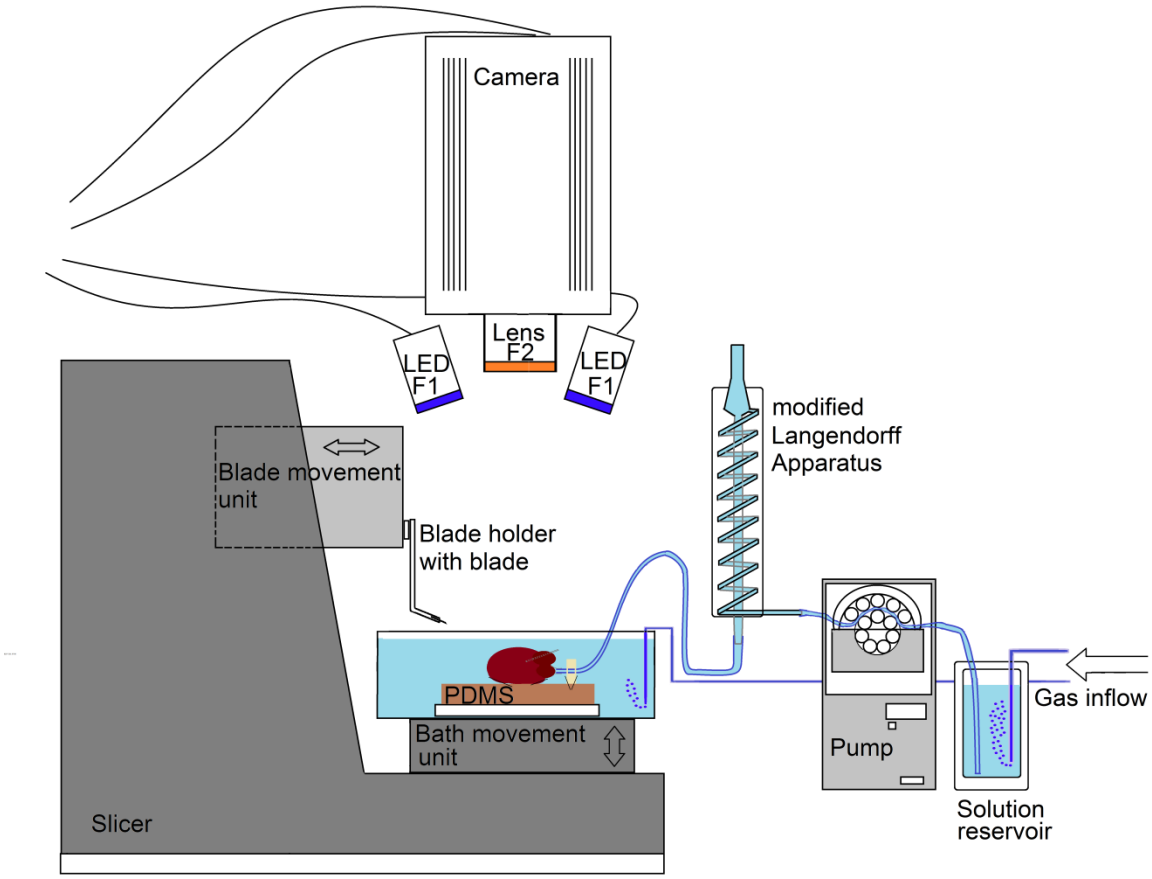

Figure 3.2: Schematic illustration of the set-up and filter configuration: diagram showing the optical mapping station for Langendorff-perfused whole hearts. The heart was placed in the slicing chamber filled with solution. The water-jacked Langendorff apparatus including the solution reservoir, and the tailor-made heated slicing chamber were maintained at 35 ± 2°C. The Langendorff set up was in recirculation mode during measurements and slicing. The solution in the reservoir was bubbled continuously with 95% O_2/5% CO_2 and the solution in the slicing chamber was bubbled throughout the slicing procedure and between mapping measurements. LED sources used are white; the filters F1 were optimized to pass blue light between 465-500 nm. The filter F2 was optimized to collect fluorescent light above 575 nm. The camera was mounted onto an adjustable focussing stand. The heart was held in place mainly by fixing the inflow cannula in place, but also by pinning down the right ventricle. Tubing was inserted into the left ventricle via the atrium to avoid pressure build-up in the left ventricle. The roller pump speed was set to 8 mL/min.

3.2.4 Optical Mapping

APs were optically mapped from epicardial/subepicardial layers of the tissue before a tissue slice was sectioned. Both the slice and the freshly exposed surface were optically mapped.

The voltage-sensitive dye in the heart was excited using white light-emitting diodes (LED) (LED-CBT-90-W; Luminus Devices) with excitation-filter D485/40m (Chroma Technology, Bellows Falls, USA) and a 500 nm short-pass filter (FES0500, Thorlabs, Ely, UK) in front. The emission fluorescence of the dye was collected using an EMCCD camera (Cascade 128+; Photometrics, Tucson, USA) through a 561 nm long-pass filter (BLP02-561R-25, Semrock, Rochester, USA: this filter shows significant transmission only at wavelengths > 575 nm) .

Red LEDs (LED-CBT-90-R, peak wavelength 624 nm; Luminus Devices, Billerica, USA) with excitation-filter D640/20x (Chroma Technology, Bellows Falls, USA) were used to excite the voltage dye in the tissue slice, and the emission was collected with an EMCCD camera (Cascade 128+) through a 700 nm long pass filter (ET700lp, Chroma Technology, Bellows Falls, USA). The schematic diagram in Figure 3.2 shows the optical mapping set up for the Langendorff-perfused whole heart (placed in the slicing chamber). The set up for slice mapping is very similar to that shown in Figure 2.1 (however only the red light source is used and the filter in front of the EMCCD camera was a single long-pass filter, ET700lp instead of a multiband filter).

The whole heart and the slices were mapped with different excitation/emission wavelengths to improve the signal quality for the slice preparation. Di-4-ANBDQBQ, when excited with red-shifted wavelength, yields a much better signal (at least 2 folds more in signal swing) than when excited with blue-shifted wavelengths. The blue light for the whole heart was used, however, to reduce the depth penetration of the excitation light. For mapping the thin tissue slice, this is not an issue (although lateral scattering is still present). Since the overall amount of tissue contributing to the signal is less in the slice preparation, compared to the whole heart, the red-shifted excitation used allows us to obtain a sufficient signal.

3.2.5 Pacing

Both the whole heart and the slices were paced with a tailor-made field stimulator (details described in Section 2.2.1.5). For the whole heart, we tried to override the sinus rhythm by using pacing frequencies higher than the sinus rhythm (i.e. around 4 or 5 Hz), and slices were paced with the same frequencies as the whole heart.

3.2.6 Analysis

The recorded trans-membrane potential data were processed to reduce the noise distortion (see chapter 2 (2.2) for the detailed data processing algorithm), APD (APD at 80 and 50% repolarisation, APD80 and APD50, respectively) were calculated on the pre-processed traces (please also refer to 2.2.1.6 for a detailed description).

3.3 Materials & Methods for Pharmacological Study on Tissue Slices

For heart isolation, voltage dye loading and slice preparation protocol please refer to section 2.2.1.1, 2.2.1.2 and 2.2.1.3 respectively.

3.3.1 Animal details

Five female guinea pigs (250-400 g) were used for this pharmacological study: 3 for the whole heart study and 2 for the tissue slice study.

3.3.1 Calcium Dye Loading

The Ca^{2+} sensitive dye Fura-4F-AM (200 μL stock solution, 1 mg/mL in DMSO, Life Technologies, Grand Island, NY) was loaded via bolus injection into the heart, and the 100 mL dye-containing perfusate (bicarbonate-buffered solution, please see 3.2.1 for composition) was re-circulated for half an hour.

3.3.2 Dual AP and CaT Optical Mapping of Slices and Whole Heart

Voltage sensitive dye di-4-ANBDQPQ in both whole heart and tissue slices was excited with a blue LED light source (CBT-90-B; peak wavelength 460 nm; Luminus Devices, Billerica, MA) mounted with an excitation filter D470/20X (Chroma Technology, Bellows Falls, USA). The Ca^{2+} sensitive dye Fura-4F-AM was excited with an UV light source (NCSU034A; peak wavelength 385 nm; Nichia, Tokushima, Japan; no excitation filter in front of the light source). Dye emission was collected by an EMCCD camera (Luca (S); Andor Technology, Belfast, Ireland) through a multi-band filter: ET585/50-800/200M (Chroma Technology, Bellows Falls, USA). Images were acquired at a rate of 195 frames per second. Figure 3.3 [88] shows a schematic diagram of the set up (in Subfigure A) and the filter and light source characteristics (Subfigure B).

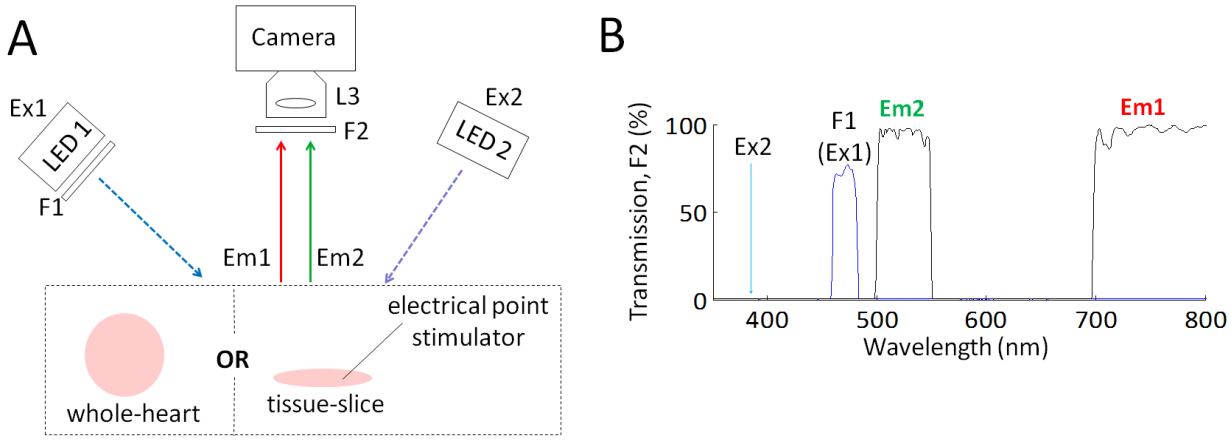

Figure 3.3: Schematic illustration of the set-up and filter configuration: A) diagram showing the optical mapping station for the Langendorff-perfused whole heart and tissue slices: Ex1 is the blue LED for excitation of voltage dye, Ex2 is the UV LED for excitation of Ca^{2+} sensitive dye, F1 is the excitation filter D470/20X, F2 is the multi-band filter ET585/50-800/200M and L3 is the lens placed in front of the camera; B) Filter/ light source spectrum characteristics: Em1 (voltage dye emission) and Em2 (Ca^{2+} sensitive dye emission) are transmission spectra of the multi-band emission filter; the excitation filter, F1 is for the voltage dye excitation source Ex1; the UV light source for the Ca^{2+} sensitive dye is indicated with its peak wavelength (there is no filter for this light source). This figure has been published in [88].

3.4 Results

3.4.1 Optimal Combination of Excitation and Emission Wavelengths for the Whole Heart and Tissue Slices: a Comparison Study

To find the optimal excitation and emission filters for guinea pig whole heart surface mapping, we tested several combinations. This part of the study is shown here as an example to demonstrate how to determine which filters and light sources to use for mapping. Different dyes have different spectral properties which can vary due to the tissue used. Species and age of the animal are factors that can contribute to variations. Therefore 'dye testing' is needed not only when a new dye or a new dye combination is used, but also when dyes are used on species (or animals with different age) that have not been tested before. For all optical mapping studies described in this thesis (either with different dye combinations or involving different species), the dye testing was performed beforehand to ensure data can be acquired with optimal signal quality given the filter availability.

From previous studies on rat hearts [59], we have evidence that di-4-ANBDQPQ can be excited with two different wavelengths (blue-shifted excitation around 470 nm, and red shifted excitation around 640 nm). Therefore we narrowed down the search to the blue area and we tested 465-500 nm for excitation first. As the emission of the dye is always at a higher wavelength compared to excitation, we first tried to collect everything above 575 nm. This combination yielded a decent signal with ~4% signal swing (please note that the signal swing is relative to the signal baseline, and can be camera and technology-dependent; therefore it only makes sense to compare signal swings captured with the same camera). We then tried to narrow down the emission wavelength by changing emission filters (please see Figure 3.4 for results). We found that most emission signals have wavelengths above 600 nm (from 560-600 nm, signal swing is only 0.1%). However if we narrow down the emission collection to 700

nm onward, only 2.5% signal swing can be obtained, as a portion of emission signal is blocked out. We also tried to use shorter wavelengths (430-450 nm) to excite the dye, and we tried to collect everything above 575 nm. However this combination yields a very poor signal, suggesting that 430-450 nm might be too short in wavelength for excitation of the dye. Therefore we set the excitation wavelength to 465-500 nm, and the emission collection to 575 nm plus for whole heart voltage mapping.

When we excite the dye with one particular wavelength, we can either get an upward signal, a downward signal, or no signal at all. The ‘no signal point’ is very important for combining this dye with other dyes for simultaneous mapping (i.e. while exciting one dye, the other dye should not be excited, or not give fluorescent signals). In case the excitation wavelength range is too wide, both upward signal and downward signal can be collected (which can cancel out emission signal swing). This situation should be avoided.

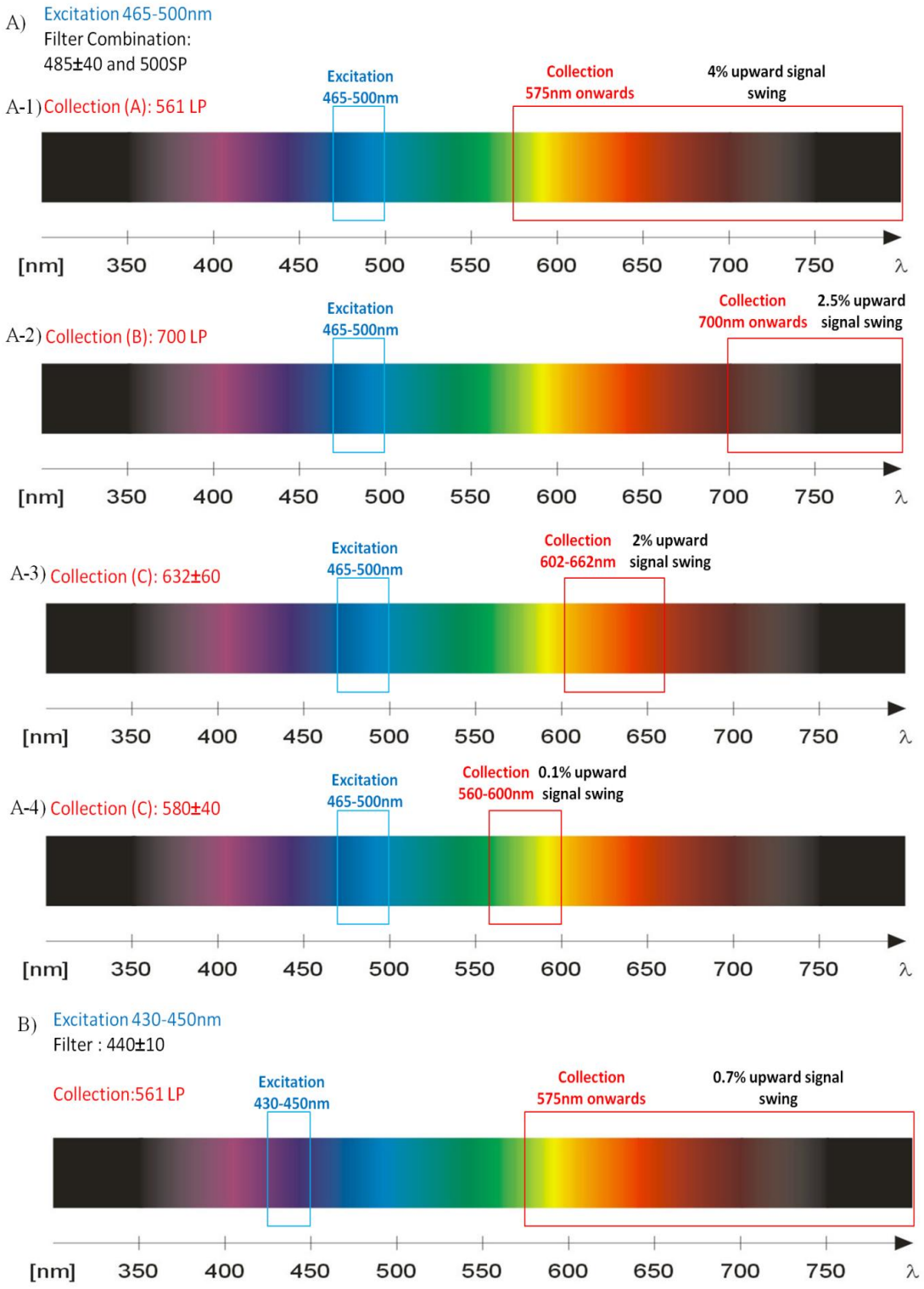

Figure 3.4: Figure summarising the dye testing result: A) excitation with 465-500 nm and emission collected at 575 nm onwards (A1), 700 nm onwards (A2), 602-662 nm (A3) and 560-600 nm (A4); B) excitation with 430-450 nm and emission collected at 575 nm onwards.

3.4.2 Comparing Action Potentials Measured from Whole Heart and from Tissue Slices

Using the method described in 3.2, we were able to collect living tissue slices from Langendorff-perfused whole hearts at body temperature. These slices showed normal, close to whole heart, AP characteristics (see Figure 3.6) shortly after sectioning. They did not show the initial sharp and short AP (shown in chapter 2, Figure 2.15 and 2.18) observed in tissue slices sectioned in ice-cold solution.

We mapped APs from whole heart epicedial/sub-epicedial regions before and after sectioning, and from the epicardial tissue slices. Upon sectioning, the heart's normal perfusion system is disturbed and, in particular at body temperature, ischaemia can develop quickly. Gradual shortening in APD was observed in the sectioned whole heart (after taking off the first epicardial slices). Therefore, it makes sense to compare in particular the epicedial surface before sectioning and the epicardial tissue slice.

We experienced difficulties in sectioning the whole heart into thin slices with even thickness. We ascertained that with very low blade-advance speed and pinning of the right ventricle tightly onto the PDMS block, it became easier to section the heart (yielding slices with more even thickness). While we were optimising the method, one of the preparations failed as the first slice was too thick and eventually became ischaemic over time. Therefore we did not include those data in the comparison.

APD50 and APD80 measured from whole heart epicaridium/subepicardium and epicardial slices paced at 4 or 5 Hz are summarised in the table below (Table 3.2). The epicedial slice from preparation 2 (as shown in the table) was sectioned with higher speed and may have slightly thicker edges which could potentially suffer from ischaemia. The slices from preparation 1 was prepared with the fine-tuned method and therefore the sectioning worked out well; this slice did not appear to have obvious thicker edges. As shown in this table, AP

measured from epicardial slices show similar duration compared to AP measured from whole heart epicardium/subepicardium.

Table 3.2: APD measured from whole heart and epicardial slice from 2 preparations

Preparation	Pacing frequency	APD50 before cut Mean ± SD (ms)	APD50 Slice 1Mean ± SD (ms)	APD80 before cut Mean ± SD (ms)	APD80 Slice 1 Mean ± SD (ms)
Preparation 1	4 Hz	114.65±3.91	113.21±3.63	130.96±3.48	130.38±3.51
Preparation 1	5 Hz	102.98±3.85	101.80±4.73	116.98±3.37	118.00±3.93
Preparation 2	4 Hz	108.40±12.11	102.56±13.25	128.40±12.91	128.56±4.92
Preparation 2	5 Hz	102.37 ±9.57	98.23± 8.64	121.21±10.08	119.11±4.10

In Figure 3.5, APD80 maps of whole heart (epicardium view) and the outermost tissue slice (from preparation 1) at 4 and 5 Hz pacing are plotted. The red circle on top of the whole heart APD80 map indicates the area where the slice was taken. Although the slice did not completely preserve the APD80 pattern from whole heart epicardium (potentially due to tissue deformation after sectioning), the overall APD80 was very similar. A histogram for APD80s measured from whole heart (area inside the red circle only) and APD80s obtained from the epicedial slice is shown in Figure 3.5B. The overall APD80 distributions (at 4 and 5 Hz pacing) in whole heart and slice appear surprisingly similar.

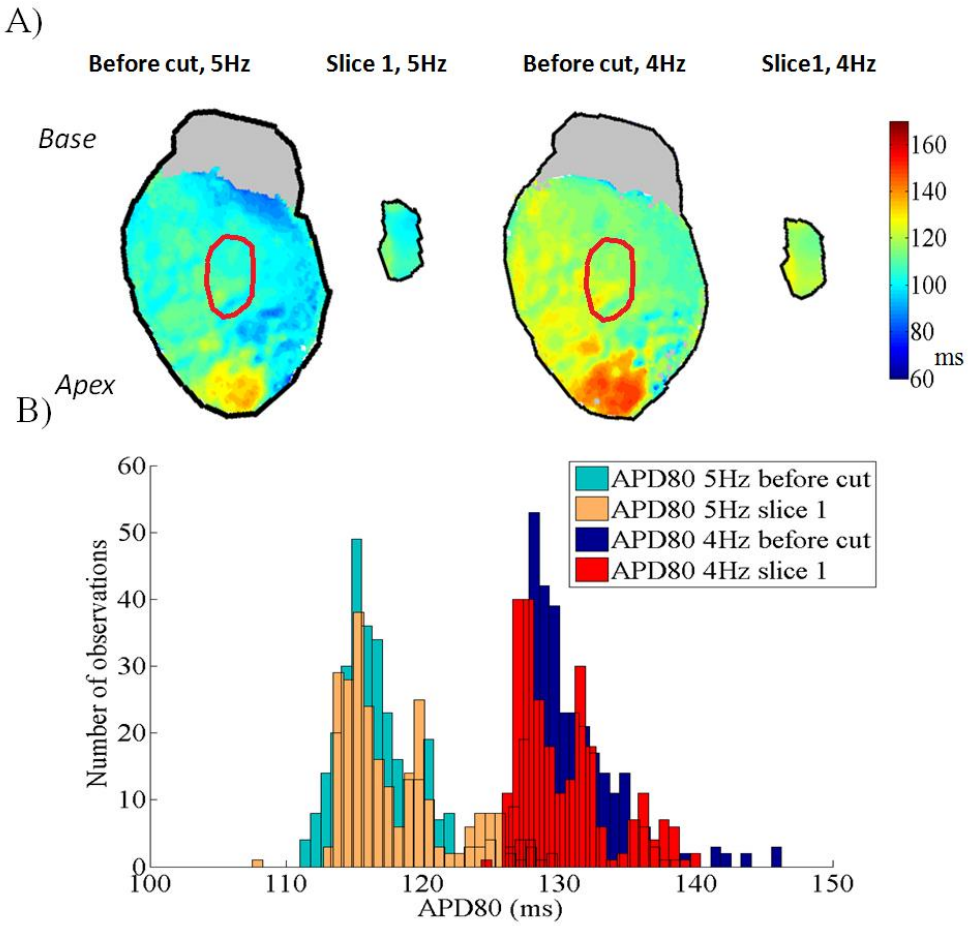

Figure 3.5: Comparison of APD from whole heart and slices: A) APD80 in an epicardial region of whole heart left ventricular free wall (sectioned area circled in red) and from the corresponding epicardial slice (slice 1) during field stimulation at 4 Hz (left) and at 5 Hz (right). B) Histogram showing APD80 from the left ventricular whole-heart slicing (the area circled in red in Subfigure A) and from the corresponding epicardial slice (field stimulation, 4 and 5 Hz).

Aside from APD, the AP shape can also be compared. The normalised area ratio (introduced in chapter 2) was used to characterise the AP shape, allowing for quantitative comparison between the whole heart and epicardial tissue slices. In Figure 3.6A, the normalised area ratio maps of the whole heart and of the epicardial slice are shown. A histogram of the whole heart (for the cut region only: inside the red circle) and the epicardial slice is provided in Figure 3.6B. The mean values and standard deviations are summarised in Table 3.3. These data seemed to suggest a slightly more triangular AP in slices. Figure 3.6C shows spatially averaged AP traces of the whole heart (area inside the red circle) and epicardial slices. We

see a difference in the depolarisation phase of these two traces (the whole heart AP shows a slower depolarisation). The repolarisation profile (especially the later phase) is similar.

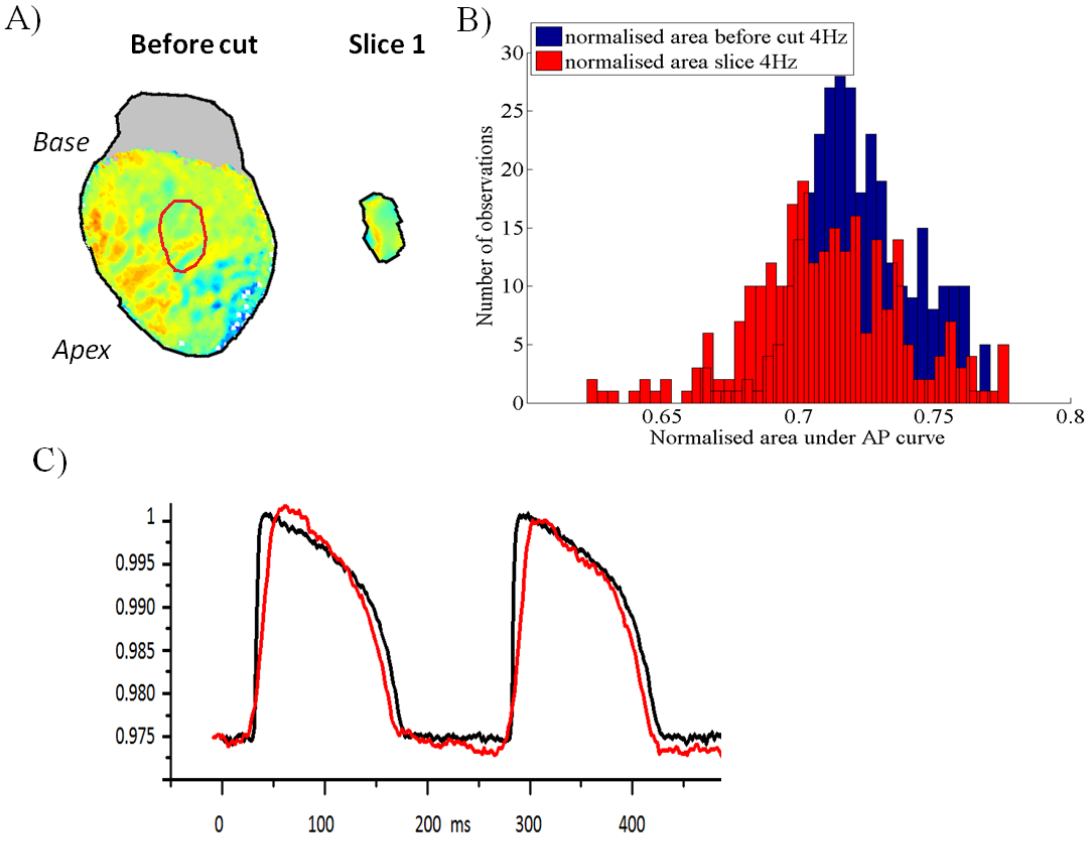

Figure 3.6: Comparison of AP shape indicators for the whole heart and slices. A): Normalised area ratio from epicardial/subepicardial region of left ventricular free wall (cut area circled in red), and from the corresponding epicardial tissue slice (field stimulation, 4 Hz). B) Histogram showing normalised area ratio from myocardial whole-heart (blue) and from the corresponding epicardial slice (red, stimulation, 4 Hz). C) Averaged trans-membrane potential traces from the whole heart (black) and epicardial slices (red).

Table 3.3: normalised area ratio measured from whole heart epicardium and from epicardial slice

Preparation	Pacing frequency	Normalised area ratio before cut Mean ± SD	Normalised area ratio Slice 1 Mean ± SD
Preparation 1	4 Hz	0.7226±0.0206	0.7096±0.0291
Preparation 1	5 Hz	0.7220±0.0192	0.6948±0.0336

3.4.3 Comparing Pharmacological Response in Whole Heart and Tissue Slice

AP and CaT were imaged before and at several time points after addition of 2 µM nifedipine in Langendorff-perfused whole hearts and left ventricular tissue slices. Figure 3.7 [88] shows the data obtained from the whole heart. Both shortening in APD and reduction in CaT, which are well-known effects of nifedipine due to L-type calcium channel block, were captured. In tissue slices, these responses were also seen (shown in Figure 3.8 [88]) indicating that dual voltage Ca^{2+} mapping is able not only to capture drug effects on AP, but also that on CaT in tissue slices. In the whole heart experiment, a slowing of heart rate was observed (effect on pacemaker tissue). Since the slice was from ventricular tissue, it showed no spontaneous activity.

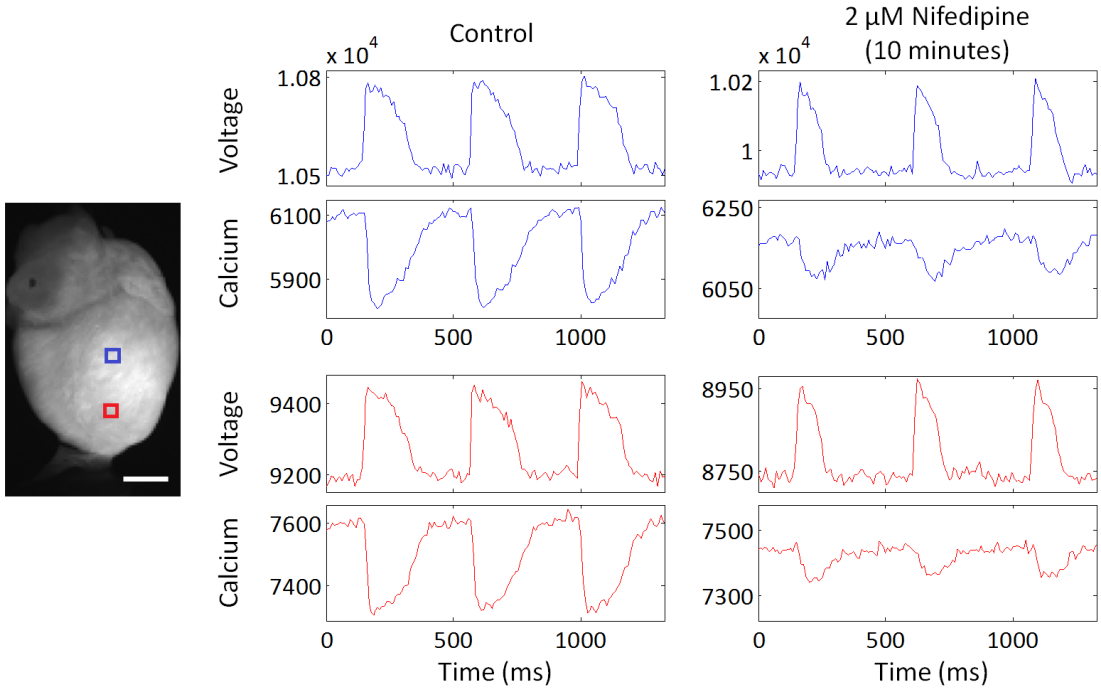

Figure 3.7: Whole-heart optical mapping of voltage and CaT. Raw (unfiltered) voltage and CaT signals are shown from two regions (6x6 pixels) of the heart in sinus rhythm. The left column shows the control signals just before drug application and the right column shows the altered signals after 10 min of exposure to 2 µM nifedipine. Note the reduction in heart rate, AP duration, and CaT amplitude. Figure was published in [88].

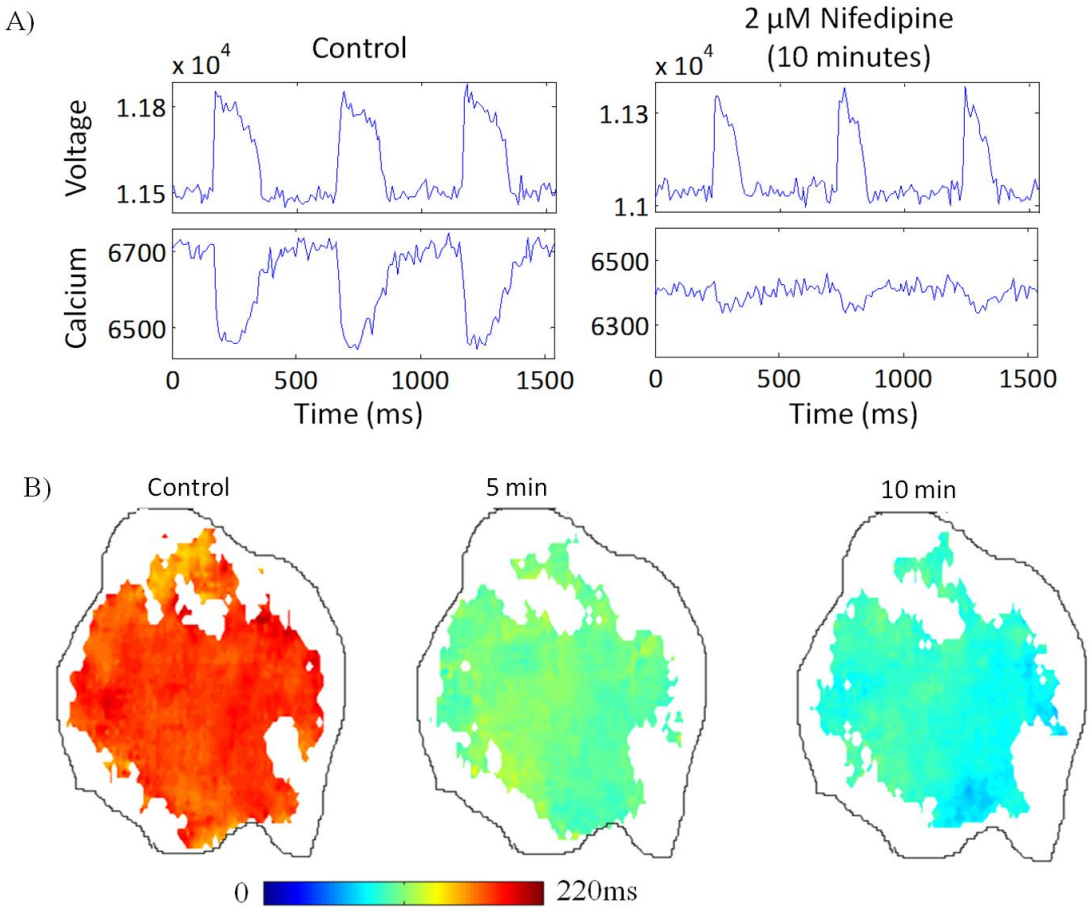

Figure 3.8: Tissue-slice optical mapping of voltage and CaT. A) Raw voltage and CaT signals are shown from a region (6x6 pixels) of the tissue-slice during 2 Hz pacing. The left column shows the control signals just before drug application and the right column shows the altered signals after 10 min of exposure to 2 µM nifedipine. B) APD80 maps for control (left), 5 min (middle) and 10 min (right) after application of nifedipine (2 µM). Part of this figure was published in [88].

3.5 Discussion

In this study, we compared AP properties (and CaT properties during drug intervention) in the whole heart and tissue slices. In the control case (no drug intervention), a comparison of AP parameters was performed on intact heart left ventricular epicardium/subepicardium and the first obtained epicardial slices aiming to compare tissue from the 'same' area before and after sectioning. We also compared the response of the whole heart and tissue slices to nifedipine (a Ca^{2+} channel blocker [128]) to see whether the well-known effects of APD shortening and CaT reduction can be seen on both preparations.

3.5.1 Comparing AP Measured from Whole Heart and from Tissue Slices

1) Vital cardiac slices can be prepared from Langendorff-perfused hearts at body temperature, avoiding the need to section from tissue block in ice cold solution. However compromised perfusion restricts this to one or two slices per heart.

2) Tissue slices differ from the intact left ventricular tissue in terms of mechanical load, electrical source-sink relations, activation pathways, etc. Slices deform after sectioning, due to the lack of mechanical strain from neighbouring tissue. Therefore, the AP pattern in slices differs from that in the whole heart.

3) Our preliminary data suggests nonetheless that slices preserve key AP characteristics, including overall AP shape and APD distribution, as well as response to stimulation rate. A higher '*n*' number is needed to confirm this finding statistically.

3.5.2 Comparing Pharmacological Response in Whole Heart and Tissue Slice

The results from this pilot study suggest that slices are able to reproduce whole heart responses to nifedipine. A more thorough study is needed to quantify the similarity: for example to find out whether the EC_{50} for whole heart and slices are similar for various drug interventions. For drugs which can be washed out easily, a direct comparison (based on the same area of the same heart) could be performed for the response from whole heart epicardium and epicardial slice using the methodology described in this chapter.

3.6 Limitations

In this study, we showed that cardiac tissue slices preserve some key electrophysiological properties of the whole heart (e.g. APD80, APD50 and AP repolarisation shape). For the depolarisation phase, APs measured from the whole heart differ from those recorded from the slice. These differences can be caused mainly by the optical recording technique and the pacing method. Although a blue LED was used as the excitation light source for reduced

tissue penetration, we record not only from the sub-epicardial tissue but also from deeper layers. In addition, the field stimulator used in this study cannot activate the whole heart at exactly the same time. Therefore, the AP depolarisation phase is blunted by 'averaging' AP upstrokes from different layers of the heart with different activation time points. Slices, in contrast, are very thin, and there is no contribution to the signal from deeper layers with delayed activation. Thus, APs recorded from tissue slices have a faster depolarisation phase compared to the whole heart recording, and they are more representative of actual local electrical behaviour. Other recording techniques such as sharp electrodes offer better means to study the AP depolarisation phase (particularly, in whole heart).

In the study where Langendorff-perfused whole hearts were sectioned, we showed that the slices show similar AP properties (especially in the repolarisation phase). For slices collected from whole-heart at body temperature, no incubation time is required to record steady state AP. However, collecting slices from whole-heart at body temperature has its limitations. As we section through the heart, coronary arteries (which run initially at the epicardial surface) get cut, and perfusion of the heart is disturbed. At body temperature, where metabolic demand is relatively high, the heart can quickly become ischaemic even after cutting just one slice. Therefore, this method is not ideal for studying multiple transmural slices.

In the study (with no pharmacological intervention), we only compared AP properties of whole hearts and slices. As an extension to this study, CaT could also be compared. A dye combination of Fura and di-ANBDQPQ (blue excitation) could be used along with the single sensor mapping technique described in chapter 2.

In this chapter, the comparison of AP properties and drug responses of whole hearts and cardiac tissue slices has been described. In the next chapter, chapter 4, we now go on to describe a study where we have explored the suitability of tissue slices as an experimental model to study mechano-electric feedback.

Chapter 4

Study of Mechano-Electric Feedback in Cardiac Tissue Slices

Brief Summary of Chapter 4

This chapter describes the proof-of-principle application of stretch to cardiac tissue slices. For cardiac tissue slices, it is possible to apply stretch perpendicular or parallel to the dominant orientation of cells, while keeping the preparation in a constant focal plane for optical mapping. AP and CaT were mapped before, during and after application of stretch. Cardiac slices show an initial shortening in both AP and CaT duration upon application of stretch, followed by a gradual prolongation of AP and CaT duration during stretch maintained up to 50 min (in most cases). A shortening in AP and CaT duration was observed shortly after releasing sustained stretch.

My contribution to this chapter:

- The tissue slice optical mapping experiments included in this chapter were performed together with Dr. Christian Bollensdorff. I was responsible for the study design, the tissue slice preparation, the mapping measurements and the data analysis.
- The histology work mentioned in this chapter was done with guidance of Dr. Padmini Sarathchandra.
- The content of this chapter has been published in Progress in Biophysics and Molecular Biology [129].

4.1 Introduction

4.1.1 The Investigation of Mechano-Electric Feedback: Preparation and Methodology

Mechano-electric feedback (MEF) is the process where a change in mechanical environment influences electrical signals in the heart [99, 130, 131]. As disturbances in mechanical activity (e.g. an abnormal stretch) can result in stretch-induced arrhythmias [131], a detailed study into the effect of stretch on cardiac electrophysiological properties is needed to identify the causes of these arrhythmia.

Investigation of MEF has been carried out in different *ex vivo* experimental models. The most commonly used preparations are isolated single cardiomyocytes [132], cell cultures [31], trabeculae and papillary muscles [133], and Langendorff-perfused whole hearts [134]. Scaling up from single cell to whole heart, the preparation reflects more of the *in vivo* situation, while the challenge involved in 'pin-pointing' underlying mechanisms increases.

A number of methodologies have been developed in a preparation-dependent manner to perform mechanical manipulation. For single isolated cardiomyocytes, stretch can be applied by attaching carbon fibres [132, 135] to both ends of the cell and stretching the cell by increasing the distance between the fibres [136]. Single cardiomyocytes can also be mechanically manipulated by a pair of glass pipettes [22, 137], a glass pipette and a glass stylus [138] or a pair of glass rods [139]. For cell cultures, cells can be seeded and cultured on deformable elastomers; mechanical manipulation can be achieved by deforming (stretching out) the elastomers [31, 140, 141]. Isolated trabeculae and papillary muscles can be suspended by two hooks (attached to the ends of the muscle preparation), with one hook attached to a tension transducer and the other end either fixed or connected to an actuator; stretch can be applied by pulling one hook away from the other [142, 143]. In Langendorff-perfused whole heart, a fluid-filled balloon can be inserted into the ventricle; stretch can be achieved by changing the volume of the balloon [144]. In a more classical approach, stretch

can be applied to the isolated whole heart by hooking weights or force transducers to the apex of the heart [145, 146]. Also other tools like the tissue impact characterisation kit have been developed to study the influence of sudden mechanical impact (which could induce arrhythmia) in the isolated whole heart [147].

4.1.2 Changes in Action Potential Observed in Different Preparations

Extensive studies have been carried out on all preparations mentioned above (from single cell to whole heart) to investigate changes in action potential (AP) shape and duration before and after mechanical manipulation. A selection of published results, grouped by preparations, is summarised below.

4.1.2.1 Isolated Cardiomyocytes

Cardiomyocytes isolated from ventricular, atrial or pacemaker tissue of different species have been used to study MEF. The trans-membrane potential was monitored via patch clamp [22, 136-138, 148-150] or optical mapping [151].

In guinea pig ventricular myocytes (stretch applied by carbon fibre), both prolongation (by 9%) [136] and shortening (by 4%) [148] of AP duration (APD) were reported after stretch. The difference in these observations may be caused by different temperatures used in the experiments. In another study where stretch was applied with a patch pipette and a glass stylus, a more complicated change in APD was observed after stretch with a decrease in APD at 20% repolarisation (APD20) and increase in APD at 90% repolarisation (APD90) [138].

Increases in both APD at 50% repolarisation (APD50) and APD90 were observed in rat cardiomyocytes (both ventricular and atrial) while stretching the cells with a pair of glass pipettes [22, 149]. In a more detailed study (also on rat ventricular myocytes) where timing and speed of stretch were tightly controlled, it was observed that both the time and the speed at which stretch is applied influence the results. It was observed that stretch applied at the

early phase of AP did not change the properties of the AP while stretch at the later phase prolonged APD. Also a positive correlation between the level of depolarisation and the speed of stretch was identified [151].

Mixed results were also reported for frog ventricular myocytes. Shortening [137], prolongation (3 out of 252 stretch trials) [150] and no significant changes (249 out of 252 stretch trials) in AP were observed after application of uniaxial stretch [150].

Stretch application to isolated sino-atrial node (SAN) pacemaker cells identified a reduction in the absolute values of maximum systolic and maximum diastolic potentials, combined with an increase in spontaneous diastolic depolarization and early systolic repolarization rates [152]. This could explain species differences in SAN pacemaker responses to stretch, as the relative durations of spontaneous diastolic depolarization and early repolarization vary as a function of background AP shape [153].

4.1.2.2 Cell Culture

Compared to the other preparations, a relatively small number of investigations have been performed on cell cultures to assess APD under stretch conditions. One study was carried out on neonatal rat ventricular myocyte cell cultures to test the effect of different mechanical actions [31]. An increase in APD after stretch was described. Another study performed with HL-1 cells, also showed a slight prolongation in APD with application of stretch [30]. Using a fluid-jet based approach and observing responses by voltage-sensitive dye application, the lab of Les Tung showed that mechanical stimulation can give rise to focal excitation and re-entry [154]. More recently, the same team explored MEF in cell cultures by relying on the cell's intrinsic activity as a mechanical stimulus, concluding that the interaction of myocytes and non-myocytes may provide additional pathways for mechanical modulation of cardiac conduction, in particular in injured tissue [155].

4.1.2.3 Trabecular and Papillary Muscle

A number of studies investigated MEF in trabeculae and papillary muscle preparations. In these studies, sharp electrodes were commonly used to monitor the trans-membrane potential [43, 156]. Both shortening and prolongation of AP were observed in cat papillary muscles, and the effect of stretch upon AP may depend on the mode of contraction, for example isotonic shortening prolongs the APD and isometric tension development shortens the APD [43]. A clear shortening of APD was seen in frog ventricular strips after application of stretch [156]. During sustained stretch, dynamic changes in APD are observed in muscle preparations, with an initial drop in APD shortly after stretch application, followed by a gradual prolongation during maintained stretch [157, 158], potentially associated with the so-called 'slow-force response' [158, 159].

4.1.2.2 Isolated Whole Heart

In rabbit isolated whole heart, an increase in APD80 was observed when stretching the left ventricle (LV) with a fluid-filled balloon [52]. An increase in APD90 was also reported in canine hearts when stretching the LV with a similar method [160]. Interestingly, the study with rabbit hearts showed no change in APD20, while the report on canine hearts demonstrated a reduction in APD20. In another study, shortening in both APD50 and APD90 were captured in canine heart [161, 162], contradicting the results shown before [160]. Shortening in APD (both APD50 and APD90) with application of stretch was also observed in frog hearts in an earlier study [163].

When applying stretch to the heart (via increasing balloon volume) in a time-controlled manner, it was found that stretch applied at the plateau phase of the AP led to transient repolarisation, while stretch applied in late systole/early diastole can result in depolarisation [144]. One study on embryonic fish hearts showed the direction at which the stretch was

applied may also play a role: a prolongation of APD was observed with axial stretch, while transverse stretch had no significant effect [164]. This suggested a sensitive dependence of APD upon stretch condition (timing and direction) which could contribute to the controversy in the published results.

MEF has also been studied in rabbit hearts whose right ventricle (RV) was cut open to form a tissue flap composed of RV free wall (one side remained attached to the LV, the other was attached to an actuator). In this study, stretch induced excitation which could lead to ventricular re-entrant arrhythmias [165].

Thus, reported stretch-effects on the AP vary, with possible explanations linked to differences in background AP shape (species and myocardial cell type differences), stretch properties (amplitude and rate of change, directionality relative to cardiac tissue), experimental conditions (temperature, electrophysiological recording techniques), repolarisation level at which APD changes are reported (APD50 *vs.* APD80), and timing of observations (acute or steady-state), to name but a few.

4.1.3 Postulated Mechanisms

Despite the variability in published results regarding AP change upon application of stretch, underlying mechanisms are also a subject of debate. The evidence for these mechanisms is briefly reviewed in the subsections below.

4.1.3.1 Mechanisms Involving Stretch Activated Ion Channels

Stretch activated channels (SAC) are a group of ion channels that respond mainly to stretch. They were first discovered in chick skeletal muscles [166]. Cardiac stretch activated channels are believed to play an important role in the change in electrophysiological properties of myocytes under the influence of mechanical stretch [167, 168]. Single channel and whole cell level studies have shown that a key group of cardiac SACs are cation non-specific and have

voltage-independent activation [149, 169]. Their reversal potential of these SAC is between 0 and -15 mV [22]. Other groups of cardiac mechano-sensitive ion channels include potassium-selective SAC [170] with reversal potentials negative to myocyte resting potentials, and cell-volume activated channels [171] such as chloride-selective channels with a reversal potential close to zero. Both potassium-SAC [172] and cell volume-activated channels [171] are likely to become more important in pathological conditions, including myocardial ischaemia (for more detailed reviews, please see [173, 174]).

Activation of SAC at negative potentials, i.e. during diastole, induces an inward current that can depolarise the membrane. At positive potentials, e.g. a stretch during the plateau phase of the AP, an outward current is induced that can shorten the initial repolarisation phase [144] [175]. The activation of SAC will therefore lead to different effects depending on timing relative to the AP (with depolarisation in the late phase of AP and repolarisation in the early phase of AP), and such effects explain both shortening and prolongation of the APD [175].

It has been difficult to irrefutably prove the role of SAC in MEF in cardiac cells. Various methods tried to isolate SAC currents from the whole cell currents for this purpose. Studies were done by blocking SAC in myocytes using Gd^{3+} [176], streptomycin [136] and GsMTx-4 [177]. Both Gd^{3+} and streptomycin are non-specific and can also block L type Ca^{2+} currents, Na^{+}/Ca^{2+} exchanger, or delayed rectifier K^{+} currents [178]. As a further note of caution, the efficacy as SAC-blockers in isolated cells and cultures, both of Gd^{3+} [179] and of streptomycin [153], may not be maintained in native tissue preparations, either because of precipitation in physiological buffer systems (Gd^{3+}), or because of apparent access restrictions to the site of action on/near SAC (streptomycin).

4.1.3.2 Mechanisms Mediated by the Calcium Handling Pathway

Other suggested mechanisms for changes in electrophysiological properties of myocytes are the changes in intracellular Ca^{2+} handling. Intracellular Ca^{2+} is known to affect the conduction properties of ionic currents in the myocyte, including L-type Ca^{2+} current, delayed rectifier current, and the Na^{2+}/Ca^{2+} exchanger current, which in turn affect the AP profile [162, 180-183]. Stretch can alter the Ca^{2+} handling in the myocyte and hence play a role for the changes in the cell's electrophysiological properties.

A number of studies in guinea pig ventricular myocytes stretched by carbon fibres have suggested an increase in resting intracellular Calcium ion concentration ($[Ca^{2+}]_i$) [132, 148, 184]. Interestingly, studies have also been published contradicting these results: a number of studies show no influence of stretch on $[Ca^{2+}]_i$ in rat atrial and ventricular myocytes [185-187]. These contradictory findings may be due to differences in species used for the study, or inconsistencies due to the different Ca^{2+} sensitive fluorescent dyes used to detect the $[Ca^{2+}]_i$.

Changes in $[Ca^{2+}]_i$ can also be caused by altered cytosolic Ca^{2+} buffering by: the sarcoplasmic reticulum, contractile filaments Ca^{2+} pump, or the Na^{2+}/Ca^{2+} exchanger [188]. Belus and White found that there was no significant increase in $[Ca^{2+}]_i$ transient (CaT) shortly after an uniaxial stretch of guinea pig ventricular myocytes. However, on maintaining the stretch, an increase in CaT was seen, which corresponded to a stretch-induced depolarizing current [143].

A delicate interplay between Ca^{2+}-mediated mechanisms and SAC has been reported. Both L-type Ca^{2+} channels [136] and intracellular Na^{+} concentration ($[Na^{+}]_i$) may play key roles in this interplay [188]. A decrease in L-type Ca^{2+} current was observed with addition of BAPTA (a Ca^{2+} chelator) and streptomycin, suggesting a potential link between L-type Ca^{2+} current and SAC activity [136]. An increase of $[Na^{+}]_i$ in myocytes could be seen during maintained mechanical stretch of cells, which has been attributed to SACs [185, 189]. It is believed that

increased $[Na^+]_i$ can result in a transient increase in $[Ca^{2+}]_i$ due to effects on the Na^+/Ca^{2+} exchanger flux balance [188].

Finally, it is important to realise that SAC are not necessarily restricted to the sarcolemma. Both the sarcoplasmic reticulum [14, 190] and mitochondria [191, 192] of cardiomyocytes appear to contain ion transport pathways that respond acutely to external mechanical stimuli. Other intracellular membrane compartments, such as the nuclear envelope, may be 'mechano-sensitive', too.

Thus, stretch affects cardiac Ca^{2+} handling, not only via sarcolemmal SAC-mediated ion flux alterations that can (directly or indirectly) alter $[Ca^{2+}]_i$ but also via direct mechanical effects on internal fluxes and buffer capacities. An added complication is the fact that observation of $[Ca^{2+}]_i$ requires addition of fluorescent dyes, which themselves are Ca^{2+}-buffers that alter the dynamics of the observed parameter.

4.1.4 Aim of this Study

The variability in the literature describing stretch-induced changes in APD makes it difficult to establish the exact mechanisms underlying cardiac electrophysiological responses to mechanical stimulation. Variations in published results can be, in part at least, attributed to different techniques and experimental conditions used, as well as to type of stretch stimulus and species differences. Beyond these considerations, there is a chasm between the desire to study MEF in experimental models that are 'as physiologically relevant as possible', and the need to link functional observations to structural information in experimental models that are 'as simple as possible' [193]. In this study we explore, therefore, the suitability of live cardiac tissue slices as models for studying MEF, and establish a method to investigate the effects of axial stretch on V_m and CaT using multi-parametric optical mapping.

4.2. Material and Methods

For heart isolation, dye loading and slice preparation protocol please refer to section 2.2.1.1, 2.2.1.2 and 2.2.1.3, for details of optical mapping setup please refer to section 2.2.1.4.

4.2.1 Animal Details

Three male rabbits (1-2 kg) were used for the study described in this chapter.

4.2.2 Stretching Device and Slice Mounting

The EDCCD camera was mounted onto a height-adjustable holder (above the stretching device). Figure 4.1A shows a schematic overview of the set-up. The stretch chamber accommodating the stretching device was kept in a bigger water bath to keep the temperature constant (see Figure 4.1B for the schematic diagram). The solution was carbogen-bubbled between the measurements to ensure sufficient oxygen content.

For mounting, the slice was placed on a wet (blebbistatin-containing bicarbonate-buffered solution) plastic sheet which was fixed on the micromanipulator surface (see Figure 4.1B). After placing the slice in the desired direction, tissue glue (WPIQ5100, WPI, Hitchin, UK) was applied to the opposite edges of the slice (see Figure 4.1B). The slice was then re-submerged into the blebbistatin-containing bicarbonate-buffered solution. After mounting the slice on to the stretching device, an adaptation time of 25 to 50 min was allowed until the signal of AP and CaT reached a steady state. The temperature of the stretching chamber was kept constant at body temperature (35 ± 2^{o}C). A scale bar was mounted beside the slice for rough quantification of the stretch.

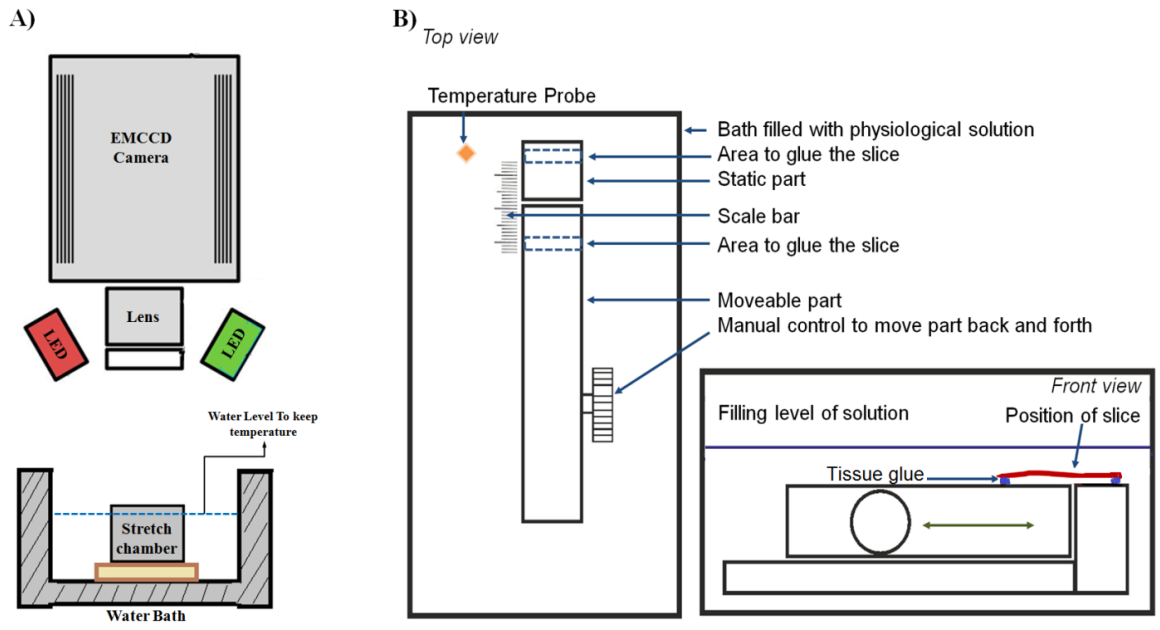

Figure 4.1: A) Schematic diagram showing the optical mapping set up and; B) a simplified stretch chamber design: a manual micromanipulator was used as the stretching device. The area where the slice was mounted was prepared with a plastic cover to avoid direct contact between the slice and the metallic parts of the manipulator.

4.2.3 Pacing

The tissue slices were stimulated with a tailor-made field stimulator with 2 platinum electrodes placed on opposite sides of the slice. The direction of the electrodes was parallel to the direction of stretch (please see section 2.2.1.5 for detailed description of stimulator and stimulation protocol).

4.2.4 Stretch Protocol

After mounting the slice on the stretcher, a recovery time of 25 to 50 min was given until a steady state of APD and CaT duration was reached. Stretch was applied manually by visual control, however the same amount of stretch could not be applied for each slice, since the area which has been used to glue the slice onto the plastic varied (discussed under limitations). During stretch, measurements were taken at different time-points, to allow

assessment of changes in AP and CaT characteristics over time. Measurements were also taken shortly after release of stretch. Figure 4.2 shows a schematic diagram of the measurement protocol.

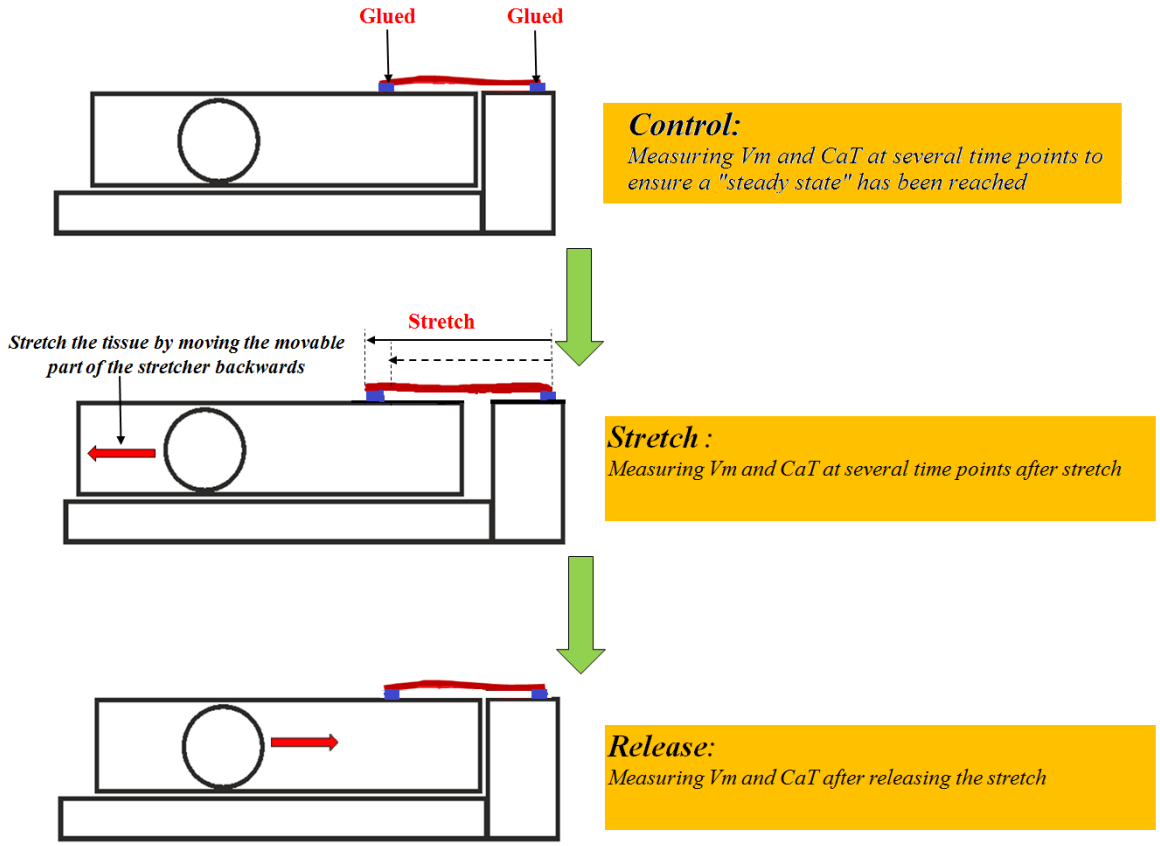

Figure 4.2: Schematic diagram showing the stretch protocol. The gap in the middle panel shows the amount of stretch experienced by the whole slice. V_m is the trans-membrane potential.

The analysis included 8 slices from 3 rabbits; one of the slices was stretched twice. We used ventricular tissue from left and the right ventricular free walls. Table 4.1 gives an overview of the slice preparations.

For most slices, the prevailing cell orientation (or 'fibre direction') can be identified by visual inspection. The cell orientation identified by eye was confirmed with a light-microscopic scan of the histologically processed slice. Figure 4.3 shows an example of a light image of one slice and a scan of a section of the same slice after histological staining.

Although the light image of the slice and the light-microscopic scan do not match completely due to deformation of the tissue sample during histological processing, it allows rough estimation of dominant fibre direction. For slices where a dominant fibre direction could be identified, we tried to stretch either parallel or perpendicular to this direction. The relation between stretch direction and dominant fibre direction of slice preparations is shown in table 4.1 (heterogeneous means a single dominant fibre direction was not identified). Table 4.1 also shows the amount of stretch applied (measured as the percentage of slice length at control). The amount of stretch and the direction of stretch in relation to the main fibre direction were not the main focus of this study; these points will be discussed in the discussion and limitation section.

Table 4.1: Overview of the cardiac slices underlying the analysis. RV - right ventricular free wall, LV - left ventricular free wall.

Slice	**Rabbit**	**Preparation**	**Slice Location**	**% Stretch**	**Stretch direction *vs* main fibre direction**	**Stretch duration before release**	**Time between stretch and first measurement**
1	i	A	RV	4.5	heterogeneous		<1min
2	ii	B	LV sub-epicardial	8.5	parallel		3 min
3	ii	C	LV mid-myocardial	6.90	parallel	17 min	<1 min
4	iii	D	LV sub-epicardial	9.8	perpendicular	53 min	~0.5 min
4	iii	E	LV sub-epicardial	8.2	perpendicular	1 min	<1 min
5	iii	F	LV mid-myocardial	18.8	perpendicular	39 min	<1 min
6	iii	G	LV mid-myocardial	6.5	parallel	42 min	<1 min
7	iii	H	LV sub-endocardial	6.9	perpendicular	17 min	~0.5 min
8	iii	I	RV	12.8	heterogeneous	30 min	<1 min

4.2.5 Histology

After a slice was removed from the micromanipulator, it was sandwiched between a sponge and a glass coverslip and placed in a typical histological processing cassette. The slice was

then fixed with fast-acting Karnovsky's fixative (2% formaldehyde, 2.5% glutaraldehyde in cacodylate buffer, Solmedia Limited, Shrewsbury, UK). The tissue sample was stored in Karnovsky's fixative until processed for embedding into wax. The wax embedded tissue was cut into 5 µm thick sections with a rotary microtome. The thin sections of tissue were then stained with Masson's trichrome. The protocol of wax embedding and Masson's trichrome staining are describe elsewhere [194]. The stained slices were imaged (see Figure 6.3B) with a digital imager (40x objective, Scanscope CS2, Leica, Milton Keynes, UK).

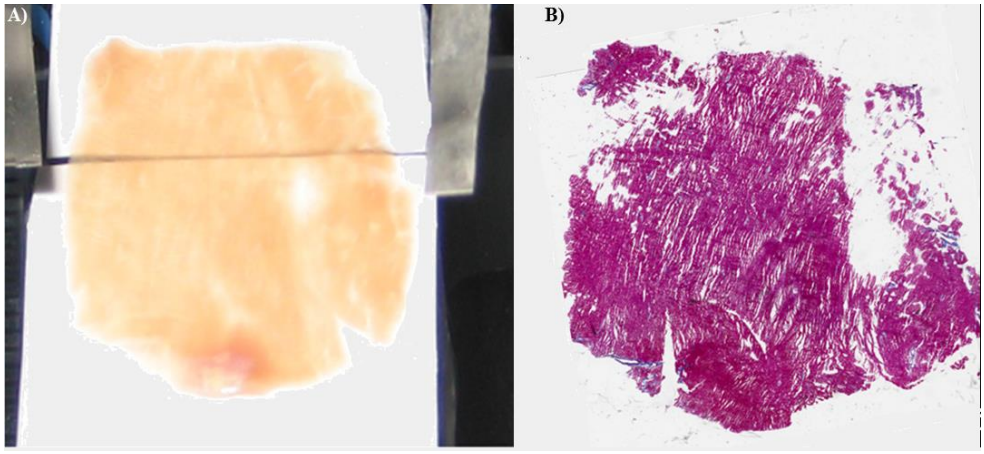

Figure 4.3: A) Light image of a slice in control state; B) Digital microscopy image of a trichrome stained 5 µm thick section of the same slice.

4.2.8 Data Analysis

4.3. Results

4.3.1 Changes in AP After Stretch

As shown in the methods section, AP and CaT were mapped before and after stretch, as well as immediately after release of stretch. APD and CaT durations measured before stretch (steady state control value) were compared with APD and CaT duration measured after stretch (within 10 min after stretch, referred to as the initial phase in this chapter). Figure 4.4 shows one slice as an example. Figure 4.4A shows the light image of the slice before and after stretch application (upper panel) as well as the averaged (spatially averaged over the

whole slice) and normalised AP trace from the state and shortly after stretch. A shortening of the APD was found after stretch. This shortening can be observed at earlier phases of repolarisation (i.e. APD50) as well as at later phases (i.e. APD80), see Figure 4.4A lower panel. Figure 4.4B shows the histogram of APD80 measured from the slice in control state and shortly after stretch. An overall shortening of APD80 can be observed as the entire APD80 distribution shifts to lower values. A similar overall shortening can be observed in APD50. Such shortening in APD80 and APD50 at the initial phase after stretch can be seen in different slices. Table 4.2 summarises the mean and standard deviation (SD) of APD80 and APD50 (mean and SD of all the APD80s and APD50s measured from the whole slice) obtained in control state and in the initial phase after stretch. A decrease in APD80 and APD50 can be seen in all 9 samples with an average decrease of 10.7% and 11.4% for APD80 and APD 50, respectively (i.e. mean APD80 and APD50 measured during initial phase of stretch are on average 89.3% and 88.6%, respectively, of the control case). Figures 4.5A and B also show an overall tendency of decrease in APD80 and APD50 during the initial phase after stretch for all slices.

Table 4.2: Comparison of APD80 and APD50 measured before and during the initial phase after stretch

Prep	Control APD80 mean (ms) ± SD	Stretch APD80 mean (ms) ± SD	APD80 stretch/ control %	Control APD50 mean (ms) ± SD	Stretch APD50 mean (ms) ± SD	APD50 Stretch/ control %l
A	129.2 ± 14.1	126.9 ± 13.8	98.2	104.8 ± 13.3	103.2 ± 11.8	98.5
B	248.3 ±28.4	195.5 ± 12.6	78.7	213.0 ± 36.0	166.6 ± 16.3	78.2
C	210.5 ±15.5	182.2 ± 22.0	86.6	179.8 ± 16.6	152.1 ± 23.3	84.6
D	182.3 ±11.4	150.5 ± 10.2	82.6	152.5 ± 12.3	122.2 ± 10.0	80.1
E	230.4 ±25.1	213.1 ± 22.0	92.5	190.5 ± 26.3	176.6 ± 21.4	92.7
F	220.7 ±19.8	203.6 ± 22.5	92.3	181.5 ± 27.3	168.1 ± 25.7	92.6
G	235.3 ±19.3	216.7 ± 17.8	92.1	201.9 ± 19.5	185.2 ± 17.7	91.7
H	255.1 ±42.4	219.5 ± 47.8	86.1	213.9 ± 46.3	179.2 ± 51.4	83.8
I	209.0 ±38.9	197.0 ± 33.5	94.2	161.9 ± 43.4	154.1 ±39.2	95.2
		Average	89.3		Average	88.6
		SD	6.2		SD	7.1

A

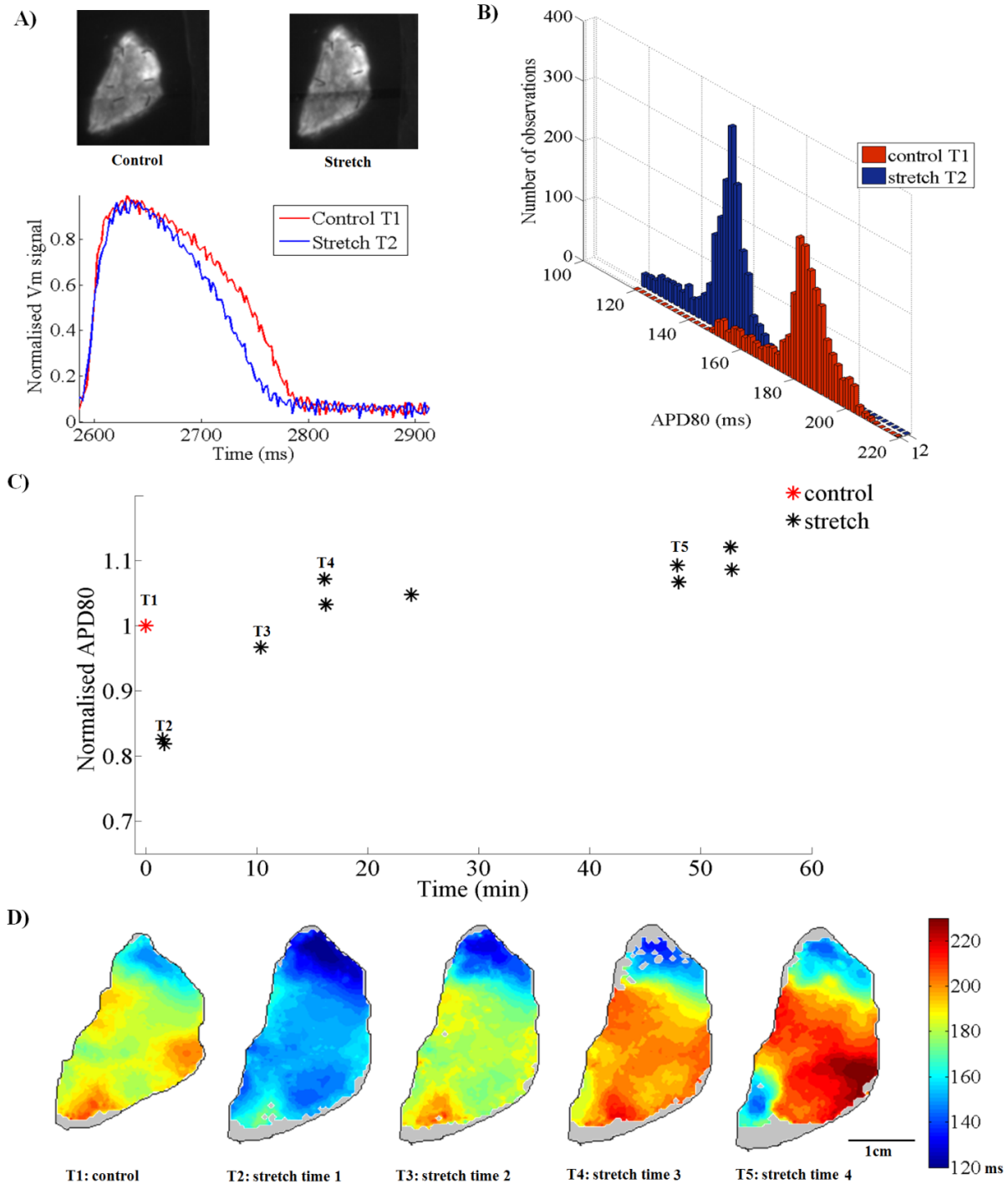

Figure 4.4: Influence of stretch upon AP: A) The upper panels in this Subfigure show the light image of the slice before and after stretch and the plot below shows the averaged AP trace (averaged over the whole slice) before (red) and shortly after stretch (blue); B) Histogram of APD80 measured from the slice before (red) and shortly (blue) after the stretch; C) Normalised APD80 (normalised to the control value) at different time points after stretch (with the reference control point showing as red star and the data points of APD80 measured

during stretch showing as black star); D) APD80 map of this slice at 5 different time points (time points T1 to T5 are marked out in Subfigure C) .

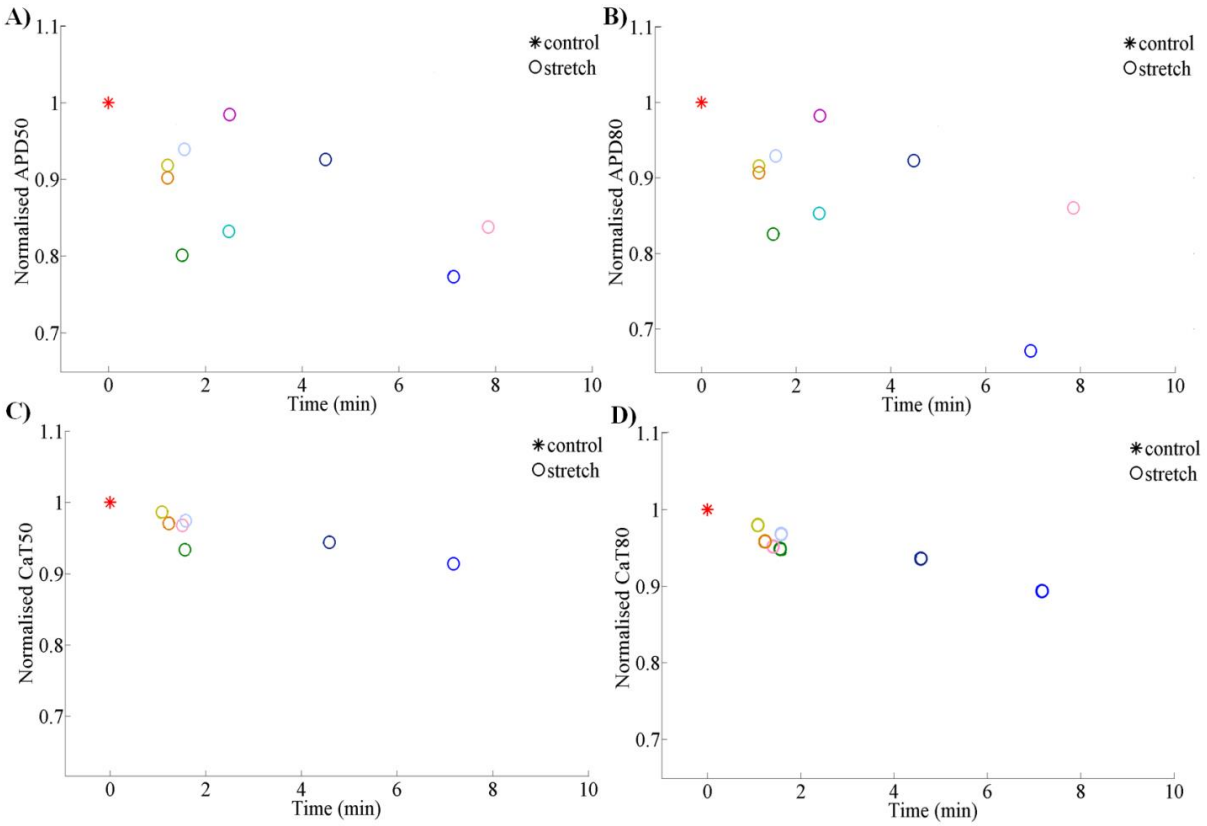

Figure 4.5: Response of APD and CaT duration shortly after stretch: Normalised (to the control value) (A) APD50, (B) APD80, (C) CaT duration at 50% decay (CaT50) and (D) CaT duration at 80% decay (CaT80) at different time points after stretch (with the reference control point showing as red star and the data points measured during stretch showing as circle, colour coded to each different slice preparations).

To investigate APD changes during sustained stretch, a series of measurements at different time points were taken (from 2 min up to 50 min). In Figure 4.4C, the normalised mean APD80s (normalised to control), measured at different time points after stretch, are plotted against time after stretch. The control value (which is 1 as it is the reference value for normalisation) is shown as red star while the data points collected during stretch are shown as black stars. A gradual increase in APD80 over time during maintained stretch can be observed, and APD80 seems to reach a new steady state which is longer than control APD80.

A similar pattern was observed in APD50 (Figure 4.6A). In Figure 4.4D and 4.6B, maps of APD80 and APD50 are plotted at five time points (T1 to T5, as marked in the figures, with T1 being the control state and T2 to T5 being time points during stretch). A decrease in APD (both APD50 and APD80) over the whole slice can be seen shortly after stretch (i.e. at T2). From T2 to T5, an increase in APD (both APD50 and APD80) over the entire slice can be observed. Comparing APD patterns between these 5 time points, the intrinsic pattern in APD (both at 50% and 80% repolarisation) gradually restored over time during stretch (with patterns at T5 closer to T1). Summarising the information from all slices, a general increase in APD (both APD50 and APD80) during stretch can be seen; however rate and amount of increase differ from case to case (see Figures 4.7 and 4.8).

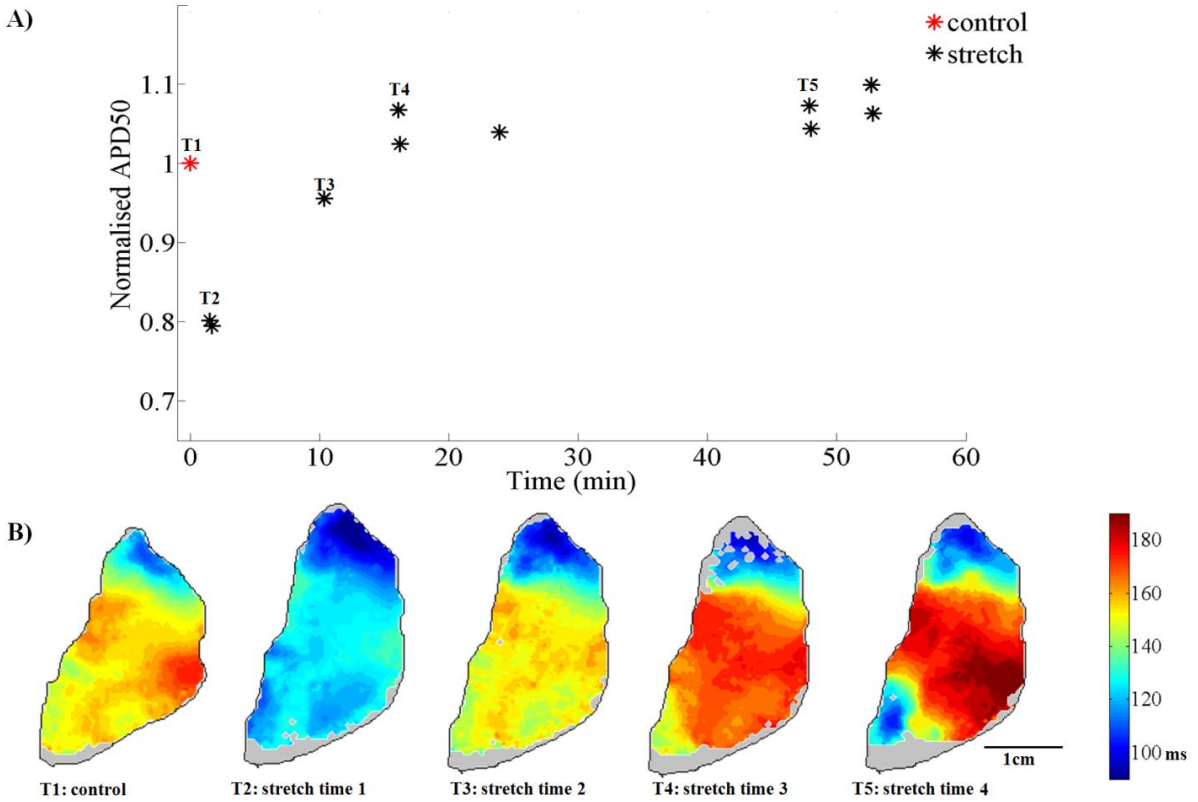

Figure 4.6: Change of APD50 during stretch: A) Normalised APD50 (normalised to control) at different time points after stretch (reference control point showing as red star, and data points of APD50 measured during stretch showing as black stars); B) APD50 map of this slice at 5 different time points (time points T1 and T5 are marked in Subfigure A).

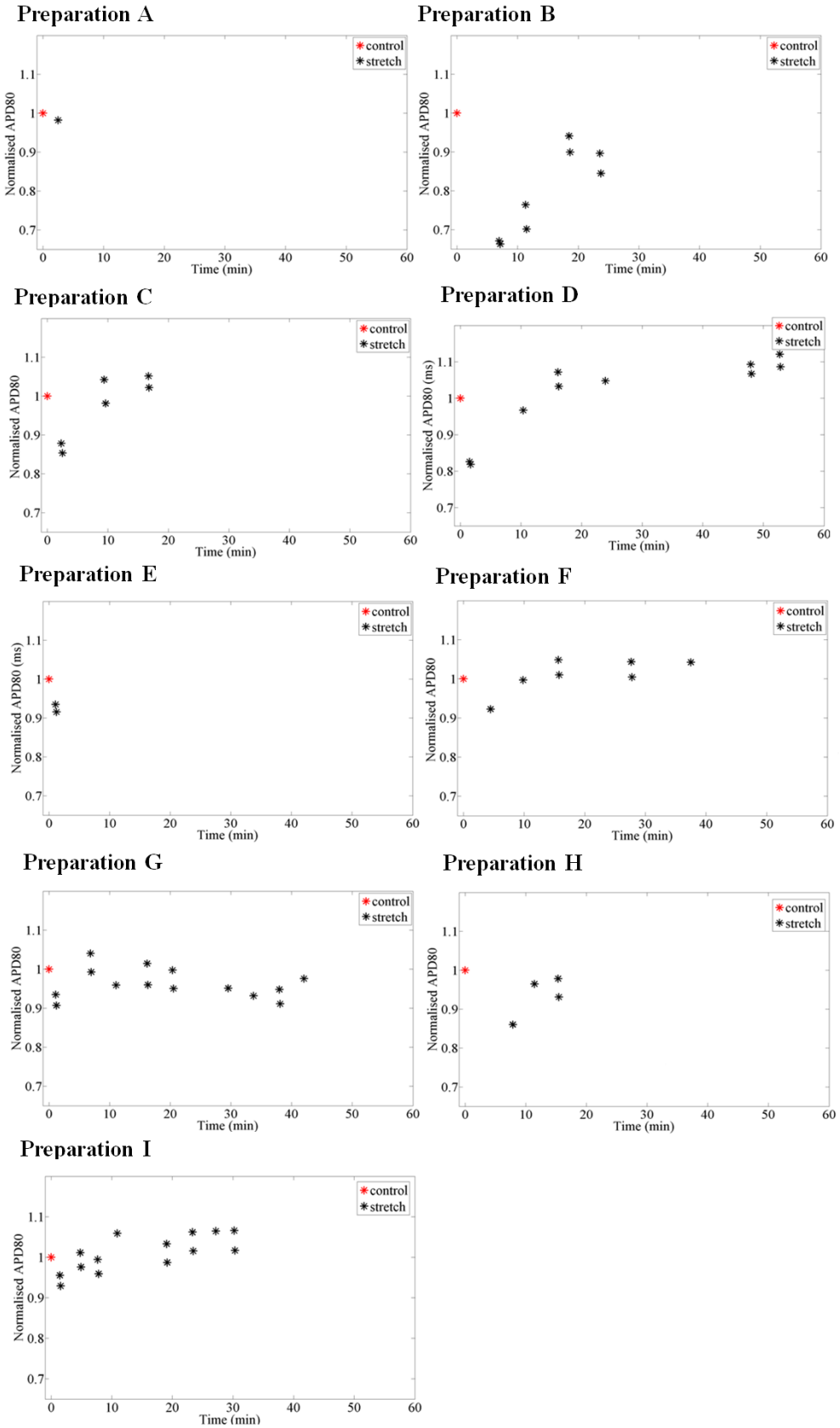

Figure 4.7: Time line of normalized APD80 for each individual slice. APD80 taken at several time points, from control before stretch (red star) and during the stretch period (black stars), normalized to the control value. X-axis shows the time (in min).

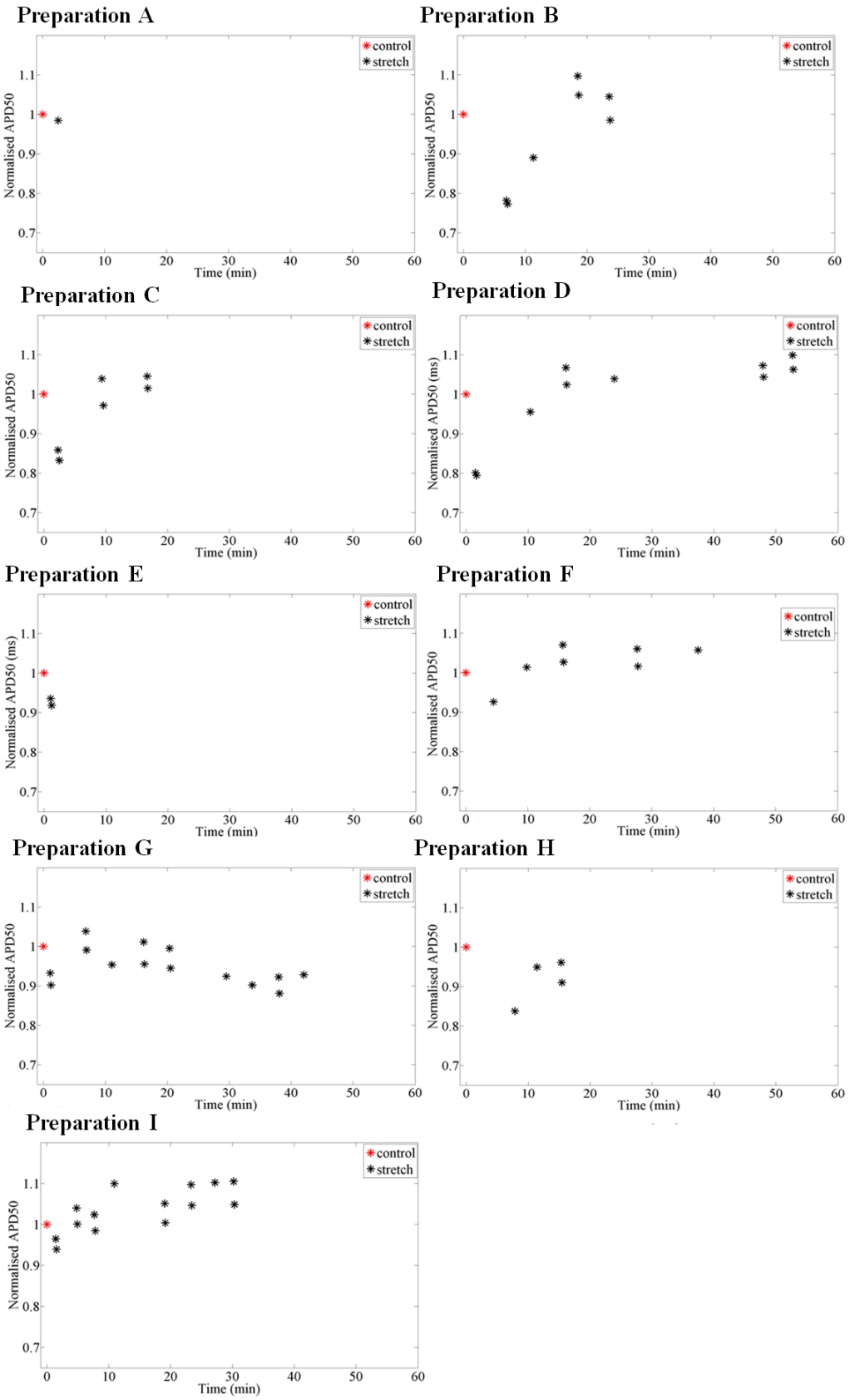

Figure 4.8: Time line of normalized APD50 for each individual slice. APD50 taken at several time points, from control before stretch (red star) and during the stretch period (black stars), normalized to the control value. X-axis shows the time (in min).

4.3.2 Change in CaT After Stretch

Results of CaT duration change during the initial phase after stretch and during extended stretch period are summarised in similar fashion as those in APD. The upper panel of Figure 4.9A shows the light image of a slice (same slice as shown in Figures 4.4 and 4.6) before and after stretch, while the lower panel shows the spatially averaged trace (averaged over the whole slice). Figure 4.9B shows the histogram of the CaT80 distribution measured from this slice before and immediately after stretch. A slight shortening of CaT duration at 80% decay (CaT80) and at 50% decay (CaT50) (94.0%, and 94.7%, respectively) compared to control value before stretch can be observed (Figure 4.9A). Table 4.3 summarises mean and SD of CaT80 and CaT50 before and shortly after stretch of different slices (the naming of slices is coherent in all tables, CaT duration for preparation A and C are not shown as they did not have a sufficient CaT signal). A shortening in CaT duration (CaT80 and CaT50) can be observed shortly after stretch. The shortening in CaT duration seems to echo the shortening observed in APD, but the extent to which CaT duration shortens is less compared to APD.

Table 4.3: Comparison of CaT80 and CaT50 measured before and during the initial phase after application of stretch.

Prep.	Control CaT80 mean (ms) ± SD	Stretch CaT80 mean (ms) ± SD	CaT80 stretch/ control %	Control CaT50 mean (ms) ± SD	Stretch CaT50 mean (ms) ± SD	CaT50 stretch/ control %
B	223.0 ± 18.0	199.3 ± 12.6	89.4	165.8 ± 15.4	151.6 ± 9.8	91.4
D	232.8 ± 11.1	218.1 ± 11.2	93.7	163.3 ± 8.0	150.6 ± 7.1	92.2
E	241.9 ± 20.3	235.1 ± 19.2	97.2	174.5 ± 15.6	171.1 ± 14.2	98.1
F	242.1 ± 15.6	226.3 ± 19.5	93.5	173.1 ± 12.5	163.3 ± 15.8	94.3
G	234.3 ± 19.3	216.7 ± 17.8	92.5	201.1 ± 19.5	185.2 ± 17.7	92.1
H	248.7 ± 24.9	235.3 ± 21.6	94.6	175.9 ± 18.8	171.0 ± 18.2	97.2
I	244.6 ± 22.6	237.4 ± 20.7	97.1	177.7 ± 21.9	173.7 ± 19.0	97.8
		Average	94.0			94.7
		SD	2.7			2.9

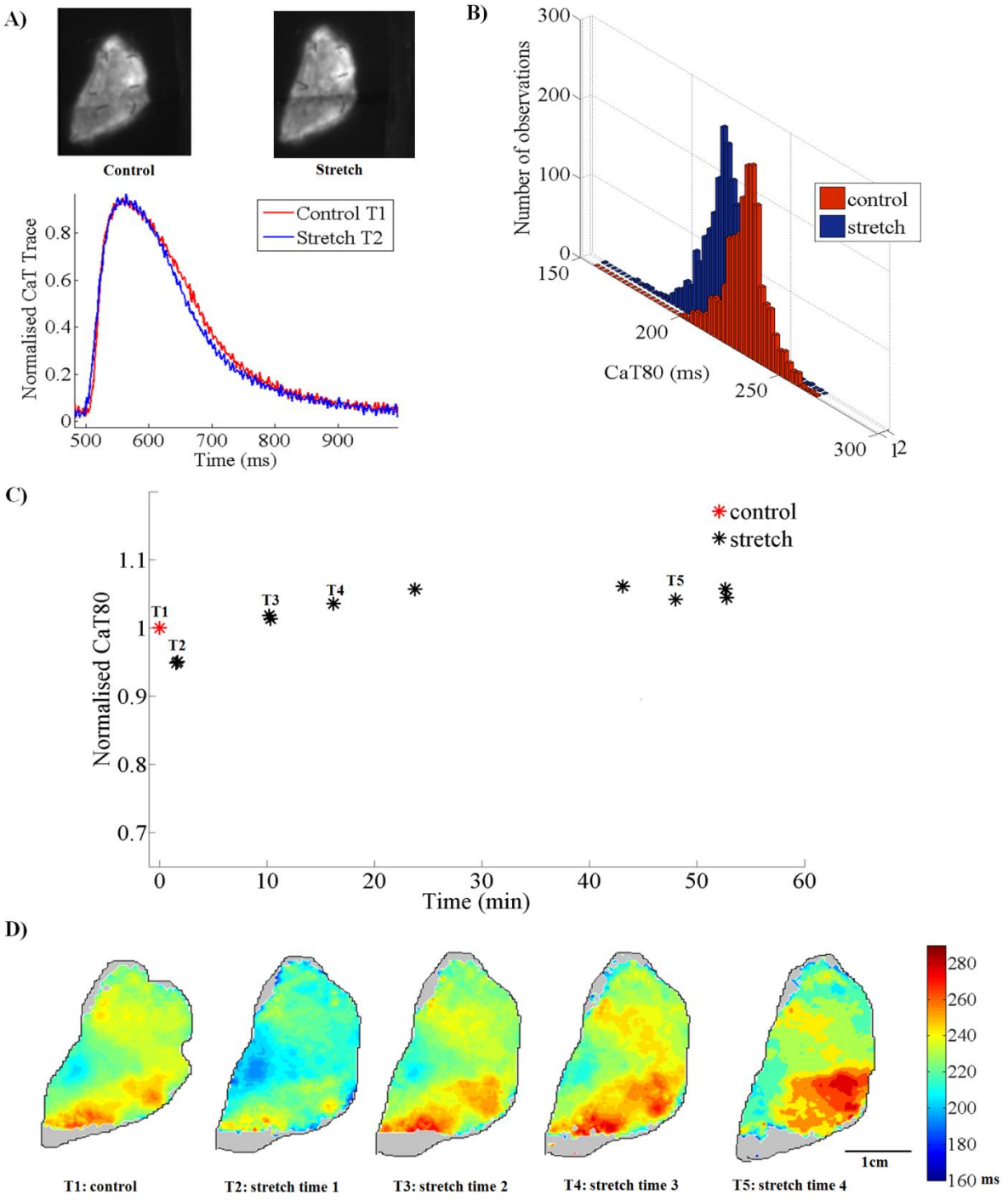

Figure 4.9: Influence of stretch upon CaT: A) The upper panels in this Subfigure show the light image of the slice before and after stretch and the plot below shows the CaT trace, averaged over the whole slice before (red) and shortly after application of stretch (blue); B) Histogram of CaT80 measured from the slice before (red) and shortly (blue) after the stretch; C) Normalised CaT80 (normalised to the control value) at different time points after stretch (with the reference control point showing as red star and the data points of CaT80 measured during stretch showing as black stars); (D) CaT80 map of this slice at 5 different time points (time points T1 and T5 are marked out in Subfigure C).

A recovery and slight prolongation can also be observed in CaT80 and CaT50 over time during sustained stretch, as shown in Figure 4.9C and Figure 4.10A, where normalised CaT80 and CaT50 (normalised to the control value) measured at different time points during stretch are plotted. Figure 4.9D and 4.10B show CaT80 and CaT50 maps, respectively, at 5 selected time points (T1 to T5, with T1 being control and T2 to T5 being time points during stretch). Similar to APD, a decrease in CaT80 and CaT50 over the entire slice can be observed during the initial phase after application of stretch. Figure 4.11 and 4.12 summarise the CaT80 and CaT50 change over time during stretch from different slices. Similar to APD, gradual increase over time during stretch was observed, although the rate of increase and amount of increase differs between slices.

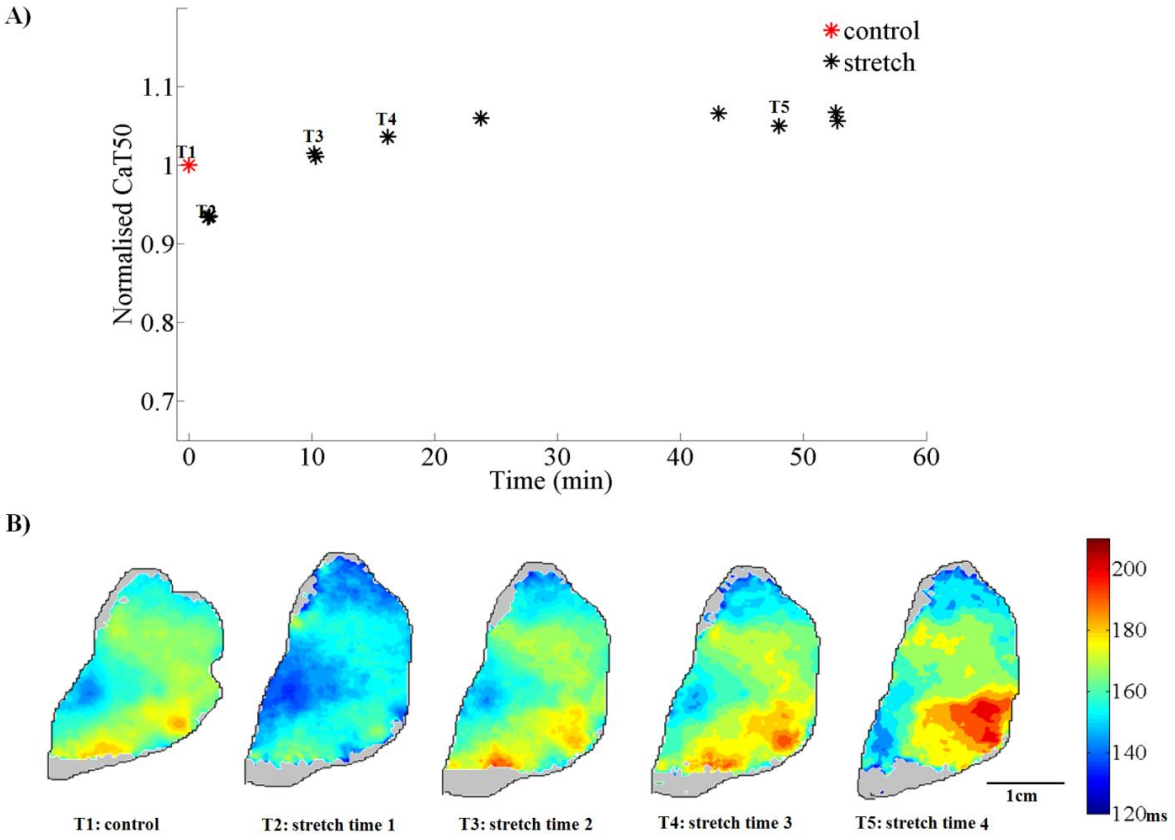

Figure 4.10: Change of CaT50 during stretch: A) Normalised CaT50 (normalised to control) at different time points after stretch, with the reference control point showing as red star and the data points of CaT50 measured during stretch showing as black stars; B) CaT50 map of this slice at 5 different time points (time points T1 and T5 are marked in Subfigure A).

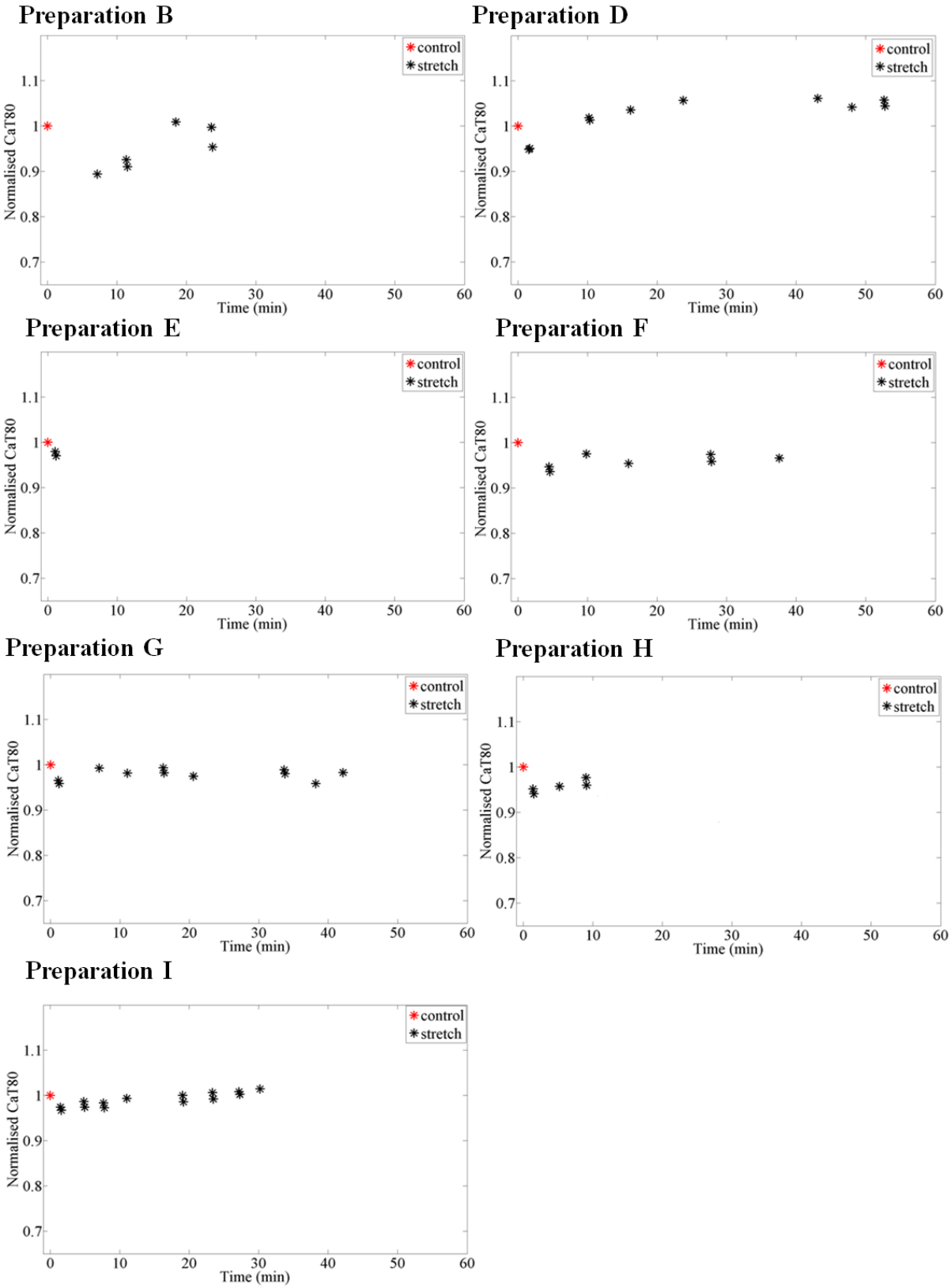

Figure 4.11: Time line of normalized CaT80. CaT80 taken at several time points at control (red star) and during the stretched period (black stars), normalized to the control value. X-axis shows the time (in min).

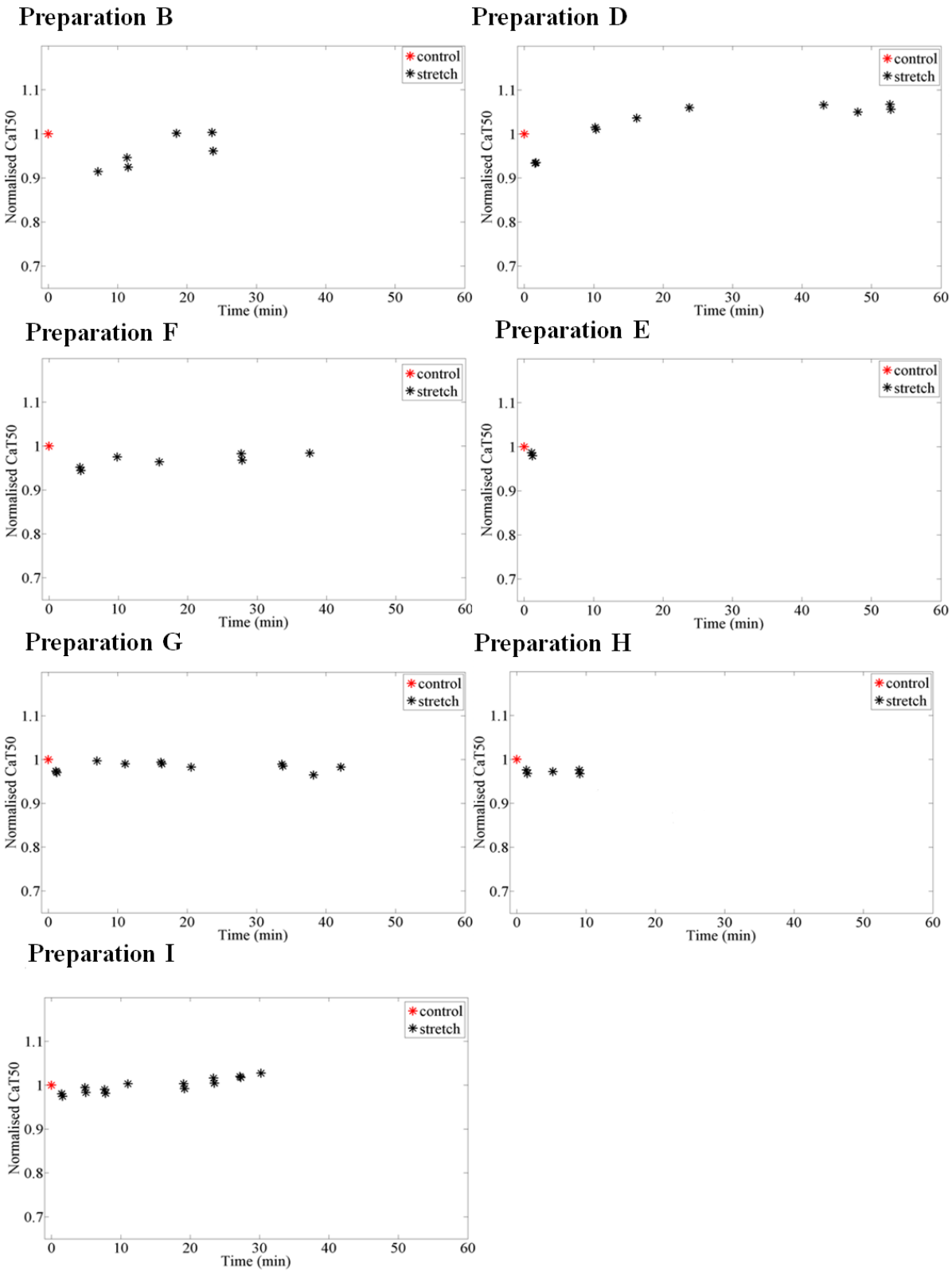

Figure 4.12: Time line of normalized CaT50. CaT50 taken at several time points at control (red star) and during the stretched period (black stars), normalized to the control value. X-axis shows the time (in min)

4.3.3 Influence of Releasing Stretch on APD and CaT

A decrease in both APD and CaT duration were not only captured shortly after application of stretch, but also after releasing stretch sustained for 30 to 50 min. Table 4.4 and table 4.5 summarise the APD changes (APD in Table 4.4 and CaT in Table 4.5) before and after stretch release. An average shortening of 6.7% and 7.9% in APD80 and APD50, respectively, were found shortly after releasing stretch. For the CaT duration, the decrease was much more subtle, with an average shortening of 1.9% and 2.0%, for CaT80 and CaT50, respectively (Table 4.5). Slice preparation A and B had to be excluded for these measurements since other pacing protocols were applied before releasing stretch. Slice preparation C had a poor CaT signal and was excluded from CaT analysis; CaT was not measured for slice preparation F after releasing stretch.

Table 4.4: Comparison of APD 80 measured before and during the initial phase after releasing stretch

Prep	Stretch APD80 mean (ms) ± SD	Release APD80 mean (ms) ± SD	APD80 release/ stretch %	Stretch APD50 mean (ms) ± SD	Release APD50 mean (ms) ± SD	APD50 release/ stretch %
C	187.2 ± 24.9	181.1 ± 21.9	96.7	154.0 ± 26.0	148.2 ± 23.4	96.2
D	201.2 ± 23.0	178.9 ± 19.9	88.9	164.8 ± 25.6	144.3 ± 22.5	87.5
E	213.1 ± 22.0	202.5 ± 17.5	95.0	176.6 ± 21.4	165.8 ± 17.7	93.9
F	217.5 ± 36.3	212.6 ± 29.9	97.7	180.0 ± 36.7	171.4 ± 34.0	95.2
G	229.6 ± 37.9	221.7 ± 38.1	96.6	187.5 ± 48.2	179.5 ± 45.9	95.7
H	189.5 ± 73.0	172.8 ± 65.6	91.2	150.2 ± 70.4	136.3 ± 63.8	90.8
I	217.6 ± 34.2	189.9 ± 34.0	87.3	174.3 ± 39.7	148.6 ± 35.6	85.3
		Average	93.3		Average	92.1
		SD	4.2		SD	4.3

Table 4.5: Comparison of CaT80 and CaT50 before and during the initial phase after releasing stretch

Prep	Stretch CaT80 mean (ms) ± SD	Release CaT80 mean (ms) ± SD	CaT80 release/ stretch/ %	Stretch CaT50 mean (ms) ± SD	Release CaT50 mean (ms) ± SD	CaT50 release/ stretch %
D	243.2 ± 15.8	234.3 ±16.2	96.3	172.2 ± 13.5	165.1 ± 13.0	95.9
E	237.4 ± 18.8	234.2 ± 19.1	98.7	172.4 ± 13.3	169.5 ± 13.9	98.3
G	231.8 ± 15.0	230.3 ± 14.7	99.3	166.8 ± 12.6	165.2 ± 13.1	99.1
H	216.6 ± 35.8	212.5 ± 33.4	98.1	154.1 ± 29.6	151.7 ± 28.8	98.5
I	245.2 ± 21.4	241.1 ± 20.2	98.3	180.8 ± 19.1	177.6 ± 18.4	98.2
		Average	98.1		Average	98.0
		SD	1.1		SD	1.2

4.4. Discussion and Limitation

4.4.1 Transient Shortening in APD and CaT Duration After Onset of Stretch

Data collected from rabbit ventricular tissue slices in this study showed a transient decrease in both APD and CaT duration during the initial phase after application of stretch, with less pronounced decrease in CaT duration than APD (Figure 4.4 and 4.6 for APD80 and APD50, respectively, and Figures 4.9 and 4.10 for CaT80, and CaT50, respectively, as well as Tables 4.2 and 4.3 for APD and CaT, respectively). Although the profile (the amount of change and the rate of change) of APD and CaT duration during stretch exhibited individual differences, most data indicate an re-lengthening in both APD and CaT duration over time during maintained stretch with ‘steady state’ APD and CaT duration often being longer than control values (as shown in Figures 4.6, and 4.9 for APD80, and CaT80, respectively). In Figures 4.7 to 4.11, the time lines are shown for all measurements. These findings suggest a dynamic change in APD and CaT duration during stretch (particularly comparing the data points collected shortly after stretch and at longer time into stretch). The dynamic nature of these

two parameters during stretch was described earlier in the literature for APD [158] and CaT [143]. The increase of CaT amplitude has been also described in connection with investigations into the slow force response [185]. To build a comprehensive picture of the effect of stretch on AP or CaT over time, a series of measurements at different time points while the sample is stretched (ideally until APD or CaT duration reach a steady state (during stretch) is necessary.

4.4.2 AP *vs.* CaT

Data collected in this study show a correlation between the response of APD and CaT duration to stretch, as described before [195]. As shown in the results part, the CaT duration changes echo APD changes, though they are relatively smaller than changes in APD. Stretch could influence both parameters through several possible mechanisms, including stretch activated channels [173] and Ca^{2+} flux balance, e.g. the slow force response [196]. The delicate interplay between trans-membrane potential and CaT can contribute to the correlation observed, making the cause-effect relationship difficult to explore. It is therefore useful to have a dual voltage-CaT mapping system (which has been used in other studies [88] to capture both parameters simultaneously). This would be a relatively easy add-on to the pioneering set-up demonstrated in this chapter. Also, interventions targeting Ca^{2+} handling pathways or a particular ion channel may help to perturb the system and therefore reveal more of the underlying relationship between AP and CaT during stretch.

CaT amplitude is an important parameter for studying stretch effects upon Ca^{2+}. This parameter is not used in this study as the measurement technique was non-ratiometric. A dual V_m CaT mapping system with a ratiometric Ca^{2+} imaging would be ideal to study stretch effects, and will be implemented in our system in the future.

The Ca^{2+}-sensitive dye used in this study, Rhod-2, has relatively high affinity for Ca^{2+}. High-affinity Ca^{2+}-sensitive dyes may suffer from saturation [197] and they are therefore not necessarily capturing the real CaT peak value. It would be useful to measure the CaT with a low-affinity Ca^{2+}-sensitive dye (like Rhod-ff) and compare it with the results obtained with higher affinity dyes.

4.4.3 Release

Similar to the controversial results of stretch effects on APD and CaT duration, observations of the effects of releasing stretch are a matter of debate, and seem to depend on timing, contractile state, amplitude and experimental environment [156, 198, 199]. Our measurements showed that APD decreased upon release of pre-existing stretch, which is in keeping with earlier published data [52]. Assuming that the slight prolongation of APD and CaT duration over time was provoked by the slow force response mechanism, it is reasonable that upon termination of the stretch the durations for AP and CaT are returning towards their initial control values, as described in [156]. The underlying mechanisms here could be very interesting and could be investigated over a longer time after releasing stretch, to capture any slowly developing response, and to assess whether the tissue undergoes 'permanent' remodelling (in terms of APD and CaT duration) after application of stretch.

4.4.4 Utility of Living Tissue Slices as a Model for Cardiac MEF Research

Cardiac tissue slices with their locally preserved cell-cell connections and cell-type distribution combine moderate complexity with the potential for effective experimental control (input) and observation (output). Of note, they are amenable to use on human cardiac tissue [82, 84]. Compared to whole heart, although the electric-coupling in the third dimension is severely reduced, and extracellular spaces are less preserved [200], the reduced complexity can be beneficial. Thus, electrical activation, for example, occurs in a much

simpler fashion, allowing control over pacing rate and site, and directionality of conduction. As an experimental model system, slices also offer the opportunity to collect multiple tissue samples, and tissue from different regions, of one heart (e.g. LV free wall *vs*. RV free wall; subepicardial, mid-myocardial or subendocardial layers) allowing multiple experimental investigations from the same sample, and exploration of regional difference in behaviour. Although we did not explore this aspect in detail here, we show that it is possible to collect multiple slices with decent trans-membrane potential and CaT signal from various transmural layers of LV tissue, and of the RV, from one and the same heart.

Since the dominant fibre direction in tangentially cut (parallel to epicardial plane) cardiac tissue slices can, in most cases, be identified with ease, stretch can be applied in principle using the dominant fibre direction as a reference (e.g. perpendicular, parallel, or at any desired angle relative to fibre orientation). This allows investigation of potential differences between stretch effects on cells depending on their orientation relative to the main direction of stretch.

Although cutting cardiac tissue slices in parallel to the epicardial plane yields sections with a high proportion of in-plane fibres [83, 104], this orderly alignment becomes less pronounced as one approaches sub-endocardial layers. When point stimulation is used to pace slices with clear fibre direction, a conduction map showing pronounced anisotropy is often captured. With algorithms such as that developed by Bayly et al. [109], conduction velocities can be estimated for each point. This makes it potentially easy to capture conduction velocity changes during stretch. However, conduction from point-stimulation sites is affected by uneven source-sink distribution, and this can yield variable results in one and the same tissue slice, depending on the stimulation site [201]. For this reason, we focussed our analysis here on field stimulation. The use of point stimulation to capture conduction velocity changes upon stretch [31, 202] is an interesting topic for further study in cardiac slices.

4.4.5 Use of Optical Mapping

Electrophysiological behaviour of cardiac tissue slices has mainly been explored using multi-electrode arrays [83]. These monitor trans-membrane potential usually without capturing AP shape, and at relatively low spatial resolution. Optical mapping addresses these limitations, and allows one to extend the study of MEF to other parameters, such as $[Ca^{2+}]_i$, and hence to capture two highly relevant parameters for cardiac electro-mechanic research.

Optical mapping can be combined with motion/deformation tracking, for example using structured light [203] or fluorescent beads [204]. This can provide information about local slice deformation, including acute and possible delayed effects (e.g. viscous re-lengthening). This data would be useful for assessing the homogeneity (or lack thereof) of stretch effects in the tissue, and for a more careful interrelation of local stretch, APD and CaT changes.

4.4.6 Limitations

This study was a first attempt to investigate the suitability of cardiac slices for stretch applications. During the experiments we came across limitations with our current methodology.

The amount, timing and speed of stretch can influence effects on APD and CaT duration [132, 144, 151]. This study was not designed to investigate the influence of these parameters; the manual stretch device would not allow an application of stretch with tight control over these three parameters. A computer controlled motorised stretcher would be necessary to apply stretch with controlled speed and timing (ideally synchronised with the electrical activity cycle), as well as more accurately controlled amplitude.

Cardiac tissue slices can be obtained from different regions of the heart and the dominant fibre direction can be tracked easily in most cases. Although we used slices from the left and the right ventricle and applied stretch perpendicular or parallel to the dominant fibre

direction, we have not analysed these subgroups separately, due to the limited n-numbers per group.

Stretch-induced tissue damage of the tissue was not examined, although we did exclude slices which showed obvious ischemic AP (very short and sharp AP) after application of stretch (this normally happened after large tissue deformation).

The use of tissue glue has several advantages. It can be used to mount slices on to the stretcher regardless of their shape. The glue acts quickly and holds the slice down relatively strongly. However, there are also disadvantages of using glue. The glue may influence the vitality of the tissue where applied. It cannot be excluded that during the gluing phase the slice was exposed already to a small amount of stretch (difficult to control). Once glued down, correction over the slice position is not possible, and slice rotation, relative to stretch direction, is challenging.

Slices were fixed immediately after the experiment, for histological examination. Masson's trichrome staining is an established method [194] to visualize cardiac muscle cells, cell nuclei, and collagen. However during histological processing, tissue undergoes a dehydration procedure which causes deformation of the tissue. That is one reason why the tissue outline of the histological slice differs from the outline obtained from the optical mapping image. Despite this deformation, the dominant fibre direction can be identified.

4.5. Conclusion

Stretch of cardiac tissue has been studied intensively for single cardiac cells, trabeculae and papillary muscle, cell cultures and whole heart preparations. Although contractility of cardiac slices has been assessed before [82, 205], MEF in slices has not been studied in detail to date. We have described in this chapter a methodology to investigate the effects of axial stretch in cardiac slices. Dual AP and CaT optical mapping opens up the possibility of studying the

interrelation of these two major players in cardiac MEF in cardiac slices, with relatively high spatial resolution.

In this chapter, we have described the preliminary study where we used cardiac tissue slices to investigate MEF. In the next chapter we now go on to consider the study of AP and CaT spatial heterogeneity in rabbit left ventricular free wall using cardiac tissue slice.

Chapter 5
Study of Spatial Heterogeneity of the Action Potential and Calcium Transient in Rabbit Left Ventricular Free Wall Using Tissue Slices

Brief Summary of Chapter 5:

This chapter describes a study where left ventricular tissue slices were used, together with dual parameter optical mapping, to investigate the spatial heterogeneity of AP and CaT duration in rabbit left ventricular free wall. A positive epi- to endocardial transmural gradient was observed for both the APD and CaT duration, with longer AP and CaT in the subendocardium. We did not find any regions in the mid-myocardium with largely prolonged APD. Our data also suggest a correlation between APD or CaT duration and onset of alternans: areas with longer APD and CaT duration can move into alternans at a lower pacing frequency. This could also explain the reason why alternans was captured more often close to the endocardium (as the subendocardium has a longer CaT and APD).

My contribution to this chapter:

- The tissue slice optical mapping experiments included in this chapter were performed together with Dr. Christian Bollensdorff. I was responsible for the study design, the tissue slice preparation, the mapping measurements and the data analysis.

5.1 Introduction & Motivation

5.1.1 Heterogeneity of Action Potentials in Different Cardiac Cell Types

Different regions of the heart have their own specialised function, for example the sino-atrial-node (SAN) pacemaker cells provide the electrical trigger signal and the His-Purkinje system serves fast conduction of excitation. These specialised regions have different electro-physiological properties. The schematic figure below (Figure 5.1) shows a sketch of typical action potential (AP) shapes of different parts of the heart. These typical electro-physiological properties can be explained by differences in ion channel expression, which leads to different ionic current balances [206].

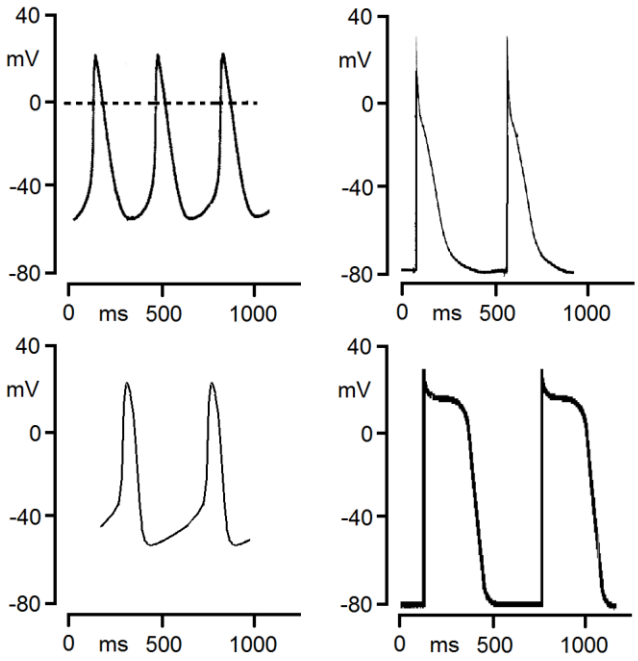

Figure 5.1: Schematic diagram showing different AP shapes from different regions of the heart: SAN [207], atrium [208], AV (atrio-ventricular) node [209], and ventricle [206]. Figures are modified from the ones in the original papers.

5.1.2 Action Potential Heterogeneity in the Left Ventricular Free Wall

Heterogeneity not only exists between different functional components of the cardiac system, but also within each component. Thus, the left ventricle (LV) is not

electrophysiologically homogenous. The heterogeneities in its electrophysiological properties are important because of their link to cardiac function. Heterogeneity can cause problems and may play a role in cardiac disease: an increase in the spatial heterogeneity of AP restitution has been linked to increased risk of ventricular tachycardia and ventricular fibrillation [210]. The increase of repolarisation dispersion can facilitate the development of a conduction delay that may induce sustained arrhythmias [211]. To demonstrate this, a very simple two dimensional (2D) simulation (see Figure 5.2) was performed using a modified Mahajan 2008 rabbit cell model (the rapidly activating delayed rectifier potassium channel current, $I_{Kr,}$ conductance was modified) [108] coupled with the mono-domain equation (isotropic conduction). The simulation was performed with Chaste software [107]. The region inside the red triangle shown in Figure 5.2a-1 displays a longer AP due to a reduced I_{Kr} conductance. And the rest of the tissue has relatively short AP due to increased I_{Kr} conductance. As the AP duration (APD) shows pronounced spatial heterogeneity, repolarisation is not synchronised with the triangular island repolarising much later compared to the rest of the tissue. During rapid pacing (~6 Hz), or with a premature stimulus, a second excitation wave cannot go through the area around the triangular island (as cells in this area still remain non-excitable) and the wave curls around that region. While the excitation wave travels around the triangular region, this region starts to repolarise and becomes excitable. Therefore the excitation wave can now enter this triangular region from the back and create a re-entry loop around the triangular region. Such re-entry can die out after one excitation and cause an ectopic beat (as shown in this simulation), or be sustained, which leads to behaviour seen in ventricular tachycardia or fibrillation.

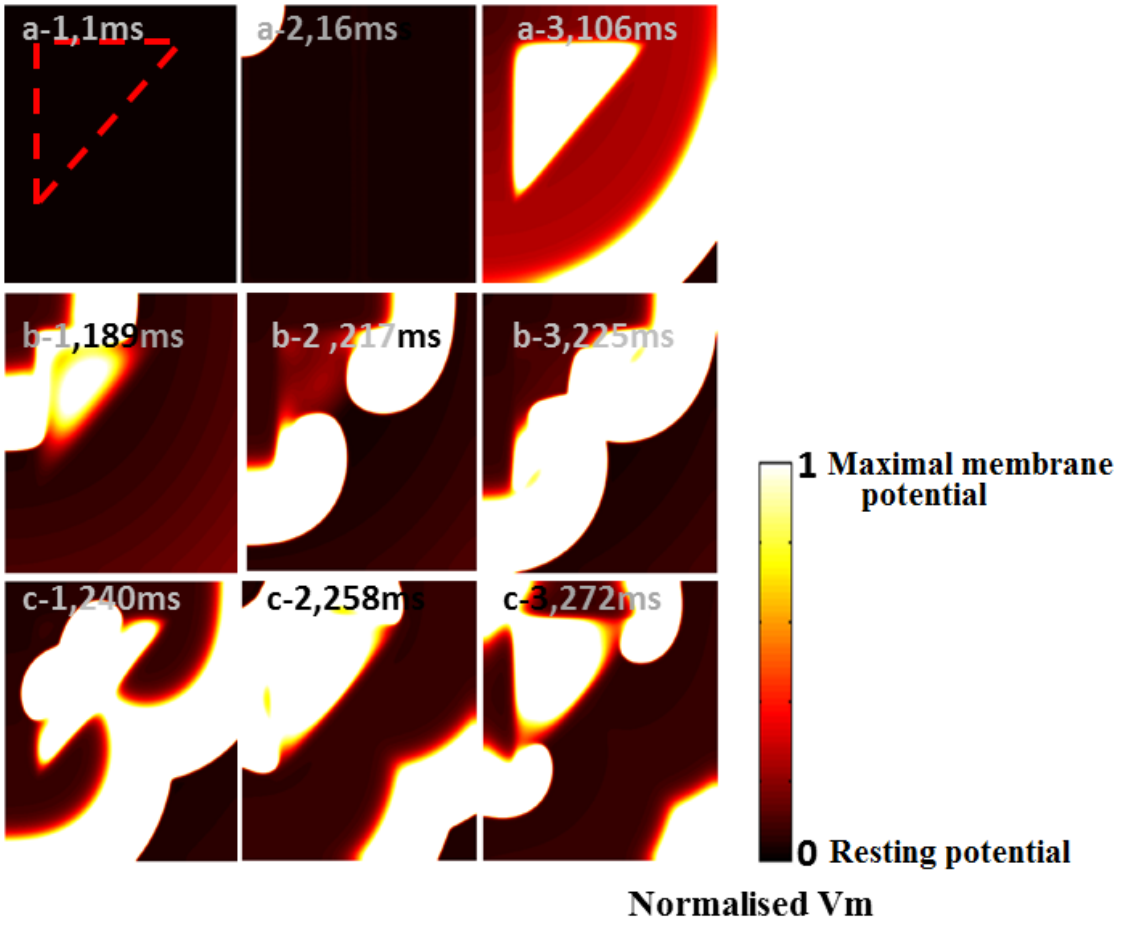

Figure 5.2: A mono-domain simulation on a 5x5 cm 2D mesh using the Mahajan 2008 rabbit myocyte model, modified to mimic cells with long (the triangular region) and short (the rest) APs. a-2) and a-3) show the first excitation wave, a long AP in the triangular area can be seen in a-3). b-1) and b-2) show the second excitation wave, the triangular region is not excitable due to the delayed recovery from refractoriness, and the excitation wave starts to curl around the area. b3-c3) show the re-entry wave around the triangular region. Such an event simulates initiation of cardiac arrhythmias. trans-membrane potential (V_m).

In the healthy heart, there is a naturally occurring AP heterogeneity in the LV, both across the ventricular wall (transmural) and from apex to base [110, 212]. This natural AP distribution may tightly correlate to cardiac function to regulate the timing of mechanical events. At the same time the AP heterogeneity can contribute prominently to the development

of cardiac arrhythmias [213]. Dispersion of APD may increase in diseases like hypertrophy [214] or heart failure [215] and increase susceptibility to arrhythmia.

Many investigators have studied this topic using different species: human [62, 216, 217], guinea pig [110, 218], rabbit [219], dog [220]; different experimental preparations such as wedge [219-221], isolated cell [222], whole heart [110]; and different measuring techniques such as optical mapping [110, 221], sharp electrodes [219, 220, 223] or patch clamp [222]. Rosenbaum et al. [110] reported an apex-to-base gradient in the guinea pig heart showing longer APD at the apex while Choi et al. [96] reported the opposite, longer APD at the base. Rudy et al. [224] showed a more complex pattern of the activation-recovery interval in the human epicardial surface with different apex-to-base gradients in the anterior and posterior surfaces. Several laboratories [218-220, 225, 226] also reported transmural gradients across the ventricular wall with a group of cells in the mid-myocardium exhibiting prominent APD prolongation (M-cells) compared to endo- and epicardium. However, the findings on transmural heterogeneity have been controversial, as no pronounced transmural heterogeneity in the activation-recovery interval was found when measuring with a bi-polar or uni-polar electrode in canine [227] and human hearts [62] during open chest surgery. The disagreements in this M-cell debate, nicely summarised in a recent mini-review series in Heart Rhythm [228-232], may be explained by:

1) the use of activation-recovery intervals as an index of APD, as the repolarisation time measured from the activation-recovery interval may not be reliable;
2) the block of the late sodium ion current, which can contribute greatly to suggested/claimed distinctive properties of M-cells, due to application of general anaesthetics in open chest surgery;

3) the limits in spatial resolution, introduced by the low number of bi-polar electrodes plunged into the tissue which could cause M-cell regions to be missed out due to the complex distribution of M-cells;
4) the experimental preparation, as preparation of wedges and isolation of cells may exaggerate the extent of spatial heterogeneity by reduction or complete removal of cell to cell coupling.

Spatial APD heterogeneity can be caused by different ionic currents in different regions of the LV which may relate to different levels of ion channel protein expression. For example it was found in rabbit isolated myocyte that the I_{Kr} tail current was significantly greater in the apex than at the base, while the slow delayed rectifier potassium ion current (I_{Ks}) tail current was significantly smaller in apical than in basal myocytes [222]. Also transmural heterogeneity of sodium ion current (I_{Na}) was detected in dogs [233]. A lower expression of I_{Ks} channels in the mid-myocardium [234] would contribute to the longer APD in the mid-myocardium compared to epi- and endocardial region. This is well reviewed by Nerbonne et al. [235-237], who explain the correlation of channel distribution and APD. APD dispersion can be reduced by cell to cell coupling [238], which can be approximated by characterising connexin levels [239]. Coupling with non-cardiomyocytes, like cardiac fibroblasts which can act as an electrical sink on myocyte trans-membrane potential, may also play a role in the myocyte AP [240, 241]. Hence, the distribution of fibroblasts may also be relevant for AP spatial heterogeneity.

Results regarding endogenously occurring spatial heterogeneity in the AP (in terms of pattern and dispersion) remain controversial. A more systematic study of AP patterns and dispersion throughout the left ventricular free wall, with high spatial resolution, would be helpful in improving our understanding of how these processes contribute to normal cardiac function, and pathological changes such as in cardiac failure.

5.1.3 Spatial Heterogeneity in Calcium Handling

Compared to the AP, spatial dispersion in Calcium handling has been studied less. Nevertheless, it is an important function-related property that determines contraction. Transmural heterogeneity in Calcium transient (CaT) duration and decay speed have been found using single isolated cells [242, 243] and tissue wedge preparations [217, 244]. Together with a long CaT duration, earlier onset of CaT alternans was found close to the endocardium [244]. An earlier onset of contraction and later time point of relaxation was found at the sub-endocardium (compared to the sub-epicardium) indicating a longer duration of contraction at the sub-endocardial layer [242, 245]. This is in keeping with the transmural gradient of CaT duration, and explains well-coordinated ventricular contraction in spite of the fact that subendocardial cells are activated earlier than subepicardial cells.

To understand the underlying mechanisms of transmural dispersion of CaT duration, the expression levels of Ca^{2+} handling proteins, the density of Ca^{2+} current in different transmural layers of ventricular wall was studied. Increased expression levels were found towards the epicardium for sarco-endoplasmic reticulum Ca^{2+} ATPase (SERCA) [244], and Na^{+}/Ca^{2+} exchanger (NCX) [246, 247]. However for L-type Ca^{2+} channel, the findings are controversial (no gradient [242] (canine), more current density close to epicardium [248, 249] (canine and murine respectively) and more current density in endocardium [250] (canine) were reported).

5.1.4 Use of Animal Models

AP properties are species-dependent. To study cardiovascular function, a wide variety of animal models are used. Small animals such as rat and mouse are advantageous in terms of cost and gestation period, but they have very different ionic mechanisms of repolarisation compared to larger mammals, including human [236]. In adult rats and mice, the primary ion

current controlling repolarisation is the transient outward current (Ito); I_{Kr} and the I_{Ks} are present in mouse and rat, but make smaller relative contributions. Also the short APD and lack of an AP plateau phase make the AP shape very different from human [251]. In contrast, rabbits share more common features in terms of cellular electrophysiology and Ca^{2+} transport with human: the main underlying repolarisation currents are the same in rabbit and human, there is a considerably larger fraction (compared to rat and mouse) of Ca^{2+} coming from Ca^{2+} entry [252]. Rabbit also responds to drug intervention and to ischaemia more close to human than mice and rats. Furthermore the rabbit, as a mid-sized animal model, provides a decent amount of tissue for multiple parallel *in vitro* experiments. Larger animal is not chosen as large ventricular wall would not fit on to the vibratome and therefore it is only possible to collect slices from a relatively small region of the ventricular wall. Therefore, the rabbit has been chosen as the animal model to study AP spatial heterogeneity in this project.

5.1.5 Aim of the Study

While the heterogeneities of APD from apex-to-base and epi- to endocardial have been described [110, 220], we know little about the 'left-right' (or, perhaps anatomically more appropriately, the anterior-to-posterior) heterogeneity of the APD [224]. Also there is not yet a three dimensional (3D) understanding of ventricular APD heterogeneity patterns, which consist of AP information from apex-to-base, endo-to-epi and anterior-to-posterior, at the level of spatial resolution achievable with optical mapping. This is partially due to the problem of limited access to mid-myocardial layers, and the predominance of preparations with only a few measurement points. Optical mapping of wedge preparations has provided AP and CaT spatial information in greater detail [217, 253], compared to sharp electrode measurements or measurements done on isolated single cells. That said, the wedge preparation provides information of both transmural and apex-base AP gradients, it does not

provide anterior-to-posterior information since wedges, although usually obtained from bigger animals, are limited and too small to represent the entire ventricular wall.

Cardiac tissue slices open up the unique possibility of accessing tissue from the mid-myocardium and are therefore potentially a good candidate to study AP and CaT spatial dispersion through the left ventricular free wall. In our study, we aim to obtain high spatial resolution AP and CaT information for the rabbit left ventricular free wall by applying optical mapping to ventricular tissue slice preparations, and to capture any potential apex-base, endo- to epicardial, and anterior-to-posterior gradients.

5.2 Materials & Methods

For heart isolation, dye loading and slice preparation protocol please refer to section 2.2.1.1, 2.2.1.2 and 2.2.1.3. And for detailed description of optical mapping setup and procedure please see 2.2.1.4.

5.2.1 Animal Details

Four male New Zealand White rabbits (1-2 kg) were used for the study described in this chapter.

5.2.2 The Location of the Slices

Figure 5.3A shows the part of LV to be excised and in Figure 5.3B, a sample slice is shown from an epicardial view with the apex facing down.

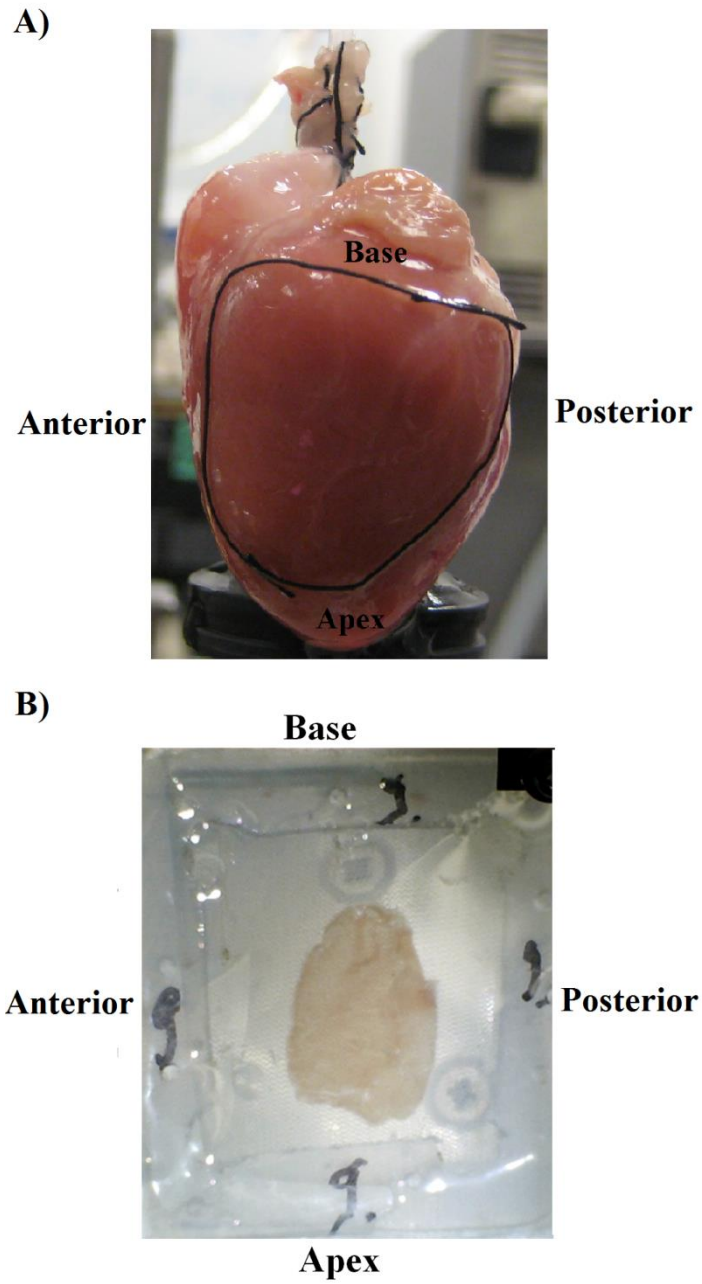

Figure 5.3: A) Picture showing the LV excision: the part of LV to be excised is labelled with black suture; B) Picture of a sample slice with the orientation marked: anterior, posterior, apex and base.

Due to the curvature of the left ventricular wall, the first epicardial slices will only include part of the tissue block. Depending on how the tissue is mounted, as well as the geometry of the heart, the locations of the first epicardial slices differ between preparations. In order to track the location of slices, a camera (USB microscope) was fixed above the slicer to take

photographic images of the tissue block after each sectioning. The Ca^{2+}-sensitive dye Rhod-2 coloured the epicedial surface slightly (a pink/ magenta colour) which enhanced the contrast. Thus, the sectioned tissue area can be clearly seen (Figure 5.4) and the contour of the slice can be traced (see section 5.2.5 for the more detailed description of imaging processing and co-registration).

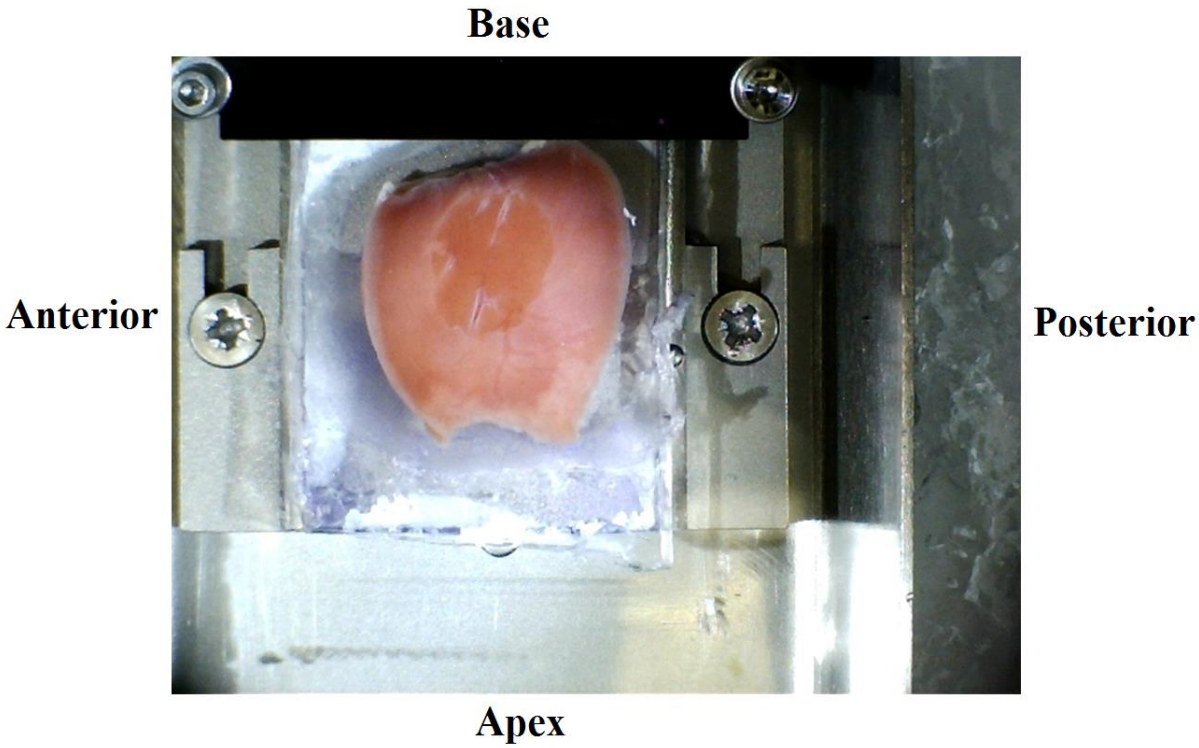

Figure 5.4: A light image of a tissue block in the slicing chamber: the contour of the cut area on the tissue block can be seen.

5.2.3 Measurement Protocol

To avoid potential source-sink mismatch induced APD pattern changes, field simulation was used to pace the slices. The field stimulator was placed parallel to the apex-base axis of the slice. Slices were paced at 1 Hz and measurements were taken at a sequence of time points to ensure steady state (in AP and CaT) had been reached. This is very important for inter-slice comparison. A script was written in MatLab to quickly calculate parameters of AP (APD at

80% and 50% repolarisation (APD80 and APD50 respectively), AP shape indicator) and CaT (CaT duration at 80 (CaT80) and 50 (CaT50) percent of decay) from spatially averaged AP and CaT traces (over the entire slice). This calculation can be carried out during the experiment to guide the measurements.

Figure 5.5 shows an example where APD steady state has been reached. The last 2 measurements (blue circled) were used for further analysis. The initial sharp change of APD is due to the adaptation of the slice to the bath environment and the pacing frequency. Figure 5.6 shows an example where AP steady state is not reached. Please note that one of the AP shape indicators, the normalised AP area ratio (shown in Subfigure 5.6C), gets progressively smaller with a sharper gradient at the later time while the AP skewness increases from negative to positive values (shown in Subfigure 5.6D). This indicates that the AP gets more and more triangular over time and suggests that this slice could potentially have been suffering from ischaemia (this slice was the last slice of the tissue block and had some tissue glue on it); it was therefore excluded from analysis. Most slices were subsequently paced with 2, 3, 4, and 5 Hz (in that order, 2 times 10 seconds recording for each of these frequencies, with at least 10 seconds exposure to the new pacing rate before the first measurement for the slice).

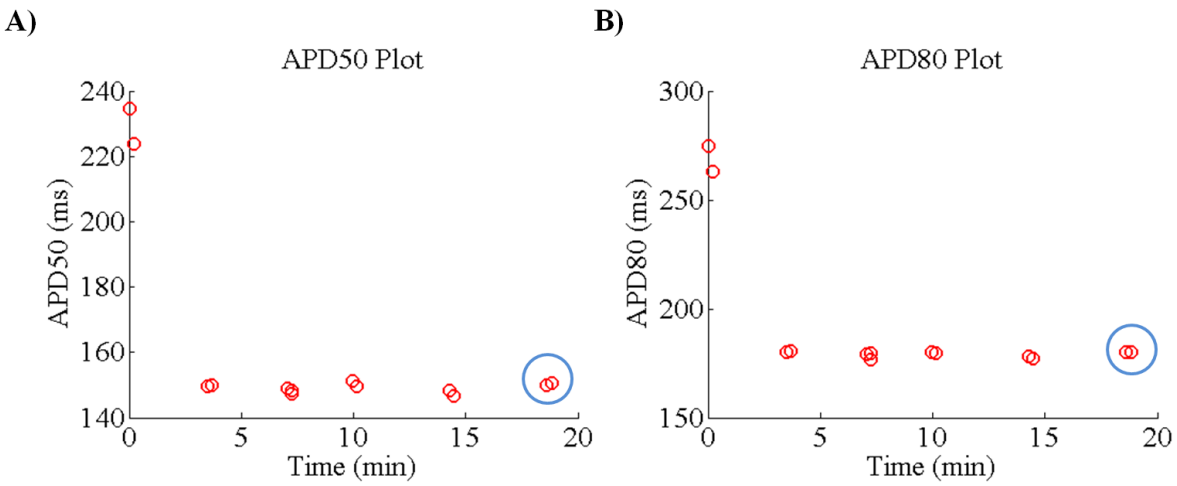

Figure 5.5: An example showing case where AP steady state was reached at 1 Hz: A) APD50 of spatially averaged AP traces measured at different time points after mounting the slice on the measurement stage; B) APD80 of spatially averaged AP traces measured at different time points after mounting the slice on the measurement stage.

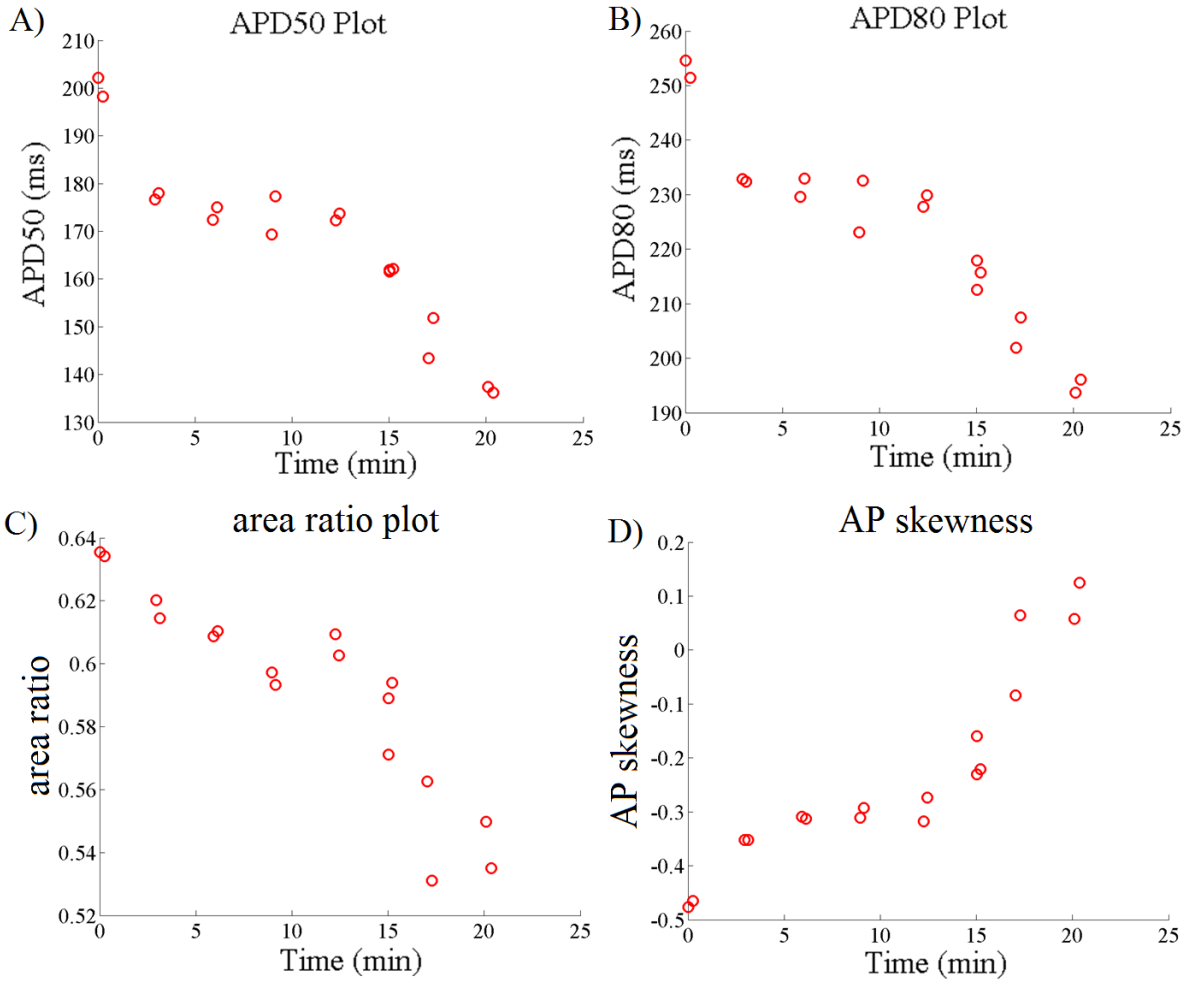

Figure 5.6: An example where AP steady state was not reached (1 Hz): Subfigure (A), (B), (C) and (D) show APD50, APD80, normalised area ratio and AP skewness, respectively, of spatially averaged AP traces measured at different time points after mounting the slice on the measurement stage.

5.2.4 Parameter Extraction from Mapping Data

The data sets measured at AP/CaT steady state were further analysed. The recorded AP/CaT data were processed to reduce noise distortion, and APD (APD80 and APD50), AP shape indicators (normalised AP area ratio, AP skewness), and CaT duration (CaT80 and CaT50)

were calculated on the pre-processed traces (see chapter 2 (2.2.1.6) for the details of the data analysis algorithm).

5.2.5 Alignment of Slice Images

One of the challenges of this study was to track the location of slices. Since the left ventricular free wall of the rabbit has a curvature, it is almost certain that a slice will contain tissue at the edges that originate from layers closer to the epicardium, than the central part of the slice. On one slice the spatial heterogeneity can be a mixture of endo-epicardial, apex-base, and anterior-to-posterior dispersion making it very hard to interpret data. Without any image alignment, it is also difficult to make cross-comparison between slices. We tried to develop a method (the steps are shown in Figure 5.7) to track the rough location of a slice (with the tissue block as a reference). We first took images of the tissue block after cutting each slice (described in 5.2.3), both the contour and the location of the slice (or the cut area) could be identified (Figure 5.7A and B). Then we took the fluorescent mapping image (rotating the image if necessary to ensure that the apex-base direction roughly aligned with the vertical axis and the apex was pointing downwards), we segmented the tissue slice contour (Figure 5.7C). The fluorescent image was translated to make the centroid of the tissue slice contour lie on top of the centroid of the cut area. The fluorescent image was then rotated to align the major axis of the tissue slice contour with the major axis of the block cut contour (this rotation angle should not be larger than 90 degree as the slice had its rough orientation marked and therefore should not be flipped) (Figure 5.7D). The fluorescent image was then translated again if necessary to ensure the centroid fits on top of the cut area centroid. Figure 5.8A shows an example of a stack of cut area contours and Figure 5.8B shows the corresponding stack of aligned tissue slice contours respectively. Contours shown in Subfigure A are smaller than that in B, but it is not necessary to work out the scaling as we

only need to know slice locations relative to each other. Figure 5.9 shows an example of APD80 map of a slice before and after alignment.

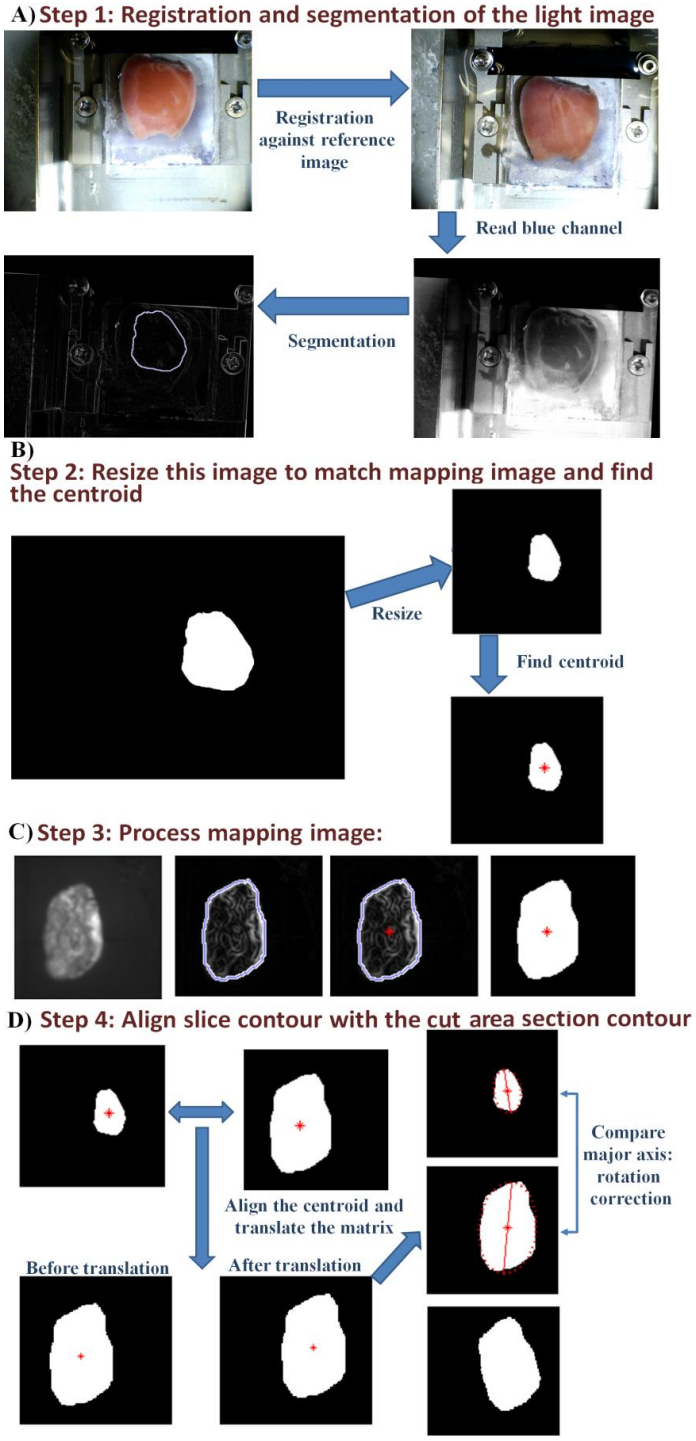

Figure 5.7: Schematic diagram showing the method to align the slice mapping images: A) step1: register and segment the light images taken at the slicer to get the location and contour of the cut area; B) step 2: resize the light image to make sure it has the same size as the fluorescent mapping image and then find the centroid of the cut area; C) step 3: segmentation of fluorescent mapping image to get the tissue slice contour and find its centroid; D) step 4: apply translation and rotation to the tissue slice contour to align it with the cut area contour.

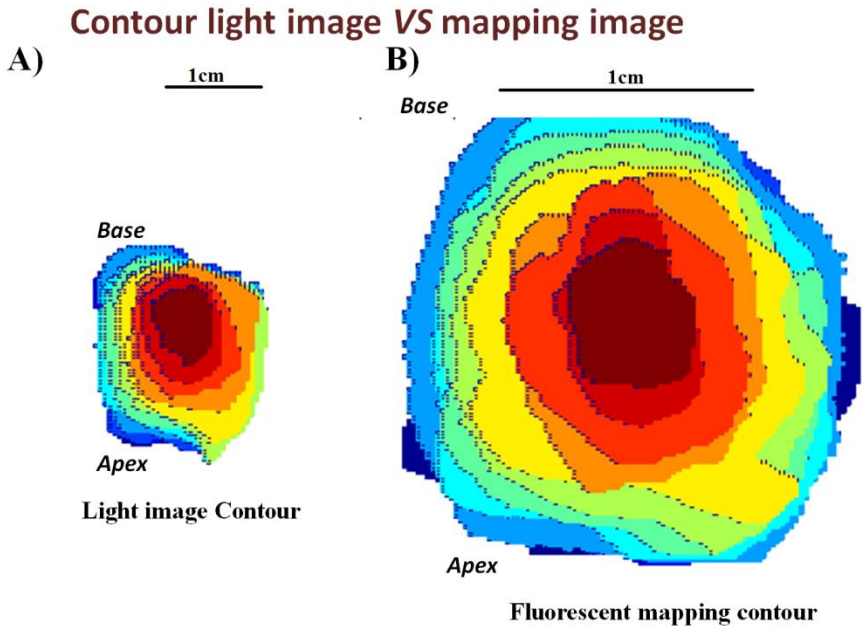

Figure 5.8: A) A stack of cut area contours (light image) contours; B) the corresponding stack of tissue slice (fluorescent mapping) contours after alignment.

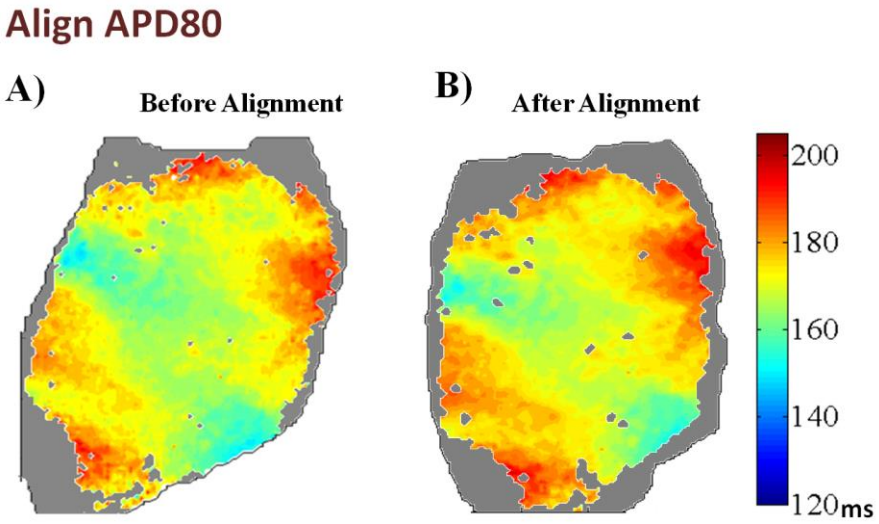

Figure 5.9: An example of an APD80 map before and after image alignment: A) APD80 map before alignment, B) APD80 map after alignment: rotation and translation have been applied to this map.

After working out the tissue slice contour interrelations, we can reconstruct the transmural layers. Instead of just looking at one slice, we gather all slices which have regions that fit onto a particular transmural layer (e.g. the pericardial surface). Each point on a transmural layer can be correlated to a point on a particular slice (an example of how to reconstruct the

APD80 map for a transmural layer is shown in Figure 5.10). Figure 5.11 shows APD80 maps before image alignment and Figure 5.12 shows the APD80 after alignment and 'reconstruction'.

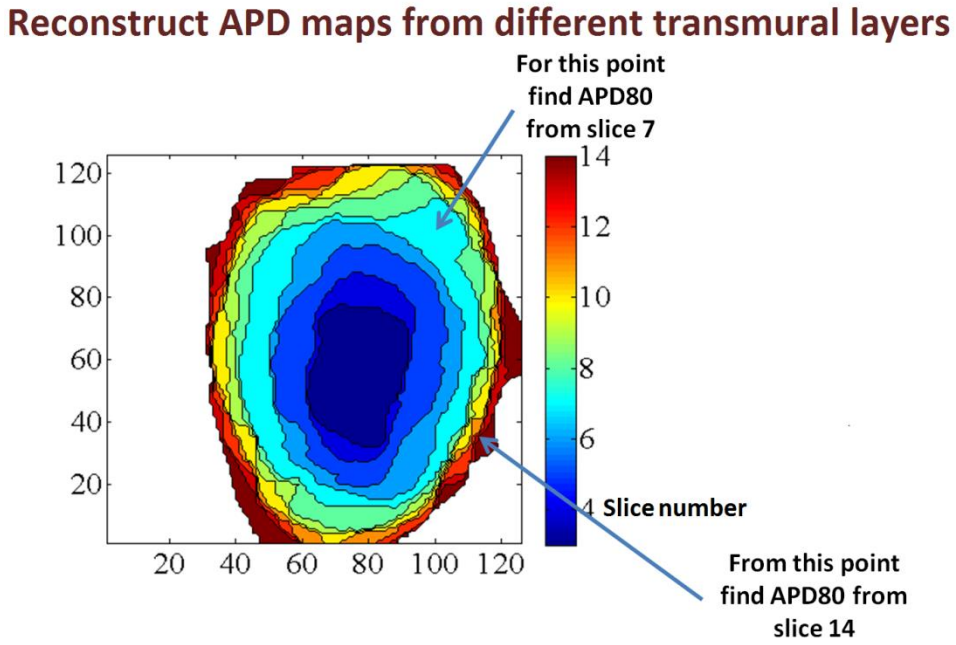

Figure 5.10: Example to show the method to reconstruct transmural layers: The figure shows a stack of tissue slices (from the mapping images), aligned according to the light image of the tissue block (taken at the slicer). The outermost epicardial layer will be reconstructed out of the first slice, and the visible "rims" of the subsequent slices. For example slice 7 has an epicardial area, (light blue colour) which would be included into the reconstructed epicardial layer.

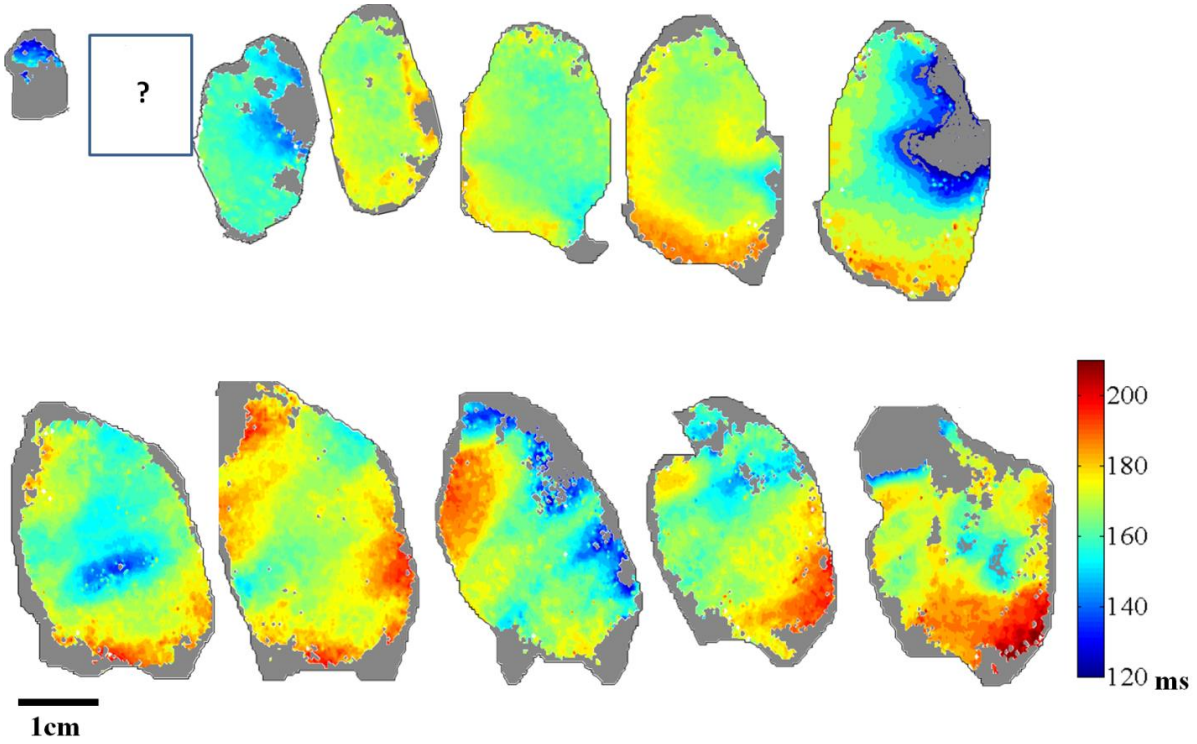

Figure 5.11: Example of APD80 maps from 12 consecutive slices (epicardial slice shown in the top left corner and the endocardial slice shown in the bottom right corner) before alignment, the second slice is shown with a question mark as it did not show any voltage signal.

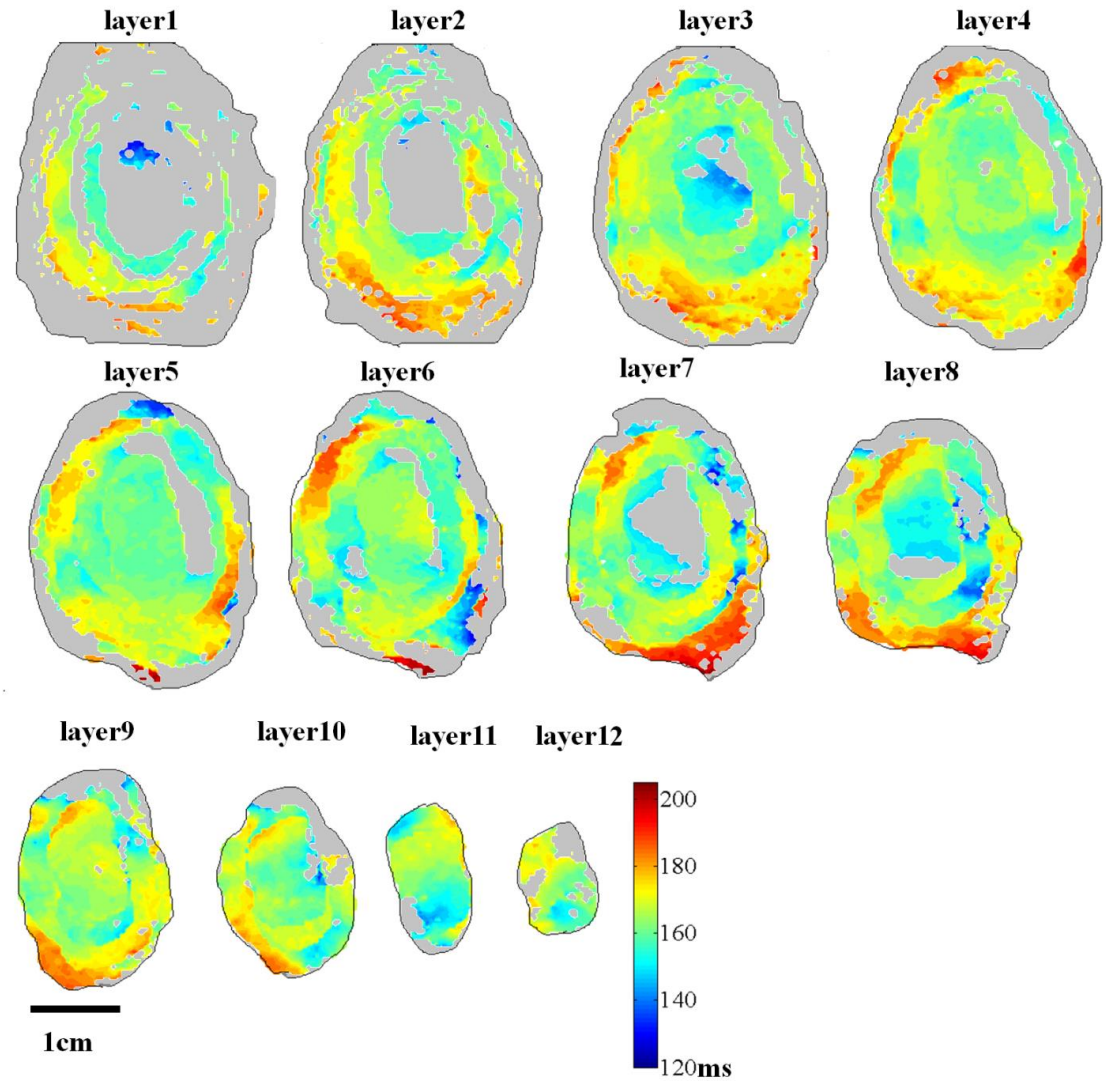

Figure 5.12: APD80 maps (the same data set as shown in Figure 5.11) of 12 transmural layers after alignment and 'reconstruction'. Layer 1 is the true epicardial layer and layer 12 is the layer closest to the endocardium.

From these reconstructed transmural layers (a parallel would be 'layers of an onion'), a base-apex profile of APD and CaT duration can be created for each transmural layer by taking an average of each line (parallel to the anterior-to-posterior axis). Values calculated from lines with less than 5 pixels showing decent signal were excluded from the profile. Since the layers close to subendocardium/endocardium are relatively small and may not have apex/base regions, they are not included in the analysis of apex-base gradients. The reconstructed epicardial/subepicardial layers may have sparse APD or CaT duration maps

(due to the fact that edges of each slice tended to have poor signal), and these layers (with sparse parameter maps) were also excluded.

In order to visualize the transmural profile of APD and CaT duration, two approaches can be taken. The first approach is the so called cylinder approach: a specific area is selected (i.e. corresponding to the shape of one slice) and this shape is traced transmurally (i.e. find the projection of this shape on each later slice). Figure 5.13 demonstrates this approach. The upper panel shows the stack (epi- to endocardial) of aligned slice contours. Any of these slices can be selected as the reference shape. For example if slice 3 is selected, we start with slice 3 and find out the projection of slice 3 on slice 4 to 14. Spatially average APD (or CaT duration) over slice 3 or areas of slice 3 projections can be calculated and plotted against the transmural location (i.e. distance to epicardium shown as the profile plotted with grey circles). To show that transmural profiles can be created with different reference shapes, slice 3, 5, 7 and 10 were selected in turn. The transmural profiles with these reference shapes were plotted (shown with different colour markers). And for this set of data, there was no major difference between transmural profiles. The second approach utilises the signal over the entire transmural (‘onion’) layer: APD (or CaT duration) was averaged spatially over each reconstructed transmural layer. This approach includes more areas in the analysis, but since the subendocardial layers are significantly smaller in size compared to the epicardial layers, the potential apex-base and anterior-to-posterior dispersion can disturb the transmural profile constructed with this approach. The first approach can exclude the possibility of mixing apex-base or anterior-to-posterior gradient into the transmural profile.

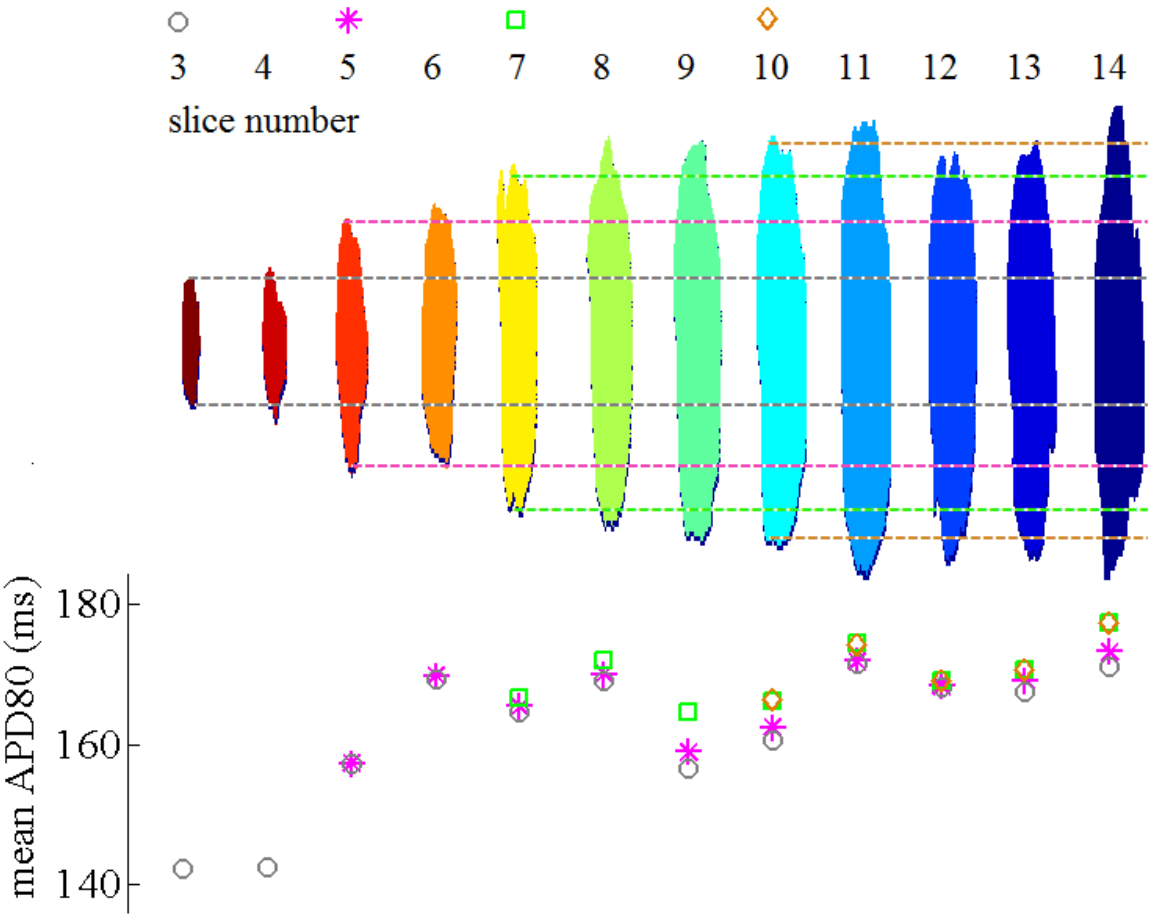

Figure 5.13: One example of an APD80 transmural profile; Slice 3 (profile shown with a grey circle), slice 5 (profile shown with a magenta star), slice 7 (profile shown with a green square) and slice 10 (profile shown with a light brown diamond) are taken in turn as the 'reference' slice.

5.3 Results

5.3.1 The APD and CaT Duration Pattern at Different Pacing Frequencies

Most slices were paced at multiple frequencies (1 to 5 Hz), and the APD50 and APD80 of these slices were calculated for each frequency. As shown in Figure 5.14A and B (data obtained from one slice as an example), a shortening in both APD50 and APD80 can be seen with increasing pacing frequency. However, the overall APD pattern does not seem to change at different pacing frequencies (see Figure 5.14C and D which show normalised APD maps).

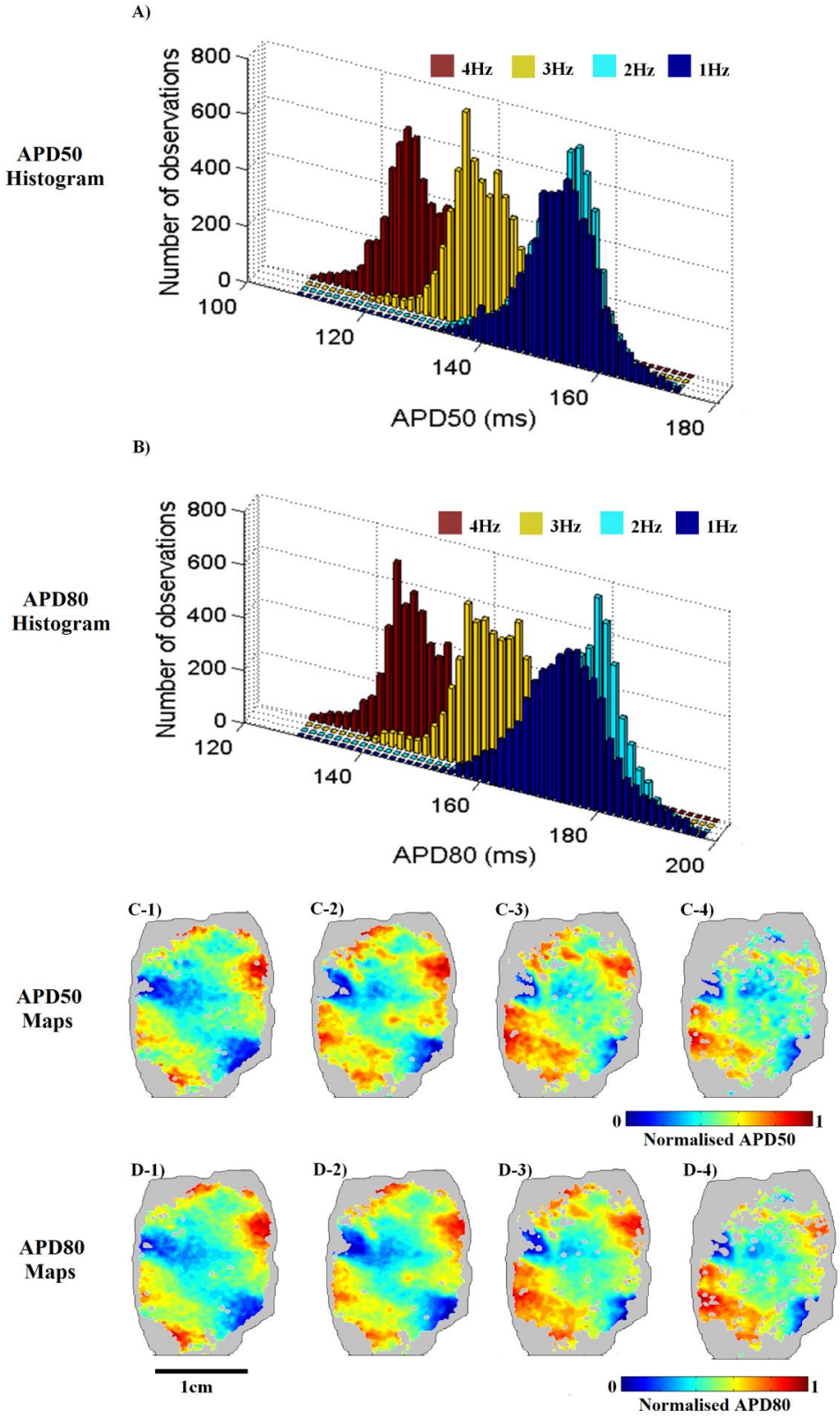

Figure 5.14: APD at different pacing frequencies: (A) histogram of APD50s with 1, 2, 3 and 4 Hz pacing (B) histogram of APD80s with 1, 2, 3 and 4 Hz pacing; (C) Normalised APD50 maps at different pacing frequencies (1 Hz: C-1, 2 Hz: C-2, 3 Hz: C-3, 4 Hz: C-4); D) Normalised APD80 maps under different pacing frequencies (1 Hz: C-1, 2 Hz: C-2, 3 Hz: C-3, 4 Hz: C-4).

At higher pacing frequencies, AP alternans can be induced in most slices. The onset of alternans occurs at different frequencies (4, 5 or 6 Hz) in different slices. Figure 5.15 shows a slice where alternans was seen at 4 Hz. Subfigure 5.15B shows in red the area where alternans was detected. The APD80 maps at 3 Hz and 4 Hz are shown in Subfigure 5.15A and C respectively. For 4 Hz, APD80 maps were plotted for even (with long APD) and odd beats (with short APD) separately. The APD pattern is not conserved during alternans (for this slice, the APD pattern for the short beat during alternans is particularly different compared to the normal APD pattern captured prior to the onset of alternans).

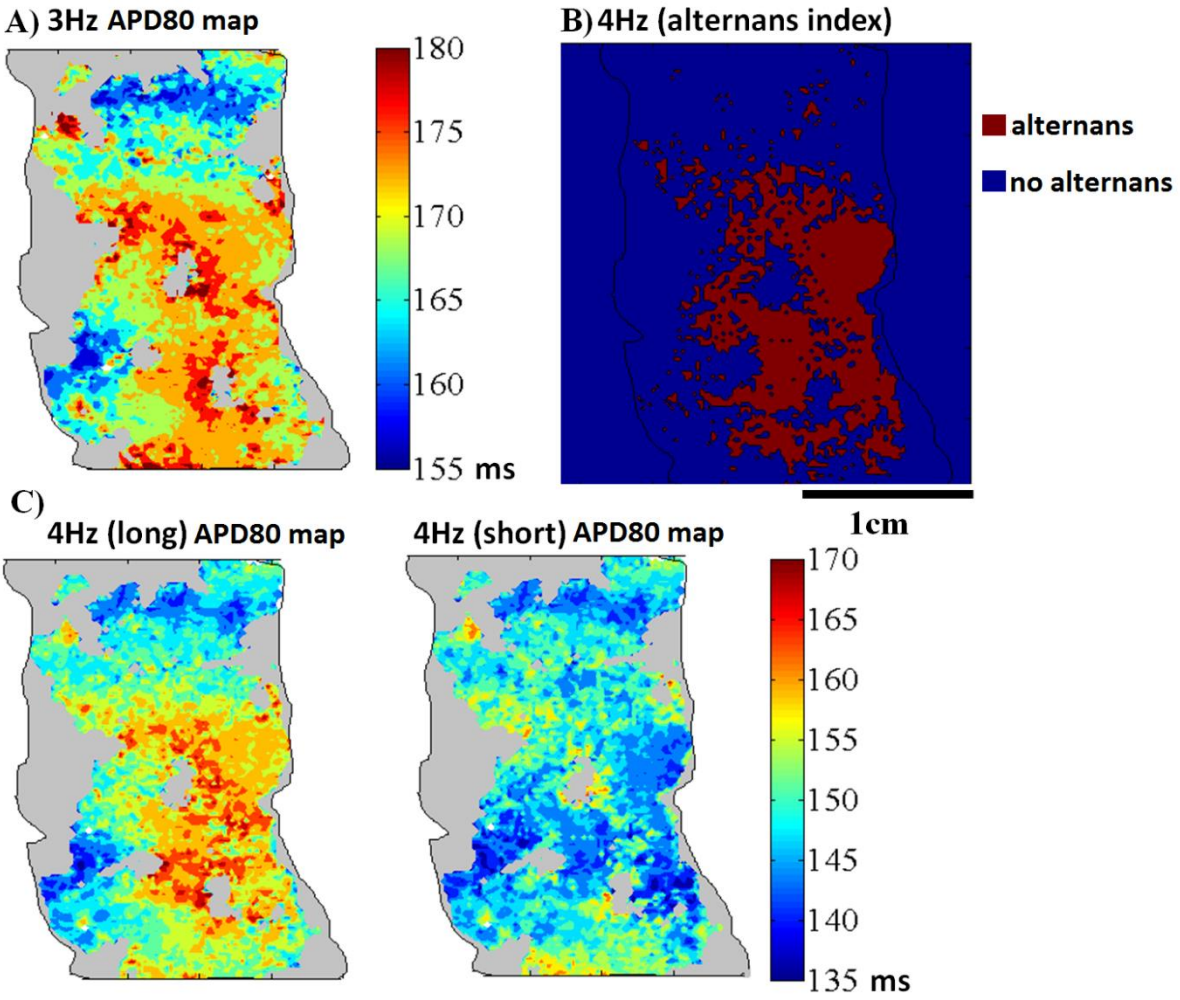

Figure 5.15: APD80 before and after onset of alternans: A) APD80 map at 3 Hz pacing (no alternans); B) alternans index map (areas with alternans are shown in red); C) APD80 map at 4 Hz pacing with even (long) and odd (short) beats plotted separately.

Similar observations were made with the CaT duration. Histograms of CaT50 and CaT80 at 1, 2, 3 and 4 Hz pacing are shown in Figure 5.16A and B respectively. A shortening in CaT50 and CaT80 can be seen with increasing pacing frequency. The CaT50 and CaT80 patterns (see Figure 5.16C and D) are conserved over different pacing frequencies. Ca^{2+} alternans (both amplitude and duration) can also be observed in slices. Figure 5.17 shows a slice where alternans was seen at 5 Hz. Similarly to APD, the pattern of CaT duration is not conserved in the case of alternans.

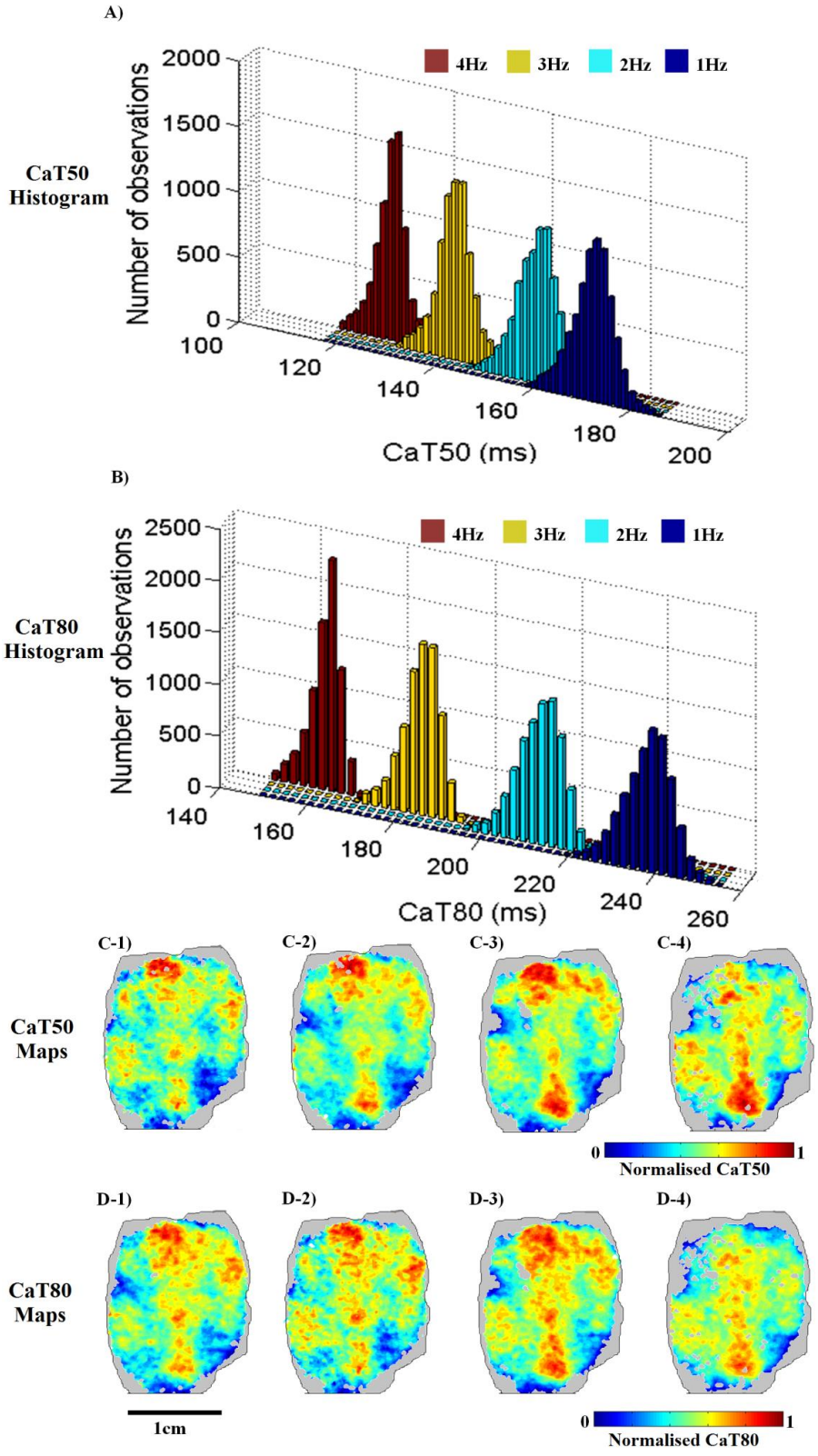

Figure 5.16: CaT duration at different pacing frequencies: A) histogram of CaT50s at 1, 2, 3 and 4 Hz; B) histogram of CaT80s during 1, 2, 3 and 4 Hz pacing; C) Normalised CaT50 maps at different pacing frequencies (1 Hz: C-1, 2 Hz: C-2, 3 Hz: C-3, 4 Hz: C-4); D) normalised CaT80 maps at different pacing frequencies (1 Hz: C-1, 2 Hz: C-2, 3 Hz: C-3, 4 Hz: C-4).

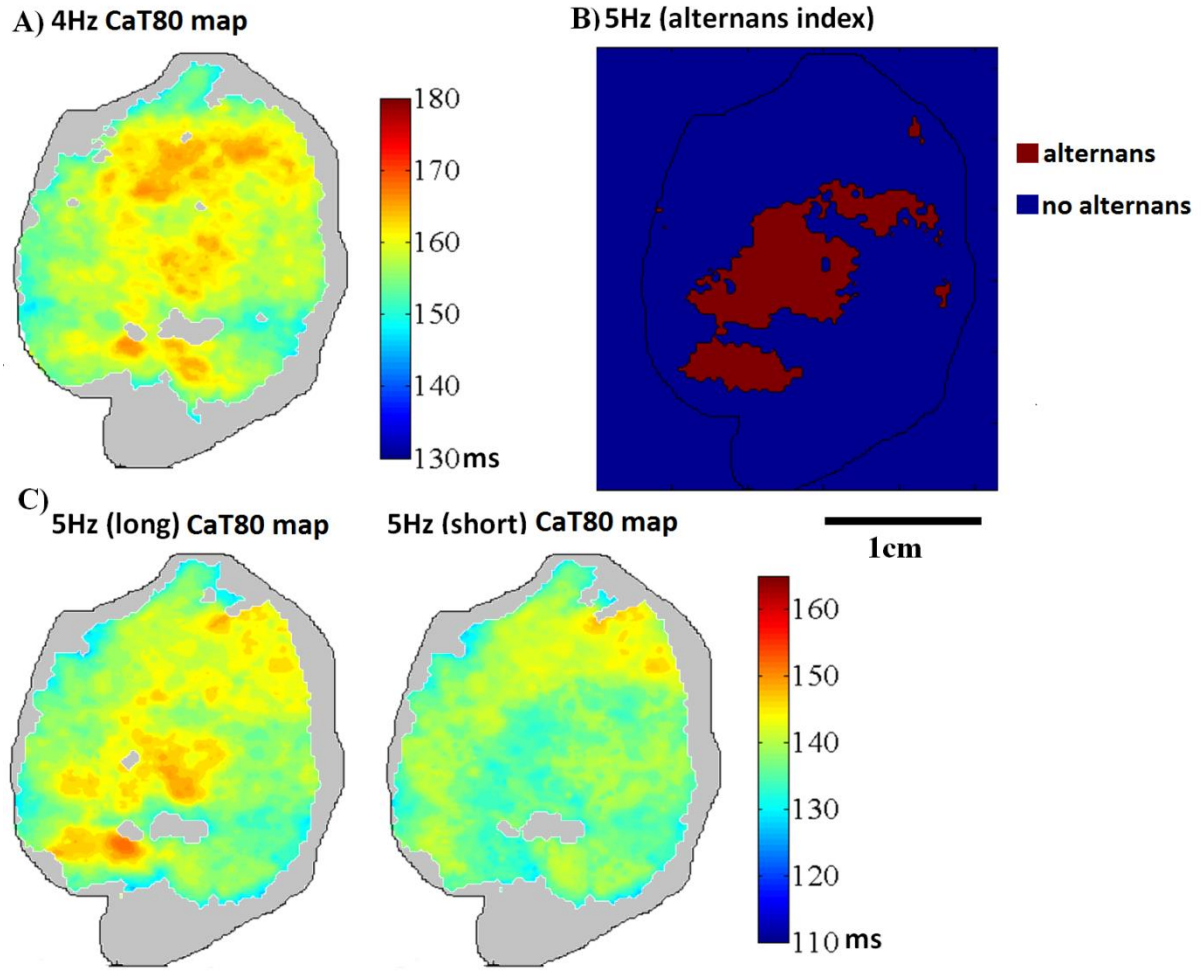

Figure 5.17: CaT80 before and after the onset of alternans: A) CaT80 map at 4 Hz pacing (no alternans); B) alternans index map (areas with alternans detected are shown in red); C) CaT80 map at 5 Hz pacing with even (long) and odd (short) beats plotted separately.

5.3.2 APD and CaT Pattern from Different Transmural Layers

As described in the methods section (5.2.7), transmural layers (epi- to endocardial) can be reconstructed after image alignment. APD and CaT duration maps for each transmural layer can then be created. Figure 5.18 and 5.19 show APD80 and CaT80 (respectively) for 11 transmural layers of one left ventricular free wall. Grey colour in these maps indicates areas with no or poor signals. For this left ventricular free wall, longer APD80 and CaT80 were

seen close to the apex on some transmural slices, and a clear epi- to endocardial gradient in CaT can also be observed. To better summarise and quantify these gradients, both apex-base and transmural gradients were constructed according to the method described in the methods section.

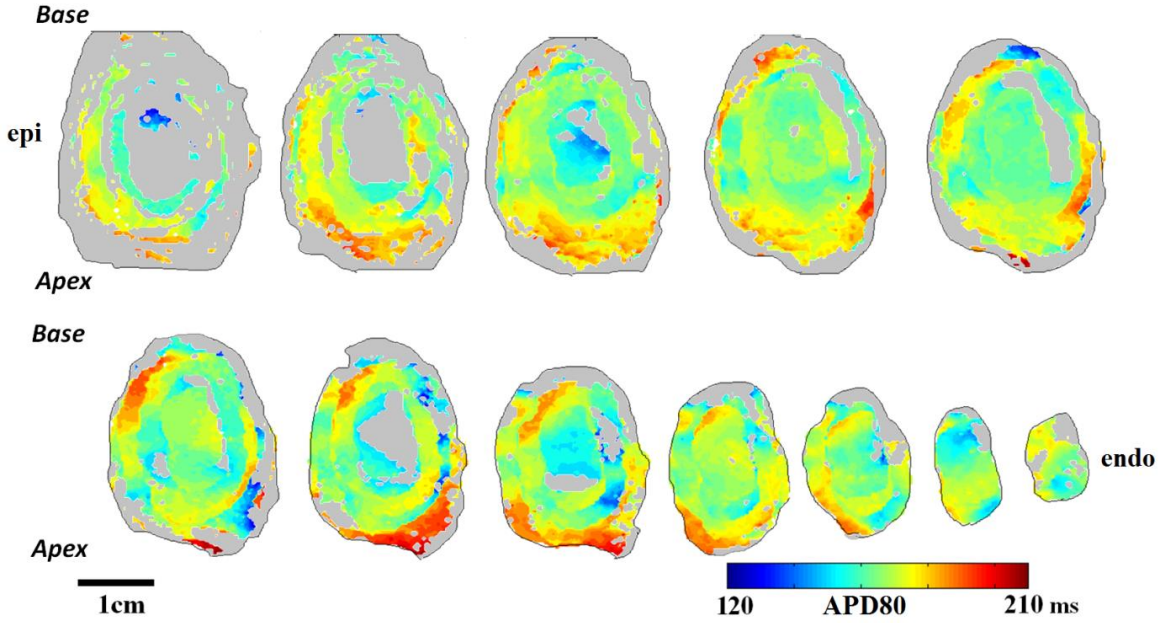

Figure 5.18: APD80 maps over 11 transmural layers with epicardial layer shown in the left-hand top corner and the endocardial layer shown in the right bottom corner.

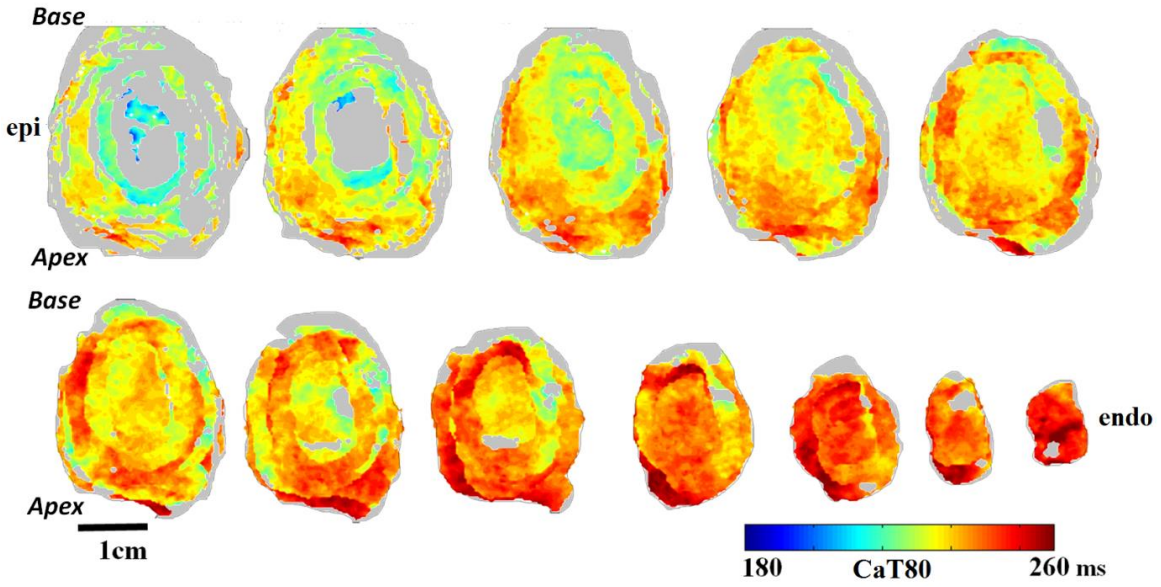

Figure 5.19: CaT80 maps over 11 transmural layers with the epicardial layer shown in the left-hand top corner and the endocardial layer shown in the right bottom corner.

5.3.3 Base-Apex Profiles of APD and CaT Duration

For each data set, three transmural layers in the subepicardium/mid-myocardium were chosen to create the base-apex profile. The reason for excluding the near-epicardial and sub-endocardial layers is explained in the methods section (5.2.7). The base-apex profiles of APD80 and CaT80 (at 1 Hz pacing) from four left ventricular walls are summarised in Figure 5.20. The base-apex profiles of APD80 (of 3 consecutive transmural layers from subepicardium to mid-myocardium for each heart) of heart 1, 2, 3 and 4 are plotted in Subfigures 5.20 A, C, E, G respectively. The base-apex profiles of CaT80 (of 3 consecutive transmural layers from which the APD80 profile was constructed) for these four hearts are plotted in Subfigure 5.20 B, D, F, H respectively. For each heart, an averaged profile was calculated out of the three base-apex profiles. These averaged base-apex profiles for the four hearts are plotted in Figure 5.21A (APD80) and B (CaT80). All slices obtained from heart 2 had very good signals and no slice was excluded (because steady state in APD and CaT duration could be reached in each of the slices). Heart 2 has the most complete APD and CaT duration maps for each transmural layer and therefore has a base-apex profile least influenced by potential outliers.

Linear fitting was performed on the averaged apex-base profile of each heart. Three out of the four hearts yielded a slight positive APD80 base-apex slope (0.08, 0.13, and 0.14 ms/pixel for heart 2, 3, and 4 respectively, suggesting longer APD80 close to the apex). The APD80 base-apex slope for heart 1 was negative (-0.43 ms/pixel, suggesting longer APD80 close to the base). Similar characteristics were observed in CaT80 profiles. A slightly positive base-apex slope of CaT80 could be found for heart 2, 3 and 4 (0.086, 0.085, 0.12 ms/pixel respectively, suggesting longer CaT80 close to the apex) and a negative slope (-0.11 ms/pixel, suggesting longer CaT80 close to the base) was found for heart 1.

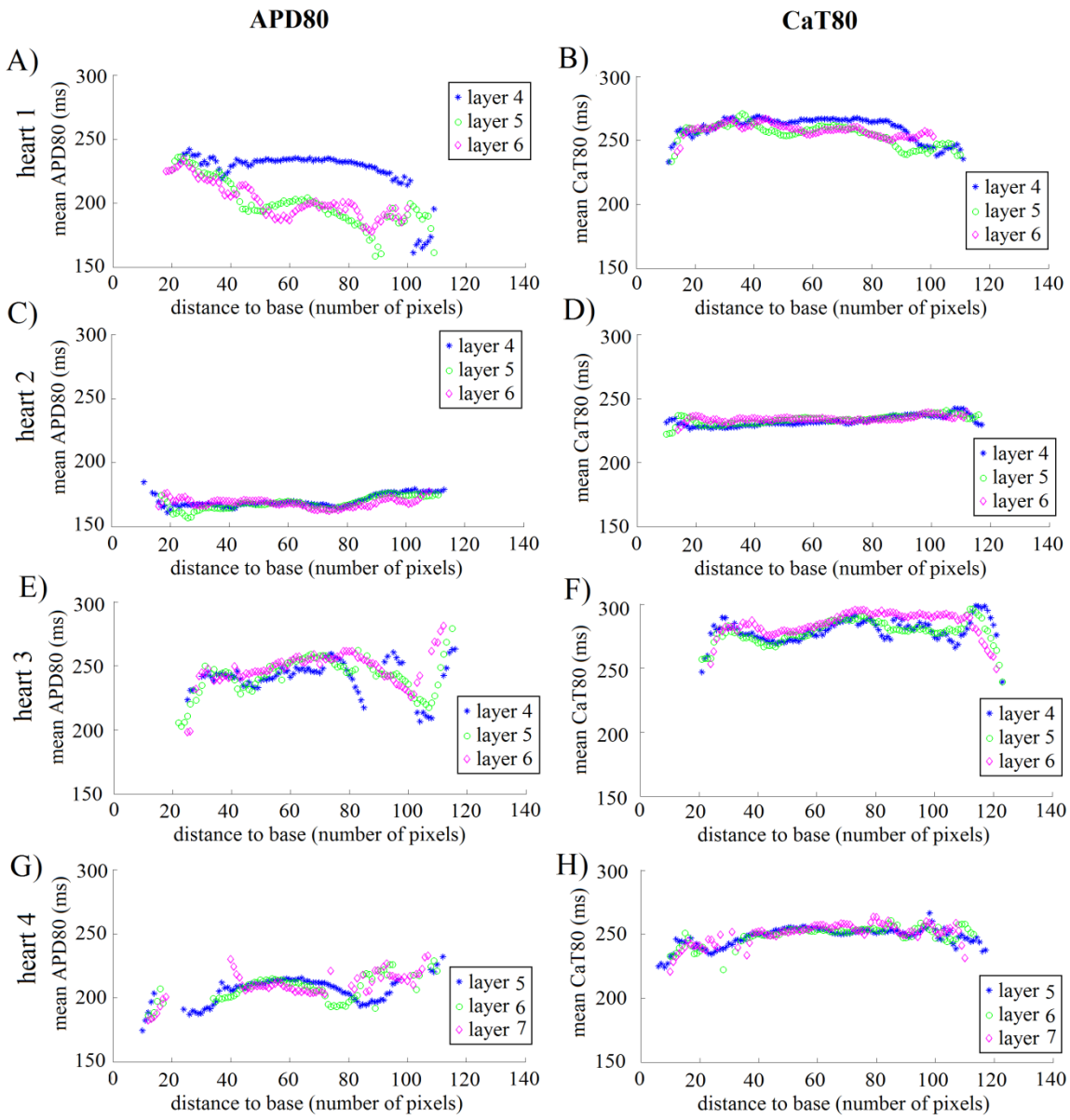

Figure 5.20: Averaged APD80 (A, C, E, G) or CaT80 (B, D, F, H) per pixel-line perpendicular to the apex base orientation from three consecutive transmural layers of 4 hearts:

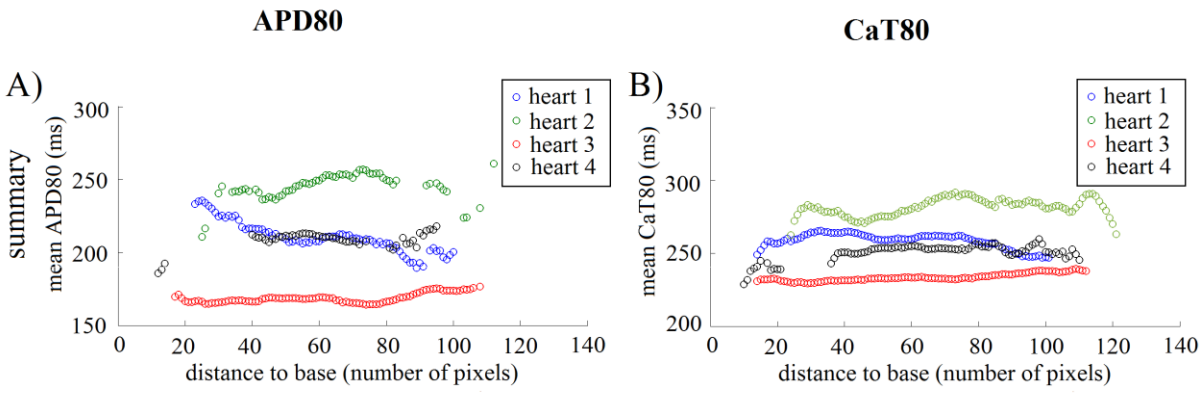

Figure 5.21: Average base-apex profiles over 3 consecutive transmural layers (from the subepicardial/midmyocardial areas) of 4 hearts: A) the averaged APD80 profile (over 3 layers as shown in Figure 5.20) from base to apex of these four hearts; B) averaged CaT80 profiles (over 3 layers as shown in Figure 5.20) from base to apex of these four hearts.

5.3.4 Transmural Profile of APD and CaT Duration

A transmural (epi- to endocardial) profile (1 Hz pacing) was constructed for each of these four hearts using the two methods described in the methods section 5.2.7 (a cylinder approach: plotted with stars in Figure 5.22; the approach that takes average over each entire transmural layer: plotted with circles in Figure 5.22). Figure 5.22A shows the APD80 transmural profiles of these four hearts. Figure 5.22B shows the CaT80 transmural profile. The profiles generated from the 'cylinder' and 'whole layer' approaches are very similar (especially for heart 2 where the signal was very good). No large APD80 prolongation was captured in the mid-myocardium and an overall positive slope from epicardium to endocardium could be found for both APD80 and CaT80 (7.0 ms/mm and 9.7 ms/mm respectively), i.e. sub-endocardial AP and CaT durations are longer. Also more (and larger) areas showing CaT and AP alternans were captured (at 4 or 5 Hz) in the region close to subendocardium compared to the epicardium.

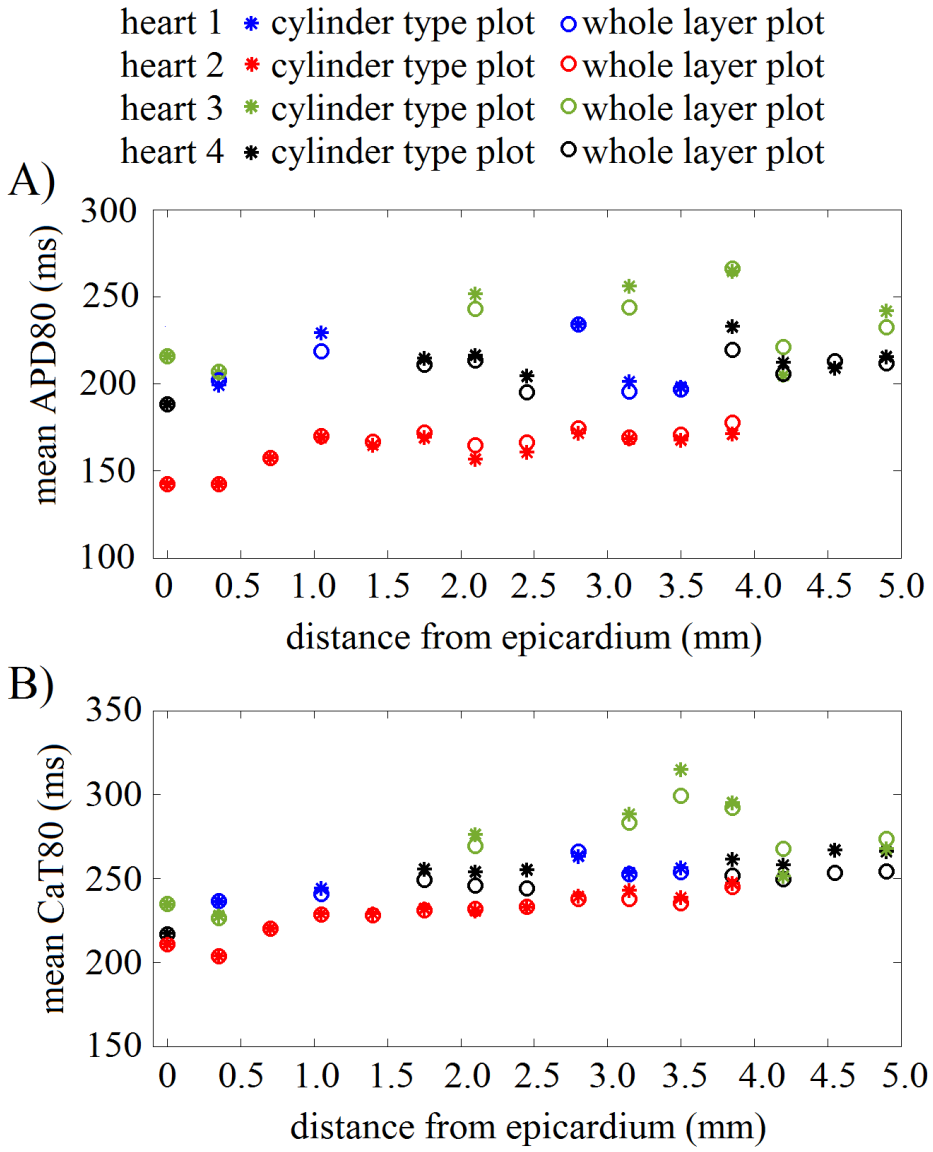

Figure 5.22: Plot of transmural profiles of APD80 (A) and CaT80 (B): Profiles constructed using the 'cylinder' approach are plotted with (*) and profiles constructed using the 'whole layer' approach are plotted with circle (o).

5.4 Discussion

5.4.1 The APD and CaT Duration Pattern at Different Pacing Frequencies

Our data indicated that APD and CaT duration patterns are conserved at different pacing frequencies. This is important for cardiac function as both the depolarisation and

repolarisation patterns and the contraction and relaxation sequence are important properties of the heart and should not be disturbed by heart rate changes. With occurrence of alternans, both APD and CaT duration patterns are altered in a beat-to-beat manner, which can change the normal depolarisation/repolarisation and the contraction/relaxation sequence. Beat-to-beat changes in depolarisation/repolarisation patterns may facilitate the formation of re-entry and therefore could be pro-arrhythmic. The change in contraction/relaxation sequence can lead to abnormal contraction of the heart and potentially result in an abnormal mechanical environment in certain regions of the heart, which can feed back to AP and CaT through mechano-electric-feedback.

Our data also suggest a correlation between APD or CaT duration and onset of alternans: areas with longer APD and CaT duration can get into alternans at a lower pacing frequency. This could also explain the reason why alternans was captured more often close to the endocardium (as the subendocardium has longer CaT and APD). Long APD and CaT durations might therefore be taken as surrogate markers for alternans risk, rather than the causes of alternans (the cause may lie in the underlying CaT handling pathway or the APD restitution).

5.4.2 Base-Apex Profile of APD and CaT Duration

Results regarding the base-apex gradient were not conclusive, based on the set of data presented in this chapter. An overall positive gradient was found in three hearts and an overall negative gradient was found in one heart. More data are needed to identify systematic differences. Whole heart data obtained prior to cutting could be used, to account for the potential error in slice alignment. An area in heart 3 close to the apex showed a much shorter APD compared to the rest although the overall base-apex gradient was still positive. The

region with very short APD could be caused by tissue damage during dissection of the LV free wall.

Controversial findings regarding the base-apex gradient have previously been reported for guinea pig whole heart [96, 110]: both positive [110] and negative [96] gradients have been found. This could be due to the fact that the hearts were mapped from slightly different angles (although both showed approximately the anterior view but one showed more the LV frontal view [110] and the other one showed the LV side view with some RV in the field of view [96]). Rudy et al. reported that the apex-base gradient could be different from different regions of the epicardial surface (anterior to posterior) [224]. Therefore viewing the LV from different angles may show different apex-base gradients and this could possibly explain the controversy. The section of LV free wall used in our study is close to that mapped in the 1991 study by Rosenbaum et al. [110], and in most cases we could show a positive base-apex gradient which is consistent with the findings presented by these authors from their whole heart mapping experiments. The set of slices (from heart 1 as shown in Figure 5.20 and 5.21) where we found a negative base-apex gradient could have been cut from a slightly different section of the LV (more towards the anterior side).

To consolidate the base-apex profile, whole heart mapping with several different views of the LV could be useful in resolving this controversy.

5.4.3 Transmural Profile of APD and CaT Duration

A positive epi- to endocardial transmural gradient was observed for both the APD and CaT duration, with longer AP and CaT in the subendocardium. A positive epi- to endocardial transmural gradient in CaT duration was also previously found for other species using isolated single cells [242, 243] and tissue wedge preparations [217, 244]. We did not find any regions in the mid-myocardium with largely prolonged APD, as identified by some single cell

studies [218, 220, 254]. One reason could be that the pacing frequencies used in our study were not unphysiologically low (such as 0.1 or 0.2 Hz which are the typical frequencies at which cells with largely prolonged APD can be identified). Another reason could be that the locally preserved cell-to-cell connections in tissue slices mask some of the APD dispersion at single cell levels [255]. The positive epi- to endocardial gradient is consistent with the reported depolarisation/repolarisation sequence, whereby the endocardium gets depolarised earlier and repolarised later compared to epicardium [256]. Slightly larger APD transmural dispersion was identified in our data compared to the *in vivo* measurement [62, 227]. This could be due to the fact that the slices lost the third-dimensional coupling, and the natural mechanical environment.

5.4.4 Limitations

There are several limitations to our study. The first limitation comes from the slice preparation. Although a slice preparation nicely preserves the natural mixture of cardiomyocytes and non-myocytes, and keeps them within a near-physiological local environment, the removal of transmural connectivity alters the natural source-sink relations, and the mechanical environment.

We tried to develop a method to trace the location and orientation of slices, but alignment is not very accurate due to the tissue deformation with highly non-uniform deformations. The curvature of the LV makes single slices prior-to-alignment impossible to use for interpolating base-apex, endo- to epicardial gradients. To avoid errors induced by alignment in studying transmural gradients, a smaller section of LV free wall (with less curvature) could be used to minimize the transmural difference appearing on one single slice from the edge to the centre.

The influence of Ca^{2+} sensitive dyes upon free $[Ca^{2+}]_i$ cannot be neglected. Rhod-2 itself is a Ca^{2+} chelator which can disturb the Ca^{2+} balance in the cardiac cell. Ideally Ca^{2+} sensitive

dyes with different affinities should be used (e.g. use Rhod-ff, a low affinity Ca^{2+} sensitive dye and compare the result obtained with the result measured using Rhod-2) to see whether the Ca^{2+} sensitive dye can change the spatial pattern of CaT.

Finally, the site of earliest activation affects APD and CaT duration in connected tissue [257]. We used field stimulation, which does not reproduce physiological activation sequences, so observed differences, in particular in base-apex gradients, may be reduced.

In this final experimental chapter, we have describes our study using cardiac tissue slices to investigate AP and CaT spatial heterogeneity in rabbit left ventricular free wall. In chapter 6, our final chapter, we give the general conclusions of this thesis together with a description of several possible future studies (both experimental and computational).

Chapter 6

Conclusions, Ongoing and Future Work

6.1 General Conclusions

In this thesis, a protocol for cardiac tissue slice preparation which yields high data reproducibility has been presented, together with a method to perform dual trans-membrane potential Ca^{2+} optical mapping on these tissue slices. A semi-automated routine to reliably extract relevant parameters has been described (with the pseudo code included in the appendix), and applied to 'real-life' biological research.

A method allowing comparison of the AP measured from whole heart and from tissue slices has been developed. The comparison showed that, at least for near-epicardial tissue, the tissue slice preparation preserved some important whole heart AP properties (e.g. the shape of AP repolarisation phase, and the AP duration (APD)). In a preliminary drug testing study, we were also able to show that tissue slices capture close to whole heart responses (in both AP and CaT) following nifedipine application.

The suitability of cardiac tissue slices for the study of mechano-electric-feedback (MEF) was also tested. Axial stretch could be successfully applied on tissue slices, relative to the dominant fibre direction. We demonstrated that axial stretch altered both the AP and the CaT in a dynamic manner. An initial shortening in both APD and CaT duration was observed shortly after stretch, followed by a gradual recovery/prolongation over time.

Since tissue slices offer a unique possibility to access mid-myocardial tissue, we tested the use of tissue slices for assessment of the spatial dispersion of AP and CaT in the left ventricular free wall. A method was developed to trace the location and orientation of

ventricular tissue slices within the ventricular wall. A transmural gradient was observed in APD and CaT duration (with the longest CaT measured at subendocardium/endocardium). No extensively prolonged APD was captured at the mid-myocardium at 1 Hz (or 2, 3, 4 and 5 Hz) pacing.

Based on the work presented in this thesis, several experimental projects have been identified that could be performed in the future (see 6.2), I would like to briefly describe some of our hypotheses and approaches here.

The moderate complexity of tissue slices makes them a promising data-source and test-bed for computer simulation. Some possible simulation work which can be performed in the future is described in 6.3.

6.2 Future Experimental Work

6.2.1 Study the Influence of Mechanical Stretch Upon Onset of Alternans Using Cardiac Tissue Slices

External mechanical challenges can induce changes in electrophysiological properties and intracellular Ca^{2+} handling, possibly leading to irregularities like arrhythmias. Mechanisms of MEF mediated arrhythmias include premature depolarization generated by mechanical impact and changes in repolarisation due to pressure load [258]. Recent work from Tsai et al. showed another possible mechanism through which stretch can increase the arrhythmic risk by lowering the threshold for onset of alternans. Stretch-induced alteration in intracellular Ca^{2+} handling was suggested to account for the reduction in alternans threshold [30].

We found in our preliminary data a correlation between APD or $[Ca^{2+}]_i$ transient (CaT) duration and the onset of alternans. Regions with long APD or CaT duration seem to have a lower frequency threshold for the onset of alternans (see chapter 5 Figure 5.17 and 5.15). This has been discussed previously [259]. Although the long APD and CaT may not be the

pure cause of earlier alternans, they could potentially act as markers for this. In our data, a prolongation in both APD and CaT duration could be seen when prolonged axial stretch was applied to slices, (see chapter 4 Figure 4.4 and 4.9). This could potentially lead to earlier onset of alternans (considered pro-arrhythmic). It would also be interesting to investigate whether alternans is driven by the voltage (via steep APD restitution slope) or by the Ca^{2+} handling.

This research could build on work described in chapter 4. Steps for this project could be the following:

(1) Build a motorised stretcher, mount one end of the slice on the motorised stretcher and the other end onto a force transducer so that the force developed during stretch can be measured.

(2) Determine (for extended stretch >60 min until new steady state in AP/CaT is reached) the relation between amount of stretch (in terms of both force developed and tissue deformation) and changes in AP/CaT. Determine differences (if any) in effect of stretch direction (with respect to dominant cell direction).

(3) Determine whether there is any change in the frequency threshold for onset of alternans before, during and after application of extended periods stretch.

(4) If there is a change in the threshold for onset of alternans, calculate the APD restitution (using both a steady state restitution protocol and a dynamic restitution protocol) before and after application of stretch.

(5) If there is a change in the threshold for onset of alternans, perturb the Ca^{2+} handling pathway (e.g. block key players like the L-type Ca^{2+} channels, ryanodine receptors, sarco-endoplasmic reticulum ATPase) and see whether onset of alternans can be influenced.

6.2.2 Study the Difference in Action Potential and CaT Characteristics Between the Left Ventricular Free Wall, Right Ventricular Free Wall and Septum

During depolarisation of the whole heart, the septum depolarises first, and in the repolarisation phase, the septum was found to repolarise last [256]. This suggests that the APD in the septum should be longer than that in both ventricular free walls. Despite being a very important component in the depolarisation/repolarisation sequence, little attention has been paid towards the septum compared to the ventricular free walls. The work by Morita et al. shows a transmural APD gradient in the septum, with the side close to the right ventricle showing a shorter APD [260].

It is possible to use tissue slices to investigate the spatial dispersion of AP and CaT in the two ventricular free walls and the septum of the same heart and to explore any differences between these three components.

The septum should be cut tangentially to one of its endocardial surfaces to yield mostly in-plane fibres [261]. We tried to section the septum in our pilot study, but the signal in the septum was weaker than that in the ventricular wall, indicating that a different loading protocol might be needed to get sufficient fluorescent signals from the septum. Since the septum has much less curvature than the ventricular walls, it is easier to reconstruct/obtain the transmural profile. However the surface of the septum is not smooth, and to section a complete slice without holes from either surface of the septum would be difficult. A relatively thick first cut (not used for measurement) should be performed before thin tissue slices can be collected.

6.2.3 Apply Dual-Voltage-Calcium Optical Mapping on Human Cardiac Tissue Slices

One of the advantages of cardiac tissue slices is the possibility of better maintenance and measurements from human biopsies (especially for small tissue blocks where large vessels in

relatively intact condition cannot be easily identified for cannulation and perfusion). It has been shown that it is possible to obtain live tissue slices from human biopsies [84] and that these slices can be successfully maintained in cultured conditions [82]. So far, the measurements performed on human tissue slices used either multi-electrode-arrays or sharp electrodes. It would be ideal to perform dual-AP/CaT mapping on human slices to increase spatial resolution and throughput. One of the big technical hurdles here will be the dye loading into the tissue, without utilising the natural intact vessel system. We tried in our study (rabbit tissue slice) to incubate voltage sensitive dye and Ca^{2+} sensitive dye into tissue slices, however the signals for both dyes were very poor (background fluorescent too high). For the incubation protocol, we did not try Ca^{2+} sensitive dye loading with addition of probenecid. The presence of probenecid improves the CaT signal significantly. It is possible that probenecid can also help Ca^{2+} sensitive dye loading into the tissue slice during incubation. For voltage sensitive dyes, it is possible that the dye only sticks to the damaged membrane on the surface of the slice, without diffusing into the live tissue. Passive diffusion may not be enough, therefore, to deliver the dye into the tissue core. There are several methods one could try:

(1) Microinjection of dye into the tissue block prior to sectioning: (this could potentially result in a patchy signal);

(2) Gently push dye containing solution (via gravity or active force) through the tissue slices;

(3) Expose the tissue slice briefly to a solution containing a very low concentration of detergent to ‘wash off’ damaged membrane on the surface.

6.3 Future Simulation Work

6.3.1 Using Data Obtained From Cardiac Tissue Slice to Test/Validate Cardiac Biophysical Models

Since the development of the first cardiac biophysics cell model by Denis Noble [262], a large number of models have been developed to simulate ionic currents, intracellular Ca^{2+} handling and the AP for different types of cardiac cells (e.g. ventricular myocytes [108, 263] and pacemaker cells [264]) from different species (e.g. rabbit [108], canine [265], and human [266]). To scale up from single cell to tissue, cardiac cell models are coupled by mono-domain or bi-domain equations to compute tissue level phenomena such as the conduction wave or arrhythmias. Cardiac models have become a popular tool to study cardiac pathophysiology, since they can help to refine experimental protocols, explore the possible underlying mechanisms, quantify conditions needed to provoke certain phenomena (e.g. level of channel conductance reduction needed to reach a certain APD prolongation) and predict the outcome of perturbations (e.g. effect of change in channel conductance or premature stimulus). Prediction from mathematical models can be particularly useful if the protocol simulated by the model is difficult to achieve experimentally or if it is not possible to monitor all the targeted parameters simultaneously through experiments. Recently, these mathematical models have also been incorporated into cardiac safety screening for pharmacological compounds [267].

With the development of new preparations and new measurement techniques (which provide more insight into cardiac pathophysiology), it is possible to refine models with data measured using these new preparations or techniques, and thus to increase the reliability of model predictions. One problem for cardiac biophysical cell models is that different electrophysiology models (of the same species, e.g. rabbit) can respond very differently to perturbations (e.g. channel block with pharmacological compounds). In Figure 6.1, we show

the response of the Mahajan 2008 model [108] and the Shannon 2004 model [268] (both are models of rabbit ventricular myocyte) to the same intervention targeting intracellular Ca^{2+} handling. Influence of sodium-calcium (Na^{+}/Ca^{2+}) exchanger (NCX) block upon AP and CaT, generated by these two models, are qualitatively comparable. However, the two models responded very differently in terms of AP and CaT to ryanodine receptor (RyR) block. For example, the Mahajan 2008 model showed a shortening in APD, while the Shannon 2004 model exhibited prolongation. It is important to screen these models against experimental findings to assess the robustness of models under different protocols or interventions.

Cardiac tissue slices have gained popularity as a candidate for drug screening due to their ability to reflect many whole-heart phenomena (e.g. conduction speed, AP duration), combined with the ease of controlling the drug concentration (compared to the whole heart) and the possibility of performing high throughput measurements [83-85, 88]. It is also relatively easy to record basic electrophysiological properties such as APD restitution in tissue slices. It is possible to use tissue slice as a data source for model testing/validation to find out which model can reproduce experimental data better, and therefore represents the underlying biophysical mechanisms more accurately.

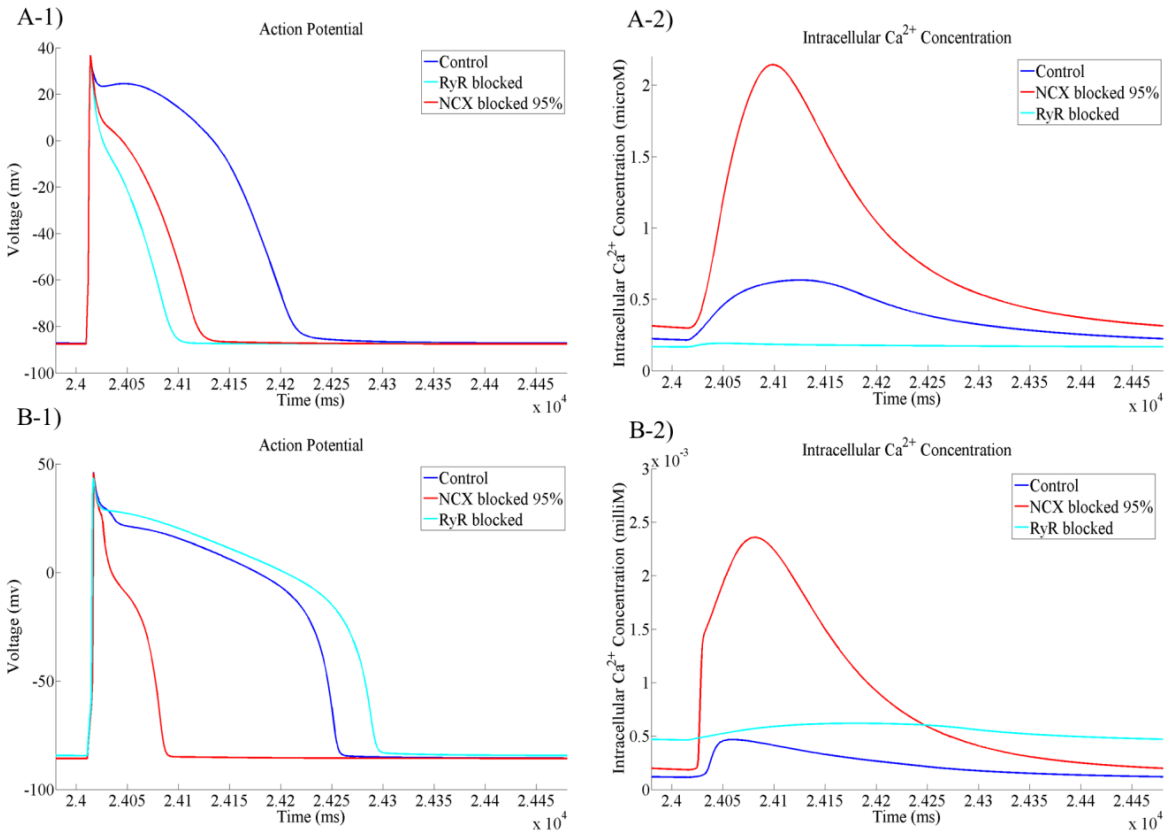

Figure 6.1: Comparison of two cell electrophysiology models under interventions targeting the Ca^{2+} handling pathway: control conditions (blue line), NCX blocked by 95% (red), block of the RyR (light blue) A-1) AP simulated from Mahajan 2008 model; A-2) CaT computed from Mahajan 2008 model; B-1) AP simulated from Shannon 2004 model; B-2) CaT computed from Shannon 2004 model. The simulation was performed with a 2 Hz pacing frequency; parameters shown in the figures are at steady state.

6.3.2 Use of Simulation to Restore the Epicardial Spatial Heterogeneity Pattern From Whole Heart Optical Mapping Data

As discussed in chapter 5, the apparent epicardial base-apex gradient can depend on the anterior-posterior location, and it would therefore be helpful to work out the base-apex gradient at different locations in the LV (e.g. frontal *vs.* side view) with whole heart mapping (since alignment of tissue slice can induce error). However, the penetration of excitation light into the tissue blurs APD patterns and combines the transmural depolarisation pattern with the APD pattern (please see Figure 6.2). Simulation can help in understanding the effect of

light penetration and photon scattering in the tissue and can therefore be used to reconstruct non-blurred original APD patterns. 3-D simulations would need to be performed with a representative fibre orientation (which can be constructed from MRI study and there is a rabbit mesh implemented in Chaste already [269, 270]) and close-to-real conduction velocity (can be obtained from tissue slice data). The APD can be homogeneous to start with (the cell model needs to be modified to fit average APD values measured experimentally on the whole heart) and a pattern of APD can be generated (which could show some heterogeneity). In the second step, one could incorporate the APD transmural gradient (could be the value extracted from tissue slice data).

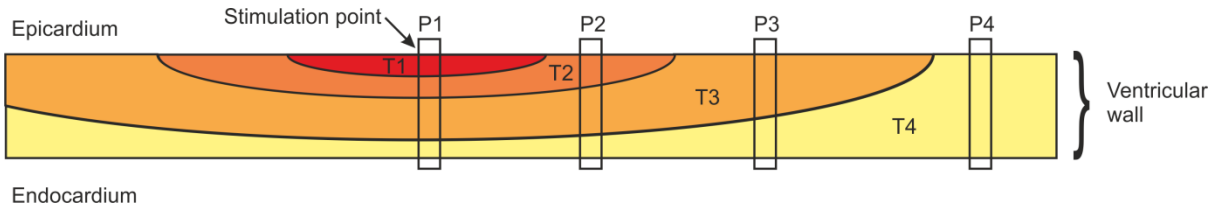

Figure 6.2: a schematic diagram demonstrating the possibility to visualize a prolongation in APD at stimulation site (P1) purely by transmural light penetration: The AP at T1 could be observed as being longest due to the conduction time needed to travel transmurally. The time points T1 to T4 are the activation time points on the tissue block. Assuming the APD is the same in the whole block, the APD visualized at observation point P1 would be longest since activation will be captured at T1 and the repolarisation will be blurred and prolonged by the transmural layers below, whereas, the observed APD at P4 should be the original APD (no prolongation).

Final Conclusion

The research work described in this thesis has shown that experimental studies using cardiac tissue slices can reflect a range of close-to-whole-hearts electrophysiological properties. In combination with multi-parametric optical mapping, cardiac slice is a promising candidate for studying many aspects of cardiac patho-physiology.

References

1. Endo, M., *Calcium release from the sarcoplasmic reticulum.* Physiol Rev, 1977. **57**(1): p. 71-108.
2. Levick, J.R., *An Introduction to Cardiovascular Physiogy* 5ed2010: Hodder Arnold
3. Bers, D.M., *Cardiac excitation-contraction coupling.* Nature, 2002. **415**(6868): p. 198-205.
4. Cavanaugh, M.W., *Pulsation, Migration and Division in Dissociated Chick Embryo Heart Cells Invitro.* Journal of Experimental Zoology, 1955. **128**(3): p. 573-589.
5. Bloom, S., *Spontaneous rhythmic contraction of separated heart muscle cells.* Science, 1970. **167**(3926): p. 1727-9.
6. Bloom, S., *Phylogenetic differences in spontaneous contractility of isolated heart muscle cells.* Comp Biochem Physiol, 1970. **37**(1): p. 127-9.
7. Vahouny, G.V., R. Wei, R. Starkweather, and C. Davis, *Preparation of beating heart cells from adult rats.* Science, 1970. **167**(3925): p. 1616-8.
8. Kono, T., *Roles of collagenases and other proteolytic enzymes in the dispersal of animal tissues.* Biochim Biophys Acta, 1969. **178**(2): p. 397-400.
9. Glick, M.R., A.H. Burns, and W.J. Reddy, *Dispersion and isolation of beating cells from adult rat heart.* Anal Biochem, 1974. **61**(1): p. 32-42.
10. Gould, R.P. and T. Powell, *Intact isolated muscle cells from the adult rat heart.* J Physiol, 1972. **225**(2): p. 16P-19P.
11. Powell, T. and V.W. Twist, *A rapid technique for the isolation and purification of adult cardiac muscle cells having respiratory control and a tolerance to calcium.* Biochem Biophys Res Commun, 1976. **72**(1): p. 327-33.
12. Wu, J.Z., R.M. Li, Z.L. Zhou, M. Xu, and D.B. Huang, *[Isolation and identification of alkaloids from Fritillaria egregia Y.K. Yang, J.Z. Wu et D.T].* Zhongguo Zhong Yao Za Zhi, 1993. **18**(4): p. 228-30, 255.
13. Lipp, P., J. Huser, L. Pott, and E. Niggli, *Subcellular properties of triggered Ca2+ waves in isolated citrate-loaded guinea-pig atrial myocytes characterized by ratiometric confocal microscopy.* J Physiol, 1996. **497 (Pt 3)**: p. 599-610.
14. Iribe, G., C.W. Ward, P. Camelliti, C. Bollensdorff, F. Mason, R.A. Burton, A. Garny, M.K. Morphew, A. Hoenger, W.J. Lederer, and P. Kohl, *Axial stretch of rat single ventricular cardiomyocytes causes an acute and transient increase in Ca2+ spark rate.* Circ Res, 2009. **104**(6): p. 787-95.
15. Hardy, M.E., C.E. Pollard, B.G. Small, M. Bridgland-Taylor, A.J. Woods, J.P. Valentin, and N. Abi-Gerges, *Validation of a voltage-sensitive dye (di-4-ANEPPS)-based method for assessing drug-induced delayed repolarisation in beagle dog left ventricular midmyocardial myocytes.* J Pharmacol Toxicol Methods, 2009. **60**(1): p. 94-106.
16. Warren, M., K.W. Spitzer, B.W. Steadman, T.D. Rees, P. Venable, T. Taylor, J. Shibayama, P. Yan, J.P. Wuskell, L.M. Loew, and A.V. Zaitsev, *High-precision recording of the action potential in isolated cardiomyocytes using the near-infrared fluorescent dye di-4-ANBDQBS.* Am J Physiol Heart Circ Physiol, 2010. **299**(4): p. H1271-81.
17. He, J.Q., Y. Ma, Y. Lee, J.A. Thomson, and T.J. Kamp, *Human embryonic stem cells develop into multiple types of cardiac myocytes: action potential characterization.* Circ Res, 2003. **93**(1): p. 32-9.
18. Fischmeister, R., L.J. DeFelice, R.K. Ayer, Jr., R. Levi, and R.L. DeHaan, *Channel currents during spontaneous action potentials in embryonic chick heart cells. The action potential patch clamp.* Biophys J, 1984. **46**(2): p. 267-71.

19. Hamill, O.P., A. Marty, E. Neher, B. Sakmann, and F.J. Sigworth, *Improved patch-clamp techniques for high-resolution current recording from cells and cell-free membrane patches.* Pflugers Arch, 1981. **391**(2): p. 85-100.
20. Tampo, A., C.S. Hogan, F. Sedlic, Z.J. Bosnjak, and W.M. Kwok, *Accelerated inactivation of cardiac L-type calcium channels triggered by anaesthetic-induced preconditioning.* Br J Pharmacol, 2009. **156**(3): p. 432-43.
21. Kuryshev, Y.A., E. Ficker, L. Wang, P. Hawryluk, A.T. Dennis, B.A. Wible, A.M. Brown, J. Kang, X.L. Chen, K. Sawamura, W. Reynolds, and D. Rampe, *Pentamidine-induced long QT syndrome and block of hERG trafficking.* J Pharmacol Exp Ther, 2005. **312**(1): p. 316-23.
22. Zeng, T., G.C. Bett, and F. Sachs, *Stretch-activated whole cell currents in adult rat cardiac myocytes.* Am J Physiol Heart Circ Physiol, 2000. **278**(2): p. H548-57.
23. Harrison, R.G., *Observations on the living developing nerve fiber.* Exp Biol Med, 1906. **4**(1): p. 140-143.
24. Burrows, M.T., *Rhythmical Activity of Isolated Heart Muscle Cells in Vitro.* Science, 1912. **36**(916): p. 90-2.
25. Jacobson, S.L. and H.M. Piper, *Cell cultures of adult cardiomyocytes as models of the myocardium.* J Mol Cell Cardiol, 1986. **18**(7): p. 661-78.
26. Passier, R. and C. Mummery, *Cardiomyocyte differentiation from embryonic and adult stem cells.* Curr Opin Biotechnol, 2005. **16**(5): p. 498-502.
27. Passier, R., D.W. Oostwaard, J. Snapper, J. Kloots, R.J. Hassink, E. Kuijk, B. Roelen, A.B. de la Riviere, and C. Mummery, *Increased cardiomyocyte differentiation from human embryonic stem cells in serum-free cultures.* Stem Cells, 2005. **23**(6): p. 772-80.
28. Ellingsen, O., A.J. Davidoff, S.K. Prasad, H.J. Berger, J.P. Springhorn, J.D. Marsh, R.A. Kelly, and T.W. Smith, *Adult rat ventricular myocytes cultured in defined medium: phenotype and electromechanical function.* Am J Physiol, 1993. **265**(2 Pt 2): p. H747-54.
29. Lee, P., M. Klos, C. Bollensdorff, L. Hou, P. Ewart, T.J. Kamp, J. Zhang, A. Bizy, G. Guerrero-Serna, P. Kohl, J. Jalife, and T.J. Herron, *Simultaneous voltage and calcium mapping of genetically purified human induced pluripotent stem cell-derived cardiac myocyte monolayers.* Circ Res, 2012. **110**(12): p. 1556-63.
30. Tsai, C.T., F.T. Chiang, C.D. Tseng, C.C. Yu, Y.C. Wang, L.P. Lai, J.J. Hwang, and J.L. Lin, *Mechanical stretch of atrial myocyte monolayer decreases sarcoplasmic reticulum calcium adenosine triphosphatase expression and increases susceptibility to repolarization alternans.* J Am Coll Cardiol, 2011. **58**(20): p. 2106-15.
31. Zhang, Y., R.B. Sekar, A.D. McCulloch, and L. Tung, *Cell cultures as models of cardiac mechanoelectric feedback.* Prog Biophys Mol Biol, 2008. **97**(2-3): p. 367-82.
32. Kaneko, T., F. Nomura, T. Hamada, Y. Abe, H. Takamori, T. Sakakura, K. Takasuna, A. Sanbuissho, J. Hyllner, P. Sartipy, and K. Yasuda, *On-chip in vitro cell-network pre-clinical cardiac toxicity using spatiotemporal human cardiomyocyte measurement on a chip.* Sci Rep, 2014. **4**: p. 4670.
33. Claycomb, W.C. and N. Lanson, Jr., *Isolation and culture of the terminally differentiated adult mammalian ventricular cardiac muscle cell.* In Vitro, 1984. **20**(8): p. 647-51.
34. Kirshenbaum, L.A., W.R. MacLellan, W. Mazur, B.A. French, and M.D. Schneider, *Highly efficient gene transfer into adult ventricular myocytes by recombinant adenovirus.* J Clin Invest, 1993. **92**(1): p. 381-7.
35. Davidson, M.M., C. Nesti, L. Palenzuela, W.F. Walker, E. Hernandez, L. Protas, M. Hirano, and N.D. Isaac, *Novel cell lines derived from adult human ventricular cardiomyocytes.* J Mol Cell Cardiol, 2005. **39**(1): p. 133-47.
36. Messina, E., L. De Angelis, G. Frati, S. Morrone, S. Chimenti, F. Fiordaliso, M. Salio, M. Battaglia, M.V. Latronico, M. Coletta, E. Vivarelli, L. Frati, G. Cossu, and A. Giacomello,

Isolation and expansion of adult cardiac stem cells from human and murine heart. Circ Res, 2004. **95**(9): p. 911-21.
37. Kreutziger, K.L. and C.E. Murry, *Engineered human cardiac tissue.* Pediatr Cardiol, 2011. **32**(3): p. 334-41.
38. Bugaisky, L.B. and R. Zak, *Differentiation of adult rat cardiac myocytes in cell culture.* Circ Res, 1989. **64**(3): p. 493-500.
39. Mitcheson, J.S., J.C. Hancox, and A.J. Levi, *Action potentials, ion channel currents and transverse tubule density in adult rabbit ventricular myocytes maintained for 6 days in cell culture.* Pflugers Arch, 1996. **431**(6): p. 814-27.
40. Camelliti, P., A.D. McCulloch, and P. Kohl, *Microstructured cocultures of cardiac myocytes and fibroblasts: a two-dimensional in vitro model of cardiac tissue.* Microsc Microanal, 2005. **11**(3): p. 249-59.
41. Rao, C., T. Prodromakis, L. Kolker, U.A. Chaudhry, T. Trantidou, A. Sridhar, C. Weekes, P. Camelliti, S.E. Harding, A. Darzi, M.H. Yacoub, T. Athanasiou, and C.M. Terracciano, *The effect of microgrooved culture substrates on calcium cycling of cardiac myocytes derived from human induced pluripotent stem cells.* Biomaterials, 2013. **34**(10): p. 2399-411.
42. Nath, S., C. Lynch, 3rd, J.G. Whayne, and D.E. Haines, *Cellular electrophysiological effects of hyperthermia on isolated guinea pig papillary muscle. Implications for catheter ablation.* Circulation, 1993. **88**(4 Pt 1): p. 1826-31.
43. Kaufmann, R.L., M.J. Lab, R. Hennekes, and H. Krause, *Feedback interaction of mechanical and electrical events in the isolated mammalian ventricular myocardium (cat papillary muscle).* Pflugers Arch, 1971. **324**(2): p. 100-23.
44. Inoue, D., T. Nakanishi, J. Asayama, H. Katsume, and H. Ijichi, *Electrophysiological effects of bethanidine sulfate on guinea-pig papillary muscle.* Eur J Pharmacol, 1985. **108**(3): p. 301-3.
45. Honerjager, P. and N. Alischewski, *Inotropic and electrophysiological effects of dantrolene on guinea-pig papillary muscle.* Naunyn Schmiedebergs Arch Pharmacol, 1983. **322**(3): p. 237-44.
46. Pelzmann, B., K. Zorn-Pauly, S. Hallstrom, H. Machler, A. Jakubowski, P. Lang, and B. Koidl, *Effects of thienopyridines and thienopyrimidinones on L-type calcium current in isolated cardiomyocytes.* Naunyn Schmiedebergs Arch Pharmacol, 2010. **382**(5-6): p. 433-40.
47. Backx, P.H. and H.E. Ter Keurs, *Fluorescent properties of rat cardiac trabeculae microinjected with fura-2 salt.* Am J Physiol, 1993. **264**(4 Pt 2): p. H1098-110.
48. Barclay, C.J., *Modelling diffusive O(2) supply to isolated preparations of mammalian skeletal and cardiac muscle.* J Muscle Res Cell Motil, 2005. **26**(4-5): p. 225-35.
49. Bell, R.M., M.M. Mocanu, and D.M. Yellon, *Retrograde heart perfusion: the Langendorff technique of isolated heart perfusion.* J Mol Cell Cardiol, 2011. **50**(6): p. 940-50.
50. Neely, J.R., H. Liebermeister, E.J. Battersby, and H.E. Morgan, *Effect of pressure development on oxygen consumption by isolated rat heart.* Am J Physiol, 1967. **212**(4): p. 804-14.
51. Sutherland, F.J., M.J. Shattock, K.E. Baker, and D.J. Hearse, *Mouse isolated perfused heart: characteristics and cautions.* Clin Exp Pharmacol Physiol, 2003. **30**(11): p. 867-78.
52. Sung, D., R.W. Mills, J. Schettler, S.M. Narayan, J.H. Omens, and A.D. McCulloch, *Ventricular filling slows epicardial conduction and increases action potential duration in an optical mapping study of the isolated rabbit heart.* J Cardiovasc Electrophysiol, 2003. **14**(7): p. 739-49.
53. Lang, D., M. Sulkin, Q. Lou, and I.R. Efimov, *Optical mapping of action potentials and calcium transients in the mouse heart.* J Vis Exp, 2011(55).
54. Black, S.C., S.O. Fagbemi, L. Chi, G.S. Friedrichs, and B.R. Lucchesi, *Phorbol ester-induced ventricular fibrillation in the Langendorff-perfused rabbit heart: antagonism by staurosporine and glibenclamide.* J Mol Cell Cardiol, 1993. **25**(12): p. 1427-38.

55. Kirchhof, P., L. Fabritz, A. Kilic, F. Begrow, G. Breithardt, and M. Kuhn, *Ventricular arrhythmias, increased cardiac calmodulin kinase II expression, and altered repolarization kinetics in ANP receptor deficient mice.* J Mol Cell Cardiol, 2004. **36**(5): p. 691-700.
56. Valentin, J.P., P. Hoffmann, F. De Clerck, T.G. Hammond, and L. Hondeghem, *Review of the predictive value of the Langendorff heart model (Screenit system) in assessing the proarrhythmic potential of drugs.* J Pharmacol Toxicol Methods, 2004. **49**(3): p. 171-81.
57. Wu, T.J., J.J. Ong, C. Hwang, J.J. Lee, M.C. Fishbein, L. Czer, A. Trento, C. Blanche, R.M. Kass, W.J. Mandel, H.S. Karagueuzian, and P.S. Chen, *Characteristics of wave fronts during ventricular fibrillation in human hearts with dilated cardiomyopathy: role of increased fibrosis in the generation of reentry.* J Am Coll Cardiol, 1998. **32**(1): p. 187-96.
58. Jeevaratnam, K., S. Poh Tee, Y. Zhang, R. Rewbury, L. Guzadhur, R. Duehmke, A.A. Grace, M. Lei, and C.L. Huang, *Delayed conduction and its implications in murine Scn5a(+/-) hearts: independent and interacting effects of genotype, age, and sex.* Pflugers Arch, 2011. **461**(1): p. 29-44.
59. Lee, P., C. Bollensdorff, T.A. Quinn, J.P. Wuskell, L.M. Loew, and P. Kohl, *Single-sensor system for spatially resolved, continuous, and multiparametric optical mapping of cardiac tissue.* Heart Rhythm, 2011. **8**(9): p. 1482-91.
60. Pedron-Torrecilla, J., A.M. Climent, J. Millet, P. Berne, J. Brugada, R. Brugada, and M.S. Guillem, *Characteristics of inverse-computed epicardial electrograms of Brugada syndrome patients.* Conf Proc IEEE Eng Med Biol Soc, 2011. **2011**: p. 235-8.
61. Schilling, R.J., A.H. Kadish, N.S. Peters, J. Goldberger, and D.W. Davies, *Endocardial mapping of atrial fibrillation in the human right atrium using a non-contact catheter.* Eur Heart J, 2000. **21**(7): p. 550-64.
62. Taggart, P., P.M. Sutton, T. Opthof, R. Coronel, R. Trimlett, W. Pugsley, and P. Kallis, *Transmural repolarisation in the left ventricle in humans during normoxia and ischaemia.* Cardiovasc Res, 2001. **50**(3): p. 454-62.
63. Chen, P.S., N. Shibata, E.G. Dixon, P.D. Wolf, N.D. Danieley, M.B. Sweeney, W.M. Smith, and R.E. Ideker, *Activation during ventricular defibrillation in open-chest dogs. Evidence of complete cessation and regeneration of ventricular fibrillation after unsuccessful shocks.* J Clin Invest, 1986. **77**(3): p. 810-23.
64. Lee, P., F. Taghavi, P. Yan, P. Ewart, E.A. Ashley, L.M. Loew, P. Kohl, C. Bollensdorff, and C.E. Woods, *In situ optical mapping of voltage and calcium in the heart.* PLoS One, 2012. **7**(8): p. e42562.
65. Warburg.O, Biochem.z, 1923. **142**: p. 317.
66. McIlwain, H. and H.L. Buddle, *Techniques in tissue metabolism. I. A mechanical chopper.* Biochem J, 1953. **53**(3): p. 412-20.
67. Graaf, I.A., G.M. Groothuis, and P. Olinga, *Precision-cut tissue slices as a tool to predict metabolism of novel drugs.* Expert Opin Drug Metab Toxicol, 2007. **3**(6): p. 879-98.
68. Henjakovic, M., C. Martin, H.G. Hoymann, K. Sewald, A.R. Ressmeyer, C. Dassow, G. Pohlmann, N. Krug, S. Uhlig, and A. Braun, *Ex vivo lung function measurements in precision-cut lung slices (PCLS) from chemical allergen-sensitized mice represent a suitable alternative to in vivo studies.* Toxicol Sci, 2008. **106**(2): p. 444-53.
69. Vickers, A.E., K. Rose, R. Fisher, M. Saulnier, P. Sahota, and P. Bentley, *Kidney slices of human and rat to characterize cisplatin-induced injury on cellular pathways and morphology.* Toxicol Pathol, 2004. **32**(5): p. 577-90.
70. Parrish, A.R., A.J. Gandolfi, and K. Brendel, *Precision-cut tissue slices: applications in pharmacology and toxicology.* Life Sci, 1995. **57**(21): p. 1887-901.
71. de Boer, T.P., P. Camelliti, U. Ravens, and P. Kohl, *Myocardial tissue slices: organotypic pseudo-2D models for cardiac research & development.* Future Cardiol, 2009. **5**(5): p. 425-30.

72. Takaki, M., H. Kohzuki, S. Sakata, Y. Ohga, S. Shimizu, H. Ishidate, H. Ito, T. Kishi, and H. Suga, *Oxygen consumption and motility of mechanically unloaded myocardial slices.* Adv Exp Med Biol, 1998. **453**: p. 499-506.
73. Neri, B., G. Cini-Neri, and M. D'Alterio, *Effect of anthracyclines and mitoxantrone on oxygen uptake and ATP intracellular concentration in rat heart slices.* Biochem Biophys Res Commun, 1984. **125**(3): p. 954-60.
74. Takaki, M., H. Kohzuki, Y. Kawatani, A. Yoshida, H. Ishidate, and H. Suga, *Sarcoplasmic reticulum Ca2+ pump blockade decreases O2 use of unloaded contracting rat heart slices: thapsigargin and cyclopiazonic acid.* J Mol Cell Cardiol, 1998. **30**(3): p. 649-59.
75. Claycomb, W.C., *Biochemical aspects of cardiac muscle differentiation. Possible control of deoxyribonucleic acid synthesis and cell differentiation by adrenergic innervation and cyclic adenosine 3':5'-monophosphate.* J Biol Chem, 1976. **251**(19): p. 6082-9.
76. Fischer, P.W. and A. Giroux, *Effects of dietary magnesium on sodium-potassium pump action in the heart of rats.* J Nutr, 1987. **117**(12): p. 2091-5.
77. Bihler, I., R.A. Prayag, P. Charles, and P.C. Sawh, *Stimulation of Na+ pump in cardiac myocytes and intact ventricles by low doses of digitaloids is independent of beta-adrenergic stimulation.* Can J Cardiol, 1986. **2**(4): p. 230-5.
78. Katano, Y., T. Akera, K. Temma, and R.H. Kennedy, *Enhanced ouabain sensitivity of the heart and myocardial sodium pump in aged rats.* Eur J Pharmacol, 1984. **105**(1-2): p. 95-103.
79. Burnashev, N.A., F.A. Edwards, and A.N. Verkhratsky, *Patch-clamp recordings on rat cardiac muscle slices.* Pflugers Arch, 1990. **417**(1): p. 123-5.
80. Bursac, N., M. Papadaki, J.A. White, S.R. Eisenberg, G. Vunjak-Novakovic, and L.E. Freed, *Cultivation in rotating bioreactors promotes maintenance of cardiac myocyte electrophysiology and molecular properties.* Tissue Eng, 2003. **9**(6): p. 1243-53.
81. Halbach, M., F. Pillekamp, K. Brockmeier, J. Hescheler, J. Muller-Ehmsen, and M. Reppel, *Ventricular slices of adult mouse hearts--a new multicellular in vitro model for electrophysiological studies.* Cell Physiol Biochem, 2006. **18**(1-3): p. 1-8.
82. Brandenburger, M., J. Wenzel, R. Bogdan, D. Richardt, F. Nguemo, M. Reppel, J. Hescheler, H. Terlau, and A. Dendorfer, *Organotypic slice culture from human adult ventricular myocardium.* Cardiovasc Res, 2012. **93**(1): p. 50-9.
83. Bussek, A., E. Wettwer, T. Christ, H. Lohmann, P. Camelliti, and U. Ravens, *Tissue slices from adult mammalian hearts as a model for pharmacological drug testing.* Cell Physiol Biochem, 2009. **24**(5-6): p. 527-36.
84. Camelliti, P., S.A. Al-Saud, R.T. Smolenski, S. Al-Ayoubi, A. Bussek, E. Wettwer, N.R. Banner, C.T. Bowles, M.H. Yacoub, and C.M. Terracciano, *Adult human heart slices are a multicellular system suitable for electrophysiological and pharmacological studies.* J Mol Cell Cardiol, 2011. **51**(3): p. 390-8.
85. Bussek, A., M. Schmidt, J. Bauriedl, U. Ravens, E. Wettwer, and H. Lohmann, *Cardiac tissue slices with prolonged survival for in vitro drug safety screening.* J Pharmacol Toxicol Methods, 2012. **66**(2): p. 145-51.
86. Davidenko, J.M., R. Salomonsz, A.M. Pertsov, W.T. Baxter, and J. Jalife, *Effects of pacing on stationary reentrant activity. Theoretical and experimental study.* Circ Res, 1995. **77**(6): p. 1166-79.
87. Pertsov, A.M., J.M. Davidenko, R. Salomonsz, W.T. Baxter, and J. Jalife, *Spiral waves of excitation underlie reentrant activity in isolated cardiac muscle.* Circ Res, 1993. **72**(3): p. 631-50.
88. Lee, P., K. Wang, C.E. Woods, P. Yan, P. Kohl, P. Ewart, L.M. Loew, D.A. Terrar, and C. Bollensdorff, *Cardiac electrophysiological imaging systems scalable for high-throughput drug testing.* Pflugers Arch, 2012. **464**(6): p. 645-56.

89. Salzberg, B.M., H.V. Davila, and L.B. Cohen, *Optical recording of impulses in individual neurones of an invertebrate central nervous system.* Nature, 1973. **246**(5434): p. 508-9.
90. Efimov, I.R., V.P. Nikolski, and G. Salama, *Optical imaging of the heart.* Circ Res, 2004. **95**(1): p. 21-33.
91. Herron, T.J., P. Lee, and J. Jalife, *Optical imaging of voltage and calcium in cardiac cells & tissues.* Circ Res, 2012. **110**(4): p. 609-23.
92. Attin, M. and W.T. Clusin, *Basic concepts of optical mapping techniques in cardiac electrophysiology.* Biol Res Nurs, 2009. **11**(2): p. 195-207.
93. Fabiato, A. and F. Fabiato, *Use of chlorotetracycline fluorescence to demonstrate Ca2+-induced release of Ca2+ from the sarcoplasmic reticulum of skinned cardiac cells.* Nature, 1979. **281**(5727): p. 146-8.
94. Wang, L., R.C. Myles, N.M. De Jesus, A.K. Ohlendorf, D.M. Bers, and C.M. Ripplinger, *Optical mapping of sarcoplasmic reticulum Ca2+ in the intact heart: ryanodine receptor refractoriness during alternans and fibrillation.* Circ Res, 2014. **114**(9): p. 1410-21.
95. Levin, A.M., D.L. Bates, A.M. Ring, C. Krieg, J.T. Lin, L. Su, I. Moraga, M.E. Raeber, G.R. Bowman, P. Novick, V.S. Pande, C.G. Fathman, O. Boyman, and K.C. Garcia, *Exploiting a natural conformational switch to engineer an interleukin-2 'superkine'.* Nature, 2012. **484**(7395): p. 529-33.
96. Choi, B.R. and G. Salama, *Simultaneous maps of optical action potentials and calcium transients in guinea-pig hearts: mechanisms underlying concordant alternans.* J Physiol, 2000. **529 Pt 1**: p. 171-88.
97. Omichi, C., S.T. Lamp, S.F. Lin, J. Yang, A. Baher, S. Zhou, M. Attin, M.H. Lee, H.S. Karagueuzian, B. Kogan, Z. Qu, A. Garfinkel, P.S. Chen, and J.N. Weiss, *Intracellular Ca dynamics in ventricular fibrillation.* Am J Physiol Heart Circ Physiol, 2004. **286**(5): p. H1836-44.
98. Li, T., N. Sperelakis, R.E. Teneick, and R.J. Solaro, *Effects of diacetyl monoxime on cardiac excitation-contraction coupling.* J Pharmacol Exp Ther, 1985. **232**(3): p. 688-95.
99. Lab, M.J., *Mechanoelectric feedback (transduction) in heart: concepts and implications.* Cardiovasc Res, 1996. **32**(1): p. 3-14.
100. Baxter, W.T., S.F. Mironov, A.V. Zaitsev, J. Jalife, and A.M. Pertsov, *Visualizing excitation waves inside cardiac muscle using transillumination.* Biophys J, 2001. **80**(1): p. 516-30.
101. Bishop, M.J., B. Rodriguez, F. Qu, I.R. Efimov, D.J. Gavaghan, and N.A. Trayanova, *The role of photon scattering in optical signal distortion during arrhythmia and defibrillation.* Biophys J, 2007. **93**(10): p. 3714-26.
102. Di Virgilio, F., T.H. Steinberg, and S.C. Silverstein, *Inhibition of Fura-2 sequestration and secretion with organic anion transport blockers.* Cell Calcium, 1990. **11**(2-3): p. 57-62.
103. Claycomb, W.C., *Biochemical aspects of cardiac muscle differentiation. Deoxyribonucleic acid synthesis and nuclear and cytoplasmic deoxyribonucleic acid polymerase activity.* J Biol Chem, 1975. **250**(9): p. 3229-35.
104. Yasuhara, S., M. Takaki, A. Kikuta, H. Ito, and H. Suga, *Myocardial VO2 of mechanically unloaded contraction of rat ventricular slices measured by a new approach.* Am J Physiol, 1996. **270**(3 Pt 2): p. H1063-70.
105. Han, J., N. Kim, H. Joo, and E. Kim, *Ketamine abolishes ischemic preconditioning through inhibition of K(ATP) channels in rabbit hearts.* Am J Physiol Heart Circ Physiol, 2002. **283**(1): p. H13-21.
106. Liu, M., J. Liu, J. Liao, and Z. Diwu, *A Functional Analysis of GPCR and Calcium Channel Targets using Cal 520 AM Ester. Biophysical Journal, Suppl. 102(3) pp. 309a - 310a* 2012.
107. Mirams, G.R., C.J. Arthurs, M.O. Bernabeu, R. Bordas, J. Cooper, A. Corrias, Y. Davit, S.J. Dunn, A.G. Fletcher, D.G. Harvey, M.E. Marsh, J.M. Osborne, P. Pathmanathan, J. Pitt-

Francis, J. Southern, N. Zemzemi, and D.J. Gavaghan, *Chaste: an open source C++ library for computational physiology and biology.* PLoS Comput Biol, 2013. **9**(3): p. e1002970.
108. Mahajan, A., Y. Shiferaw, D. Sato, A. Baher, R. Olcese, L.H. Xie, M.J. Yang, P.S. Chen, J.G. Restrepo, A. Karma, A. Garfinkel, Z. Qu, and J.N. Weiss, *A rabbit ventricular action potential model replicating cardiac dynamics at rapid heart rates.* Biophys J, 2008. **94**(2): p. 392-410.
109. Bayly, P.V., B.H. KenKnight, J.M. Rogers, R.E. Hillsley, R.E. Ideker, and W.M. Smith, *Estimation of conduction velocity vector fields from epicardial mapping data.* IEEE Trans Biomed Eng, 1998. **45**(5): p. 563-71.
110. Rosenbaum, D.S., D.T. Kaplan, A. Kanai, L. Jackson, H. Garan, R.J. Cohen, and G. Salama, *Repolarization inhomogeneities in ventricular myocardium change dynamically with abrupt cycle length shortening.* Circulation, 1991. **84**(3): p. 1333-45.
111. Pillekamp, F., M. Halbach, M. Reppel, O. Rubenchyk, K. Pfannkuche, J.Y. Xi, W. Bloch, N. Sreeram, K. Brockmeier, and J. Hescheler, *Neonatal murine heart slices. A robust model to study ventricular isometric contractions.* Cell Physiol Biochem, 2007. **20**(6): p. 837-46.
112. Choi, B.R., F. Burton, and G. Salama, *Cytosolic Ca2+ triggers early afterdepolarizations and Torsade de Pointes in rabbit hearts with type 2 long QT syndrome.* J Physiol, 2002. **543**(Pt 2): p. 615-31.
113. Christini, D.J., *Action potential voltage alternans: an indicator of calcium handling dysfunction during heart failure?* Heart Rhythm, 2010. **7**(8): p. 1102-3.
114. Lou, Q., W. Li, and I.R. Efimov, *Multiparametric optical mapping of the Langendorff-perfused rabbit heart.* J Vis Exp, 2011(55).
115. Markhasin, V.S., A.A. Balakin, L.B. Katsnelson, P. Konovalov, O.N. Lookin, Y. Protsenko, and O. Solovyova, *Slow force response and auto-regulation of contractility in heterogeneous myocardium.* Prog Biophys Mol Biol, 2012. **110**(2-3): p. 305-18.
116. Choi, B.R., T. Liu, and G. Salama, *Calcium transients modulate action potential repolarizations in ventricular fibrillation.* Conf Proc IEEE Eng Med Biol Soc, 2006. **1**: p. 2264-7.
117. Matiukas, A., B.G. Mitrea, M. Qin, A.M. Pertsov, A.G. Shvedko, M.D. Warren, A.V. Zaitsev, J.P. Wuskell, M.D. Wei, J. Watras, and L.M. Loew, *Near-infrared voltage-sensitive fluorescent dyes optimized for optical mapping in blood-perfused myocardium.* Heart Rhythm, 2007. **4**(11): p. 1441-51.
118. Tian, Q., L. Kaestner, and P. Lipp, *Noise-free visualization of microscopic calcium signaling by pixel-wise fitting.* Circ Res, 2012. **111**(1): p. 17-27.
119. Fedorov, V.V., L. Li, A. Glukhov, I. Shishkina, R.R. Aliev, T. Mikheeva, V.P. Nikolski, L.V. Rosenshtraukh, and I.R. Efimov, *Hibernator Citellus undulatus maintains safe cardiac conduction and is protected against tachyarrhythmias during extreme hypothermia: possible role of Cx43 and Cx45 up-regulation.* Heart Rhythm, 2005. **2**(9): p. 966-75.
120. Asirvatham, J.R., V. Moses, and L. Bjornson, *Errors in potassium measurement: a laboratory perspective for the clinician.* N Am J Med Sci, 2013. **5**(4): p. 255-9.
121. Giles, W.R. and Y. Imaizumi, *Comparison of potassium currents in rabbit atrial and ventricular cells.* J Physiol, 1988. **405**: p. 123-45.
122. Attwell, D., I. Cohen, and D.A. Eisner, *The effects of heart rate on the action potential of guinea-pig and human ventricular muscle.* J Physiol, 1981. **313**: p. 439-61.
123. Klein, M.G., A. Lacampagne, and M.F. Schneider, *Voltage dependence of the pattern and frequency of discrete Ca2+ release events after brief repriming in frog skeletal muscle.* Proc Natl Acad Sci U S A, 1997. **94**(20): p. 11061-6.
124. Zhang, P., J. Su, and U. Mende, *Cross talk between cardiac myocytes and fibroblasts: from multiscale investigative approaches to mechanisms and functional consequences.* Am J Physiol Heart Circ Physiol, 2012. **303**(12): p. H1385-96.
125. Smaill, B.H., J. Zhao, and M.L. Trew, *Three-dimensional impulse propagation in myocardium: arrhythmogenic mechanisms at the tissue level.* Circ Res, 2013. **112**(5): p. 834-48.

126. Fagbemi, O.S., K. Brack, S. Golar, D. Crisp, and A. Economides, *Electrophysiological and biochemical changes in rabbit hearts stored at 4 degrees C for 6 or 24 h.* Clin Sci (Lond), 2001. **101**(4): p. 367-76.
127. Iost, N., L. Virag, M. Opincariu, J. Szecsi, A. Varro, and J.G. Papp, *Delayed rectifier potassium current in undiseased human ventricular myocytes.* Cardiovasc Res, 1998. **40**(3): p. 508-15.
128. Katz, A.M. and N.M. Leach, *Differential effects of 1,4-dihydropyridine calcium channel blockers: therapeutic implications.* J Clin Pharmacol, 1987. **27**(11): p. 825-34.
129. Wang, K., D. Terrar, D.J. Gavaghan, U.M.R. Mu, P. Kohl, and C. Bollensdorff, *Living cardiac tissue slices: An organotypic pseudo two-dimensional model for cardiac biophysics research.* Prog Biophys Mol Biol, 2014.
130. Calkins, H., J.H. Levine, and D.A. Kass, *Electrophysiological effect of varied rate and extent of acute in vivo left ventricular load increase.* Cardiovasc Res, 1991. **25**(8): p. 637-44.
131. Lab, M.J., *Mechanosensitivity as an integrative system in heart: an audit.* Prog Biophys Mol Biol, 1999. **71**(1): p. 7-27.
132. Le Guennec, J.Y., E. White, F. Gannier, J.A. Argibay, and D. Garnier, *Stretch-induced increase of resting intracellular calcium concentration in single guinea-pig ventricular myocytes.* Exp Physiol, 1991. **76**(6): p. 975-8.
133. Nakagawa, A., M. Arita, T. Shimada, and J. Shirabe, *Effects of mechanical stretch on the membrane potential of guinea pig ventricular muscles.* Jpn J Physiol, 1988. **38**(6): p. 819-38.
134. Pathak, C.L., *The influence of stretch stimuli on the chronotropic response of the frog's isolated whole heart and its individual chambers.* Indian J Med Sci, 1957. **11**(10): p. 808-12.
135. Le Guennec, J.Y., N. Peineau, J.A. Argibay, K.G. Mongo, and D. Garnier, *A new method of attachment of isolated mammalian ventricular myocytes for tension recording: length dependence of passive and active tension.* J Mol Cell Cardiol, 1990. **22**(10): p. 1083-93.
136. Belus, A. and E. White, *Streptomycin and intracellular calcium modulate the response of single guinea-pig ventricular myocytes to axial stretch.* J Physiol, 2003. **546**(Pt 2): p. 501-9.
137. Tung, L. and S. Zou, *Influence of stretch on excitation threshold of single frog ventricular cells.* Exp Physiol, 1995. **80**(2): p. 221-35.
138. Kamkin, A., I. Kiseleva, and G. Isenberg, *Stretch-activated currents in ventricular myocytes: amplitude and arrhythmogenic effects increase with hypertrophy.* Cardiovasc Res, 2000. **48**(3): p. 409-20.
139. Prosser, B.L., C.W. Ward, and W.J. Lederer, *X-ROS signaling: rapid mechano-chemo transduction in heart.* Science, 2011. **333**(6048): p. 1440-5.
140. Gopalan, S.M., C. Flaim, S.N. Bhatia, M. Hoshijima, R. Knoell, K.R. Chien, J.H. Omens, and A.D. McCulloch, *Anisotropic stretch-induced hypertrophy in neonatal ventricular myocytes micropatterned on deformable elastomers.* Biotechnol Bioeng, 2003. **81**(5): p. 578-87.
141. Camelliti, P., J.O. Gallagher, P. Kohl, and A.D. McCulloch, *Micropatterned cell cultures on elastic membranes as an in vitro model of myocardium.* Nat Protoc, 2006. **1**(3): p. 1379-91.
142. Allen, D.G. and J.C. Kentish, *Calcium concentration in the myoplasm of skinned ferret ventricular muscle following changes in muscle length.* J Physiol, 1988. **407**: p. 489-503.
143. Allen, D.G. and S. Kurihara, *The effects of muscle length on intracellular calcium transients in mammalian cardiac muscle.* J Physiol, 1982. **327**: p. 79-94.
144. Zabel, M., B.S. Koller, F. Sachs, and M.R. Franz, *Stretch-induced voltage changes in the isolated beating heart: importance of the timing of stretch and implications for stretch-activated ion channels.* Cardiovasc Res, 1996. **32**(1): p. 120-30.
145. Langendorff, O., *Untersuchungen am uberlebenden Saugethierherzen.* Pflügers Arch, 1895. **61**: p. 291– 332.
146. Botchway, A.N., M.A. Turner, D.J. Sheridan, N.A. Flores, and C.H. Fry, *Electrophysiological effects accompanying regression of left ventricular hypertrophy.* Cardiovasc Res, 2003. **60**(3): p. 510-7.

147. Cooper, P.J., A. Epstein, I.A. Macleod, S.T. Schaaf, J. Sheldon, C. Boulin, and P. Kohl, *Soft tissue impact characterisation kit (STICK) for ex situ investigation of heart rhythm responses to acute mechanical stimulation.* Prog Biophys Mol Biol, 2006. **90**(1-3): p. 444-68.
148. White, E., J.Y. Le Guennec, J.M. Nigretto, F. Gannier, J.A. Argibay, and D. Garnier, *The effects of increasing cell length on auxotonic contractions; membrane potential and intracellular calcium transients in single guinea-pig ventricular myocytes.* Exp Physiol, 1993. **78**(1): p. 65-78.
149. Zhang, Y.H., J.B. Youm, H.K. Sung, S.H. Lee, S.Y. Ryu, W.K. Ho, and Y.E. Earm, *Stretch-activated and background non-selective cation channels in rat atrial myocytes.* J Physiol, 2000. **523 Pt 3**: p. 607-19.
150. Riemer, T.L. and L. Tung, *Stretch-induced excitation and action potential changes of single cardiac cells.* Prog Biophys Mol Biol, 2003. **82**(1-3): p. 97-110.
151. Nishimura, S., Y. Kawai, T. Nakajima, Y. Hosoya, H. Fujita, M. Katoh, H. Yamashita, R. Nagai, and S. Sugiura, *Membrane potential of rat ventricular myocytes responds to axial stretch in phase, amplitude and speed-dependent manners.* Cardiovasc Res, 2006. **72**(3): p. 403-11.
152. Cooper, P.J., M. Lei, L.X. Cheng, and P. Kohl, *Selected contribution: axial stretch increases spontaneous pacemaker activity in rabbit isolated sinoatrial node cells.* J Appl Physiol (1985), 2000. **89**(5): p. 2099-104.
153. Cooper, P.J. and P. Kohl, *Species- and preparation-dependence of stretch effects on sino-atrial node pacemaking.* Ann N Y Acad Sci, 2005. **1047**: p. 324-35.
154. Kong, C.R., N. Bursac, and L. Tung, *Mechanoelectrical excitation by fluid jets in monolayers of cultured cardiac myocytes.* J Appl Physiol (1985), 2005. **98**(6): p. 2328-36; discussion 2320.
155. Thompson, S.A., C.R. Copeland, D.H. Reich, and L. Tung, *Mechanical coupling between myofibroblasts and cardiomyocytes slows electric conduction in fibrotic cell monolayers.* Circulation, 2011. **123**(19): p. 2083-93.
156. Lab, M.J., *Transient depolarisation and action potential alterations following mechanical changes in isolated myocardium.* Cardiovasc Res, 1980. **14**(11): p. 624-37.
157. DG, A., *The variations in contractility of cardiac muscle. Ph.D. Thesis, University of London.* 1975.
158. Allen, D.G., *On the relationship between action potential duration and tension in cat papillary muscle.* Cardiovasc Res, 1977. **11**(3): p. 210-8.
159. Allen, D.G., *The variations in contractility of cardiac muscle. Ph.D. Thesis, University of London.* 1975.
160. Franz, M.R., D. Burkhoff, D.T. Yue, and K. Sagawa, *Mechanically induced action potential changes and arrhythmia in isolated and in situ canine hearts.* Cardiovasc Res, 1989. **23**(3): p. 213-23.
161. Lerman, B.B., E.D. Engelstein, and D. Burkhoff, *Mechanoelectrical feedback: role of beta-adrenergic receptor activation in mediating load-dependent shortening of ventricular action potential and refractoriness.* Circulation, 2001. **104**(4): p. 486-90.
162. Lerman, B.B., D. Burkhoff, D.T. Yue, M.R. Franz, and K. Sagawa, *Mechanoelectrical feedback: independent role of preload and contractility in modulation of canine ventricular excitability.* J Clin Invest, 1985. **76**(5): p. 1843-50.
163. Lab, M.J., *Mechanically dependent changes in action potentials recorded from the intact frog ventricle.* Circ Res, 1978. **42**(4): p. 519-28.
164. Werdich, A.A., A. Brzezinski, D. Jeyaraj, M. Khaled Sabeh, E. Ficker, X. Wan, B.M. McDermott, Jr., C.A. Macrae, and D.S. Rosenbaum, *The zebrafish as a novel animal model to study the molecular mechanisms of mechano-electrical feedback in the heart.* Prog Biophys Mol Biol, 2012. **110**(2-3): p. 154-65.
165. Seo, K., M. Inagaki, S. Nishimura, I. Hidaka, M. Sugimachi, T. Hisada, and S. Sugiura, *Structural heterogeneity in the ventricular wall plays a significant role in the initiation of*

stretch-induced arrhythmias in perfused rabbit right ventricular tissues and whole heart preparations. Circ Res, 2010. **106**(1): p. 176-84.
166. Guharay, F. and F. Sachs, *Stretch-activated single ion channel currents in tissue-cultured embryonic chick skeletal muscle.* J Physiol, 1984. **352**: p. 685-701.
167. Hu, H. and F. Sachs, *Stretch-activated ion channels in the heart.* J Mol Cell Cardiol, 1997. **29**(6): p. 1511-23.
168. Bustamante, J.O., A. Ruknudin, and F. Sachs, *Stretch-activated channels in heart cells: relevance to cardiac hypertrophy.* J Cardiovasc Pharmacol, 1991. **17 Suppl 2**: p. S110-3.
169. Sasaki, N., T. Mitsuiye, and A. Noma, *Effects of mechanical stretch on membrane currents of single ventricular myocytes of guinea-pig heart.* Jpn J Physiol, 1992. **42**(6): p. 957-70.
170. Kim, D., *A mechanosensitive K+ channel in heart cells. Activation by arachidonic acid.* J Gen Physiol, 1992. **100**(6): p. 1021-40.
171. Baumgarten, C.M. and H.F. Clemo, *Swelling-activated chloride channels in cardiac physiology and pathophysiology.* Prog Biophys Mol Biol, 2003. **82**(1-3): p. 25-42.
172. Van Wagoner, D.R. and M. Lamorgese, *Ischemia potentiates the mechanosensitive modulation of atrial ATP-sensitive potassium channels.* Ann N Y Acad Sci, 1994. **723**: p. 392-5.
173. Baumgarten, C.M., *Origin of Mechanotransduction: Stretch-Activated Ion Channels*, in *Madame Curie Bioscience Database* 2000, Landes Bioscience: Austin (TX).
174. Reed, A., P. Kohl, and R. Peyronnet, *Molecular candidates for cardiac stretch-activated ion channels.* Global Cardiology Science & Practice 2014.
175. Isenberg, G., D. Kondratev, V. Dyachenko, V. Kazanski, and M.F. Gallitelli, *Isolated Cardiomyocytes: Mechanosensitivity of Action Potential, Membrane Current and Ion Concentration*, in *Mechanosensitivity in Cells and Tissues*, A. Kamkin and I. Kiseleva, Editors. 2005: Moscow.
176. Yang, X.C. and F. Sachs, *Block of stretch-activated ion channels in Xenopus oocytes by gadolinium and calcium ions.* Science, 1989. **243**(4894 Pt 1): p. 1068-71.
177. Suchyna, T.M., J.H. Johnson, K. Hamer, J.F. Leykam, D.A. Gage, H.F. Clemo, C.M. Baumgarten, and F. Sachs, *Identification of a peptide toxin from Grammostola spatulata spider venom that blocks cation-selective stretch-activated channels.* J Gen Physiol, 2000. **115**(5): p. 583-98.
178. Ward, M.L., I.A. Williams, Y. Chu, P.J. Cooper, Y.K. Ju, and D.G. Allen, *Stretch-activated channels in the heart: contributions to length-dependence and to cardiomyopathy.* Prog Biophys Mol Biol, 2008. **97**(2-3): p. 232-49.
179. Caldwell, R.A., H.F. Clemo, and C.M. Baumgarten, *Using gadolinium to identify stretch-activated channels: technical considerations.* Am J Physiol, 1998. **275**(2 Pt 1): p. C619-21.
180. Lee, K.S., E. Marban, and R.W. Tsien, *Inactivation of calcium channels in mammalian heart cells: joint dependence on membrane potential and intracellular calcium.* J Physiol, 1985. **364**: p. 395-411.
181. Tohse, N., *Calcium-sensitive delayed rectifier potassium current in guinea pig ventricular cells.* Am J Physiol, 1990. **258**(4 Pt 2): p. H1200-7.
182. Janvier, N.C. and M.R. Boyett, *The role of Na-Ca exchange current in the cardiac action potential.* Cardiovasc Res, 1996. **32**(1): p. 69-84.
183. duBell, W.H., M.R. Boyett, H.A. Spurgeon, A. Talo, M.D. Stern, and E.G. Lakatta, *The cytosolic calcium transient modulates the action potential of rat ventricular myocytes.* J Physiol, 1991. **436**: p. 347-69.
184. Gannier, F., E. White, Garnier, and J.Y. Le Guennec, *A possible mechanism for large stretch-induced increase in [Ca2+]i in isolated guinea-pig ventricular myocytes.* Cardiovasc Res, 1996. **32**(1): p. 158-67.

185. Alvarez, B.V., N.G. Perez, I.L. Ennis, M.C. Camilion de Hurtado, and H.E. Cingolani, *Mechanisms underlying the increase in force and Ca(2+) transient that follow stretch of cardiac muscle: a possible explanation of the Anrep effect.* Circ Res, 1999. **85**(8): p. 716-22.
186. Hongo, K., E. White, J.Y. Le Guennec, and C.H. Orchard, *Changes in [Ca2+]i, [Na+]i and Ca2+ current in isolated rat ventricular myocytes following an increase in cell length.* J Physiol, 1996. **491 (Pt 3)**: p. 609-19.
187. Tavi, P., C. Han, and M. Weckstrom, *Mechanisms of stretch-induced changes in [Ca2+]i in rat atrial myocytes: role of increased troponin C affinity and stretch-activated ion channels.* Circ Res, 1998. **83**(11): p. 1165-77.
188. Youm, J.B., J. Han, N. Kim, Y.H. Zhang, E. Kim, C.H. Leem, S.J. Kim, and Y.E. Earm, *Role of Stretch-activated Channels in the Heart: Action Potential and Ca2+ Transients*, in *Mechanosensitivity in Cells and Tissues*, A. Kamkin and I. Kiseleva, Editors. 2005: Moscow.
189. Isenberg, G., V. Kazanski, D. Kondratev, M.F. Gallitelli, I. Kiseleva, and A. Kamkin, *Differential effects of stretch and compression on membrane currents and [Na+]c in ventricular myocytes.* Prog Biophys Mol Biol, 2003. **82**(1-3): p. 43-56.
190. Iribe, G. and P. Kohl, *Axial stretch enhances sarcoplasmic reticulum Ca2+ leak and cellular Ca2+ reuptake in guinea pig ventricular myocytes: experiments and models.* Prog Biophys Mol Biol, 2008. **97**(2-3): p. 298-311.
191. Belmonte, S. and M. Morad, *'Pressure-flow'-triggered intracellular Ca2+ transients in rat cardiac myocytes: possible mechanisms and role of mitochondria.* J Physiol, 2008. **586**(5): p. 1379-97.
192. Belmonte, S. and M. Morad, *Shear fluid-induced Ca2+ release and the role of mitochondria in rat cardiac myocytes.* Ann N Y Acad Sci, 2008. **1123**: p. 58-63.
193. Garny, A., D. Noble, and P. Kohl, *Dimensionality in cardiac modelling.* Prog Biophys Mol Biol, 2005. **87**(1): p. 47-66.
194. Plank, G., R.A. Burton, P. Hales, M. Bishop, T. Mansoori, M.O. Bernabeu, A. Garny, A.J. Prassl, C. Bollensdorff, F. Mason, F. Mahmood, B. Rodriguez, V. Grau, J.E. Schneider, D. Gavaghan, and P. Kohl, *Generation of histo-anatomically representative models of the individual heart: tools and application.* Philos Trans A Math Phys Eng Sci, 2009. **367**(1896): p. 2257-92.
195. Kaufmann, R.L., H. Antoni, R. Hennekes, R. Jacob, M. Kohlhardt, and M.J. Lab, *Mechanical response of the mammalian myocardium to modifications of the action potential.* Cardiovasc Res, 1971. **Suppl 1**: p. 64-70.
196. von Lewinski, D., J. Kockskamper, and B. Pieske, *Stretch-induced Slow Force Response in Mammalian Ventricular Myocardium*, in *Mechanosensitivity in Cells and Tissues*, A. Kamkin and I. Kiseleva, Editors. 2005: Moscow.
197. Woods, C.E., D. Novo, M. DiFranco, and J.L. Vergara, *The action potential-evoked sarcoplasmic reticulum calcium release is impaired in mdx mouse muscle fibres.* J Physiol, 2004. **557**(Pt 1): p. 59-75.
198. Hennekes, R., R. Kaufmann, M. Lab, and R. Steiner, *Feedback loops involved in cardiac excitation-contraction coupling: evidence for two different pathways.* J Mol Cell Cardiol, 1977. **9**(9): p. 699-713.
199. Lab, M.J., *Contraction-excitation feedback in myocardium. Physiological basis and clinical relevance.* Circ Res, 1982. **50**(6): p. 757-66.
200. Anyukhovsky, E.P., E.A. Sosunov, R.Z. Gainullin, and M.R. Rosen, *The controversial M cell.* J Cardiovasc Electrophysiol, 1999. **10**(2): p. 244-60.
201. Wang, K., P. Lee, G. Mirams, D.J. Gavaghan, P. Kohl, and C. Bollensdorff, *Reliable extraction of action potential and calcium transient data from guinea pig and rabbit ventricular tissue slices.* Pflugers Arch, Under Review.
202. Dominguez, G. and H.A. Fozzard, *Effect of stretch on conduction velocity and cable properties of cardiac Purkinje fibers.* Am J Physiol, 1979. **237**(3): p. C119-24.

203. Laughner, J.I., S. Zhang, H. Li, C.C. Shao, and I.R. Efimov, *Mapping cardiac surface mechanics with structured light imaging.* Am J Physiol Heart Circ Physiol, 2012. **303**(6): p. H712-20.
204. McCulloch, A.D., J.O. Gallagher, S.N. Bhatia, T.K. Borg, and J.H. Omens, *Three-Dimensional Micropatterned Cardiac Tissue Cultures.* Microscopy and Microanalysis, 2005. **11**(SupplementS02): p. 110-111.
205. Xi, J., M. Khalil, N. Shishechian, T. Hannes, K. Pfannkuche, H. Liang, A. Fatima, M. Haustein, F. Suhr, W. Bloch, M. Reppel, T. Saric, M. Wernig, R. Janisch, K. Brockmeier, J. Hescheler, and F. Pillekamp, *Comparison of contractile behavior of native murine ventricular tissue and cardiomyocytes derived from embryonic or induced pluripotent stem cells.* FASEB J, 2010. **24**(8): p. 2739-51.
206. Schram, G., M. Pourrier, P. Melnyk, and S. Nattel, *Differential distribution of cardiac ion channel expression as a basis for regional specialization in electrical function.* Circ Res, 2002. **90**(9): p. 939-50.
207. Wu, J., R.B. Schuessler, M.D. Rodefeld, J.E. Saffitz, and J.P. Boineau, *Morphological and membrane characteristics of spider and spindle cells isolated from rabbit sinus node.* Am J Physiol Heart Circ Physiol, 2001. **280**(3): p. H1232-40.
208. Spach, M.S., P.C. Dolber, and P.A. Anderson, *Multiple regional differences in cellular properties that regulate repolarization and contraction in the right atrium of adult and newborn dogs.* Circ Res, 1989. **65**(6): p. 1594-611.
209. Munk, A.A., R.A. Adjemian, J. Zhao, A. Ogbaghebriel, and A. Shrier, *Electrophysiological properties of morphologically distinct cells isolated from the rabbit atrioventricular node.* J Physiol, 1996. **493 (Pt 3)**: p. 801-18.
210. Pak, H.N., S.J. Hong, G.S. Hwang, H.S. Lee, S.W. Park, J.C. Ahn, Y. Moo Ro, and Y.H. Kim, *Spatial dispersion of action potential duration restitution kinetics is associated with induction of ventricular tachycardia/fibrillation in humans.* J Cardiovasc Electrophysiol, 2004. **15**(12): p. 1357-63.
211. Kuo, C.S., K. Munakata, C.P. Reddy, and B. Surawicz, *Characteristics and possible mechanism of ventricular arrhythmia dependent on the dispersion of action potential durations.* Circulation, 1983. **67**(6): p. 1356-67.
212. Sicouri, S. and C. Antzelevitch, *Electrophysiologic characteristics of M cells in the canine left ventricular free wall.* J Cardiovasc Electrophysiol, 1995. **6**(8): p. 591-603.
213. Antzelevitch, C., *Role of spatial dispersion of repolarization in inherited and acquired sudden cardiac death syndromes.* Am J Physiol Heart Circ Physiol, 2007. **293**(4): p. H2024-38.
214. Yan, G.X., S.J. Rials, Y. Wu, T. Liu, X. Xu, R.A. Marinchak, and P.R. Kowey, *Ventricular hypertrophy amplifies transmural repolarization dispersion and induces early afterdepolarization.* Am J Physiol Heart Circ Physiol, 2001. **281**(5): p. H1968-75.
215. Wang, Y., J. Cheng, R.W. Joyner, M.B. Wagner, and J.A. Hill, *Remodeling of early-phase repolarization: a mechanism of abnormal impulse conduction in heart failure.* Circulation, 2006. **113**(15): p. 1849-56.
216. Drouin, E., F. Charpentier, C. Gauthier, K. Laurent, and H. Le Marec, *Electrophysiologic characteristics of cells spanning the left ventricular wall of human heart: evidence for presence of M cells.* J Am Coll Cardiol, 1995. **26**(1): p. 185-92.
217. Lou, Q., V.V. Fedorov, A.V. Glukhov, N. Moazami, V.G. Fast, and I.R. Efimov, *Transmural heterogeneity and remodeling of ventricular excitation-contraction coupling in human heart failure.* Circulation, 2011. **123**(17): p. 1881-90.
218. Sicouri, S., M. Quist, and C. Antzelevitch, *Evidence for the presence of M cells in the guinea pig ventricle.* J Cardiovasc Electrophysiol, 1996. **7**(6): p. 503-11.
219. Idriss, S.F. and P.D. Wolf, *Transmural action potential repolarization heterogeneity develops postnatally in the rabbit.* J Cardiovasc Electrophysiol, 2004. **15**(7): p. 795-801.

220. Sicouri, S. and C. Antzelevitch, *A subpopulation of cells with unique electrophysiological properties in the deep subepicardium of the canine ventricle. The M cell.* Circ Res, 1991. **68**(6): p. 1729-41.
221. Efimov, I.R., Q. Lou, V.V. Fedorov, A.V. Glukhov, N. Moazami, and V.G. Fast, *Transmural Heterogeneity and Remodeling of Ventricular Excitation-Contraction Coupling in Human Heart Failure.* Circulation, 2011. **123**(17): p. 1881-+.
222. Cheng, J., K. Kamiya, W. Liu, Y. Tsuji, J. Toyama, and I. Kodama, *Heterogeneous distribution of the two components of delayed rectifier K+ current: a potential mechanism of the proarrhythmic effects of methanesulfonanilideclass III agents.* Cardiovasc Res, 1999. **43**(1): p. 135-47.
223. Dourin E, C.F., Gauthier C, Laurent K, Le Marec H, *Electrophysiological characteristics of cells spanning the left ventricular wall of human heart.* J Am Coll Cardiol 1995. **26**: p. 185-192Electrophysiological characteristics of cells spanning the left ventricular wall of human heartElectrophysiological characteristics of cells spanning the left ventricular wall of human heart.
224. Ramanathan, C., P. Jia, R. Ghanem, K. Ryu, and Y. Rudy, *Activation and repolarization of the normal human heart under complete physiological conditions.* Proc Natl Acad Sci U S A, 2006. **103**(16): p. 6309-14.
225. Akar, F.G., G.X. Yan, C. Antzelevitch, and D.S. Rosenbaum, *Unique topographical distribution of M cells underlies reentrant mechanism of torsade de pointes in the long-QT syndrome.* Circulation, 2002. **105**(10): p. 1247-53.
226. Ueda, N., D.P. Zipes, and J. Wu, *Functional and transmural modulation of M cell behavior in canine ventricular wall.* Am J Physiol Heart Circ Physiol, 2004. **287**(6): p. H2569-75.
227. Janse, M.J., E.A. Sosunov, R. Coronel, T. Opthof, E.P. Anyukhovsky, J.M. de Bakker, A.N. Plotnikov, I.N. Shlapakova, P. Danilo, Jr., J.G. Tijssen, and M.R. Rosen, *Repolarization gradients in the canine left ventricle before and after induction of short-term cardiac memory.* Circulation, 2005. **112**(12): p. 1711-8.
228. Janse, M.J., R. Coronel, and T. Opthof, *Counterpoint: M cells do not have a functional role in the ventricular myocardium of the intact heart.* Heart Rhythm, 2011. **8**(6): p. 934-7.
229. Janse, M.J., R. Coronel, and T. Opthof, *Rebuttal to M cells are present in the ventricular myocardium. Counterpoint.* Heart Rhythm, 2011. **8**(7): p. 1100.
230. Wilson, L.D., M.M. Jennings, and D.S. Rosenbaum, *Rebuttal to M cells are not present in the ventricular myocardium. Point.* Heart Rhythm, 2011. **8**(7): p. 1099.
231. Wilson, L.D., M.M. Jennings, and D.S. Rosenbaum, *Point: M cells are present in the ventricular myocardium.* Heart Rhythm, 2011. **8**(6): p. 930-3.
232. Nattel, S., C. Antzelevitch, and D. Noble, *Resolving the M-cell debate: why and how.* Heart Rhythm, 2011. **8**(8): p. 1293-5.
233. Barajas-Martinez, H., V. Haufe, C. Chamberland, M.J. Roy, M.H. Fecteau, J.M. Cordeiro, and R. Dumaine, *Larger dispersion of INa in female dog ventricle as a mechanism for gender-specific incidence of cardiac arrhythmias.* Cardiovasc Res, 2009. **81**(1): p. 82-9.
234. Liu, D.W. and C. Antzelevitch, *Characteristics of the delayed rectifier current (IKr and IKs) in canine ventricular epicardial, midmyocardial, and endocardial myocytes. A weaker IKs contributes to the longer action potential of the M cell.* Circ Res, 1995. **76**(3): p. 351-65.
235. Nerbonne, J.M. and R.S. Kass, *Molecular physiology of cardiac repolarization.* Physiol Rev, 2005. **85**(4): p. 1205-53.
236. Pond, A.L. and J.M. Nerbonne, *ERG proteins and functional cardiac I(Kr) channels in rat, mouse, and human heart.* Trends Cardiovasc Med, 2001. **11**(7): p. 286-94.
237. Nerbonne, J.M., *Molecular basis of functional voltage-gated K+ channel diversity in the mammalian myocardium.* J Physiol, 2000. **525 Pt 2**: p. 285-98.

238. Lesh, M.D., M. Pring, and J.F. Spear, *Cellular uncoupling can unmask dispersion of action potential duration in ventricular myocardium. A computer modeling study.* Circ Res, 1989. **65**(5): p. 1426-40.
239. Poelzing, S., F.G. Akar, E. Baron, and D.S. Rosenbaum, *Heterogeneous connexin43 expression produces electrophysiological heterogeneities across ventricular wall.* Am J Physiol Heart Circ Physiol, 2004. **286**(5): p. H2001-9.
240. Jacquemet, V. and C.S. Henriquez, *Loading effect of fibroblast-myocyte coupling on resting potential, impulse propagation, and repolarization: insights from a microstructure model.* Am J Physiol Heart Circ Physiol, 2008. **294**(5): p. H2040-52.
241. Vasquez, C., P. Mohandas, K.L. Louie, N. Benamer, A.C. Bapat, and G.E. Morley, *Enhanced fibroblast-myocyte interactions in response to cardiac injury.* Circ Res, 2010. **107**(8): p. 1011-20.
242. Cordeiro, J.M., L. Greene, C. Heilmann, D. Antzelevitch, and C. Antzelevitch, *Transmural heterogeneity of calcium activity and mechanical function in the canine left ventricle.* Am J Physiol Heart Circ Physiol, 2004. **286**(4): p. H1471-9.
243. Chung, C.S. and K.S. Campbell, *Temperature and transmural region influence functional measurements in unloaded left ventricular cardiomyocytes.* Physiol Rep, 2013. **1**(6): p. e00158.
244. Laurita, K.R., R. Katra, B. Wible, X. Wan, and M.H. Koo, *Transmural heterogeneity of calcium handling in canine.* Circ Res, 2003. **92**(6): p. 668-75.
245. Ashikaga, H., B.A. Coppola, B. Hopenfeld, E.S. Leifer, E.R. McVeigh, and J.H. Omens, *Transmural dispersion of myofiber mechanics: implications for electrical heterogeneity in vivo.* J Am Coll Cardiol, 2007. **49**(8): p. 909-16.
246. Xiong, W., Y. Tian, D. DiSilvestre, and G.F. Tomaselli, *Transmural heterogeneity of Na+-Ca2+ exchange: evidence for differential expression in normal and failing hearts.* Circ Res, 2005. **97**(3): p. 207-9.
247. Xu, L., J. Chen, X.Y. Li, S. Ren, C.X. Huang, G. Wu, and X.J. Jiang, *Analysis of Na(+)/Ca (2+) exchanger (NCX) function and current in murine cardiac myocytes during heart failure.* Mol Biol Rep, 2012. **39**(4): p. 3847-52.
248. Banyasz, T., L. Fulop, J. Magyar, N. Szentandrassy, A. Varro, and P.P. Nanasi, *Endocardial versus epicardial differences in L-type calcium current in canine ventricular myocytes studied by action potential voltage clamp.* Cardiovasc Res, 2003. **58**(1): p. 66-75.
249. Xu, L., X.Y. Li, Y. Liu, H.T. Li, J. Chen, X.J. Jiang, G. Wu, Y.H. Tang, X. Wang, and C.X. Huang, *The mechanisms underlying ICa heterogeneity across murine left ventricle.* Mol Cell Biochem, 2011. **352**(1-2): p. 239-46.
250. Wang, H.S. and I.S. Cohen, *Calcium channel heterogeneity in canine left ventricular myocytes.* J Physiol, 2003. **547**(Pt 3): p. 825-33.
251. *European Agency for the Evaluation of Medicinal Products (EMEA). ICH Topic S7B: note for guidance on the nonclinical evaluation of the potential for delayed ventricular repolarisation (QT interval prolongation) by human pharmaceuticals.* 2005: p. CPMP/ICH/423/02.
252. Bers, D.M., *Excitation–Contraction Coupling and Cardiac Contractile Force*2001: Kluwer Academic Publishers, Dordrecht, Netherlands
253. Glukhov, A.V., V.V. Fedorov, Q. Lou, V.K. Ravikumar, P.W. Kalish, R.B. Schuessler, N. Moazami, and I.R. Efimov, *Transmural dispersion of repolarization in failing and nonfailing human ventricle.* Circ Res, 2010. **106**(5): p. 981-91.
254. Sicouri, S. and C. Antzelevitch, *Afterdepolarizations and triggered activity develop in a select population of cells (M cells) in canine ventricular myocardium: the effects of acetylstrophanthidin and Bay K 8644.* Pacing Clin Electrophysiol, 1991. **14**(11 Pt 2): p. 1714-20.

255. Conrath, C.E., R. Wilders, R. Coronel, J.M. de Bakker, P. Taggart, J.R. de Groot, and T. Opthof, *Intercellular coupling through gap junctions masks M cells in the human heart.* Cardiovasc Res, 2004. **62**(2): p. 407-14.
256. Meijborg, V.M., C.E. Conrath, T. Opthof, C.N. Belterman, J.M. de Bakker, and R. Coronel, *Electrocardiographic T wave and its relation with ventricular repolarization along major anatomical axes.* Circ Arrhythm Electrophysiol, 2014. **7**(3): p. 524-31.
257. Solovyova, O., L.B. Katsnelson, P. Konovalov, O. Lookin, A.S. Moskvin, Y.L. Protsenko, N. Vikulova, P. Kohl, and V.S. Markhasin, *Activation sequence as a key factor in spatio-temporal optimization of myocardial function.* Philos Trans A Math Phys Eng Sci, 2006. **364**(1843): p. 1367-83.
258. Link, M.S., *Commotio cordis: ventricular fibrillation triggered by chest impact-induced abnormalities in repolarization.* Circ Arrhythm Electrophysiol, 2012. **5**(2): p. 425-32.
259. Krogh-Madsen, T. and D.J. Christini, *Action potential duration dispersion and alternans in simulated heterogeneous cardiac tissue with a structural barrier.* Biophys J, 2007. **92**(4): p. 1138-49.
260. Morita, S.T., D.P. Zipes, H. Morita, and J. Wu, *Analysis of action potentials in the canine ventricular septum: no phenotypic expression of M cells.* Cardiovasc Res, 2007. **74**(1): p. 96-103.
261. Lohezic, M., C. Bollensdorff, M. Korn, T. Lanz, V. Grau, P. Kohl, and J.E. Schneider, *Optimized radiofrequency coil setup for MR examination of living isolated rat hearts in a horizontal 9.4T magnet.* Magn Reson Med, 2014.
262. Noble, D., *A modification of the Hodgkin--Huxley equations applicable to Purkinje fibre action and pace-maker potentials.* J Physiol, 1962. **160**: p. 317-52.
263. Luo, C.H. and Y. Rudy, *A model of the ventricular cardiac action potential. Depolarization, repolarization, and their interaction.* Circ Res, 1991. **68**(6): p. 1501-26.
264. Kurata, Y., I. Hisatome, S. Imanishi, and T. Shibamoto, *Dynamical description of sinoatrial node pacemaking: improved mathematical model for primary pacemaker cell.* Am J Physiol Heart Circ Physiol, 2002. **283**(5): p. H2074-101.
265. Hund, T.J. and Y. Rudy, *Rate dependence and regulation of action potential and calcium transient in a canine cardiac ventricular cell model.* Circulation, 2004. **110**(20): p. 3168-74.
266. ten Tusscher, K.H., D. Noble, P.J. Noble, and A.V. Panfilov, *A model for human ventricular tissue.* Am J Physiol Heart Circ Physiol, 2004. **286**(4): p. H1573-89.
267. Mirams, G.R., M.R. Davies, Y. Cui, P. Kohl, and D. Noble, *Application of cardiac electrophysiology simulations to pro-arrhythmic safety testing.* Br J Pharmacol, 2012. **167**(5): p. 932-45.
268. Shannon, T.R., F. Wang, J. Puglisi, C. Weber, and D.M. Bers, *A mathematical treatment of integrated Ca dynamics within the ventricular myocyte.* Biophys J, 2004. **87**(5): p. 3351-71.
269. Bishop, M.J., G. Plank, R.A. Burton, J.E. Schneider, D.J. Gavaghan, V. Grau, and P. Kohl, *Development of an anatomically detailed MRI-derived rabbit ventricular model and assessment of its impact on simulations of electrophysiological function.* Am J Physiol Heart Circ Physiol, 2010. **298**(2): p. H699-718.
270. Bernabeu, M.O., M.J. Bishop, J. Pitt-Francis, D.J. Gavaghan, V. Grau, and B. Rodriguez, *High Performance Computer Simulations for the Study of Biological Function in 3D Heart Models Incorporating Fibre Orientation and Realistic Geometry at Para-Cellular Resolution.* Computers in Cardiology 2008. **35**: p. 721-724.

Appendix

Detailed Explanation for Data Analysis Routine

The detailed explanation of the data analysis algorithms given here is broken down into several sections with subheadings corresponding to the subheadings in Figure 2.2. The actual algorithm is colour coded in blue with comments shown in green.

A) Trace inversion

Invert row trace: i.e. Trace= -Trace

B) Initial filtering to filter out high frequencies to get upstroke time points

A Butterworth filter was chosen to yield the flattest (i.e. no ripples) response at the passband. The order of the filter was chosen to be the minimum order that fits the chosen pass (60 Hz) and stop (75 Hz) frequencies ensuring ripples of no more than 3 dB at the passband and a stopband attenuation of at least 60 dB. The typical order of Butterworth filter used for our data (with sampling frequency of ~510 Hz) is 28 with corresponding cut off frequency at 60.23 Hz.

The data analysis routine was written in Matlab using the built in functions *buttord* (the function to figure out the minimum order of Butterworth filter needed for the given passband and stopband conditions), *butter* (the function to design the digital Butterworth filter) and *filtfilt* (which evaluates the filtered signal trace with given filter parameters). The Matlab code to perform the filtering is shown below. More detail about on how to design and implement the Butterworth filter is given in the documentation for the three Matlab functions mentioned above, or in the book from Rabiner and Gold [1].

```
PassFrequency= 60;   % Set the chosen pass frequency
```

```
StopFrequency =75;   %Set the chosen stop frequency
NormalisingFrequency = 1000/frameperiod/2;
% calculate the frequency to which the pass and stop frequency can be normalised
NormalisedPassFreq= PassFrequency/ NormalisingFrequency;
% Pass frequency normalisation
NormalisedStopFreq = StopFrequency/ NormalisingFrequency;
% Stop frequency normalisation
[Order,CutoffFreq] = buttord (NormalisingFrequency, NormalisingFrequency, 3, 60);
% Call built in function buttord to calculate the minimum order and corresponding cut off frequency needed for the chosen pass (60 Hz) and stop (75 Hz) frequencies ensuring ripples of no more than 3 dB at the passband and a stopband attenuation of at least 60 dB
[NumeratorCoef, DenominatorCoef] = butter (Order, CutoffFreq, 'low');
% Call built in function butter to calculate the nth order coefficients for the numerator and denominator where n is the  filter order determined previously
FilteredTrace= filtfilt (NumeratorCoef, DenominatorCoef, Trace);
% Call built in function filtfilt to evaluate the filtered signal with the given coefficients
```

C) Detect upstroke points using the first derivative of the trace

The filtered traces were normalised before estimating the first derivative. The normalisation was performed to ensure consistency in the first derivative cut-off value that we set for each different data set (as different data sets may have very different signal quality resulting in very different first derivative values). The first derivative was estimated between two consecutive data points and was calculated as:

$$\frac{(V_m(t_{n+1}) - V_m(t_n))}{(t_{n+1} - t_n)}$$

where V_m refers to the normalised filtered trace and, t_n is the point in time where this first derivative value is estimated, and t_{n+1} is the adjacent time point of t_n (towards the positive infinity side). For our data, t_n and t_{n+1} are 1.96 ms apart from one another. Thresholding is applied to the first derivative to pick out the parts of the trace with a rapid increase (i.e. large first derivative). For our data a threshold of 0.002 was used, but this value may need adjustment depending on signal quality and upstroke velocity. The brief steps to identify the upstroke time point on the filtered trace are summarised below:

Find the minimum and maximum values of the filtered trace

Normalise the filtered trace to the difference between the minimum and maximum values

Calculate the first derivative for every point (apart from the last point) on the normalised filtered trace

Apply the threshold on the first derivatives calculated to pick out sections of the normalised filtered traces which can potentially be the upstroke phase of the AP

Find the maximum rise in signal amplitude (i.e. in the y direction) of these identified chunks

Apply a threshold on these rises in amplitude to pick out the sections which is more likely to be an upstroke than a noise peak (assuming the noise is lower in amplitude than the actual signal upstroke)

The first points in these selected signal sections (after applying first derivative and amplitude thresholds) are identified as the upstroke time points

The last points in these selected signal sections (after applying first derivative and amplitude threshold) are identified as the end of upstroke time points

D) Find baseline and define maximum signal for each AP

After identifying the upstroke time points, the raw signal trace can be divided into individual APs (i.e. signal domains between two identified upstroke time points). These individual APs are then processed separately to identify the baseline value (F_0) and the

'maximal' value (F_{max}). F_0 and F_{max} are then used to calculate the signal swing (an indication of how good the signal is for this trace compared to other traces). As these measured traces are noisy (even with frequency filtering), F_0 and F_{max} cannot be taken simply as the minimal and maximal points of the trace. In our routine, a histogram approach is used to identify F_0 and F_{max}. The histogram (or distribution) of each AP signal is drawn (the number of bins to divide an AP signal into depends on the range of values of the AP signal). For each AP which has some baseline following the repolarisation (this is normally the case given our pacing range: 1-5 Hz, but would not work for very high pacing frequency, or pacemaker tissue), these baseline related values should be at the left end of the distribution. Therefore to identify F0 using our histogram approach, we look within the bottom third of the signal distribution and identify a 'peak' (i.e. a bin with more observations than others) in this region of the histogram. After such a 'peak bin' is identified, bins around this 'peak bin' are selected (different thresholds may be needed for different signals; a typical cut-off value for our data traces was 4 bins away from the peak) as the baseline-associated values. The baseline-associated data values in the raw trace (assuming there is no dramatic irregular shift in the baseline) can be viewed as the real signal baseline with noise distortion, and such noise distortion can be approximated by a Gaussian distribution. A Gaussian distribution is then fitted over these selected baseline associated bins (Matlab built in function *fitdist* is used here) and the mean value of the Gaussian distribution is taken to be the baseline value of this AP. As mentioned before, this histogram method does not work in the case of rapid pacing (where there is no baseline included in the AP signal). In this case, the value at the depolarisation time point of the AP (or depolarisation value of the upcoming AP, or the mean of these two depolarisation values) can be used. F_{max} is set as the 95^{th} percentile of the AP distribution. For very slow pacing, this value may need to be adjusted (for example the 99^{th} percentile may be practical for 0.1 Hz pacing).

The signal swing (percentage) is calculated as:

$$Percentage\ Signal\ Swing = \frac{(F_{max} - F_0)}{F_0} \times 100\%$$

E) Fit the upstroke phase with a straight line

Although the upstroke phase of an AP should be less influenced by the noise compared to the repolarisation phase, in our routine a linear fitting is still performed on the upstroke phase to smooth out any potential noise-induced deviations. This linear fitting is also necessary to correct the upstroke time points (especially the starting point of the upstroke phase), since the upstroke time points (both the start and the end points of the upstroke phase) were identified on the filtered trace (which, potentially, has a flattened upstroke phase as a consequence of high frequency signal/noise filtering). As the initial identification of the upstroke start and end points are approximations only, the beginning and end of the initially identified upstroke phase can be noisy. Therefore only data points from the mid-third of the upstroke phase are included in the fitting. A straight line is fitted though these data points using Matlab built in function *polyfit*. After applying the linear fitting, the intersection points of the fitted upstroke phase with the previously identified baseline and the maximal signal are identified. These two intersection points are then set to identify the corrected upstroke start and end time points, respectively (replacing the initially approximated points from the first derivative).

F) Fit the repolarisation phase with a 4th order polynomial

The repolarisation phase of an action potential normally contains a plateau phase and a 'fast decay' phase. APs measured from rat or mouse heart has only the decay phase with almost no plateau phase. 4th order polynomials were used to fit the decay phase which worked well for action potentials with and without plateau phase. The routine is described below:

% identify the 'end of repolarisation point'

For each AP

Calculate the end of repolarisation threshold which is set to be the baseline value of that AP + 0.05* (maximal signal – baseline)

% the reason for not setting the repolarisation threshold to be directly the baseline but a little bit above this baseline is to avoid noise distortion at the baseline

Look for the first point after the end of upstroke time point that is smaller than the repolarisation threshold and set it as the end of repolarisation point

Pick out the data points between the end of upstroke time point and the end of repolarisation point

Fit a 4^{th} order polynomial through these data points

Find the intersection of this fitted repolarisation phase with the baseline and set it as the new end of repolarisation point

G) Linear baseline motion correction

Although the optical mapping data is collected from immobilised tissue (decoupled with chemical uncouplers like blebbistatin), a certain level of baseline drift is not uncommon (for example due to bleaching of the dye, or small movements in tissue and/or solution). In our routine, a linear correction is used to correct for changes induced by such motion. This does not address the non-linear dynamics of the baseline drift, but such drift is not a major issue of our data.

For each AP from the second to the second to last AP in the trace

Fit a straight line through the end of repolarisation point of the previous AP and the upstroke starting point of the next AP

Use this line as a reference for motion correction by dividing each point of this AP signal with the corresponding point on the line (i.e. the point with same time or x axis value)

For the first AP (i.e. between the first point and the end of repolarisation point of this AP)

Divide each data point on the AP by the baseline value of this AP

For the last AP (i.e. between the upstroke starting point to the last point in the data trace)

Divide each data point on the AP by the baseline value of this AP

I) APD Estimation

As mentioned in the main text, APD estimation was performed with a modified method where the AP peak value is replaced by the 95th percentile. For data with a very slow pacing frequency (and, hence, a large proportion of baseline data points, e.g. collected at 0.1Hz) a higher percentile (e.g. 99th or even 99.5th percentile) may be appropriate, as the 95th percentile may cut off some of the AP plateau as well. To identify the 95th percentile, the Matlab built in function *prctile* is used, please refer to the Matlab online documentation for more details about how to write a function to identify percentiles. The AP amplitude for APD calculation with this modified method is defined as the AP 95th percentile value minus the AP baseline. Matlab code for this APD calculation is provided below for the reader's information:

```
%% Calculate APD
% Preset the size of  APD80, APD 50 and APPeakValue 'vectors' with length equal to
number of APs identified in the data trace (for now set them as 'vectors' with zeros as entries)
APD50 = zeros(1,NumberOfAPUpstroke);
APD80 = zeros(1, NumberOfAPUpstroke);
AP_peak_value = zeros(1, NumberOfAPUpstroke);
```

```
% After linear motion correction, all baselines are now -1, as everything else is divided by
this previous baseline value
Baseline = -1*ones(1,NumberOfAPUpstroke);

% Loop over all the APs identified (the last one is processed separately after the loop)
for r = 1: NumberOfAPUpstroke -1
        % Call the function FindAllAPD to calculate APD for each AP
        [APD,APPeakValue(r)] = FindAllAPD
        (FittedTrace(UpstrokePointStart(r):UpstrokePointStart(r+1)),UpstrokePointStart(r),
        UpstrokePointEnd(r),Baseline(r),Frameperiod, FitPolyCoefficient(:,r))
        % The FitPolyCoefficients are the coefficients of the 4th order polynomial fitted over
        the repolarisation phase of the AP, and Frameperiod the time between two camera
        frames (in our case is 1.96ms)

        if isempty(APD.APD80)~=1
            APD80(r)= APD.APD80;
        end
        if isempty(APD.APD50)~=1
           APD50(r)= APD.APD50;
        end

end

% Calculate APD for the last AP in the data trace
```

```
[APD,APPeakValue(end)] = FindAllAPD (FittedTrace(UpstrokePointStart (end) : end) ,
UpstrokePointStart (end), UpstrokePointEnd (end),Baseline (end),Frameperiod,
FitPolyCoefficient(:,end));
if isempty(APD.APD80)~=1
   APD80(end)= APD.APD80;
end
 if isempty(APD.APD50)~=1
     APD50(end)= APD.APD50;
 end

function [APD,PeakValue] = FindAllAPD(APTrace,UpstrokePointStart, UpstrokePointEnd,
Baseline,Frameperiod,FitPolyCoefficient)
% This function returns APD50 and APD80 and identified AP peak value (i.e. 95th percentile)

%  This function takes in:
%  Trace for one action potential (fitted/processed)
%  Start of upstroke time point for this action potential
%  End of upstroke point for this action potential
%  Baseline (holding potential value)
%  Frame period
%  Coefficient for the 4th order polynomial fitted over the repolarisation phase

PeakValue = prctile (trace, 95);
```

```
[APD50TimePoint,Threshold50] = GetAPDTimePoint (50, UpstrokePointStart,
UpstrokePointStart, UpstrokePointEnd,PeakValue, Baseline, Frameperiod,
FitPolyCoefficient);

[APD80TimePoint,Threshold80] = Get_APD_time_point (80, UpstrokePointStart,
UpstrokePointEnd,PeakValue, Baseline, Frameperiod, FitPolyCoefficient);

APD = struct('APD80',APD80TimePoint,'APD50',APD50TimePoint);

function [APDTimePoint,Threshold] = GetAPDTimePoint (APDNumber, UpstrokeTimeStart,
UpstrokeTimeEnd, PeakValue, Baseline, Frameperiod, FitPolyCoefficient)
%% This function finds the point for APDXX and APDYY (e.g. APD50, APD20 or APD90)
% This function takes a single AP trace and the user need to input which
% APD is required
% The start and end of upstroke point
% AP peak value and baseline value
% Frame period
%  Coefficient for the 4th order polynomial fitted over the repolarisation phase

Threshold = Peakvalue-APDNumber/100*(Peakvalue-Baseline);

% Compute the intersection points of this fitted polynomial with the xx% of repolarisation
% threshold
FitPolyCoefficient (end) = FitPolyCoefficient(end)-Threshold;% compute the constant term
if isnan(FitPolyCoefficient)~=1
```

```
   root_vector = roots(FitPolyCoefficient);  % find all the roots
   root_vector = sort(FitPolyCoefficient);
   for i = 1 :length(FitPolyCoefficient)
      if isreal(FitPolyCoefficient (i))==0
         FitPolyCoefficient (i)=0;
      end
   end
  APDTimeIndex = find(root_vector >(UpstrokePointEnd- UpstrokePointStart )
*frameperiod,1,'first');
   APDTimePoint =root_vector(APDTimeIndex);
else
   APDTimePoint = 0;
end
```

J) Calculate AP Area Ratio (Normalised Area under the AP Curve)

A function written in Matlab is used to calculate the AP area ratio (normalised area under the AP curve: an AP shape descriptor) as shown below. This function used a trapezium rule approach to estimate the area under the AP curve. Since the AP repolarisation phase is fitted with a polynomial function already, we can also use actual integration as well.

```
function [area_under_AP,area_ratio]=
find_area_APD(AP_trace,baseline,frame_period,baseline_intresection,APD80, peak_value)
%% This function evaluates the area under the action potential curve
% This function uses the trapezium rule to estimate the area under curve
```

```
% This function takes: the fitted trace of one action potential(i.e. from the start of upstroke
point to the next upstroke point), baseline of that action point, time between two camera
frames, end of repolarisation point, APD80, AP peak value
%% code


accumulate_area_vector = [];
if APD80 ~=0  %only look for area under the curve for a well fitted curve
   if floor(APD80/frame_period)>2 % only find the area if the AP is long enough to use the
trapezium rule
      for i = 2:baseline_intresection
         area = (min(AP_trace(i),peak_value)-baseline+min(AP_trace(i- 1),peak_value)-
         baseline)*frame_period/2;  %trapezium calculation
         if isempty(accumulate_area_vector)~=1
                  accumulate_area_vector = [accumulate_area_vector,
                  area+accumulate_area_vector(end)];
         else
                  accumulate_area_vector= [accumulate_area_vector,area];
         end
      end
   else
      accumulate_area_vector =0;
      disp('this AP is too short to find area')
      area_ratio=0;
   end
```

```
    if isempty(accumulate_area_vector)~=1
        area_under_AP = accumulate_area_vector(end);
    else
        area_under_AP =0;
        disp('no area found ')
        area_ratio=0;
    end

    square_area = (peak_value-baseline)*(baseline_intresection-1)*frame_period;
    area_ratio = area_under_AP/square_area;
    if area_ratio >1
        disp('there is something wrong in area under the curve')
    end

else
    area_under_AP = 0;
    area_ratio = 0;
end
```

H) Calculation of AP skewness

The script, written in Matlab, to calculate AP skewness (another AP shape descriptor) is shown below. AP skewness is calculated with the Matlab built-in function skewness.

```
% Preset the size of APD80, APD 50 and APPeakValue 'vectors' with length equals to
APSkewness = zeros(1,NumberOfAPUpstroke);
```

```
% Loop over each AP
for s = 1:length(NumberOfAPUpstroke)
        APSkewness(s) =
        skewness(FittedTrace(UpstrokePointStart(s):UpstrokePointStart(s)+BaselineIntersecti
        onTimePoint(s)-1));
       % Calculate the skewness of the AP signal (between start of upstroke time point to the
       end of repolarisation point)

end
```

Appendix References

1. Rabiner, L. and B. Gold, *Theory and Application of Digital Signal Processing*1975: Englewood Cliffs.